Optimisation de la réalisation d'un élément de compresseur / Etude de l'interaction entre la microstructure du matériau, le procédé de transformation et la performance du produit fini

Nader Zirak

HESAM UNIVERSITÉ

Arts et Métiers Sciences et Technologies

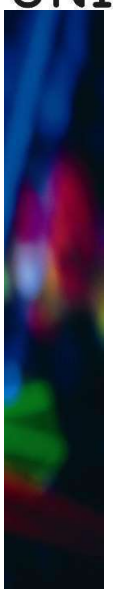

École doctorale n° 432 : Sciences des Métiers de l'ingénieur

Doctorat

T H È S E

pour obtenir le grade de docteur délivré par

l'École Nationale Supérieure d'Arts et Métiers

Spécialité " Matériaux et procédé "

présentée et soutenue publiquement par

Nader ZIRAK

le 3 octobre 2023

Optimisation de la réalisation d'un élément de compresseur / Étude de l'interaction entre la microstructure du matériau, le procédé de transformation et la performance du produit fini

Directeur de thèse : **Professeur Abbas TCHARKHTCHI**

Co-encadrement de la thèse : **Docteur Michaël DELIGANT** et **Docteur Mohammadali SHIRINBAYAN**

Jury

Mme. Marie-France LACRAMPE	**Professeur, École des Mines de Douai**	**Rapporteuse**
Mme. Zaida ORTEGA	**Professeur, ULPGC-Espagne**	**Rapporteuse**
M. David CHALET	**Professeur, École Centrale de Nantes**	**Présidente**
M. Grzegorz ŻYWICA	**Professeur, (IMP PAN)- Pologne**	**Examinateur**
M. Manuel HENNER	**Docteur, Directeur de la Discipline Génie Mécanique Simulation et Fiabilité Valeo**	**Examinateur**
M. Abbas TCHARKHTCHI	**Professeur, Arts et Métiers**	**Directeur de thèse**
M. Michaël DELIGANT	**MC-HDR, Arts et Métiers**	**Co-encadrant**
M. Mohammadali SHIRINBAYAN	**Docteur (HDR), Arts et Métiers**	**Co-encadrant**

T H È S E

Arts et Métiers – Campus de Paris
Laboratoire de Procédés et Ingénierie en Mécanique et Matériaux
Laboratoire d'ingénierie des fluides et des systèmes énergétiques

Acknowledgements

I extend my sincere appreciation to those who have played a pivotal role in the realization of this thesis, contributing their expertise, guidance, and unwavering support.

I extend my deep appreciation to the distinguished members of my thesis committee, Professors Marie-France Lacrampe, Zaida Ortega, David Chalet, Grzegorz Zywica and Dr. Manuel Henner, whose discerning feedback and scholarly critique have significantly elevated this work.

Foremost, I express my profound gratitude to my esteemed thesis advisors, Prof. Abbas Tcharkhtchi, Dr. Michaeal Deligant and Dr. Mohammadali Shirinbayan for their invaluable mentorship, scholarly insight, and steadfast support.

I wish to thank also Prof. Farid Bakir, Dr. Joseph Fitoussi and Dr. Khaled Benfriha for their precious guidance.

I would like to express my immense gratitude to the funding "The French Environment and Energy Management Agency" at large for their support.

I would like to thank my lab mates and friends for the cherished time spent together.

Finally, I would like to thank my parents as well as my brother who have always supported me and without whom I would not be here today.

Résumé

Cette thèse porte sur l'amélioration des performances de différents éléments d'un compresseur innovant pour l'industrie automobile. Les performances de ces éléments, notamment du rotor, sont sans doute liées à la microstructure du matériau utilisé pour la fabrication. Dans des conditions de contraintes mécaniques extrêmes, cette microstructure est fortement influencée par les différents paramètres liés, d'une part, à la nature du matériau et, d'autre part, aux conditions de mise en œuvre. Ainsi, pour améliorer les performances du produit, il est nécessaire de modifier les microstructures du matériau en choisissant, d'une part, un matériau fiable et, d'autre part, en optimisant les paramètres du procédé. À cet égard, différents types de polymères sont utilisés pour fabriquer la roue d'un compresseur par différentes techniques de fabrication additive et leurs performances sont étudiées. L'interaction entre la microstructure du polymère et les performances de l'élément compresseur est étudiée. Pour cela, un compresseur centrifuge est conçu sur la base de calculs itératifs d'un modèle 0D en combinaison avec des modèles de perte. Le modèle peut fournir une géométrie préliminaire du compresseur selon les spécifications. Ensuite, la géométrie 3D du compresseur a été optimisée par la dynamique des fluides computationnelle (CFD) pour trouver la meilleure géométrie et prédire ses performances. De plus, l'aspect structurel du rotor du compresseur a été analysé à l'aide d'un modèle numérique. La microstructure des matériaux à l'aide de différentes méthodes d'analyse et de caractérisation a été étudiée.

Mots-clés : Procédé, Matériaux polymères, Fabrication additive, Compresseur, Roue de compresseur

Abstract

This thesis focuses on improving the performance of different elements of an innovative compressor for the automotive industry. The performance of these elements, particularly the rotor, is undoubtedly linked to the microstructure of the material used for manufacture. Under conditions of extreme mechanical stress, this microstructure is strongly influenced by the various parameters linked on the one hand to the nature of the material and on the other hand to the conditions of implementation. Thus, to improve the performance of the product, it is necessary to modify the microstructures of the material by choosing, on the one hand, a reliable material and, on the other hand, by optimizing the parameters of the process. In this regard, different types of polymers are used to manufacture the impeller of a compressor by different additive manufacturing techniques and their performance is studied. The interaction between the polymer microstructure and the performance of the compressor element is studied. For this, a centrifugal compressor is designed based on iterative calculations of a 0D model in combination with loss models. The model can provide a preliminary geometry of the compressor according to the specifications. Then, the 3D geometry of the compressor was optimized by computational fluid dynamics (CFD) to find the best geometry and predict its performance. In addition, the structural aspect of the compressor rotor was analyzed using a numerical model. The microstructure of materials using different analysis and characterization methods has been studied.

Keywords: Process, Polymer materials, Additive manufacturing, Compressor, Compressor wheel

ABSTRACT

Table of contents

List of tables

List of figures

Introduction

General context

In recent decades, the automotive industry has been interested in the development of new technologies capable of guaranteeing energy efficiency and environmental protection and effectively reducing emissions of pollutants and greenhouse gases. In this regard, electric or hybrid vehicles have been at the center of the attention of car manufacturers. Studies on the evolution of the automotive market predict that a third of light vehicles will be electrified in the next decade. The advantages of these vehicles for the environment and onboard energy management are undeniable, but the final price of product, speed of recharging, and the thermal management of passenger compartment are among the challenges in this field. The rapid advances observed in recent years in materials, design, and processes make it possible to imagine new solutions to reduce costs while improving the efficiency of certain components of these vehicles. This thesis entitled "optimization of the production of a compressor element: Study of interaction between processing of microstructure of material and performance of the finished product" is carried out as part of the Ecolocar project to solve this challenge with the collaboration of the PIMM and LIFSE laboratories of ENSAM - Paris to meet the request of the company Valeo within the framework of the ADEME financing, which is based on the application of a centrifugal compressor. In a centrifugal compressor, the impeller can be referred to as a key component, and recent studies have been focused on using polymers thanks to their very low density and economic efficiency. In addition, additive manufacturing methods to fabricate this part due to providing unique advantages such as increased design flexibility, rapid prototyping, and the ability to manufacture complex geometries have been at the center of attention. In fact, manufacturing the part of a compressor by fused filament fabrication (FFF) through thermoplastic polymers such as Polyamide (PA) has been realized [1]. In this method, the fabrication will occur by deposition of a hot filament

onto filaments that were previously deposited. In a thesis, Vanaei [2] showed the quality of a fabricated part corresponds to the problem of bonding quality by this method, which involves controlling the material's viscosity evolution with respect to the temperature profile during the process. Recently, studies have effectively undertaken investigated and conceptualized the interlayer fusion of layers at a more fundamental scale. In this regard, converting the non-isothermal temperature condition in FFF method to equivalent isothermal weld times, interlayer adhesion has been investigated, and molecular diffusion as a key parameter in interlayer strengths has been predicted based on in-line temperature and viscosity measurements [3, 4]. In addition, in 2021 and 2022, observation of the weld zone has been analyzed directly on Poly(lactic acid) (PLA) and polyether ether ketone (PEEK). Based on this, it can be said that an investigation of viscosity dependence with respect to the process parameters on the weld zone would be a subject that seems to need more research. On another point, manufacturing the impeller through stereolithography approach (SLA) which has been used in some studies was evaluated in this thesis [5]. This method is among the common additive manufacturing and referred to in the 1980s which is a "reactive" technology by using the thermoset polymers. Suitable curing during this process can be addressed as a key parameter that affects the final part properties manufactured. That unreacted monomers caused reducing the mechanical performance of the fabricated parts. Generally, acrylates, vinyl ethers, and epoxides have been among the types of multifunctional monomers which were used for laser-induced polymerization. In the different types of multifunctional resin production, the mechanism of polymerization occurs by the reaction of the acrylate group and an epoxy group through a radical and cationic mechanism, respectively. In this context, we have endeavored to develop the main lines of research as follows:

• We study the optimization of the FFF and SLA process using the interaction of process variables. This optimization will be performed in FFF process through rheological characteristics and in-situ thermal measurements. In SLA method, the interaction of process and post-process on the mechanical and physicochemical properties have been evaluated. Finally, we were interested in the analysis of the effect of microstructure and dimensional stability of the fabricated impeller on the final performance of the centrifugal compressor. The thesis outlines comprises six chapters, in following, we will give a brief explanation of these chapters: The first chapter of this thesis "Bibliographic Study", provides a comprehensive and systematic review of the relevant literature pertaining to the wide range of polymers used in pump impeller fabrication, including but not limited to thermoplastics and ther-

mosetting polymers. It examines the unique properties and characteristics of each polymer and their suitability for specific applications in terms of strength, durability, chemical resistance, and thermal stability. Additionally, it investigates the influence of processing techniques on the microstructure of these polymers and the resulting impact on the performance of the finished product. Chapter 2, titled "Materials, Methods and Compressor Dimensional" delves into the experimental materials, methods, and compressor design developed during this thesis. In the first section materials including PLA, Polyphenylene sulfide (PPS) and an acrylate-based resin were introduced. PLA was chosen as a biosource and biodegradable thermoplastic with a potentially infinitely reusable polymer. Considering that high rotational speeds were of interest to study in this thesis, a high-performance polymer, PPS was also used. In addition, acrylate-based resin due to high accuracy and low cost was selected as a thermoset polymer. The characterization methods and manufacturing of the samples were explained in following sections of this chapter. The method of design of this high-speed centrifugal compressor was explained in the last section of this chapter. Includes iterative calculations of a 0D model in combination with loss models and computational fluid dynamics (CFD) to predict the performance. Chapter 3 presents the process optimization in FFF method by analyzing the interfacial bonding. The first section will discuss the primary characterization of materials. In the second section formation of interface and interphase with respect to the different parameter processes have been done by temperature profile, rheological characterization, atomic force microscopy, and optical microscopy. Mathematical modeling and optimization were applied in the last section and the impeller was fabricated with optimum parameters. Chapter 4 presents the optimization of process and post-process parameters on SLA method. In this regard, thermal and physicochemical properties were analyzed in the first section. Mechanical characterization from quasi-static to high strain rate loadings considering the different percentages of polymerization and build orientation was investigated. Finally, fractography of samples by scanning electron microscopy was performed. Structural analysis of the fabricated impeller can be mentioned as the first step to analyzing the performance of the final compressor. Chapter 5 provides a numerical model for structural analysis. The model was applied to the optimized manufactured component. In the next section of this chapter, final performance of the compressor considering the microstructure and geometric accuracy of manufactured impellers is presented. Finally, the achievements of the thesis are presented in chapter 6 "conclusions". The bibliography showed the huge studies on using the polymeric impeller in the pumps application fabricated by additive manufacturing technology. In ad-

dition, the importance of suitable interlayer adhesion in FFF was shown in the bibliography, however, the lack of information concerning the analysis of the weld zone led us to characterize this area with respect to the process parameters. Also, the results of this work showed the vital role of this aspect on the final performance of the compressor from flow analysis. The feasibility of using SLA fabricated impeller to use at high rotational speed has been shown. In this regard, a physical-chemical and high strain rate effect on the mechanical behavior was investigated. Finally, results show the impact of the microstructural of manufactured parts from different process parameters on the final performance.

Chapitre 1

Literature review

Content

1.1 An overview of the compressors

In particular, the function of a compressor can be defined as a system to compress and increase the pressure of the working fluid. Providing air for combustion, compressed air for application in pneumatic tools, transport process of fluid by pipelines, and a certain process for the fluid circulating process among the purposes of using compressors are mentioned. Turbojet engines used in aerospace propulsion, power generation using industrial gas turbines, turbocharging of internal combustion engines, and pressurization of gas and fluids in the process industry are the examples that attracted the attention of the studies [6]. Generally, compressors can be divided into two categories positive displacement and continuous flow. The different categories of compressors are presented in Figure 1.1. Positive displacement compressors are compressors in which one or more volumes decrease and increase kinematically. In other words, in these compressors, the successive limitation of fluid volume increases the fluid pressure which can be used for intermittent flow in a closed space. Positive displacement compressors were divided into two types: either reciprocating or rotary type. The pressure in the reciprocating compressor increased by reciprocating the motion of a piston in the cylinder. In rotary positive displacement compressors, compression, and displacement happen by rotating elements. Sliding vane, liquid piston, straight-lobe, and helical-lobe are the rotary positive displacement subdivides [7]. The continuous-flow type compressors are the compressors with the capability of converting the velocity of the enclosed inlet fluid mixture by a high-velocity gas or steam jet to pressure in the diffuser for compressing the fluid. Dynamic and ejector compressors are the class of this category. In a dynamic compressor increasing the pressure provides by converting the velocity of fluid which was caused by a rotational element to the pressure. Centrifugal, axial-flow, and mixed-flow are listed under this category of compressors. It is worth noting that the type of flow gas created in centrifugal, axial, and mixed flow is radial, and axial and combines some characteristics of centrifugal and axial flow, respectively [8]. As mentioned, there are many categories of compressors existing and the selection of compressors depending on the situation will be different. Low maintenance costs, compact size, and suitable weight are among the important properties of the centrifugal compressor which has led to its differentiation from other compressors.

In general, axial-flow compressors are used for providing high flows and low-pressure ratios. The efficiency of axial-flow compressors is more than that of centrifugal compressors; however, axial com-

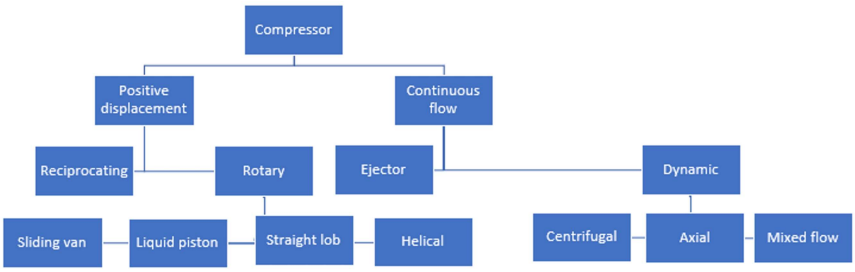

FIGURE 1.1 – Categories of compressors

pressors have shown a smaller operating region. Centrifugal compressors are used at medium flow rates and high-pressure ratios which are very efficient in this situation. In low flow rates and high-pressure ratios, rotary and reciprocating, compressors are usually applied [8, 9]. Centrifugal compressors have been one of the most applicable compressors in the industry. Some of the important properties of this type are given below:

- Smooth operation,
- Large tolerance for process fluctuations,
- Higher reliability compared to other types of compressors,
- Ability to work with gases with low molecular weight

Output pressure for centrifugal compressors up to 70 MPa has been reported. Generally, The drive of this kind of compressor gas turbine or electric motor which in some cases, such as downstream applications, steam turbines or turboexpanders can be used. Operating speed in centrifugal compressors can consist of various rang, for example in the case of aircraft and space applications is in the range of 50,000 - 100,000 rpm. In the case of gas transmission applications, 8,000 – 14,000 rpm were reported [10]. The process of transferring fluid in a typical centrifugal compressor takes place in such a way that the fluid is compressed by converting the velocity of the fluid to the pressure by an impeller that is rotating rapidly. In this way, the velocity of the fluid is increased by the impeller, and the conversion of the velocity of the fluid into the pressure is done in the diffuser. Normally half the pressure is increased in the impeller and the other half in the diffuser (Figure 1.2) [11]. As mentioned, the flow of fluid in the centrifugal compressor is radial this follows the entry of gas in the axial direction of the compressor and is delivered radially to the diffuser. Another part of the compressor is the volute. The function of the volute (also known as a scroll or a collector) is simply to collect the diffuser exit flow

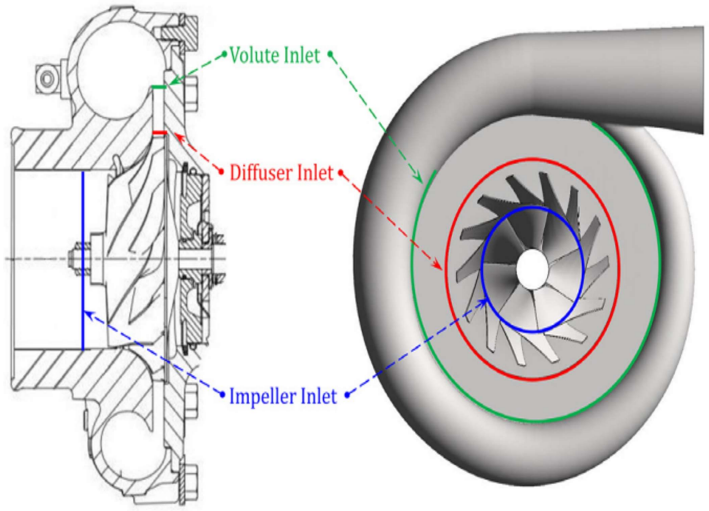

FIGURE 1.2 – Schematic of the components of a centrifugal compressor [11]

and to guide it as efficiently as possible to the compressor outlet, without impeding the effectiveness of the diffuser [12].

1.2 Materials used for fabrication of impellers

Impellers are referred to as a key component of turbomachinery [13]. By rapidly rotating the impeller can force the working fluid by converting the velocity of the fluid to pressure [14]. Considering the use of impellers in different rotary machinery systems, they have played a vital role in various applications such as aerospace [15], automotive [16], and medical [17] applications. Many studies have attracted attention to improving a system's efficiency by impellers [18]. To this end, in general, studies based on geometry optimization [19], the use of high-performance materials [20], and suitable manufacturing processes [13] have tried to improve the system. Weight loss of the impeller, along with the optimization of the impeller with a proper manufacturing process, can lead to achieving an ideal impeller. So that the use of lighter materials with high strength and an ability to withstand forces during working is considered an effective step to increasing efficiency [5]. Metal [21], polymeric [22] and composite [23] materials are the main categories of materials that have been used for the fabrication of rotors and impellers. In general, the weight, the high cost of raw materials, the fact that common methods of fabrication have led to increasingly high manufacturing costs, and the high maintenance cost

of metallic rotors, have all proved to be the main disadvantages of metals [21]. All these problems have led to polymers and composites being at the center of attention about studies. Micro Organic Rankine Cycle (mORC), Heating, Ventilation, and Air Conditioning (HVAC), and refrigeration systems are among the systems which have the potential to replace their rotary components with polymer or polymer composites. For example, in the case of the micro Organic Rankine cycle, which is one of the important systems for handling fossil fuel sources (flue gases and waste heat) and renewable energies, the replacement of metal rotors with polymer and composite rotors has been mentioned as an important factor in dealing with the limited use of these turbines due to their uneconomical cost [22]. Using polymers and composites due to their low weight, good chemical resistance, and good strength has been a good choice for use instead of metals in the manufacture of rotors and impellers [24]. Also, the use of these materials in manufacturing can involve methods with lower costs compared to traditional methods for producing metal parts such as forging and casting. In general, thermoplastic polymers and thermoset polymers were among the polymers that have been used to fabricate the rotors. In thermoplastic polymers, acrylonitrile butadiene styrene (ABS) [22], polylactic acid (PLA) [25], and polyether ether ketone (PEEK) [26] are the examples that have been used for fabricating the impellers. On the other hand, composites have been used in situations where a material with a higher strength is required [23]. Among the composites, PEEK-GF30 has been one of the composites that have been used for this purpose. Given the vital role of materials used in rotary components fabrication, concerning the production of the different components and working conditions, the selection and manufacture of materials have been among the most important thing [16]. In this regard, great progress has been made in the materials used for the fabrication of impellers. As mentioned, metals, polymers, and composites have been the main materials used to fabricate impellers. In general, in the metals class, stainless steel, titanium, aluminum, and nickel alloys are among the metal-based alloys widely used to produce rotors, impellers, and fans [16]. Nickel alloys have been used in high-temperature applications, such as a combustion chamber or turbine inlet, which are known as “hot zones”. On the other hand, titanium alloys have been used in zones with lower operating temperatures, known as “cold zones”, such as compressor inlets and turbine outlets [15]. Considering the reasons mentioned, the focus of this study will be on polymers and polymer composites. Good resistance to impact loads [27], fatigue [28], erosion [29], and a high ratio between mechanical resistance and material density [5] are among the properties that are exemplary when using polymers and polymer composites in the production of impellers, and,

as such, they have been a decisive choice.

1.2.1 Polymeric impellers

In different kinds of systems, to increase the efficiency of compressors and pumps and economic efficiency, polymers have been introduced for the fabrication of rotors [16, 22, 30, 31]. Polymers defined as macromolecules consist of large numbers of smaller molecules, or repeating units, called monomers, which are formed chemically bonded. Polymer molecules can have a degree of order, relative orientation and a kind of monomer that can vary within the same polymer molecules [32]. Low price, ease of manufacture, resistance to water and versatility have been among the advantages of polymers, and these factors have led to their application in the industry [33]. Polymers can exist in different forms of powders, granolas, filaments and res,ins, which are selected depending on the fabrication process. In general, polymers used for the fabrication of impellers can be divided into two categories of thermoplastic and thermoset polymers.

1.2.1.1 Impellers based on thermoplastics

Thermoplastics have been used to fabricate impellers in many studies. Generally, considering the ability of this group to soften and melt when heated, a two-state fabrication based on the heat-softening or liquid state is preferable [34]. Injection molding [35] and 3-D printing-based processes such as fused deposition modeling (FDM) [36] or selective laser sintering (SLS) [37] are the methods by which thermoplastics are used for parts fabrication. Thermoplastics are divided into two groups amorphous and semi-crystalline. Powders, granola, and filament are different forms of thermoplastics polymers. Recyclability, good ductility, and impact resistance compared to thermosets are the advantages of this class of polymer. In general, thermoplastic parts show a modulus lower than 5 GPa, which depends on the chemical composition and fabrication method as it can be changeable [34]. Figure 1.3 shows the different types of thermoplastic polymers concerning ultra-performance, engineering-grade, and general-purpose categories that represent the different classes of polymer materials.

Among the different types of thermoplastic polymers, ABS [22], PLA [25], Polyethylene terephthalate (PETG) [38], PEEK [26], and Polyphenylene sulfide (PPS) [39] are the examples that have been used for the fabrication of rotating components. Table1.1. shows the physical and mechanical properties of these polymers. Modulus, cost, degradability, and water absorbability were the important

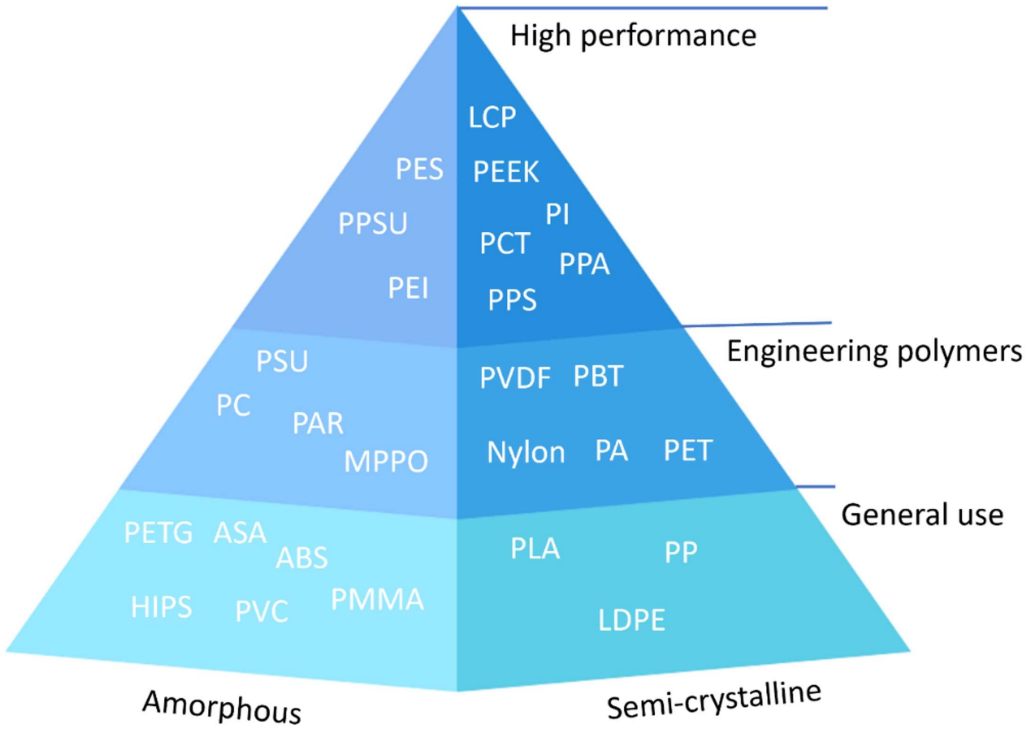

FIGURE 1.3 – Different types of thermoplastics polymer

Table 1.1 – Process Parameters of FFF Printed rotors

Column 1	PLA	ABS	PPS	PETG	PEEK
Glass transition temperature (°C)	56–63	102–115	75–85	49–75	142.85
Melting temperature (°C)	125–178	-	285	-	342.85
Modulus (GPa)	1.03–4.0	1.8–2.39	3.9–4.1	0.9–1.6	3.6
Tensile strength (MPa)	51.7–80.9	42.5–44.8	79	44.12–57	107
Ref.	[40]	[41]	[42]	[43, 44]	[45]

parameters that impacted the candidate selection.

ABS is an amorphous thermoplastic polymer that has been applied to the fabrication of rotary components in micro Organic Rankin Cycle (mORC) [22, 46], pumps [24, 47–49] and the rotor blades of drones [50, 51]. Hernandez-Carrillo et al. [22] studied the use of an ABS impeller in the mORC. This study was performed by increasing the efficiency of the mORC by reducing the conventional weight of the impeller. Working conditions of the impeller, such as inlet temperature and pressure were 55 °C, 4 Bar and the outlet temperature and pressure were 44.9 °C, and 2.5 Bar, respectively. Also, the rotational speed was 36,000 rpm. Considering the working condition and factor of safety (FoS), which represents the ratio of yield strength per the maximum equivalent stress, the ABS impeller provided the expected operating condition. Reducing the cost of the fabrication of the impeller by using the ABS, which can cause the mass production of mORC, was one of the important advantages of applying this polymer. Also, according to their simulation results, with respect to the working fluid of Penta-fluoro-propane (R45fa), the isentropic efficiency of the impeller was estimated to be 76–86%. However, the limited operation of ABS under 89.9 °C was mentioned as one of the narrow operation capabilities. Pavlovic et al. [47] investigated the mechanical properties of ABS in the fabrication of impeller pumps and showed that ABS can be considered a good candidate for the fabrication of impellers. Polak [48] studied the ABS impeller for a radial centrifugal pump by verifying the hydraulic parameters. The results showed an increase in efficiency in rotational speed of 2950 rpm. The surface smoothness of the ABS impeller was mentioned as an effective parameter in increasing efficiency. PLA is a semi-crystalline thermoplastic polymer that is derived from renewable resources, such as corn starch or sugarcane. Biodegradability and composability of the PLA are among the properties of this polymer [52]. Economic cost, environment-friendly biocompatibility, and suitable physic mechanical properties of this polymer have made this a suitable choice when compared to other polymers. PLA has been used for the fabrication of impellers for pumps [24, 53, 54], compressors [55] and marine

[25] applications. For the fabrication of impellers in pumps and marine applications, PLA has been used. However, considering the accessibility of two polymers of PLA and ABS, these two kinds of thermoplastic have been compared in many studies as impellers of pumps. In general, considering the high level of the brittleness of PLA when compared to ABS [47], it can be said that application by more stress ABS has been preferred. Birosz et al. [55] studied the PLA wheel for compressors given the importance of creep and orientation properties of the material, which are essential to designing the impeller of the compressor during rotation. Regarding tensile strength, creep and bending properties were considered when analyzing the PLA. Creep performance results showed that PLA creeps behavior was most similar to the weakly cross-linked elastomer so that at low loads, the creep curve was held to a constant limit. According to their results, PLA was introduced as a material worth choosing when seeking long-term service. PETG is an amorphous thermoplastic that has been used in the fabrication impellers for pumps [56, 57] and mORC [46] applications. The good water resistance and biodegradability of this polymer [58] are reasons for choosing this polymer in the manufacture of pump blades. Odetti et al. [57] investigated the PTEG impeller in the application of a Pump-Jet Module (PJM). Considering the rotational speed of 1200 rpm that led to a thrust of 14 N, a PTEG impeller showed suitable properties during the working for this application. Polyether-ether-ketone (PEEK) is a high-performance semi-crystalline thermoplastic polymer [45]. Excellent mechanical and thermal properties and good chemical resistance are among the bold advantages of this polymer [59]. PEEK impeller has a high position in pump and compressor applications for different industries such as automotive [59], aerospace [60], and medical [17]. In the case of medical applications, using the PEEK impeller in the centrifugal pump due to its improved durability and strength has attracted a lot of studies' attention [17, 61, 62]. Similarly, in the case of heart failure, using the PEEK impeller in the centrifugal pump of a HeartWare Ventricular Assist Device (HVAD) due to the improved durability and strength it offers has attracted a lot of studies' attention. In the HVAD, the rotational speed of the PEEK impeller is in the range of 1800–4000 rpm and generates flows up to 10 l/mL [17]. Also using the PEEK impeller with the aim of reduction in wear, reduced noise levels, and more consistent running properties by replacing stainless steel for regenerative pumps was another application of this polymer [60]. In general thermomechanical properties, due to the thermal stress during increased temperature, are one of the important factors that can lead to the limitation of using polymers as impellers in various applications. Zywica et al. [26] studied the use of plastics to use them as an impeller for the ORC

system. In this study, PPS and PEEK were considered thermoplastic polymers. The rotational speed for the impeller was 120,000 rpm. The simulation results based on heat resistance, chemical resistance, strength properties, and thermal expansions showed that PEEK polymer can be considered a good material for the fabrication of impellers.

1.2.1.2 Impellers based on thermosets

The thermosetting polymer can be defined as a soft solid or viscous state prepolymer that can be changed to the infusible, insoluble polymer network (thermoset) by curing. Curing of the prepolymer can be performed based on heating or suitable radiation. During the curing, cross-linking the materials leads to them setting and they can no longer flow [63]. The main components of thermosets consist of monomers, co-monomers (hardeners), catalysts, and initiators. Also for improving the mechanical properties and reducing the costs, some fillers such as calcium carbonate, sawdust, recycled powdered thermosets, etc., can be used in the formulation of thermosets [64]. In addition, the use of the short fiber to improve the mechanical properties is one of the important ways to increase the mechanical properties [65], which will be discussed in the composite section. Thermosets are divided into epoxy resins, phenolic resins, amine–formaldehyde, polyurethanes, silicones, cyanates, vinyl esters, dicyclopentadiene, and other metathesis thermosets. Depending on the different formulations, different physical and mechanical properties can be achieved from the thermosets. For example, glass transition temperature can vary in the range of 20 to 200 °C [66]. Modulus can be achieved for light-cured resin [67] and continuous carbon fiber-reinforced thermosetting composites [68] in the range of 0.18 and 161.4 GPa, respectively. Thermoset manufacturing processing is divided into categories: additive manufacturing techniques; solid thermoset processing; and liquid thermoset processing [69]. Matveev et al. [70] studied the thermoset impellers fabricated by the SLA method. High chemical resistance, practically inert to liquid hydrocarbons (gasoline, kerosene, petroleum, and synthetic oils,) and hot streams (up to 100 °C) of water and air fabrication were some requirements of their study. In their study, thermoset impellers fabricated by 3D printing were considered as parts that fully meet the requirements of the experimental samples for gas-dynamic studies. In the case of the turbocharger, Andrearczyk et al. [5] investigated the wheel printed by a thermoset. The size of the rotor was 42.5 mm in diameter (Figure 1.4a) and the maximum rotational speed was selected at 100,000 rpm. According to the simulation results, the maximum stress on the impeller for a rotational speed of 90,000 rpm was

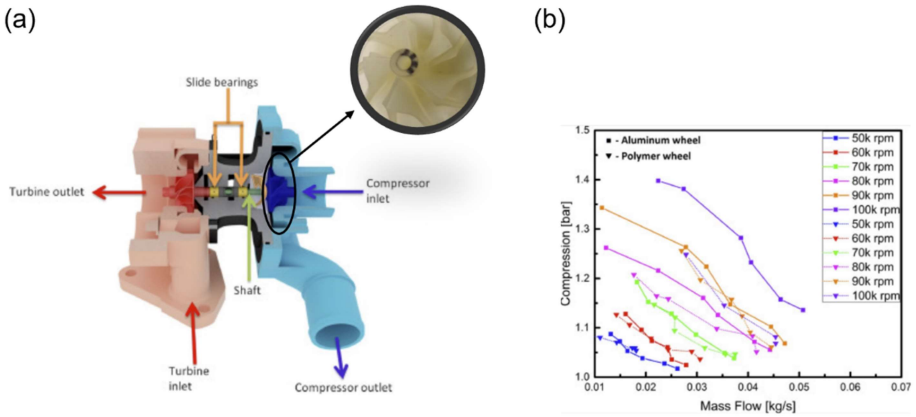

FIGURE 1.4 – (a) Cross section of the turbocharger with compressor wheel fabricated by MJP and (b) experimental results of polymeric (dotted lines) and aluminum (solid lines) compressor wheels

27 MPa, whereas the yield stress of the resin printed was 54 MPa. We should mention that the results obtained from the compressor wheels, which were fabricated by polymer and aluminum, showed that at 90,000 rpm the polymeric wheel can operate like an aluminum wheel (Figure 1.4b).

1.2.2 Polymer Composites Impellers

The key role of composite materials, considering their weight reduction effect without sacrificing robustness, has been shown in modern industry [71]. In this section, only the polymer matrix composite will be discussed. In the polymer matrix composite, the mechanical properties of the materials will be improved by using fiber as reinforcement in the matrix of the polymer. Considering the type of matrix and reinforcement, the composites can have different categories. In general, reinforcement fiber can be divided into inorganic, glass, and carbon fibers [72], and composite reinforced with either glass fibers (GF) or carbon fibers (CF) have been included in more than 90% of the studies [73]. Thermoplastic [74] or thermoset [75] polymers have been used as polymeric matrices for the fabrication of impellers.

1.2.2.1 Carbon Fiber as Reinforcement in Fabrication of Impellers

Carbon fiber polymer-matrix composites have been introduced as one of the efficient classes of material, in the place of metals. Depending on the type of fiber condition, be it short or continuous, these types of composites can be classified. PPS, PEEK, PI and PEI are the thermoplastics and

epoxy is the thermoset, which has been widely used as a matrix for these composites [76]. PEEK [77, 78] and epoxy [78, 79], car-bon-fiber-reinforced, are the composites that have been most used in the fabrication of impellers. PEEK reinforced with carbon fibers has been one of the exemplary composites used in the fabrication of rotary components of pumps and compressors [80, 81]. PEEK composites reinforced with polyacrylonitrile short carbon fibers, 30% in weight, which is called CF30 PEEK is a famous commercial type of this composite [82]. Garcia-Gonzalez et al. [45] investigated the energy absorbed to analyze the mechanical impact behavior of short carbon fiber reinforced PEEK composites and unfilled PEEK. The tensile elastic modulus of GF30 PEEK in transversal, longitudinal conditions, and unfilled fiber PEEK were 12.6, 2,4 and 3.6 GPa, respectively. According to their results, reinforced composites showed a brittle failure. The direction of fibers and degree of crystallization played a key role in the mechanical properties. The homogenization of elastic material and anisotropic damage for failure prediction has been proposed in their study. Investigating the vapor-grown carbon nanofibers for use as reinforcement for PEEK showed that by increasing the nano-fiber, the modulus of composites increases, which refers to the effect of fiber on the crystallization of PEEK. Also, the effect of carbon nanofiber as a lubricant, which was associated with significant decreases in the wear rate of the composite, was shown [83]. Yang et al. [84] studied the effect of the surface modification of carbon fiber on the mechanical properties of CF PEEK composites. Their method was introduced as one of the main solutions to enhancing the interface and led to reaching an interfacial shear strength of 83.13 MPa. The investigation of the PEEK carbon-reinforced impeller in the case of a micro-turbine generator introduced this composite as a suitable material instead of an aluminum impeller [22, 46]. We should mention that the mechanical properties of the impeller at the rotational speed of 32,040 and 40,500 rpm were appropriate. However, considering the importance of the chemical reaction of working fluid with an impeller in ORC and refrigeration systems, the final approval of the substance was considered dependent on more studies [46]. Martynyuk et al. [23] investigated using a polymer reinforced with carbon fiber for the fabrication of a centrifugal compressor wheel. The maximum working temperature was 287 °C, and the outlet pressure was 7 bar. The calculations showed that carbon fibers UMT 49S and phthalonitrile binder PN-3M, which have been used as reinforcing parts, can be used to fabricate the wheel of a centrifugal compressor. Also, the use of composite resulted in a 45% reduction in rotor weight compared to the similar aluminum specimen. Using carbon fiber in the matrix of thermosets (especially epoxy) to improve the properties, has

been used to fabricate impellers in pump and compressor applications [75, 76, 79]. In general, resisting moisture and other environmental influences, offering lower shrinkage and better mechanical properties are among the points that lead to the selection of epoxy resins as a polymeric matrix [85]. Shah et al. [86] studied the thermomechanical characterization of different types of epoxy resin of HinpoxyC, Hin-poxyVB, ARL135, and ARL136 epoxy resin systems reinforced by HCU200/A45 carbon fiber. The tensile strength of the reinforced epoxy resin systems of HinpoxyC, HinpoxyVB, ARL135, and ARL136 were achiwas at 745, 752, 698, and 830 MPa, respectively. In general, the final properties can be variable depending on the type of matrix, carbon reinforcement, and fabrication process. For example, Ming et al. [87] studied the different parameters in 3D-printed continuous carbon fiber reinforced thermosetting epoxies, such as printing speed, printing space, printing thickness, curing pressure, and curing temperature with the ato optimizeeters. According to their results, optimized conditions with 58 wt.% fiber led to them achieving the maximum flexural strength and modulus of 952.89 MPa and 74.05 GPa, respectively. Furthermore, Pérez-Pacheco et al. [88] studied the effect of moisture absorption on damage accumulation in carbon fiber–epoxy composite laminates with respect to the two dconcerningicial carbon fiber treatments. In their studies, the interphase microstructure has been mentioned as a critical aspect of the moisture diffusion mechanism. Considering the number of hydrogen bonds between the water and epoxy resin network, and the two different activations of energy, subsequently, different phenomena such as swelling or degradation can happen. Also, the sensibility of matrix failure mechanisms caused by hydrolysis has been discussed. Uhlig et al. [89] studied the highly stressed bladed rotor fabricated by epoxy resin and reinforced with 60% carbon fiber. According to their results, the explosion rational frequency of the rotor was in the range of 1080–1100 Hz. Also, the stress exposure factor for the fiber fracture at the explosion frequency range was about 0.8, so this factor for the inter-fiber fracture should not have exceeded the failure limit of 1. The composite rotor has been considered a suitable candidate to improve the efficiency compared to aluminum alloy rotors. Liu et al. [90] used carbon fiber reinforced shape memory epoxy composites to fabricate the wind blades. The stiffness under good shape memory fixation at room temperature and switching temperature (Tsw) reached 37 and 4.4 GPa, respectively. According to their results, a sustainable continuous stable mechanical state has been observed. Also, variable wind speed in the range of 9–10 m $s^{-1}$was provided.

1.2.2.2 Glass Fiber as Reinforcement in Fabrication of Impellers

Umaras et al. [39] studied the impeller fabricated by reinforced PPS with 40% fiber-glass in the application of an automotive water pump. The rotational speed was 4500 rpm, and the working fluid was water and ethylene-glycol in the temperature range of 80–100 °C. Maximum radial and tangential stresses due to the press fit on the impeller have been calculated at 100 and 83.5 MPa, respectively. Considering the physicomechanical properties of PPS reinforced with glass and maximum stress on the impeller this material has been considered a suitable selection in this situation. In the case of a micro-turbine-generator, PEEK-GF30 radial turbine impeller has been considered as one of the suitable candidates. Hernandez-Carrillo et al. [46] investigated the fabrication of a microturbine generator for an Organic Rankine Cycle (ORC) to replace polymers with metals, and they considered the high technical and economic potential of polymers. For this purpose, the rotor was produced by the FDM process by using polymer and composite materials and the diameter of the impeller was 45 mm. The results showed the ability to rotate the rotor at a rotational speed of 32,040 rpm and a peak rotational speed of 40,500 rpm. Also, due to the importance of the final surface obtained for the rotors and impellers on the final efficiency [91], it was shown that an acceptable final surface has been obtained by this method for the fabricated rotor. In another study, Organic Rankine Cycle microturbines fabricated by aluminum, ABS and PEEK-G30 were compared together. The diameter and rotational speed of the impeller were 49 mm and 36,000 rpm and the R245fa fluid was used as a working fluid. According to their study, in addition to the fact that the PEEK-GF30 and ABS showed they were suitable for mass production processes, the economic benefits, properties such as chemical resistance and lower inertia, with the latter characteristic helping to minimize imbalance, shaft fatigue, and damage of the casing in case of failure, were all among the other advantages they found. In addition, the results of a simulation showed that PEEK-GF30 and ABS can be good candidates in these operating conditions and are good alternatives to aluminum in this application [22]. In general, required properties for working conditions, economic efficiency, and manufacturing methods are among the parameters that can impact the selection of polymers or polymer composites to fabricate the impellers. Also, the recyclability of the materials, and any ecological problems they present, are important parameters to consider when choosing the materials. So, thermoplastics can show more compatibility to this end, compared to thermosets and polymer composites.

1.3 Manufacturing Process

The important effect of the manufacturing method can be linked to the energy consumed during the process and impeller performance [13, 15]. The ability to be mass-produced, the attainability of suitable mechanical properties, a good surface, high precision for complex geometries, and economic efficiency are among the criteria to be considered when selecting the fabrication process of impellers. Additive manufacturing, milling, and injection molding have been among the methods used to fabricate the polymeric and composite impellers.

1.3.1 Conventional Impeller Manufacturing

Conventional impeller manufacturing has consisted of a process in which the impeller is fabricated through the machining processes in a subtractive way. In this way, by removing additional layers, the desired shape with different accuracy will be manufactured depending on the selected machining and parameters process. Turning, milling, drilling, and grinding are among the conventional manufacturing which can be applied for machining polymeric and composite materials [92]. Mainly, parameters that impact the final polymer or composite machined product can be divided into three categories: machine and environmental variables; tool design and machining conditions; and composition of the substances. The machine and environmental parameters such as slide straightness, temperature stability, and vibration are the general parameters that controlled the dimension on a large scale. Surface roughness and delamination factor have been effect by tool design and machining conditions such as rake angle, tip radius, depth of cut, and cutting speed. Another important parameter referred to is the composition, which depends on the different physical and chemical properties as machinability will be variant. Also when comparing the polymers and composites, polymers are more homogeneous and have been accompanied by better machining capabilities. Delamination, cracking, fiber pull-out, and burning are among the defects which can happen during composite machining. Among the different machining processes, milling has been severally applied to the fabrication of polymeric and composite impellers [22, 46, 93, 94]. The most common milling machining can be divided into peripheral milling or profiling and end milling. In this method, extra material will be removed by rotating a cutter head with control based on computer numerical control (CNC) which is called CNC milling [95]. Hernandez-Carrillo et al. [46] investigated the PEEK-GF30 impeller fabricated by five-axis CNC milling. According to their

study, the fabricated impeller showed good surface and acceptable mechanical properties against the centrifugal force load. Mentzos et al. [93] investigated the polymeric impeller fabricated by the CNC milling process in a pump application. Effect of process parameters such as cutting speed, feed rate, and depth of cut has been considered in the final roughness surface of the impeller. Their results showed that by reducing the tool step-over and feed rate a smoother surface was obtained.

1.3.2 Injection Molded Impellers

Injection molding consists of four steps of the cyclic process that includes the phases of filling, packing, cooling, and ejection to fabric the parts. Granola, or powder under pressure and temperature will be molted and used to fill the mold. Depending on several parameters, such as raw materials, mold design, and process-specific parameters the final quality of the parts can be different [96]. Cost reduction and production in a short time have been among the parameters which attracted the attention of studies to fabricate the injected impellers [95, 97]. In general, the cost of fabricated parts can be estimated by the parameters such as mold base, number of cavities, and injection mold. As to increasing the performance of the hydraulic pump from the injected impeller, adjusting the distance of the front shroud and rear shroud, namely the impeller outlet width, has been the most economical way to increase efficiency through the injected impeller [39, 95, 98]. Process parameters of injection molding such as molding temperature, melt temperature, injection pressure, and injection time have been introduced as important parameters of the properties and cost of fabricated parts [99]. The optimization of this parameter for the fabrication of the injected impellers attracted the attention of a lot of studies. Rosli et al. [100] have studied the optimization of process parameters of injected blower impeller fans with respect to the melting temperature, molding temperature, injection time, and injection pressure processing parameters. Polypropylene has been used to fabricate the impellers. Given that in the response surface methodology, the results optimum of mold temperature, melt temperature, injection time, and injection pressure have been 110 °C, 210 °C, 0.8 s, and 212.81 MPa. Shen et al. [101] have investigated the mold cooling design optimization for the fabrication of the injected impeller. The melting temperature of the polymer was 230 °C. According to their study, the maximum ejection temperature of the impeller had reduced from 53 °C to 33 °C with a conformal cooling channel. Also, their mold provided a higher cooling efficiency and a more uniform cooling. Topology optimization to reduce the mass of the mold showed the total mass reduction was about 20%.

1.3.3 Additive Manufacturing (AM) in Fabrication of Impellers

Additive manufacturing (AM) is a manufacturing process based on the fabrication of parts by joining the materials, directly from the 3d model. Since 1980 some sources have fabricated part of what was produced directly by a suitably formatted data file in a layer-by-layer fashion, and this can therefore be considered as the start date of AM processing. Over the past years, due to the significant increase in mechanical properties obtained by the production of AM, this method has been introduced as a desirable and reliable method for the production of parts. Selective laser melting (SLM) [102, 103], electron beam melting (EBM) [104, 105], stereolithography (SLA), fusion deposit modeling (FDM), and MultiJet printing technique (MJP) are the AM methods that have been used for rotor and impeller fabrications [106]. One of the most common and low-cost methods in the AM process is FDM. In this method, the melting of the thermoplastic filament from a nozzle at a certain speed means parts can be prepared [107]. In several studies, FDM has been used to produce the compressor and pump impellers. Quail et al. investigated the pump impeller by the FDM method. Quail et al. [108] studied the pump impeller fabricated by the FDM method. The impeller was 75 mm in diameter and 1.3 mm in thickness. The impeller was fabricated for use in a pump by a 3-kW induction motor and a rotational speed of 3000 rpm. According to their results, the impeller produced by this method was ensured to show qualities that included strength, performance, and speed of manufacture. In a study by Fernandez et al. [24] FDM-impeller fabricated for pump purposes has been analyzed. Their study showed that the impeller fabricated by FDM had a similar performance to the original impeller of the rotodynamic hydraulic pump. Also, considering the important effect of impeller roughness on the performance of compressors and pumps, the inherent roughness of the external impeller surfaces had no limitation in the results of the head-flow curve of the pump. In another study by Priyanka and Varaprasada Rao [109] they concluded that an impeller produced by FDM can be introduced as a deserving method, which can replace traditional manufacturing techniques in the industries. However, the difference of mechanical properties in various directions (anisotropy) has been one of the problems that have always existed in parts made by the FDM process [110]. Badarinath et al. [111] investigated the development and characterizes the performance of a robotic FDM system instead of FDM machines based on the three-axis cartesian system. They showed that an impeller fabricated by this method had regions of infill and perimeter overlap in the base and was free from voids and over-deposition. The results also indicated that a uniform deposition at regions of directional changes has parts with complex geometry.

This method can be used for the fabrication of parts with more complex geometries Stereolithography (SLA) is a technique where the polymerization of a photocurable liquid monomer in a spatially selective manner occurs using ultraviolet light (or a laser). The 3D structure is achieved by alternating between the thin liquid films and spatially controlled photopolymerization steps [112]. Generally, rotors or impellers fabricated by this method are used for two goals: directly used as a rotor or impeller, or used in casting methods [113]. In an industrial case, Przybylski et al. [114] investigated the SLA impeller fabricated for a pump. The pump rotor, which was in the medium range size, analyzed the pump at the nominal load and 3000 rpm rotational speed. According to their study, the rotor produced by this method had acceptable results compared to rotors that were commonly used. In the study by Hernandez-Carrillo et al. [22], the AM method was applied for the fabrication of an impeller for the Organic Rankine Cycle (ORC) radial microturbine. In this study, a thermoplastic impeller (ABS) with a diameter of 49 mm was used for rotation at a speed of 36,000 rpm. The results of their study showed that the rotor made by this method could compete with the aluminum sample. In addition, the latter characteristic helped to minimize imbalance, shaft fatigue, and damage to the casing in case of failure and was among the advantages achieved by this method. Inkjet printing (IJP) can be defined as a technology for printing by depositing tiny droplets onto a substrate without dependence on the high-speed operation of mechanical printing elements. Polyjet and multijet printing are famous processes based on this technique [115]. In this method, photocurable resin by a piezo printed process can be layer by layer fabricated. The high precision of this method to fabricate complex geometries is one of the highlight features of this technique. Studies have introduced this technique as a high-performance method for making rotors and impellers [116].

1.3.3.1 Fused Filament Fabrication

Fused filament fabrication (FFF) is a 3D printing process that is often used in the manufacturing of polymeric components, including impellers. An impeller is a rotating component of a pump, usually made of plastic or metal, that is designed to move fluid by converting rotational energy into fluid movement. Polymeric impellers are used in various industries, such as chemical, food processing, and pharmaceuticals. FFF involves melting a polymer filament and depositing it layer by layer to build a three-dimensional object. The process begins with the creation of a 3D model using computer-aided design (CAD) software. The model is then sliced into layers, and the FFF printer uses the sliced data

to create the object by depositing the melted filament layer by layer. The process is repeated until the entire object is created. One of the advantages of using FFF in polymeric impeller manufacturing is the creation of complex geometries that would be difficult or impossible to produce with traditional manufacturing methods. Additionally, FFF can produce impellers with high precision and accuracy, which is essential for ensuring that the impeller performs its intended function. Another advantage of FFF is that it is a relatively fast and cost-effective process. This is particularly useful for creating prototypes or small batches of impellers. FFF can also be used to create customized impellers, which is useful in applications where a specific impeller design is required. However, there are also some limitations to using FFF in polymeric impeller manufacturing. One limitation is that the mechanical properties of the printed parts may not be as good as those produced with traditional manufacturing methods. The strength and durability of the impeller may be compromised, especially when exposed to high temperatures or corrosive fluids. It is important to carefully select the polymer material and the printing parameters to ensure that the final product meets the requirements. In summary, FFF is a useful 3D printing technique for manufacturing polymeric impellers, offering advantages such as the ability to produce complex geometries, high precision and accuracy, and cost-effectiveness. However, careful consideration should be given to the material selection and printing parameters to ensure that the impeller has the necessary mechanical properties to perform its intended function. Considering some advantages of the FFF method such as:

• Lightweight: the parts can be manufactured with different fill percentages, so the parts can be fabricated with different weights.

• Cost-efficiency: FFF is among the cost-effective manufacturing method that allows for the production of complex geometries without the need for expensive tooling which results in lower manufacturing costs for polymeric impellers.

• Customization: for improving the performance of the system, this method can provide custom impeller designs [117]. This method has been used to fabricate the impellers in the turbomachinery field. Fernandez et al. [24] studied the Fused Deposition Modeling (FDM) technology in the production of functional hydraulic pump impellers. The effect of materials used and the printing parameters of the fabricated impeller that impact final performance like geometrical accuracy, material properties, and the surface finish has been investigated. materials used and the printing parameters. According to their results, the FDM-produced impellers exhibited good performance and durability, comparable

to traditional manufacturing methods. In addition, optimizing the process parameters, such as layer height, infill density, and orientation that can be caused to improve the performance was suggested. Çelik et al. [118] analyzed the feasibility of manufacturing complex turbomachinery geometries by the FFF due to the intention of more cost-effective regarding doing away with time-consuming and expensive procedures that arise due to the presence of multiple parts, diverse manufacturing techniques, coordination of various subcontractors, and complicated assembly procedures. The architecture of this system is made up of two parts: a static casing with a hydrostatic bearing and a rotating monolithic shell structure with a radial turbine. Polyethylene terephthalate (PETG) has been used to fabricate the parts in this study. The ventilator design had the characteristics for creating a flow of 400 L/min at 2000 Pa, requiring 35 W of shaft power supplied by the turbine. The turbine flow rate has been worked at 4 g/s at an inlet pressure of 2.5 bar. The diameter of the impeller was 41 mm with a rotational speed of 36000 rpm. The aerodynamic performances of the system were analyzed at the rotational speed of 25 to 38 KRPM. According to the results, a maximum pressure coefficient of around 0.08 was achieved for a flow coefficient of around 0.01. Weiß et al. [1] studied the potential of additive manufacturing for the fabrication of different components of the ORC system by introducing a micro-turbine-generator-construction-kit (MTG-c-kit) in a customized turbogenerator (Figure 1.5a). As such, the air turbine was fabricated at 120 mm in diameter. Selective Laser Sintering (SLS) and FDM were the additive manufacturing methods used for the fabrication of this turbine through the Nylon and ABS, respectively. In this study, achieving a good surface quality of fabricated rotors was mentioned as an important parameter that can impact performance. The surface quality of the fabricated rotor through the SLS and FDM is shown in Figure 1.5b. According to their results for the fabricated wheel with Nylon by SLS, the first performance of the system was around 10%, which with sufficient sealing of the surroundings of the stator nozzles increased to 20%. This maximum efficiency was achieved at the design pressure ratio and rotational speed of 1.4 bar and 6000 rpm, respectively. Also considering the better surface quality of the FDM compared to the SLS, the performance in the pressure ratio of 1.6 was similar. We should mention that the notches on the surface of the FDM rotor were perpendicular to the airflow.

Studies showed the feasibility of using FFF-printed rotary parts in pumps and compressors with different geometry and rotational speeds based on a variety of polymers such as PA, PLA, ABS, and PEEK. Materials selection to fabrication of the parts has been based on different aspects such as me-

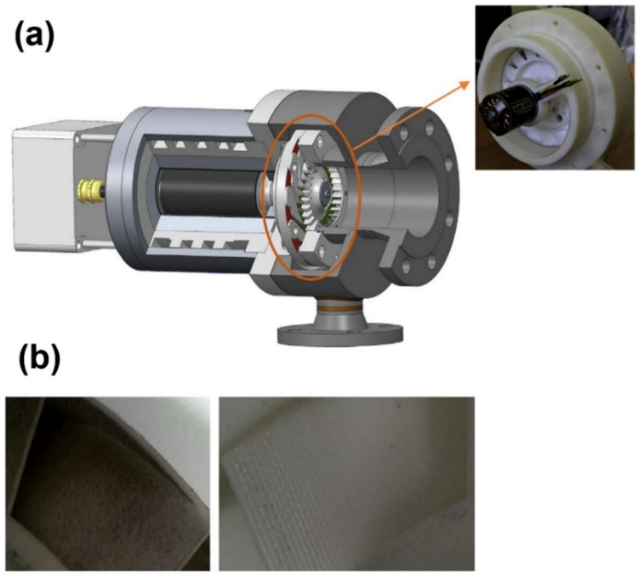

FIGURE 1.5 – (a) Schematic of developed radial quasi impulse cantilever design and (b) left: fabricated rotor by SLS right: fabricated stator by FDM+SLS [1].

chanical, thermomechanical, and physicochemical properties. For example, tensile and bending tests on the standard printed samples have been performed to analyze the mechanical performance [47]. In addition, the glass temperature of polymers plays an important role in the material selection and fabrication of impellers. It means that during the operation of the compressor, the temperature will be increased by enhancing the rotational speeds, so low glass temperature will lead to insufficient thermomechanical properties [46]. In addition to choosing the suitable material, process parameters should be set in such that lead to the maximum mechanical performance and good geometrical and surface roughness properties [119]. Liu et al. [120] studied the effect of the blade surface roughness on the compressor performance in a turbocharger. In their study, nine different blades with different surface roughnesses were considered and analyzed numerically. The results showed the inverse effect of surface roughness on performance. This parameter can induce the compressor performance degradation mechanism, so that by increasing the surface roughness, the reverse flow near the leading edge of the blades was more severe, which means that the compressor flow rate is influenced by roughness. Considering the layer-by-layer manufacturing of parts by additive manufacturing, different geometric accuracies can be obtained depending on the precision of the technique [121]. Layer heights during fabrication have been considered an important parameter that can impact final surface roughness. For

example, printing a cylindrical shape with respect to its central axis parallel to the x direction is accompanied by less surface roughness with respect to the inclined direction between x and y [122, 123]. In general, interlayer welding plays a critical role in the final properties like mechanical, thermomechanical, and chemical behavior of the FFF printed parts. That good interlayer is accompanied by the proper performance of the parts and, in contrast, unsuitable interlayer welding increases the anisotropy in the samples. This subject will be discussed in the following section.

1.3.3.2 An overview of FDM

All industries have changed their focus from traditional manufacturing methods to rapid prototyping (RP) procedures to reduce part manufacturing cycle times while maintaining essential mechanical properties. This helps to keep industries competitive in the market- place. RP processes were first established in the 1980s, known as Additive Manufacturing (AM), layer manufacturing, additive processes, free-form fabrication, and additive techniques. This technology builds objects by adding material in laa yered format with the use of Computer-Aided Design (CAD) [124]. The additive manufacturing (AM) method includes several techniques that allow the development of three-dimensional objects with complex geometries. AM has been used in building and construction, the automotive sector, aerospace, art, the and food industry [125]. Material Extrusion (ME), Material Jetting (MJ), Powder Bed Fusion (PBF), Sheet Lam- nation (SL), Binder Jetting (BJ), Vat Photo Polymerization (VP), and Directed Energy Deposition (DED) are seven types of AM methods that have been developed over the years [126]. In the FFF process, a polymer is supplied into a liquefier, which extrudes a filament while moving in successive X-Y planes along the Z-axis to layer-by-layer build a 3D object [127]. Different parts of the FFF 3D printer are shown in Figure1.6 [128]. Polylactide (PLA), Polyamide (PA), Polycarbonate (PC), Acrylonitrile Styrene Acrylate (ASA), Nylon, Acrylonitrile Butadiene Styrene (ABS) and, Polyether Ether Ketone (PEEK) seem to be the most often utilized thermoplastic polymers used in the FFF technique to make 3D parts [129]. One of the most widely used semi-crystalline thermoplastics, which has excellent mechanical and thermal properties, is polyamide, which is used in the automotive, oil and gas industries, etc.; depending on its constituent monomers, it comes in different forms such as PA6, PA12, and PA66. Among these polyamides, PA6 (nylon 6) is the most widely used material that has excellent mechanical performance and surface quality [130]. The most significant disadvantages of this approach include poor surface quality, slow build speed, and anisotropic

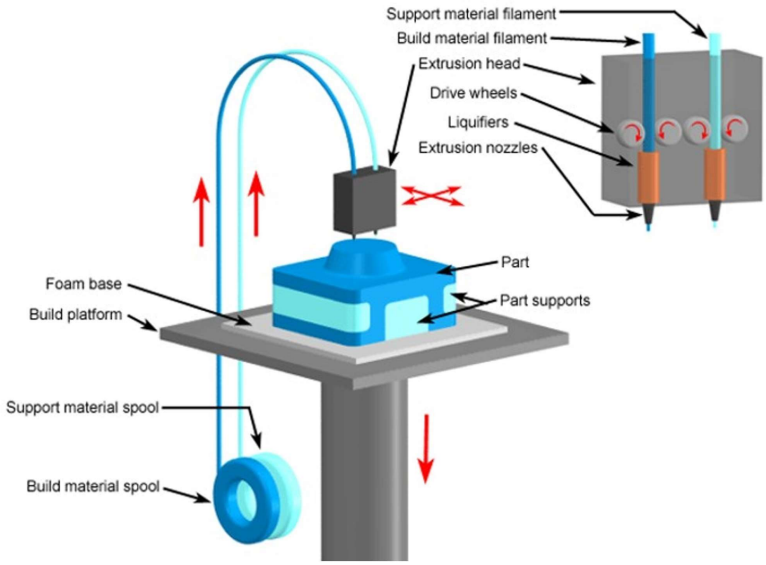

FIGURE 1.6 – FFF 3D printer; a) German RepRap X500®3D printer (FFF),b) Schematic of FFF 3D printer [133].

mechanical properties resulting from the layer-by-layer strategy [131, 132]. Because many parameters might impact the printing process, manufacturers' default configuration of printing process parameters cannot guarantee the quality of printed products. Various process parameters with multiple responses control the FFF process. From the perspective of analysis, this makes it a rather tricky procedure. Extensive research is being conducted to determine the impact of various FFF process parameters on the different responses [133].

1.3.3.3 Bonding formation

Fabrication of the parts through the FFF method shows weaker mechanical properties compared to the other conventional methods like injection modeling and compression molding. This challenge is refer to the quality of welding of each layer during manufacturing. The creation of voids, delamination between the layers, and insufficient adhesion which is related to intermolecular diffusion between layers are among the parameters that can impact and control the weld quality. Between these, intermolecular diffusion can be mentioned as the most important parameter that can affect the final properties [110]. Bonding formation during the printing can be divided into three process surface contact, neck growth driven by surface tension and molecular diffusion, and entanglement across the inter-filament interface.

The thermal history and extrusion pressure during the fabrication can drive the process of welding. The formation of an interface between two polymers can be explained by polymer healing by Wool and O'Connor [134]. According to this theory, different stages of healing consist of 5 steps including (1) surface rearrangement, (2) surface approach, (3) wetting, (4) diffusion, and (5) randomization. That, intermolecular diffusion in the wetted area leads to the increase of this interface. Random locations in the wetted area at a certain zone is the place of nucleation of intermolecular diffusion. The theory of Wool et al. [135] can explain the welding at a polymer interface regarding the time-dependent structure of the welding interface which is determined in terms of the molecular dynamics of the polymer chains. The molecular dynamics of the polymer chains have been modeled by reputation theory. In this theory, polymer chains are assumed to be in a tube according to topological constraints. This tube can configure the polymer chain, which is considered a range for the movement of the polymer chain. Figure1.7 schematically shows this configuration concerning different times of a chain in the molten state. Passing time in this state, the chain by Brownian motion can back and forth in the tube. The time that the chain needs for tube disengagement or relaxation time is called T_r. That, less than this time leads to minor chain motion.

Following this theory molecular interdiffusion at the interface of two polymers by considering the instantaneous wetting can be explained. Figure2.3 schematically shows the molecular interdiffusion between two surfaces of wetted polymers. T=0 indicates the molecular contact, and after that, passing time is accompanied by reptate the randomly distributed of chains in space.

According to the reptation theory, the relation between the length of minor chains with the time that has a square root correlation can be realized as follows:

$$\frac{l}{L} = (\frac{t}{T_r})^{0.5} \tag{1.1}$$

In order to investigate the interdiffusion of chains for x distance the following equation can be applied:

$$\frac{x}{x_\infty} = (\frac{t}{T_r})^{0.25} \tag{1.2}$$

In 1991 Bastien and Gillespie [136] proposed a model to predict the strength and toughness in non-isothermal conditions based on the healing theory for amorphous polymers. In their study to estimate

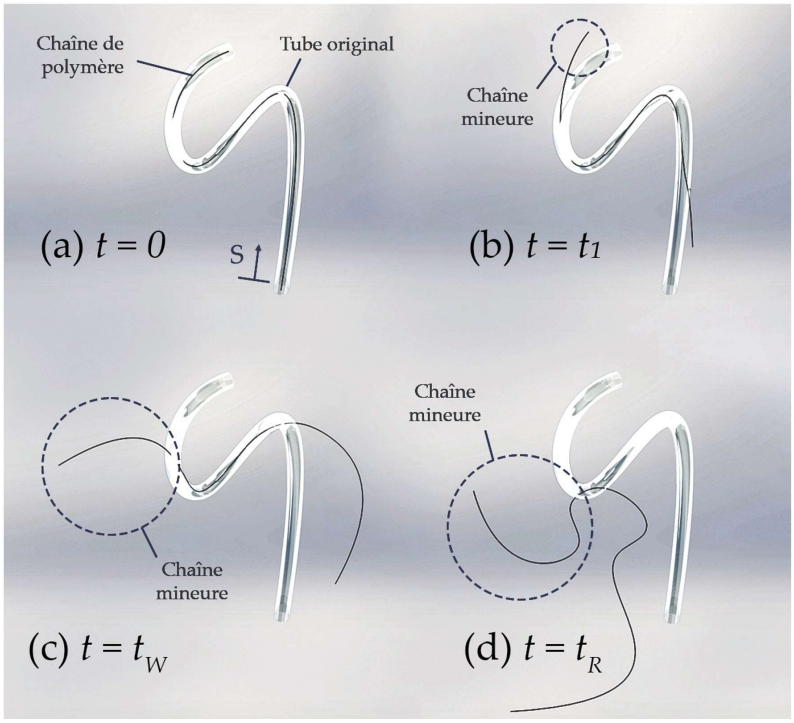

FIGURE 1.7 – Schematic of reptation model for healing

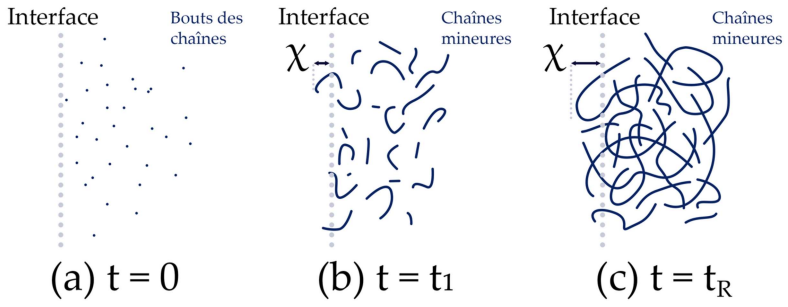

FIGURE 1.8 – Reptation dynamics across a polymer/polymer interface

the reptation time they used three alternate and independent methods including isothermal welding at a temperature very close to the Tg of the polymer, creep measurements, and dynamic shear analysis. According to their results, the interpenetration of the chains at the interface of the polymers was the most representative of the physical phenomena for predicting the strength and toughness. Yang and Pitchumani [137] developed a model for the healing process under non-isothermal conditions based on the reptation theory of polymer chains. It can be said that the model was modified from the model Bastien and Gillespie by considering smaller temperature gradients. The dependency of bond strength via temperature history and welding time has been investigated in their study. By the analytical model presented, the degree of healing, which is attributed to the term of quantifies the fraction of diffusion across layers, with time is as follows:

$$D_h(t) = \left[\int_0^t \frac{1}{t_w(T)} dt\right]^{0.25} \tag{1.3}$$

The time welding, t_w, has been calculated by fitting the Arrhenius model on the different results of shear specimens fabricated at isothermal conditions at various temperatures. Considering the critical role of interdiffusion of the layers on the mechanical behavior of the parts in FFF method, studies focused on the investigation of this zone in non-isothermal conditions, though the non-isothermal nature of this process, and predict the mechanical properties. Yin et al. [138] studied the interfacial bonding in FFF process by developing a model based on heat transfer-based polymer inter-molecular diffusion theory. In this regard, multi-material thermoplastic polyurethane and acrylonitrile butadiene styrene have been used. The effect of processing parameters such as nozzle temperature, building stage temperature, and printing speed was considered on interfacial bonding strength. They showed a 93% increase in the strength by increasing the bed temperature which was considered the most important parameter compared to the other one during their work. Coogan et al. [139] predicted the bond strength of FFF printed part through a healing simulation. The diffusion in the interlayer has been analyzed by rheological measurement for acrylonitrile butadiene styrene. The total predicted diffusion has been calculated based on the temperature-dependent diffusion coefficient. The measured temperature at the interface bond by thermocouples was used for the thermal history. The integral of the diffusion coefficient from the WLF model fit against the time profile has been referred to as the total diffusion. According to their results, increasing the interlayer diffusion has been followed by enhancing the bond strength. Investigation of the interface in the weld zone of FFF printed based on reptation theory

has been hugely used in recent studies [4, 140]. Lacambra-Andreu et al. [141] studied the interlayer molecular diffusion of Poly(D,L-lactic acid) (PDLLA) during FFF process by reptation theory. For that purpose, the temperature profile was predicted by heat transfer in transient conditions, rheological characterization was analyzed to estimate viscosity and relaxation time. According to the results, the polymer diffusion at the interphase was predicted by influencing the degree of healing and they showed the impact of this aspect on the strength of printed samples. FigureB.5a shows a schematic of welding formation in layers 1 and 2 based on retention theory. Interfacial interface against the time has been shown in FigureB.5b for a temperature nozzle of 190 °C at the interface of these layers. The results showed an interphase with 17.2 nm thickness at the interface. The key role of temperature profile on the healing process was shown, that increasing the temperature is accompanied by improving healing and better welding between adjacent filaments.

Considering the importance of the weld zone on the final behavior of FFF fabricated parts, analyzing this zone is the center of attention lot of studies. In general, to characterize the interlayer bond interface quality. The methods can be divided into different groups of mechanical tests, mesostructures investigation, and microstructure analysis [142]. Windheim et al. [143] studied the effect of interlayer adhesion on the mechanical properties of PLA 3D printed parts. The process parameters were nozzle speed, layer height and annealing time. In this study, the weld interface has been analyzed by atomic force microscopy (AFM). The results showed an interface of 1.4 μm, which is variable by changing the annealing time (Figure1.10). In this study, not suitable molecular mobility has been referring to the spherulites which create in the interface. Increasing the annealing time was along with reducing the weld zone.

Collinson et al. [144] directly investigated the microstructure of the weld zone by AFM for FFF-printed PEEK samples. Figure1.11 shows the crystal transition region of the sample printed. According to the results, an interface of 4 µm can be observable between two printed layers which show less height compared to the interior of the extruded layer. In addition, they found that the formation of a solid, fixed outer layer composed of crystals occurs on the surface of the PEEK extruded layers during the process of crystallization. This outer layer forms prior to the effective bonding of subsequent layers, causing a decrease in the strength of the welded area.

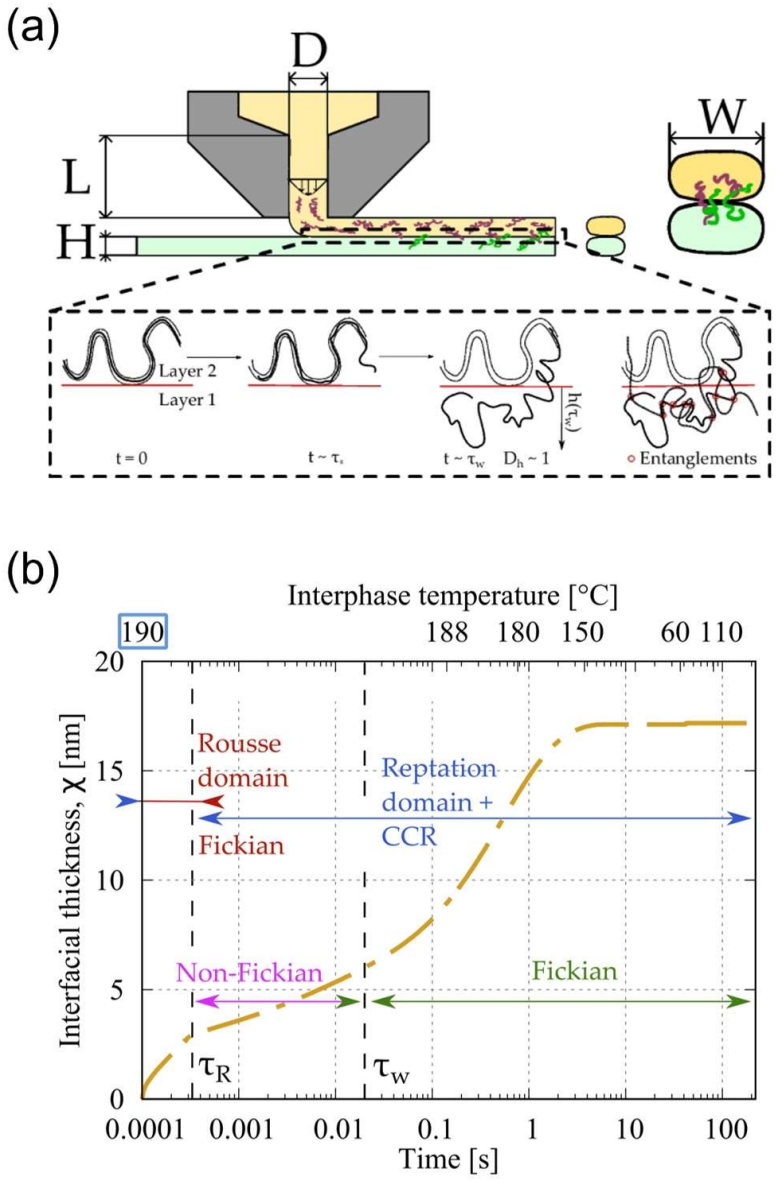

FIGURE 1.9 – (a) Schematic of a printing process by chains interdiffusion with deposition time and (b) Interfacial thickness evolution between layers 1 and 2 at a nozzle temperature of 190 °C [141].

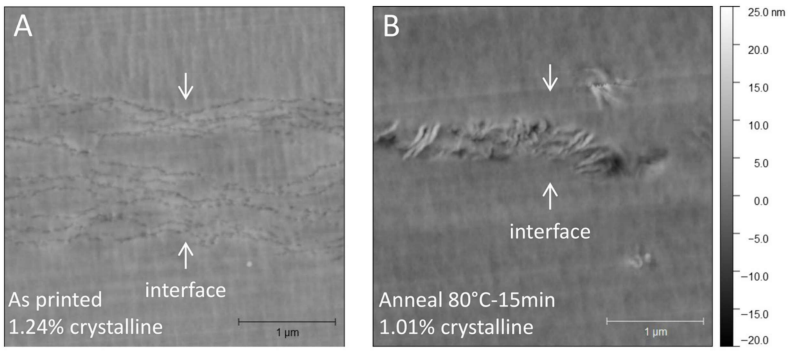

FIGURE 1.10 – Scan of 3.5 * 3.5 µm collected at a scan rate of 0.5 Hz [143].

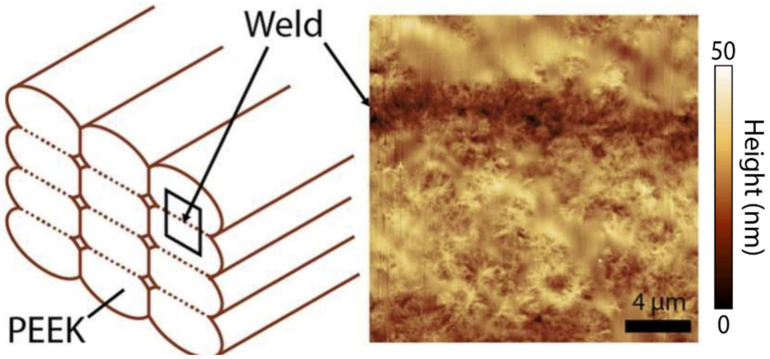

FIGURE 1.11 – Weld interface in a transition region with moderate crystallinity [144] .

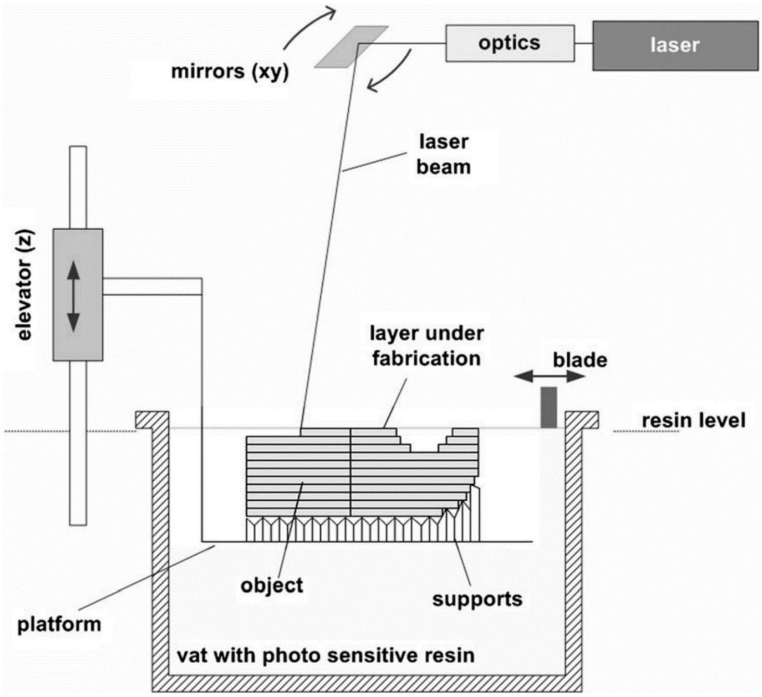

FIGURE 1.12 – Weld interface in a transition region with moderate crystallinity [144] .

1.3.3.4 Stereolithography approach

Stereolithography (SLA) is a popular 3D printing method that was first developed in the 1980s. It is a form of additive manufacturing that uses a liquid resin material to create 3D objects layer-by-layer. SLA is commonly used for producing high-resolution, intricate parts with excellent surface finish and dimensional accuracy. The process begins with the creation of a 3D model of the object to be printed using computer-aided design (CAD) software. The digital file is then loaded into the SLA printer, and exposed to ultraviolet (UV) laser beam radiation, which induces a localized polymerization process to solidify the liquid resin layer-by-layer to form manufactured parts directly from 3D computer data. As the laser beam scans each layer of the object, it selectively solidifies the resin at specific points, following the shape of the 3D model. The printer platform is then lowered slightly and the process repeats, building up the object layer by layer until it is complete. Figure 1.14 indicates this approach schematically.

The percentage of polymerization in the manufactured parts can be mentioned as a key parameter

that impact on the physicochemical, mechanical, and thermomechanical properties. In general, This percentage can be achieved up to 80% for a green part and the post-processing method can increase this value to 95%. Different post-processing methods can be found in the literature corresponding to washing the samples immediately after printing and post-curing by keeping the samples in the presence of UV radiation with or without temperature. In addition, microwave radiation is another post-curing method to increase the curing percentage. Generally, rotors or impellers fabricated by this method are used for two goals: directly used as a rotor or impeller, or used in casting methods [111]. In an industrial case, Przybylski et al. [114] investigated the SLA impeller fabricated for a pump. The pump rotor, which was in the medium range size, analyzed the pump at the nominal load and 3000 rpm rotational speed. According to their study, the rotor produced by this method had acceptable results compared to rotors that were commonly used. In the study by Hernandez-Carrillo et al. [22], the AM method was applied for the fabrication of an impeller for the Organic Rankine Cycle (ORC) radial microturbine. In this study, a thermoplastic impeller (ABS) with a diameter of 49 mm was used for rotation at a speed of 36,000 rpm. The results of their study showed that the rotor made by this method could compete with the aluminum sample. In addition, the latter characteristic helped to minimize imbalance, shaft fatigue, and damage to the casing in case of failure and was among the advantages achieved by this method. Inkjet printing (IJP) can be defined as a technology for printing by depositing tiny droplets onto a substrate without dependence on the high-speed operation of mechanical printing elements. Polyjet and multijet printing are famous processes based on this technique [113]. In this method, photocurable resin by a piezo printed process can be layer by layer fabricated. The high precision of this method to fabricate complex geometries is one of the highlight features of this technique. Studies have introduced this technique as a high-performance method for making rotors and impellers [114]. Resin-based 3D printing technologies, also known as vat photopolymerization, use liquid photopolymer resins that are cured with a light source to create a solid object layer by layer. There are several types of resin-based 3D printing technologies, including Stereolithography (SLA), Digital Light Processing (DLP), PolyJet printing, and Continuous Liquid Interface Production (CLIP). SLA is one of the earliest and most established resin-based 3D printing technologies. It uses a laser to selectively cure the resin layer by layer, creating a solid object. SLA is known for producing high-resolution and accurate parts with a smooth surface finish. DLP is similar to SLA but uses a digital projector instead of a laser to cure the resin layer by layer. DLP can produce

parts with high accuracy and speed. PolyJet printing uses an inkjet-style printing process to jet layers of liquid photopolymer onto a build platform. Each layer is cured with UV light as it is deposited, creating a solid object. PolyJet printing can produce parts with high detail and multiple materials. CLIP is a newer resin-based 3D printing technology that uses a special liquid resin that is selectively cured with UV light and oxygen to create a solid object. CLIP can produce parts with a smooth surface finish and high accuracy. Andrearczyk and Żywica [145] fabricated the compressor wheel and turbine wheel by MJP with the purpose of using them in the turbocharger. According to their study, the pressure range of the compressor was in the range of 0 to 1.6 MPa. Also, considering the tensile strength of this photopolymer, which mentioned around 65 MPa, and the working temperature of 88 °C, this process by this type of photopolymer was an assured method to fabricate the mentioned parts of the turbocharger. A study by Artur Andrearczyk et al. [146] using the MJP investigated the range of applications of this method concerning the design, testing, and optimization of the elements of fluid-flow machines. In this study, the polymeric fabricated rotor was in the range of 42.5 mm, which was applied in the compressor inlet of the turbocharger (turbochargers are fluid-flow machines with one of the highest nominal rotational speeds). The temperature range was 50 to 150 °C for the inlet air of this machine. The rotational speed up to 100,000 rpm was analyzed in this experiment. We should mention that the results obtained from the compressor wheels, which were fabricated by polymer and aluminum, showed that at 90,000 rpm the polymeric wheel can operate like the aluminum wheel. While the tensile strength and glass transition of the standard experiment of this polymer, which has been used in this study, differed from the aluminum wheel. Khalil et al. [147] studied the effect of different blade heights of rotors on the performance of a micro-scale axial turbine. Different parts of this system, with respect to the exploded assembly drawing, are shown in Figure1.13a. In this study, different parts of this system such as reducer, stator, disc, rotor, rotor case, and closing were fabricated by a Polyjet printing technique and using a resin (RGD525) material. The three different blade height sizes of the rotors were 4, 6, and 8 mm (Figure1.13b). The experiment was performed in environment temperature and at pressure ratios in the range of 1.2 to 1.75, and rotational speeds of 4000 to 16,000 rpm. According to their results, fabricated rotors with blade heights of 4, 6, and 8 mm were able to produce power up to 630.75, 694.1, and 796.89 W, respectively, at an expansion ratio of around 1.75 and through the rotational speed of around 16,000 rpm.

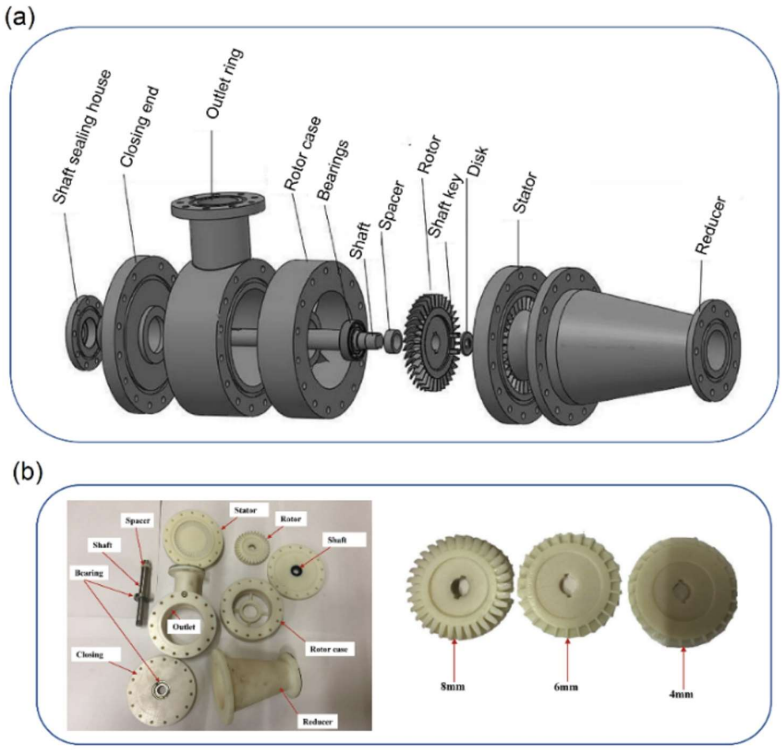

FIGURE 1.13 – (a) Exploded schematic of micro-scale axial turbine and (b) left: fabricated all turbine parts and right: fabricated rotors with different blade heights [147]

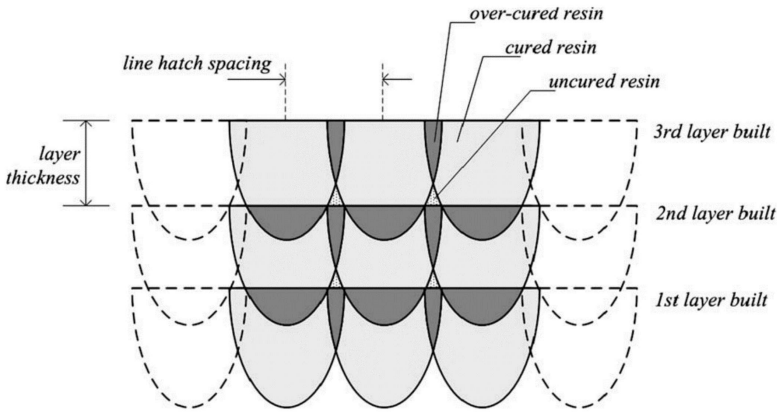

FIGURE 1.14 – Schematic of cured and uncured regions in SLA parts [144]

1.3.3.5 Post-curing and manufacturing parameters

Parameters such as laser power distribution and scanning speed during construction, and resin characteristics (such as monomers, oligomers, and curing agent compositions) can play a decisive role in the maximum density of cross-linking and consequently final properties [148, 149]. Generally, acrylates, vinyl ethers, and epoxides have been among the types of multifunctional monomers which were used for laser-induced polymerization [150, 151]. In the different types of multifunctional resin production, the mechanism of polymerization occurs by the reaction of the acrylate group and an epoxy group through a radical and cationic mechanism, respectively [152, 153].

Due to its parabolic shape, uncured regions formed between each successive bullet-line result in an inhomogeneous microstructure. Increasing laser power or slowing scanning speed can affect energy density resulting in bullet lines with a greater degree of cure, and less liquid resin inside the parts (Figure1.14).

According to the applications mentioned for this method, having suitable properties play an important role in the efficiency of the parts produced by this process. For this purpose, the polymerization of the polymer has played the most important role in determining the final behavior of the parts [154, 155]. After fabrication, the sample is quite hard, but an increase in the polymerization by the post-curing apparatus is an important step in increasing the cross-link density and removing residual resin [30]. In most cases, produced parts can be cured by the use of high-intensity ultraviolet (UV) light

and temperature [156, 157]. Resin composition and production parameters have a determining role in the degree of cure. Uzcategui et al. [158] studied the effect of processing parameters on mechanical properties and developed a dual-cure system with an ability of 100% conversion on a multi-functional acrylate-based resin. For post-processing, removing the unreacted monomer by a solvent was the first post-processing. Considering the plasticization effect of unreacted monomers, they showed a key importance role of using a solvent for removing these monomers for improving mechanical behavior. Also, thermal post-curing significantly has increased the modulus of samples. This increase was from 7 to 15 MPa through thermal cure. However, studies have shown that the degree of cure in the parts fabricated without post-curing was about 80%, and subsequent treatment operations were necessary to achieve more than 90% curing. In a study by Fuh et al. [148] 94% degree of cure by using UV light for 120 seconds was achieved. On the other hand, the use of temperature has been another method of curing, used in many studies. In this method, using the sample in a chamber at a constant temperature for a certain period leads to an increase in the amount of cross-links density. In general, depending on the composition, the temperature range can consist of 40 to 140 °C. Also, the curing time has been in the range of several min to several hours. Hague et al. [156] studied the effect of UV and thermal post-curing of the Acura SI40 and SL 7560 resins. They showed the important role of the thermal post-curing cycle on mechanical properties. Post-curing was performed by using the UV and thermal conditions in the time range of 90 and 120 min, respectively. However, optimization and using the best condition during post-curing by evaluating various parameters, including changes in time and temperature have been studied in many types of research. It is worth noting that the effect of temperature and time on creating residual stresses in the end parts should be considered. Therefore, clarifying the relationship between mechanical properties and post-curing from the parts by considering the properties of the resin plays an important role to achieve the set of the best parameters [159, 160]. Among the resins, acrylate-based resins due to their high hydrophobicity, high accuracy, and low cost have attracted the attention of many studies [161, 162] which using a broad range of multi-functional acrylate in the system can lead to the excellent performance of the produced parts [163]. In this method, polymerization of a photocurable liquid resin can happen through exposure to ultraviolet laser radiation and subsequently lead to solid objects. Fabrication of the parts is layer by layer of cured resin. The passage of the laser according to the pre-determined design causes the formation of solid layers mounted on a platform immersed in the resin bath. The curing of the resin

during the fabrication is accompanied by entrapped uncured monomers between the solid layers. In general, curing up to 65 percent can be achieved considering the kind of polymer and laser source in the samples during the process [164]. There are a lot of parameters that can impact the final part properties, nevertheless, the percentage of curing and orientation of printing have been among the key parameters that changed the properties such as the mechanical behavior of the parts.

1.4 Evaluation of compressor: Numerical and experimental

1.4.1 Structural stress and flow analysis

Numerical analyses for parts designed with consideration of working conditions have been one of the most critical steps in the investigation of materials [165]. Regarding impellers there are no exceptions to this, and numerical evaluations have always been one of the vital steps in the investigation of materials for this component. In other words, numerical analyses can be considered as a tool to balance performance and reliability during the development and design of the products [166]. In this section, numerically analyzing the centrifugal impellers and rotors of compressors will be discussed. As mentioned, properties such as modulus of elasticity, thermal expansion, fracture toughness, fatigue strength, thermal conductivity, specific heat capacity, corrosion resistance, and thermal stability have been among the parameters considered in the selection of materials for the fabrication of impellers and rotors of compressors [167]. We should mention that centrifugal stress due to rotational forces, bending stress due to fluid pressure and change of momentum, and thermal stresses due to thermomechanical load are the properties that were considered effective factors in the simulations. So, by examining the materials under the mentioned forces, the authority of the material will be assayed in simulation [168]. Structural analysis is the most common application of finite element analysis which allows for the investigation of different types of loads, including stress, strain, deformation, and so on. The linear structural static equations are as follows [169]:

$$\frac{\partial \sigma_x}{\partial x} + \frac{\partial \tau_{xy}}{\partial y} + \frac{\partial \tau_{xz}}{\partial z} + F_{bx} = 0 \tag{1.4}$$

$$\frac{\partial \tau_{yx}}{\partial x} + \frac{\partial \sigma_y}{\partial y} + \frac{\partial \tau_{yz}}{\partial z} + F_{by} = 0 \tag{1.5}$$

$$\frac{\partial \tau_{zx}}{\partial x} + \frac{\partial \tau_{zy}}{\partial y} + \frac{\partial \sigma_z}{\partial z} + F_{bz} = 0 \tag{1.6}$$

where σ represents the normal stress, τ shows the shear stress, Fbx, Fby and Fbz are the body forces per unit volume acting along the directions x, y, and z, respectively. Centrifugal force per area of the blade appears as centrifugal stresses, which can be written generally as follows:

$$F_C = mr\omega^2 \tag{1.7}$$

where FC represents the centrifugal force, ω is a rotational speed, r and m show the radius and mass of the considered section, respectively. In the thermal condition, control equations for linear elastic and isotropic three-dimensional solid materials to consider the thermal load are as follows [170]:

$$\varepsilon = \ (D-1)\sigma + \alpha \Delta T \tag{1.8}$$

$$\Delta T = T - T_{Ref} \tag{1.9}$$

where ϵ, σ, T_{Ref}, D and α are the total strain vector, stress vector, referenced temperature, material elastic stiffness matrix and matrix of thermal expansion coefficient, respectively. Fluid-structure interaction (FSI) is the approach that can be used for the structural examination of the impeller. In this method, the effect of the fluid dynamics on the structural mechanics of the impeller based on computational fluid dynamics (CFD) and structural finite element analysis (FEA) can be analyzed [171]. Solving the Reynolds-averaged Navier–Stokes (RANS) equations has been one of the most used methods in CFD [172], the equations are as follows [170]:

$$\nabla(\rho V) = 0 \tag{1.10}$$

$$\nabla.(\rho VV) = \rho f - \nabla p + \nabla.T \tag{1.11}$$

$$\nabla.(\rho hV) = \rho f.V + \nabla.(T.V) - \nabla.q \tag{1.12}$$

where V, f, p, T, h, and q are the velocity vector of the fluid, body force vector per unit mass, pressure, viscous stress tensor, volumetric enthalpy, and heat flux vector, respectively. Andrearczyk et al. [5] investigated the plastic wheel in turbocharger application. In this experiment, the rotor has been fabricated by the MultiJet 3D printing method with a diameter of 42.5 mm. For calculation strength analyses, rotational speed and temperature were sets of 100,000 rpm and 55 °C, respectively. According to their results, the maximum deformation and the maximum stress on the impeller geometry were 192 m and 27 MPa, respectively. Figure1.15 shows the stress and deformation results. Also, the performance of the compressor was simulated based on solving RANS by ANSYS to achieve the compressor performance map. Their results showed the streamlines in a relative reference frame, in which the rotational speed and mass flow rate were 200,000 rpm and 0.09 kg/s, respectively.

Kar et al. [28] studied a polymeric impeller in centrifugal pump applications. The impeller had a diameter of around 5.08 cm and has been fabricated by polyetherimide. Structural stress analysis was performed by finite element analysis (FEA) under maximum centrifugal conditions concerning the rotational speed of 72,000 rpm and gravitational load. Their results showed that the maximum stress on the impeller was 5.45 MPa. Hernandez-Carrillo et al et al. [22] investigated a different polymer, composite, and metal impeller together to evaluate the feasibility of developing a simplified turboexpander. Calculations under different loadings were examined in this study. Full load conditions, a rotor blocked, which is full flow and being supplied with the rotor stopped, and 27% over-speed due to the consideration of international standards were the conditions that were considered. The rotational speed was 36,000 rpm and the diameter of the impeller was 49 mm. Figure 1.16(a, c, and e) shows the equivalent stress on the PEEK impeller under different loading conditions. Their results showed that the obtained stress showed high sensitivity to rotational force and pressure loading. The equivalent stress on the PEEK impeller in different conditions of loading has been performed and according to their results, the maximum stress on the blade was 10 MPa. Also, the value of the factor of safety for aluminum, PEEK reinforced with 30% glass fiber, and ABS were 19.92, 22.25, and 13.32, respectively, with an analysis of 27% over-speed. These values were greater than the minimum requirement. Considering their simulation, additional stress caused by temperature was analyzed. The simulated efficiency was 86%, 0%, and 84% for the full load, rotor blocked, and 27% over-speed situations, respectively.

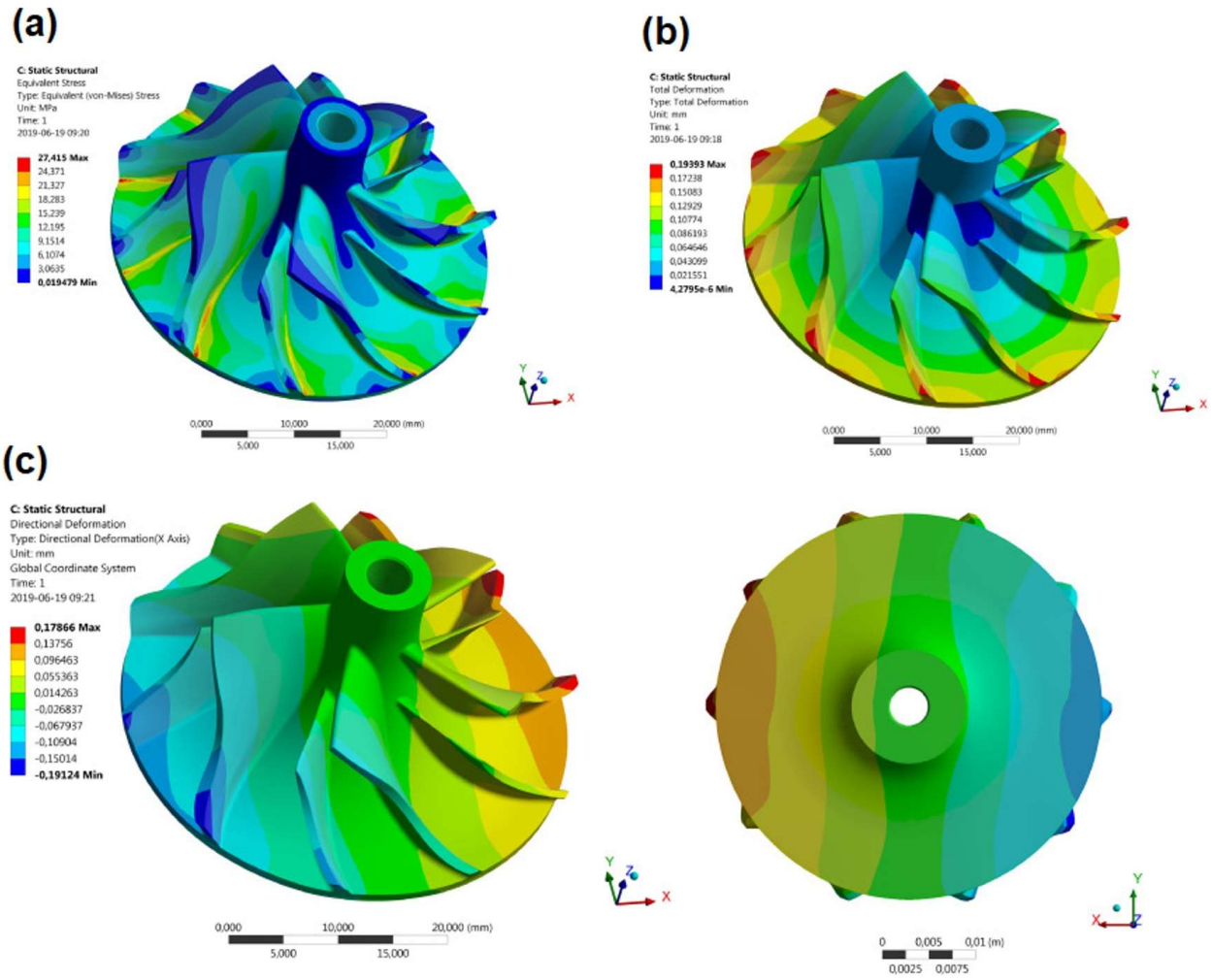

FIGURE 1.15 – (a) stress distribution, (b) deformation distribution (c) deformation in the X as isometric bottom view on the rotor [5].

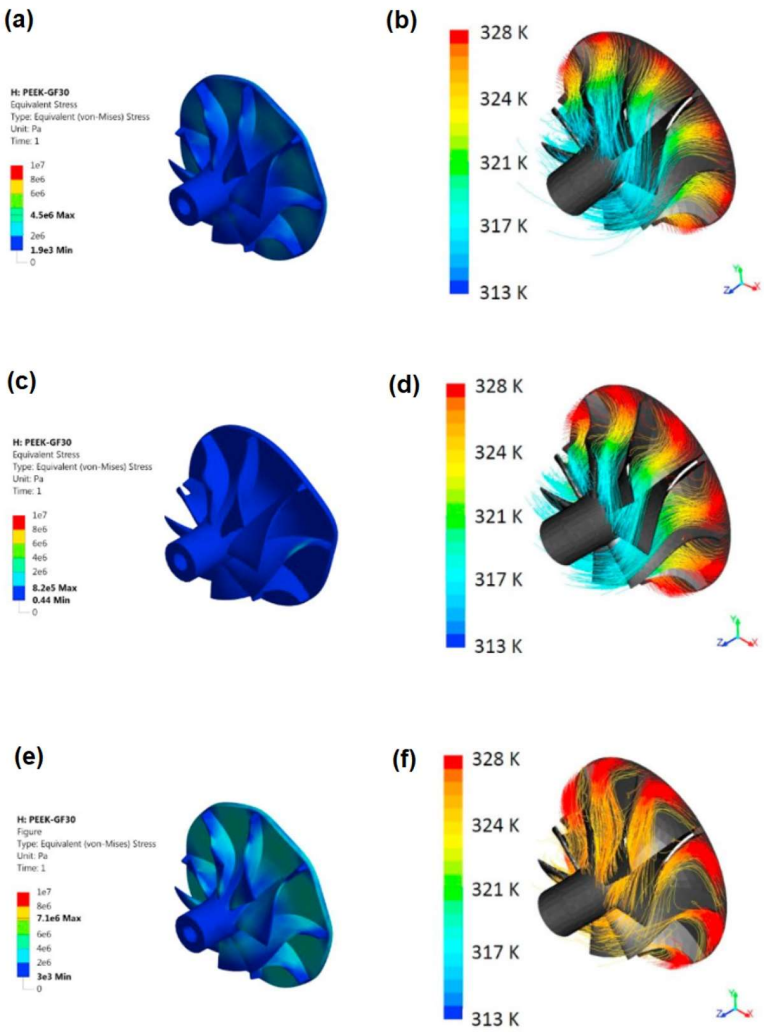

FIGURE 1.16 – Stress (Pa) contours for PEEK impeller (a, c, and e) and relative streamlines colored by total temperature in Kelvin (b, d and f) full load (a and b), locked rotor (c and d) and 27% overspeed (d and f) [22].

1.4.2 Experimental evaluation of the final performance of compressors

An accurate performance evaluation of the impeller in the pump, compressor, or turbine is essential due to it confirming the ability of the machine to respond to working conditions, as well as the correct energy consumption. In this regard, performance investigation is possible through the analysis of work done on working fluid. In general, inlet temperature, inlet pressure, discharge temperature, discharge pressure, rotational speed, differential pressure across the flow meter (or pitot traverse), temperature and pressure at the flow meter are among the measurements to determine the machine performance [14, 173]. In addition, the investigation of vibration has been considered to confirm the dynamic performance. Furthermore, the tribological behavior of the impeller under working conditions is another parameter that should be considered. Depending on the application, such as the pump or compressor, the environment of the test bench would be different [174]. We should mention that performance tests will be performed to achieve the compressor map, which represents the corrected flow versus the pressure rise at various aerodynamic speeds [175]. Measuring the pressure is essential to investigate the performance of the system. So, during the experiment input and output pressure are measured by a pressure gauge. Depending on the kind of pressure being measured such as static, or dynamic pressure, the installation place of the gauge can be different. For example, output pressure can be measured by a pressure gauge installed along the discharge path. Mojaddam and Torshizi [176] studied the impeller hub and shroud of a radial flow compressor by implementing different meridional contours on the same impeller characteristics. Evaluation of performance was performed by considering the pressure ratio from a compressor inlet to a diffuser outlet. According to the comparison of compressor performances for both cases, in circular and elliptical hub and shroud curves, pressure ratio and the isentropic efficiency in different mass flow rates at a fixed rotational speed have been shown. The difference in pressure ratio was minimal at low rotational speed, so that the maximum difference was 1.4% at the highest mass flow rate. For their design rotational speed differences were considerable at 3% and at the maximum mass flow rate at approximately 10%. Also at high rotational speed, the pressure ratio was the same. In conclusion, pressure ratio and total-to-total isentropic efficiency for both impellers along with inlet section and vane-less diffuser were selected to evaluate the newly suggested curves. Their results showed that the elliptical curves have acceptable performance in comparison with circular curves. Li et al. [177] investigated the impact of the blade angle of the plastic impeller on the performance of the centrifugal pump. They analyzed the pressure fluctuation at

the outlet of the impeller. According to their results increasing the outlet angle and inlet angle played a key role in machining the optimal performance. The best results have been achieved for an outlet angle of 35° plastic impeller, in which efficiency and head were 81.02% and 35.80 m, respectively. In general, the optimal performance of the printed impeller has been shown according to the simulation and experimental results. To analyze the system performance and achieve the compressor and pump maps, measurement of the mass flow is essential. This parameter can be measured by a flow meter. Mass flow rate refers to the product of the working fluid density, the cross-sectional area and the flow velocity [178]:

$$\dot{m} = \rho \; A \; V \tag{1.13}$$

In the case of compressors, the corrected mass flow rate can be calculated by the following equation [179]:

$$\dot{m}^* = \dot{m} \left[\frac{P_{ref}}{P_{in,\ 0}} \right] \sqrt{\frac{T_{in,\ 0}}{T_{ref}}} \tag{1.14}$$

where T_{in}, 0 and P_{in}, 0 are the total temperature and total pressure at the compressor inlet, respectively, and Tref and Pref are 288.15 K and 1 atm, respectively.

Sun et al. [180] evaluated the influence of humidity on the performance of a centrifugal compressor. Their results showed that pressure ratio and peak isentropic efficiency have been decreased by increasing the humidity. Also, the variation in performance was analyzed by measuring the mass flow at different rotational speeds in humid and dry air conditions. The mechanism of influence on performance was analyzed by measuring the mass flow in dry and humid conditions. According to their results, at the same rotational speed, the mass flow of humid air was smaller than that of dry air. Figure1.17 shows the differences between saturated humid air at 100% design rotational speed and its corresponding dry air.

The importance of analyzing the vibration of impellers has been mentioned in a lot of studies [180]. Increasing cyclic stress and fatigue failure, a collision of the rotor with stationary parts, seized bearings, vibrating force transmission to stationary parts, and induced vibration of peripheral units have been among the problems due to the rotor's vibration. The natural frequency from the impeller or rotor vibration by the 3-D finite element method has been analyzed by considering the difference

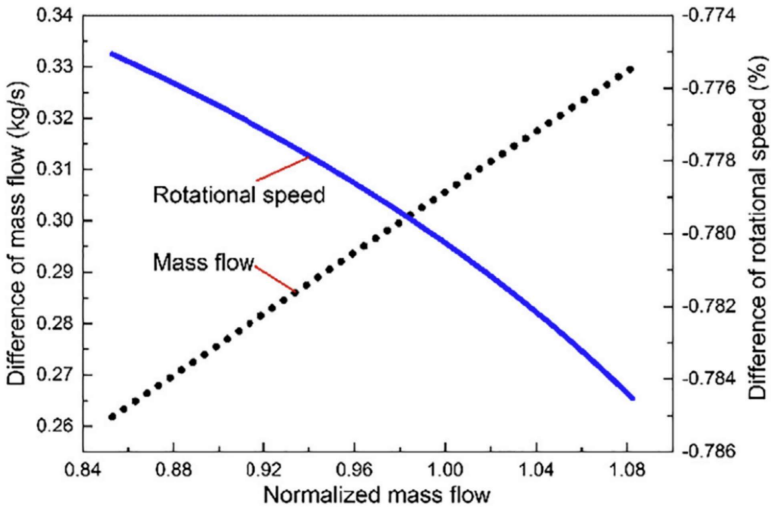

FIGURE 1.17 – Differences between saturated humid and corresponding dry air [180].

between the inertial coordinate system fixed to the stationary side and the rotational coordinate system fixed to the rotor. Due to the symmetry of the impellers with respect to the center of rotation, the analysis of rotating structures by 3-D finite elements is considered cyclic symmetry [181]. Vibration measurements can be performed by a vibration analyzer [182] or digital image correlation (DIC) by cameras [183]. In this way, amplitude in the different ranges of frequency or displacement magnitude against the time in a certain frequency is achievable. Barone et al. [184] described a measurement system to investigate the impeller damping (Figure1.18a) by measuring the excitation force during the test with respect to the response and the load amplitude. The vibrational measurements in the high-frequency range of 2568 Hz, 6239 Hz, and 6357 Hz showed a harmonic response and frequency values in combination with the low response amplitudes, in the range of 10 µm. Their results in the high frequency of 6239 Hz in the cylindrical reference frame coordinates showed a smooth map for all three directions (Figure1.18b).

Mousmoulis et al. [185] studied the vibration of pump impeller considering the important effect of cavitation in the steady and dynamic operation of a pump. In this regard, vibration measurements for the inception of cavitation have been performed in the frequency range of 5–10 kHz. Given that the impellers with different geometries have been considered, the lower incidence angle and the use of splitter blades showed the er noise and vibration characteristics through the entire Thoma number

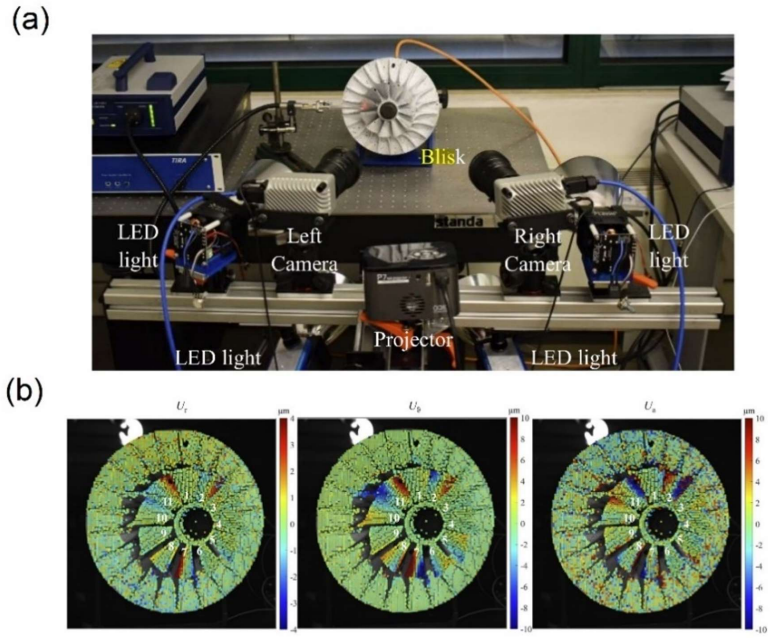

FIGURE 1.18 – (a) Optical setup of the stereo-digital image correlation measurement and (b) Displacement maps for the 6239 Hz excitation frequency [184].

range tested. Also, they mentioned that increases vibration band power at part load conditions can be due to the increasing turbulence intensity and the backflow cavitation mechanism. Tribology can be defined as the science of surfaces in contact with each other and consists of friction, lubricant and wear [185]. Considering the interaction between working fluid and impeller, investigation of wear resistance and friction can play an important role in the efficiency of the machine. So, analyzing tribology behavior, which is the science of interacting surfaces in relative motion, has a high position [186]. For example, different friction on the impeller caused by various viscosity of fluids impacts the performance of the system. On the other hand, the viscosity of fluid has affected the friction losses and can change the performance, such that increasing the fluid viscosity causes a reduction in performance [187, 188]. So, the viscosity of the fluid can change the characteristic curve of the systems. Considering the characteristic curves, viscosity correction factors can be obtained and viscosity correction factor can be defined through the η/η water, where η and η water are the efficiencies of fluid and water, respectively [187]. The wear of the impeller during working is another important parameter that should be considered in analyzing the performance of systems. Wear is defined as the removal of material from a solid surface caused by friction or impact. Jiang [29] studied the wearing properties of the fabricated impellers of PLA, ABS and VeroGray by a 3D printing method. The wear test was performed in different concentrations of erodent material for 110 h. During the experiment after every 5 h, the weight loss of the impellers to calculate the wear rate was measured. According to their primary results, the VeroGray impeller fabricated by Polyjet 3D printer highly reduced the experimental time and cost and was chosen as the impeller for analysis of the wear test. VeroGray impeller at a rotational speed of 1200 rpm and in the presence of 5% concentrations of erodent during the 110 h showed a mass loss percentage of around 8.08%. Upadhyay et al. [25] investigated the tribotechnological and mechanical properties of PLA propeller blades in marine applications. They studied the friction and wear behavior with its sliding wear mechanism, due to the importance of tribotechnological, and studied soft and hard interfaces with degradation properties. Figure1.19a shows the PLA-propeller blades and (b) represents the result of the coefficient of friction (COF) of the PLA sample for smooth and rough surfaces at a relative humidity of 40%. The average COF of the PLA sample at the top and the bottom surface was 0.158 and 0.56, respectively, with respect to the immersion time, which was 30 days in seawater. The wear microstructure at the top and bottom surface of the PLA sample was shown in Figure1.19c. Sliding at the polymer sample's top surface provides a smooth transition to the

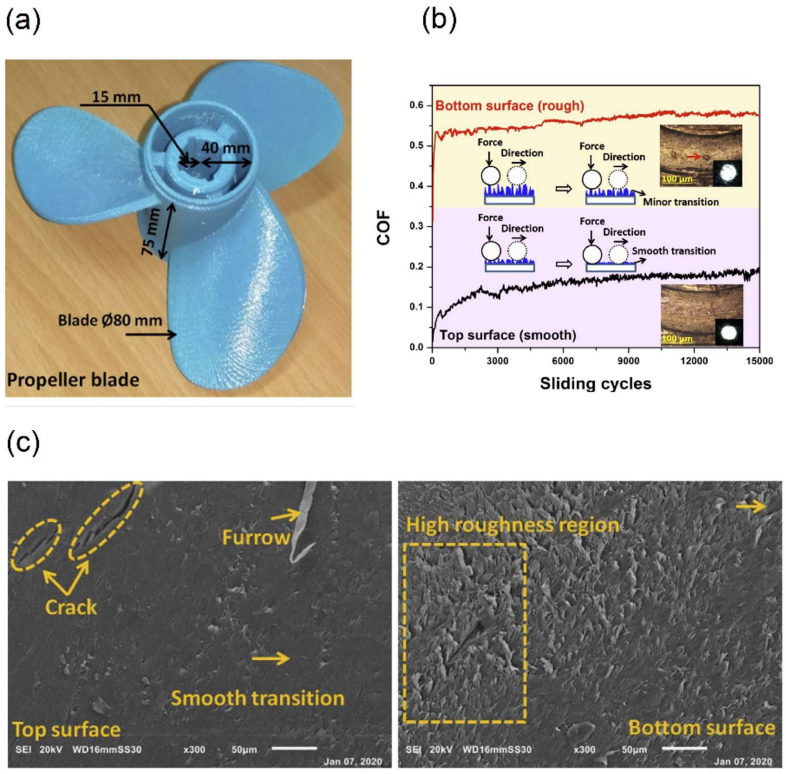

FIGURE 1.19 – (a) 3D printed propeller blade, (b) Friction performance of PLA sample at the top and the bottom surface and (c) wear microstructure of PLA samples [25] .

ball material due to low surface roughness. According to their results, they justified the immediate suitability of 3D-printed PLA parts for practical marine applications by designated tests of sliding and degradation.

1.5 Conclusion

Studies have shown increased efficiency and effectiveness using polymer rotors and polymer composites. Among thermoplastic polymers and composites, PEEK and PPS with and without reinforcements have been introduced as suitable options for wheel manufacturing. On the other hand, in the case of turbochargers, the use of resins to manufacture the wheels has been recognized as a suitable option. According to the studies done on the wheel manufacturing process, additive manufacturing, injection molding and conventional wheel manufacturing were the common methods of wheel production. In

general, the surface smoothness obtained by various processes had an acceptable level for use in the field of compressors and pumps. However, the time-consuming nature of the 3D printing method, for example, compared to the injection method will require further improvements. However, among 3D printing methods, SLA and MultiJet printing methods can provide a more suitable surface than other methods due to their process. High anisotropy in FFF samples is also a challenge to use this method in impeller construction, which requires further study. In injection molding and conventional machining methods, they can be examined to manufacture the geometries with less complexity compared to additive manufacturing. Fluid-structure interaction, as well as performance evaluation to analyze the wheel, are key steps in the final evaluation of the manufactured wheel.

Chapitre 2

Materials, methods and Compressor dimensional

Content

2.1 Materials

In this study, two kinds of thermoplastic polymers including polylactic acid (PLA) and polyphenylene sulfide (PPS) as filaments in a diameter of 1.75 mm to use in the fused filament fabrication were selected. A photocurable resin based on urethane dimethacrylate (UDMA) diluted with the corresponding methacrylate monomers, and bis(2,-4,6-trimethylbenzoyl) phenylphosphine oxide as a photoinitiator was chosen as a thermoset polymer to fabrication the parts by SLA method.

• PLA is a biodegradable and bio-based thermoplastic polymer derived from renewable resources such as corn starch or sugarcane. In this study, commercially available PLA filaments with a nominal molecular weight of 37,000 g/mol were used in two colors red and white. The PLA filaments were purchased from Ultrafuse.

• PPS is a high-performance thermoplastic polymer known for its excellent mechanical and thermal properties. The PPS filament used in this research was obtained from 3DXTECH Additive Manufacturing.

• The photoresist polymer with the commercial name of Black Resin (product code: FLGPBK04) was purchased from Formlabs (Berlin, Germany). The main characteristics of the PLA, PPS filaments, and urethane dimethacrylate (UDMA) resin are presented in Table 2.1 :

Post-processing of the fabricated samples by SLA, consisting of washing, has been done by isopropyl alcohol with 99.9% purity.

TABLE 2.1 – Properties of the polymers used, according to the producer

Characteristics	PLA	PPS	UDMA
Density g/cm^3	1.24	1.28	1.09
Glass transition temperature (°C)	60	85	85
Melting temperature (°C)	175	285	-
Tensile strength (MPa), ISO 527	37	50	38 - 65
Tensile modulus (GPa), ISO 527	2.08	2.65	1.6

2.2 Characterization methods

2.2.1 Microscopic observation

To analyze the mesostructure, microstructure and fracture surface the samples were probed by SEM (SEM, JSM-7800 F, Tokyo, Japan), operated at an acceleration voltage of 10 kV. In this regard, the samples were probed before and after loading. Such that before loading a small part of the samples were couped and investigated, and after loading the surface of the fracture of samples was probed. To analyze the interphase of FFF-printed neighbor layers.

2.2.2 Atomic Force Microscopy (AFM)

A Bruker Multimode 8 microscope, controlled by a Nanoscope V controller and operating in Peak-Force QNM mode, was utilized to mitigate potential surface damage resulting from tip contact. The analysis employed ScanAsyst-AirHR cantilevers with a nominal frequency of 130 kHz, a nominal spring constant of 0.4 N/m, and a nominal tip radius of 2 nm. Topographical and mechanical images were scrutinized to delineate the morphologies of distinct samples. For high-temperature in-situ AFM analyses, Tapping mode® was implemented, employing ScanAsyst-Air cantilevers with a nominal frequency, spring constant, and tip radius of 70 kHz, 0.4 N/m, and 2 nm, respectively.

2.2.3 Differential Scanning Calorimetry (DSC)

Differential Scanning Calorimetry (DSC) was carried out (Q1000 V9.0 Build 275 DSC, TA instrument) to investigate the physical transformations taking place and the degree of crystallinity of the FFF samples and polymerization degree of the resin in different manufacturing conditions. In this regard, approximately 8 g of each sample was removed, and then the thermogram heating was carried out from room temperature up to 250 °C. The heating rate and nitrogen gas flow were 10 °C/min and 50 ml/min, respectively. The following equation was used for the calculation of crystallinity:

$$X_c = 100 \times \frac{\Delta H_m - \Delta H_{cc}}{\Delta H_m^0} \tag{2.1}$$

where ΔH_m is the enthalpy of melting, ΔH_{cc} represents the enthalpy of cold crystallization, and ΔH_m^0 refers to the melting enthalpy of 100% crystalline PPS which is equal to 93.7 J/g [189].

2.2.4 Thermo Gravimetric Analysis (TGA)

The thermal stability of samples was analyzed by thermogravimetric analysis (TGA), using a METTLER TOLEDO 822e instrument (Ohio, U.S.). Regarding, samples were weighted in the range of 9 - 10 mg. The test was performed at a temperature from 25 to 800 °C by a heating rate of 10 °C/min under a nitrogen flow of 50 mL/min.

2.2.5 Fourier-Transform Infrared Spectroscopy (FTIR)

Fourier-transform infrared spectroscopy (FTIR) was used to analyze the chemical composition of the samples to study their degradation by examining the changes in area or disappearances of certain characteristic peaks. In addition, the residual percentage of unreacted urethane dimethacrylate in the samples was investigated by this method. An FTIR spectrometer was used for the tests and the wavenumber was in the range of 4000 - 400 cm^{-1}.

2.2.6 Tensile testing

For analyzing the mechanical properties quasistatic tensile tests were performed by using the MTS 830 hydraulic machine with a loading cell of 10 kN at a constant ramp speed of 5 mm/min. At least four repetitions were performed for each tensile test, and the average of the results was finally reported.

2.2.7 Geometrical accuracy

The geometric precision of the wheels is studied using a 3D laser scanner (Solutionix D500). The method consisted of collecting the blue light reflected by the object's surface by the lens of a camera. The object is illuminated by a blue light source. The STL format file thus obtained from the scanner was superimposed on the CAD file using the Geomagic® Control X software to calculate the geometric deviation error. Figure2.1 shows the Solutionix scanner and scanning process.

2.2.8 In situ monitoring of temperature profile of filaments

The FFF process's thermal history of printed parts plays a critical role in the final properties. Improving the properties can be varied by local temperature between the inter-deposited layers. To understand the effect of different process parameters on mechanical properties, an Optris PI450 infrared

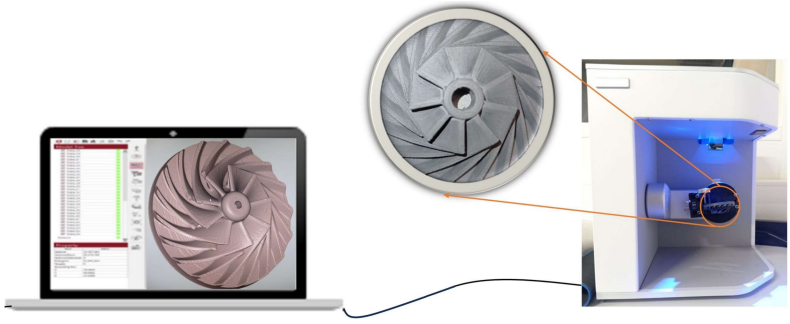

FIGURE 2.1 – Scanner Solutionix

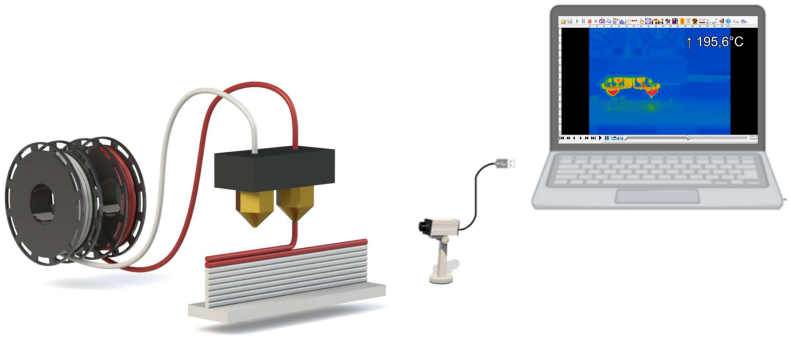

FIGURE 2.2 – Schematic of in situ monitoring of temperature profile during FFF printing

camera has analyzed the local temperature. In this regard, thin polymeric walls with two different colors of PLA (white and red) were printed. The red filament has been deposited on the top of the wall on white filaments (Figure2.2). The nozzle temperature and nozzle speed were set in the range of 210 to 230 °C and 10 to 30 mm/s, respectively. Bed temperature and layer height have been fixed at 60 °C and 0.15 mm, respectively.

2.2.9 Mounting and polishing

Mounting of the samples was performed by using IP epoxy which the maximum temperature of the resin during the polymerization is not passed 30 °C this temperature is less than the glass transition of PLA so, the polymerization has no effect on the intermolecular adhesion during mounting. After that, the sanding of the samples was started by a single-station automatic polishing machine (Mecatech 334). Finally, the samples were washed with an ultrasonic washing machine for 20 min.

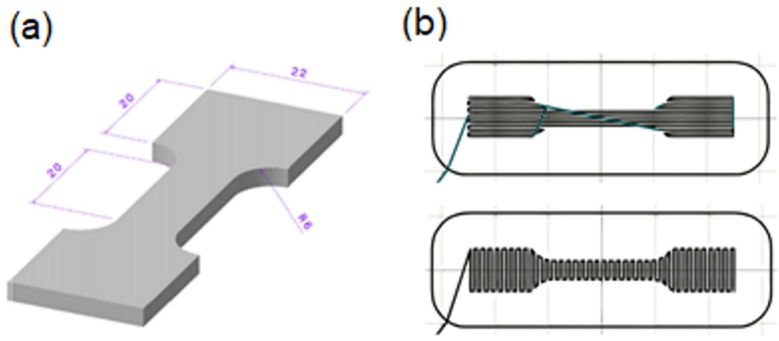

FIGURE 2.3 – (a) Nominal dimensions of tensile test specimen and (b) Tensile test in 0° and 90° orientation

TABLE 2.2 – Samples code

Sample code	Nozzle temperature (°C)	Nozzle speed (mm/s)
1.1	210	18
2.1	210	30
3.1	210	40
4.1	210	50
5.1	210	60
2.2	230	30

2.3 Samples preparation

2.3.1 In the sample scale

2.3.1.1 Fused filament fabrication

As mentioned two different types of semi-crystalline thermoplastic polymers were selected to use in FDM method. First, the fabrication of the samples with polylactic acid (PLA) is described. The tensile test specimens were printed according to Figure2.3 and this shape has been used in other studies [196]. The specimens were sliced using the Simplify 3D software and were manufactured using a Reprap 3D printer with a 0.4 mm nozzle. The print speed, nozzle temperature, and layer thicknesses were 18-60 mm/s, 210 °C, and 0.3 mm, respectively. Furthermore, for the investigation of interfacial weld strength and the mechanical anisotropy of printed parts, specimens were printed with respect to the 0° and 90° raster angles (Figure2.3b). Table2.2 shows the printing parameters to fabricate the samples.

Fabrication of the samples by polyphenylene sulfide (PPS) consisting of the specimen's geometry

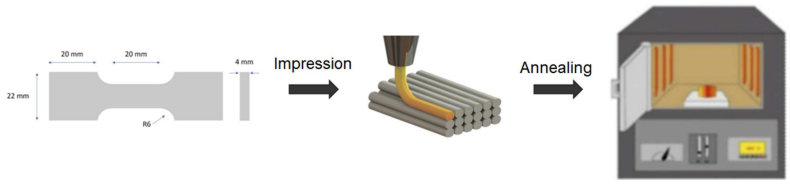

FIGURE 2.4 – Sample geometry and a schematic of fabrication process of samples

TABLE 2.3 – The process parameters and their levels

Level	Printing temperature (°C)	print speed (mm/s)	Annealing time (h)
1	320	10	24h
2	330	20	non
3	340	30	6h
4	350	40	1h:30min

and process is shown in Figure2.4. The specimens were sliced using the Simplify 3D software and manufactured using an FFF 3D printer with a 0.4 mm nozzle diameter. The layer thickness was set to 0.15 mm and to analyze inter-layer bond strength, raster angles of 90° were determined. In addition in order to improve the mechanical performance and interlayer bond adhesion, the samples were annealed at 200 °C in a different range of time from 1 to 24 hours. The different level setting of the experiment is shown in Table2.6. The samples code from left to right shows the nozzle temperature (°C), nozzle speed (mm/s), and annealing time (h), respectively.

2.3.1.2 Stereolithography approach

Formlabs Form 3-printer machine was used to fabricate the samples. Then, by the Preform software, the tensile samples (ISO 3167 type B29) were prepared in stl. file format for printing. The different orientations in 0°, 45°, and 90° (with respect to the x direction) with automatic support were prepared. The thickness of the layers was selected at 100 microns. Figure2.5 shows the schematic of printed samples in different sub-build orientations. Immediately washing was performed in an alcohol bath for 30 min after printing. Then the support was separated from the samples and green samples were produced. The green samples in different directions for the post-curing process were collected. The post-curing was applied for 30 min with two posturing mechanisms: using UV without heating and UV with the heating in the temperature range of 40, 50, 60, and 80 °C.

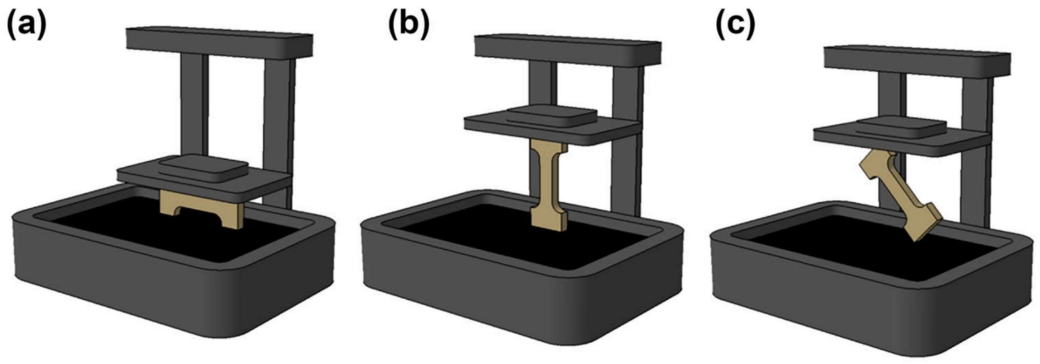

FIGURE 2.5 – Schematic of different build orientation directions of samples printing: a) 0°, b) 90°, and c) 45°

2.3.2 Manufacturing the compressor rotor

Two types of polymers were used in this study, consisting of a thermoplastic polymer and a thermoset. The thermoplastic polymer was polyphenylene sulfide (PPS) which is a semi-crystalline polymer with a glass transition temperature between 80 and 90 °C and a melting point of around 285 °C. The PPS is presented in the form of a filament, manufactured and supplied by the company 3DXtech. The second polymer was polyacrylic under the name Rigid10k, supplied as a liquid mixture (resin) of base molecules from Formlabs (Berlin, Germany). For the synthesis of the polymer, the procedure was as follows. The resin consisted of urethane dimethacrylate (UDMA) diluted with the corresponding methacrylate monomers, a filler, and a photoinitiator. According to the datasheet, 100% pure ethanol was used to clean the samples after printing. These complementary parts will be used in both cases to compare the performance of the rotors obtained by the two manufacturing processes. Two AM techniques are used for the production of the rotor:

- Fused Filaments Fabrication (FFF)

PPS filaments were used in a Creatbot 3D printer. The latter makes it possible to manufacture parts with high-performance polymers thanks to a maximum extrusion temperature of 420 °C. The manufacturing parameters of the FFF printed rotors are shown in Table2.4. As can be seen in this table, the difference in printing parameters comes from the temperature of the extruder nozzle which is either 320 or 340 °C, and the filling rate.

- Stereolithography (SLA)

TABLE 2.4 – Process Parameters of FFF Printed rotors

Sample code	Raster angle	Nozzle temperature (°C)	Print speed (mm/s)	Filling percentage (%)
PPS-320	45° and -45°	320	20	30
PPS-340	45° and -45°	340	20	100

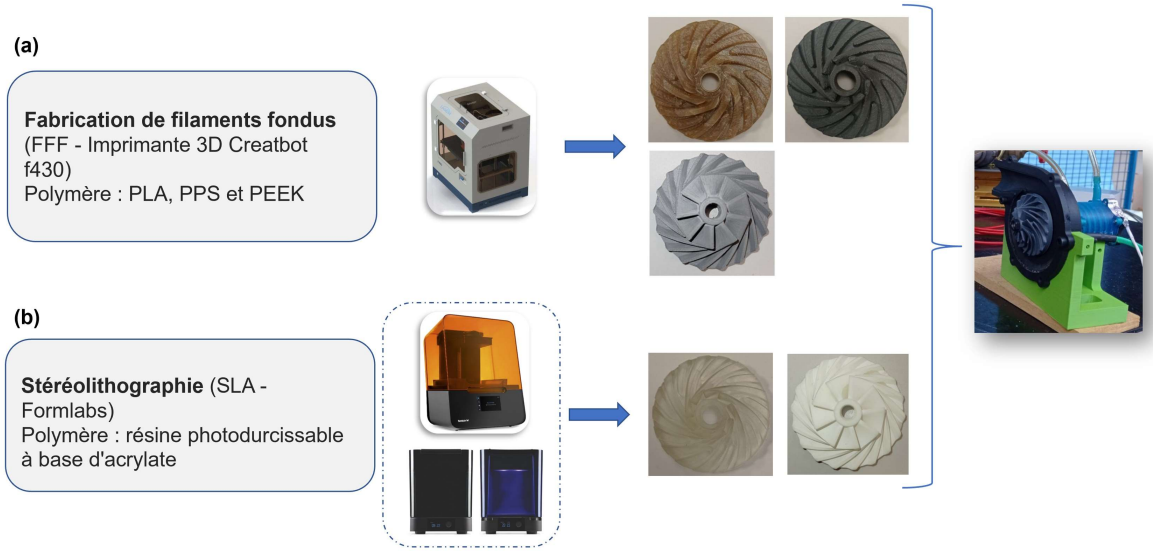

FIGURE 2.6 – Composants imprimés par : (a) stéréolithographie (SLA), (b) Creatbot F430

Rigid10k resin was used for the rotor manufactured by SLA, with a Formlabs 3D printer. The rotor made by SLA with Rigid 10k resin was printed with 0.1mm layer height and 30° underbuilds orientation. The impellers manufactured by FFF and SLA are shown in Figure2.7. After printing, the parts are first washed with isopropanol and then treated with a post-cure to complete the crosslinking between the resin components. The other parts of the compressor, such as the volute and the cooling system, were manufactured by the stereolithography method using the Formlab 3D printer. These complementary parts will be used in both cases to compare the performance of the rotors obtained by the two manufacturing processes.

2.4 Compressor dimensional and performance prediction CFD

The main purpose of the thesis is to study the material selection, strength, and manufacturing process that would be suitable for a high-speed centrifugal compressor. The detailed design and per-

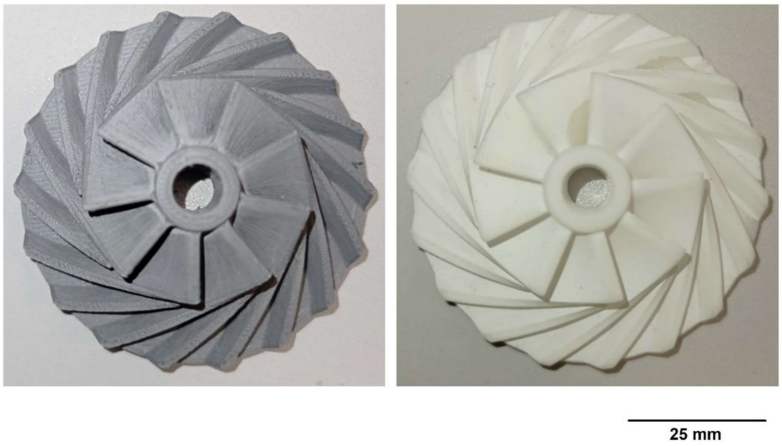

FIGURE 2.7 – 3D printed rotor (left: PPS by FFF and right: Rigid 10k by SLA)

formance optimization are thus out of the scope. However, state-of-the-art compressor design is carried out with the objective of being representative of a high-speed centrifugal compressor that could feed a hydrogen fuel cell system. The choice of the design operating point is also limited by the characteristics of high-speed motors that are easily available and affordable to develop the experimental test bench. For this study, the following limits are considered:

• Electric motor:

o Rotational speed N=90 000 rpm

o Shaft power P=1.5 kW

This corresponds to easily available motors for the experiments. These motors come from the manufacturer Neumotor and are usually used for radio-controlled models.

• Design operating point

The choice of this parameter also corresponds to a point of best efficiency for the radial compressor design according to Balje [190], see Figure2.9.

It can be noticed that the specific speed of 0.7 corresponds to the maximum efficiency on Balje Diagram.

The Balje diagram allows us to read the specific diameter given the best efficiency for a given specific speed. For N_s=38, D_s=3.5. This allows us to compute the geometrical diameter or the outer

TABLE 2.5 – Technical specifications of compressor

Parameter	Value	Unit
N	90000	rpm
Shaft Power	1500	W maxi
nc_{is}	70%	estimation
Pressure ratio	1.4	-
P1	1.00	bar
T1	293.15	K
rho1	1.19	kg/m^3
P2	1.40	bar
$T2_is$	322.73	K
T2	335.41	K
dh_is	29714	J/kg
dh	42449	J/kg
gm	0.0353	kg/s
Omega dh_is	0.718	-

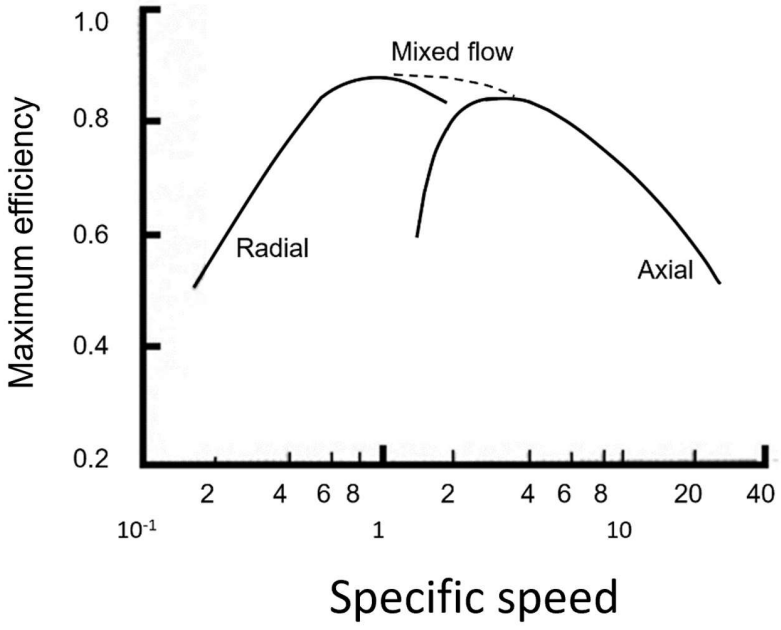

FIGURE 2.8 – Maximum efficiency against the specific speed

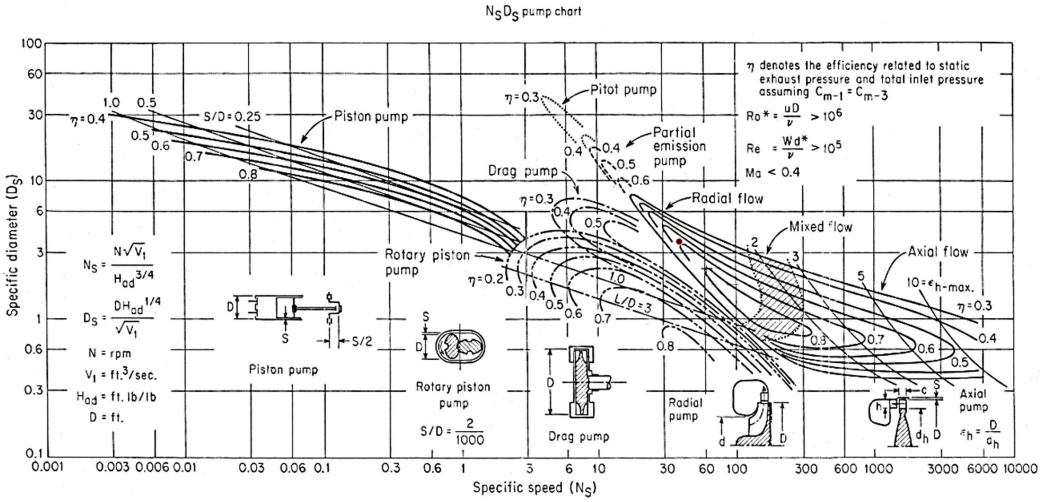

FIGURE 2.9 – Balje Diagram

radius r_2.

2.4.1 The primary model

For the preliminary design, a 0D model based on the boundary conditions was calculated for the rotor of a high rotational centrifugal compressor with a speed of up to 90,000 rpm. The compressor specifications included compression ratio, power and mass flow of 1.4, 1.6 (KW) and 35 (g/s), respectively. In this method, a preliminary calculation of the rotor geometry based on Cordier's curve [186] was applied by the interpolation method. The two most important parameters used in this method are the specific velocity and the specific radius. The specific speed is as follows:

$$\Omega = \omega \frac{\sqrt{\frac{\dot{m}}{\rho_1}}}{\delta h_{is}^{0.75}} \tag{2.2}$$

The specific radius is:

$$R_s = 1.8031 N_s^{-0.61} \tag{2.3}$$

From the value of the specific radius, the radius of the rotor can be calculated by the equation below:

$$r_2 \;=\; R_s \,\frac{\sqrt{\frac{\dot{m}}{\rho_1}}}{\left[\frac{\delta h_{is}}{\eta_{is}}\right]^{0.25}} \tag{2.4}$$

Then, the size of rotor inductor is calculated based on the method of minimizing the relative Mach number at the inlet blade tip to avoid jamming [187]. The relationship between the relative Mach number and inductor size is shown in Equation 4:

$$M_{1s} \;=\; \frac{1}{\sqrt{\gamma \;\times\; R \;\times\; T_1}}\;\frac{\dot{m}}{\rho_1 \;\times\; \pi \;\times\; (r_{1s}^2 \;-\; r_{1h}^2) \;-\; Z \;\times\; t_b \;\times\; (r_{1s} \;-\; r_{1h})}\;\frac{1}{\cos\beta_{1s}} \tag{2.5}$$

2.4.2 Models for losses

To design the compressor rotor to meet the technical requirements, we used loss models coupled with the preliminary calculation model. This iterative calculation will make the rotor geometry more accurate, ensuring greater reliability in the design process. We used 10 loss mechanisms, including incidence losses, blade loading losses, friction losses, backlash losses, mixing losses, disk friction losses, recirculation losses, leakage losses, vaneless diffuser losses, and volute losses. The details of each model are shown below:

Impact losses [191]:

$$\delta h_{inc} = 0.4\frac{\left(W_1 - \frac{C_1}{sin\beta_1}\right)^2}{U_2^2} \tag{2.6}$$

Blade load losses [192]:

$$\delta h_{bl} = 0.05 D_f^2 U_2^2 \tag{2.7}$$

Where D_f is scatter factor and calculated as:

$$D_f = 1 - \frac{W_2}{W_{1s}} + \frac{0.6 U_2 Cu_2}{U_2^2}\frac{W_2}{\left(\frac{Z}{\pi}(1 - \frac{r_{1s}}{r_2}) + 2\frac{r_{1s}}{r_2}\right) W_{1s}} \tag{2.8}$$

Friction losses [193]:

$$\delta h_{fric} = \frac{2C_f LB}{D_{hyd}} W_{avr}^2 \tag{2.9}$$

C_f is the friction factor:

$$C_f = 0.0412 Re^{-0.1925} \tag{2.10}$$

LB indicates length of the rotor flow is determined by:

$$LB = \frac{\pi}{8}\left(2r_2 - (r_{1h} + r_{1s} - b_2 + 2Z_{ax})\right)\left(\frac{2}{\frac{cos\beta_{1h}+cos\beta_{1s}}{2} + cos\beta_{2b}}\right) \tag{2.11}$$

With D_{hyd}, the mean hydraulic diameter of the rotor:

$$D_{hyd} = 2r_2 \frac{cos\beta_{2b}}{2\frac{2Z}{\pi} + 2r_2\frac{cos\beta_{2b}}{b_2}} + \frac{\frac{r_{1s}}{2r_2} + \frac{r_{1h}}{r_2}\frac{cos\beta_{1s}+cos\beta_{1h}}{2}}{\frac{Z}{\pi} + \frac{r_{1h}+r_{1s}}{r_{1h}-r_{1s}} + \frac{cos\beta_{1h}}{2}} \tag{2.12}$$

and W_{avr} is the average relative speed:

$$W_{avr} = \frac{2W_2 + W_{1h} + W_{1s}}{4} \tag{2.13}$$

Operating clearance losses [193]:

$$\delta h_{cl} = 0.6 \times Cl \times \frac{C_{u2}}{b_2 U_2^2}\sqrt{\frac{4\pi(r_{1s}^2 - r_{1h}^2)C_{u2}C_{m1}}{b_2 Z(r_2 - r_{1s})\left(1 + \frac{\rho_2}{\rho_1}\right)}} \tag{2.14}$$

Where Cl is the compressor operating clearance, $Cl = 0.1 \times b_2$

Mixing zone losses [194]:

$$\delta h_{mix} = \left[\frac{\left(1 - \epsilon - \frac{b_3}{b_2}\right)}{1 - \epsilon}\right]^2 \frac{C_2^2}{2\left(1 + tan^2\alpha_2\right)} \tag{2.15}$$

where the wake fraction ϵ varies from 0 to 1.

Disc friction losses [195]:

$$\delta h_{disfr} = \frac{0.0622}{R_e^{0.02}} \times \frac{\rho_{avr} \times r_2^2 \times U_2^2}{4\dot{m}} \tag{2.16}$$

Recirculation losses [196]:

$$\delta h_{recir} = 8 \times 10^{-5} sinh(3.5 \times \alpha_2^3) \times D_f^2 \times U_2^2 \tag{2.17}$$

Leakage losses [191]:

$$\delta h_{recir} = \dot{m}_{cl} U_{cl} \frac{U_2}{2\dot{m}} \tag{2.18}$$

Where $\dot{m}_{cl}$ is the leakage rate:

$$\dot{m}_{cl} = \rho_1 \times Z_{ef} \times Cl \times LB \times U_{cl} \tag{2.19}$$

Z_{ef} is the number of blades:

$$Z_{ef} = Z + 0.5Z \tag{2.20}$$

U_{cl} is the escape velocity:

$$U_{cl} = 0.816\sqrt{\frac{2 \times \Delta P_{cl}}{\rho_2}} \tag{2.21}$$

ΔP_{cl}, pressure losses due to leaks are calculated as:

$$\Delta P_{cl} = \dot{m} \frac{r_2 C_{u2}}{Z(b_1 + b_2) \times 0.5(r_{1m} + r_2) \times 0.5 \times LB} \tag{2.22}$$

Losses of a diffuser without blades [9]:

$$\delta h_{vaneless} = \frac{C_f \times r_2 \times \left[1 - \left(\frac{r_2}{r_4}\right)^{1.5}\right] \left(\frac{C_2}{U_2}\right)^2}{1.5 \times b_2 \times cos\alpha_2} \tag{2.23}$$

Losses of a volute [192]:

$$\delta h_{volute} = \frac{0.5 \times C_4^2}{2} \tag{2.24}$$

The flowchart consists of the preliminary rotor design process is shown in Figure2.10. The detailed dimensions of the rotor, calculated according to the preliminary results, are shown in Table2.6. Also, Figure2.11. shows the geometry obtained from this method respecting the different views.

2.4.3 Flow analysis

To assess the performance of the designed rotor beforehand, a CFD numerical simulation model was carried out with StarCCM+ software. This model is built from the actual geometry of the compressor,

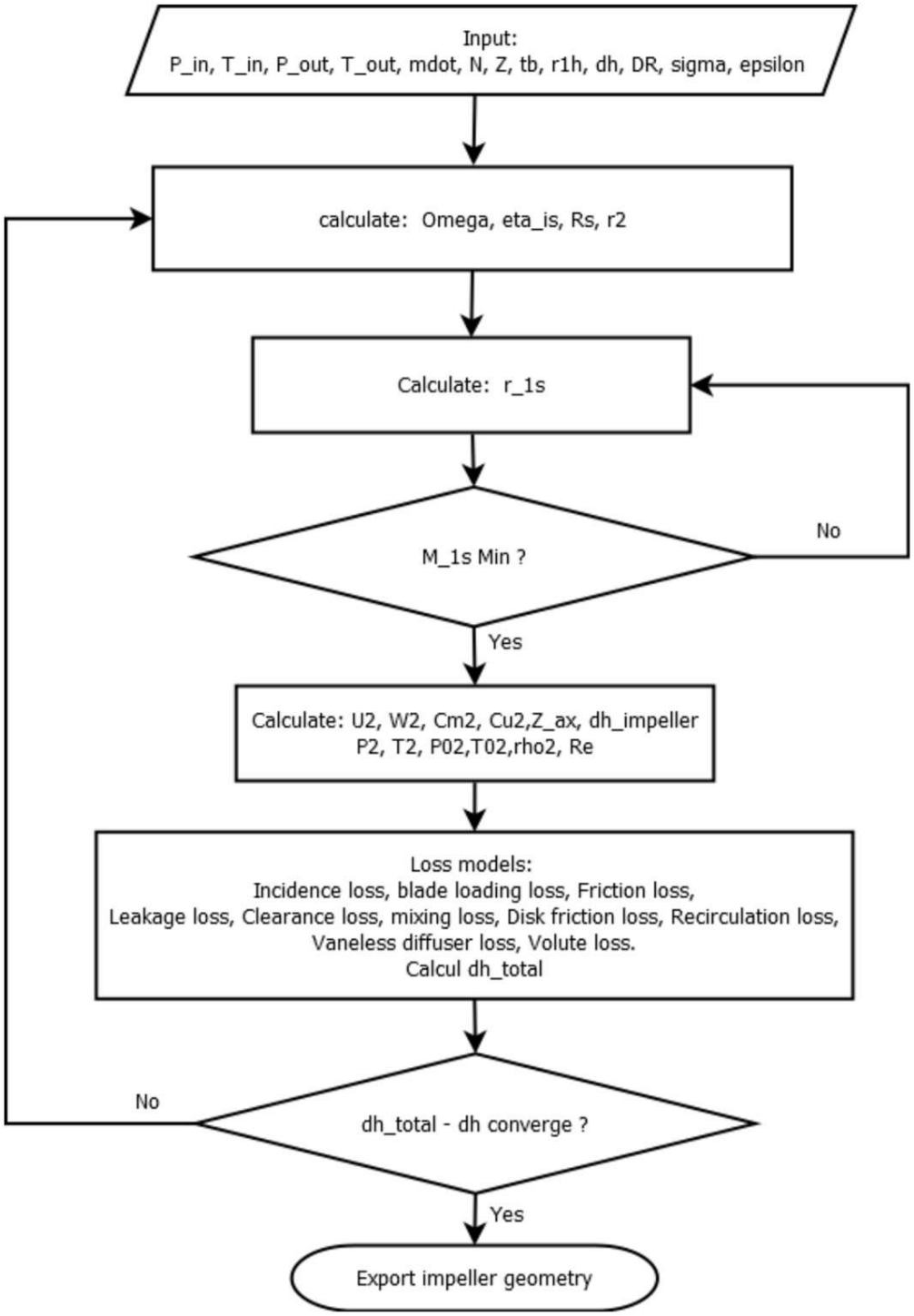

FIGURE 2.10 – The preliminary rotor design process flowchart

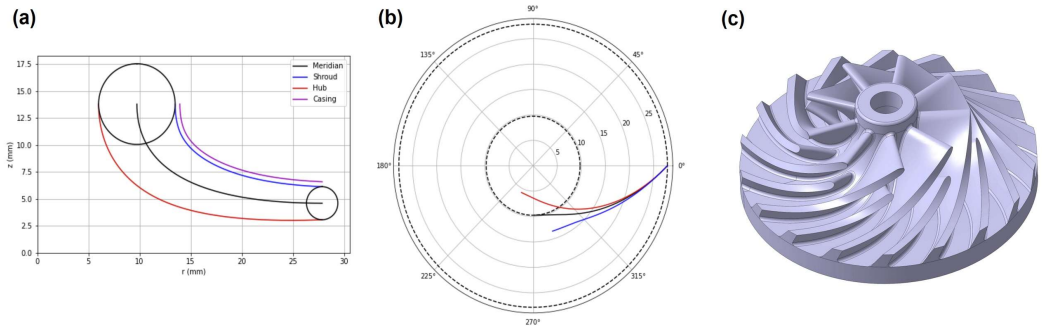

FIGURE 2.11 – Wheel geometry obtained by preliminary design method: (a) Meridian view, (b) Front view, and (c) 3D geometry

TABLE 2.6 – Detailed dimensions of the rotor

Parameter	Value	Parameter	Value
Hub radius (r1h)	6 mm	1h	32.6°
Arnaud radius (r1s)	14.6 mm	1s	57.45°
Exit radius (r2)	28.56 mm	2b	45°
b2	3 mm	Clearance	0.3 mm
Axial Length (max)	12.5 mm	Number of blades (Z)	9+9

with a complete rotor. In order to analyze the performance of the compressor, a method of solving RANS (Reynold-Averaged Navier-Stokes) equations was used. A "coupled flow" solver which allows solving the transport equations simultaneously with a second-order discretization by a stationary simulation has been applied. The "k-omega SST" turbulence model was used. The interface between the fixed and rotating domains is direct and the ideal gas model was used. A temperature of 293K and a pressure of 1 bar (absolute) are imposed at the compressor inlet. The outlet pressure is gradually increased until it becomes unstable while the rotational speed of the rotor is kept unchanged. In most cases, sufficient convergence has been achieved for the residuals to be kept below 1×10^{-4}. The performance of the compressor obtained by CFD simulation is shown in Figure 2.12. At the design point with a flow rate of 35 g/s, the compression ratio is slightly higher than expected, while the isentropic efficiency is lower than expected. However, the results of the CFD calculation show a deviation of 5% from the specifications. This shows that the preliminary design model meets the design requirements.

Figure 2.13 shows the flow streamlines in the compressor at 90,000 rpm. It can be seen that there

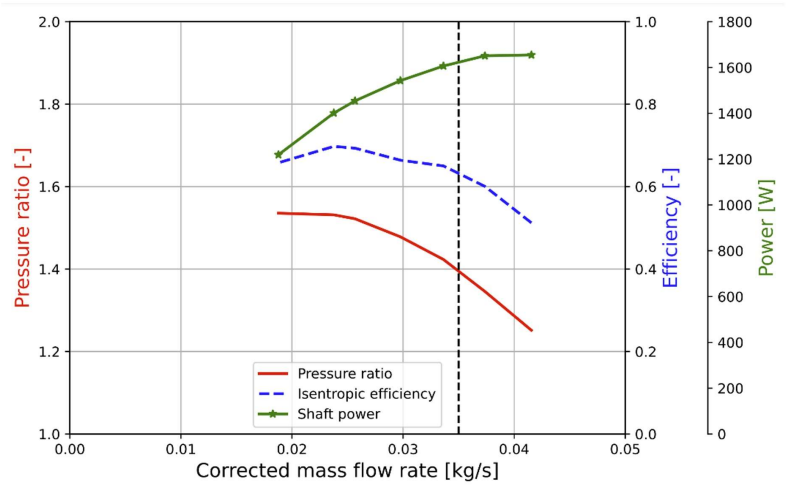

FIGURE 2.12 – Compressor performance obtained by CFD simulation at 90,000 rpm

is no recirculation in the passages of the rotor blades as well as in the volute that is refer to optimal performance. However, leakage flows can be observed at the blade tips due to the operating clearance between the rotor and the housing.

Figure 2.13a represents the distribution of the pressure on the average surface between the hub and casing. It can be seen that the pressure gradient increases progressively from the inlet of the rotor to the outlet of the volute. The static pressure increases rapidly inside the volute because most of the kinetic energy of the fluid flow is converted into static pressure. At the volute outlet, static pressure is fully recovered based on the scroll performance. Figure 2.13b shows the velocity distribution on the mean surface. It is easy to see that the separation occurs near the exit of the rotor causing losses. The cause of the separation is related to the Coriolis acceleration.

2.5 Study of the compressor performance

The LIFSE has been working on the design of a centrifugal compressor test bench, and it has been created to consist of a centrifugal compressor that is linked to an open-loop pipe. The centrifugal compressor takes in air at room temperature via a long pipe that is regulated by a control valve. After the air is taken in, it enters the compressor where it is compressed before being blown out into the atmosphere via a muffler. A diagram of the test bench is available, which includes a sensor

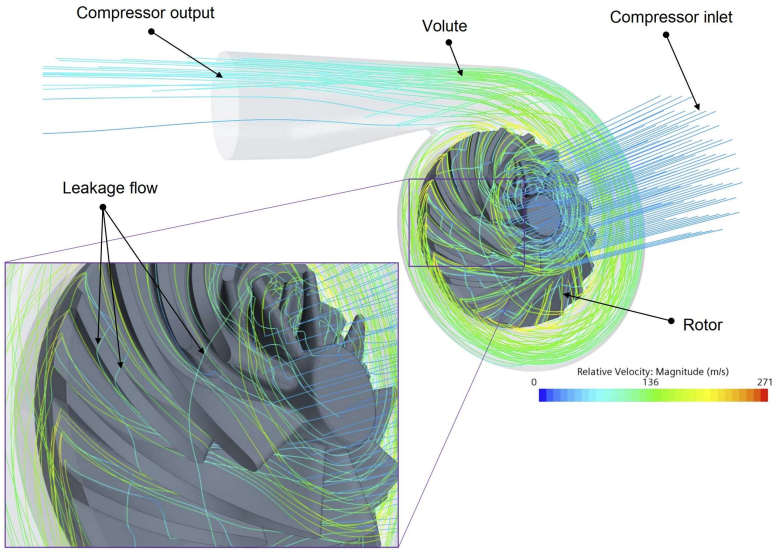

FIGURE 2.13 – Streamlines in computational domains

system at both the inlet and outlet of the compressor that is used to determine the operational parameters. Characteristics can be obtained by modifying the mass flow rate at a constant speed, and the combination of the characteristics at different constant speeds forms the performance map. To test the performance of the rotor fabricated by the two AM techniques, a turbocharger test bench is developed (Figure 2.15). This bench uses piezoresistive pressure sensors, PT100 probes, and a thermal mass flow meter to measure parameters at the inlet and outlet of the compressor. All the data from these sensors were analyzed using the Lab View software. The rotation speed of the compressor was controlled using an OPTEL-THEVON optical probe connected to a tachometer. It should be mentioned that the PPS-320 and PPS-340 rotors (manufactured by FFF) were studied without any post-processing to improve the surface quality. The rotational speed during the experiment was chosen at 52,000 rpm. All the results of the temperature and pressure measurements were recorded to calculate the isentropic efficiency of the compressor from the following equation.

Nomenclature

d_{hb} Hydraulic diameter, m

D_f Blade diffusion factor,

$\dot{m}$ Mass flow rate, Kg/s

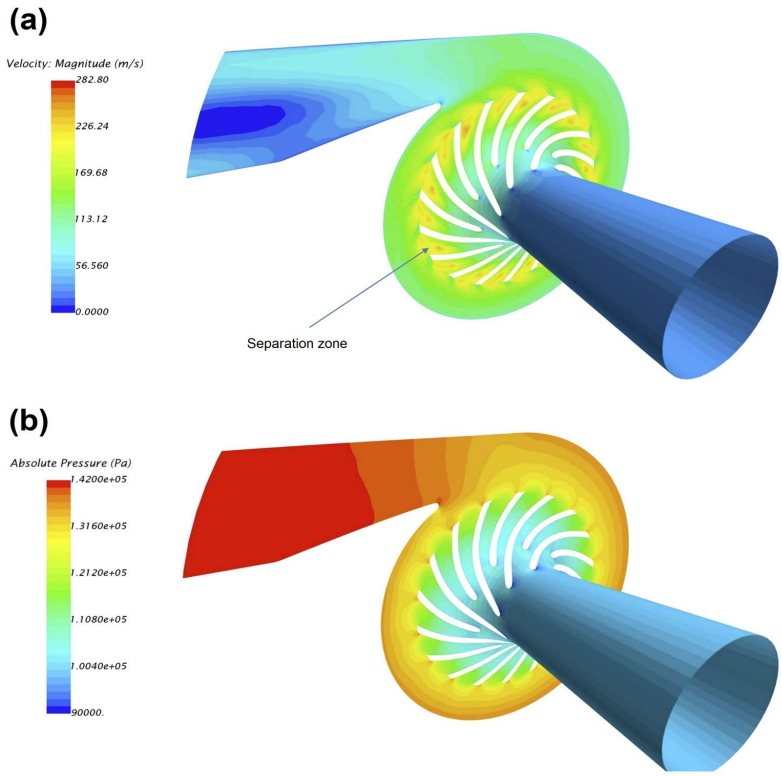

FIGURE 2.14 – (a) Pressure Fields and (b) velocity fields of mean surface

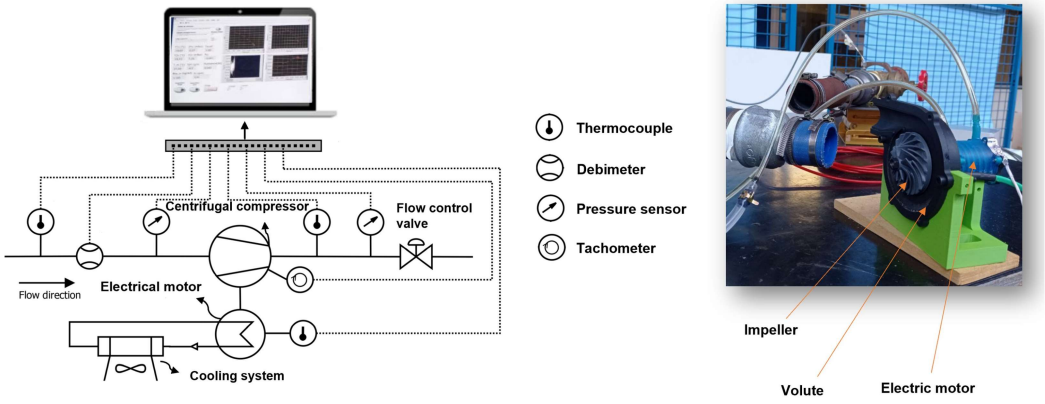

FIGURE 2.15 – Test bench used to determine the characteristics of the compressor

h	Specific enthalpy, J/kg
k_s	Blade surface roughness, m
r	Radius, m
Re	Reynolds number,
S	Specific entropy, J/(kgK)
C	Absolute velocity, m/s
C_f	Diffuser friction factor
t	Trailing edge thickness, m
T	Temperature, K
U	Peripheral velocity, m/s
K	Total pressure loss coefficient
L_b	Blade hydraulic length, m
W	Relative velocity, m/s
Z	Number of blades

Greek symbols

α	Absolute flow angle, deg
β	Relative flow angle, deg
ρ	Density, kg/m^3
Ω	specific angular velocities, rads^{-1}
ω	Rotational speed, rpm

Chapitre 3

Relation between manufacturing process and properties: Interfacial bonding in FFF process

Content

3.1 Characterization

3.1.1 Effect of nozzle speed on crystallization behavior

The crystallization behavior, glass transition, and melting of the samples were analyzed by DSC. The results are compiled in Table 3.1. Figure3.1 shows the results of DSC for supplied commercial PLA and the FFF printed parts. This figure presents two endothermic peaks related to the glass transition and crystal melting, and one exothermic peak corresponding to cold crystallization. The onset of glass transition for PLA filament and the FFF-printed parts was 60 ± 1 °C. The achieved glass transition of PLA filament is in good agreement with the study [197], also the results showed that the selected parameters for the fabrication of specimens have not shown a significant effect on glass transition. The results show the cold crystallization with a start temperature of around 103 °C for the samples (as shown in Table3.1). It should be mentioned that cold crystallization occurs due to a cooling rate that was rapid enough so the polymer has not enough time to crystallize and rearrange the chains [198]. According to the results, the enthalpy of cold crystallization has not shown a considerable difference considering the different printing parameters, which can be justified by considering the same cooling conditions in the samples. The percentage of crystallinity according to Equation 2.1 shows the decrease in the X_C with increasing the nozzle speed at 210 °C. One of the important parameters which can impact the X_C is chain mobility. Increasing the chain mobility leads to increasing the higher crystallinity [189]. Due to the effect of temperature on the mobility of polymer chains [198], it can be said that reducing the nozzle speed provides more time at higher temperatures which causes better mobility of chains. In addition, increasing the nozzle temperature to 230 °C indicated an increase in the Xc compared to 210 °C at the same nozzle speed. Due to the fact that the supercooling range plays a vital role in crystal nucleation and growth increasing the supercooling range can provide more time for nucleation and growth [198]. Therefore, increasing the nozzle temperature leads to an increasing supercooling range which is accompanied by increasing X_C. After cold crystallization, two melting peaks are identified in the melting zone which refers to the presence of different crystal morphology. The peak maxima for melting appeared at 150 and 155 °C, showing the spherulites and hexagonal crystals morphology, respectively [199]. The results showed an increase in melting entropy with decreasing print speed and increasing nozzle temperature. On the other hand, less nozzle speed had a greater effect on increasing the melting entropy of spherulites. In general, it can be said that

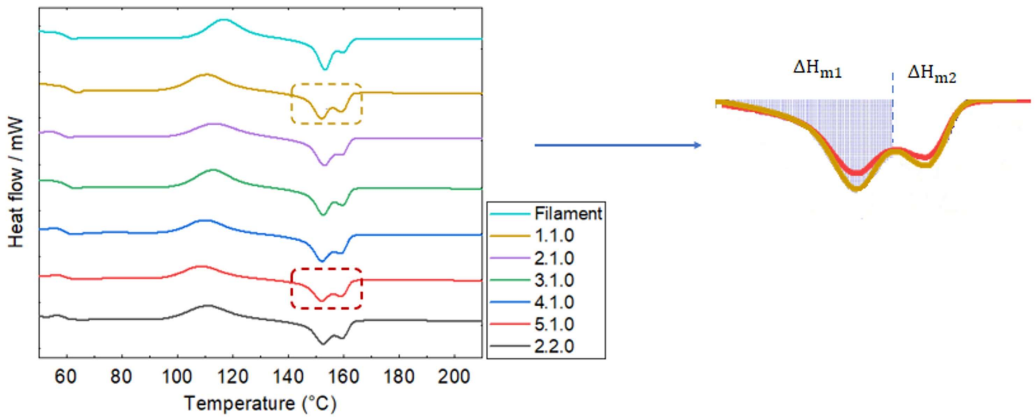

FIGURE 3.1 – The results from DSC curve

TABLE 3.1 – Process Parameters of FFF Printed rotors

Sample	Tg (°C)	Tpeak of cold crystalization (°C)	Tm_1 (°C)	Tm_2 (°C)	$\Delta Hm(J/g)$	Xc (%)
Filament	60.58	117.21	153.08	160.3	20.62	1.90
1.1	59.53	114.37	152.99	159.82	25.38	10.01
2.1	60.57	110.51	152.63	159.89	21.29	8.93
3.1	59.16	113.28	152.23	158.90	21.21	6.24
4.1	60.10	109.20	151.98	159.19	19.16	5.61
5.1	61.00	116.98	158.96	159.93	13.81	3.12
2.2	59.97	111.59	152.54	159.76	23.07	9.51

decreasing the velocity and increasing the nozzle temperature had a greater effect on the crystallization in the spherulite crystal forms.

The results obtained from FTIR for filament, printed samples with different nozzle speeds, and temperatures are shown in Figure 3.2. Considering the fact that the change in the intensity and/or position of peaks can indicate a change in the average change size of the polymer, the results of FTIR were investigated. The peaks including the –C–H stretching modes between 2998-2847 cm^{-1}, the –C=O stretching band at 1745 cm^{-1}, the ester –C–O– symmetric stretching at 1187 cm^{-1}, and –C–O–C– asymmetric stretching at 1072 cm^{-1} [200]. The peak at 1428 cm^{-1} represents the CH_2 bending vibrations. The peak at 861 cm^{-1} and 756 cm^{-1} was identified as the amorphous and crystalline part of PLA, respectively [201].

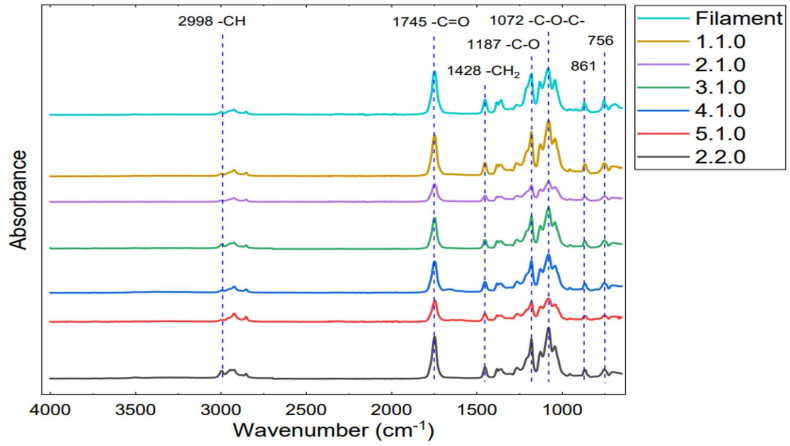

FIGURE 3.2 – FTIR Spectra of filament and samples for 0° raster angle

3.1.2 Mechanical properties

To evaluate the effect of printing speed on the mechanical properties of parts, tensile tests were performed on FFF-printed parts with 0° and 90° raster angles. Figure 3.3 shows the results of the mechanical tests (the experiment for each sample consisted of three replications), the results showed a considerable difference in the 0° samples, while the 90° samples did not show a significant difference. The modulus for 0° parts for different printing speeds (mm/s) increases in the following rank: 18 > 30 > 40 > 50 > 60. To evaluate the effect of printing speed on the mechanical properties of parts, tensile tests were performed on FFF-printed parts with 0° and 90° raster angles. The tensile strength for 90° parts for different printing speeds (mm/s) increases in the following rank: 18 > 30 > 40 > 50 > 60 mm/s. According to the tensile results 0° raster angle did not show much difference in tensile strength, however, reducing the nozzle speed increased the tensile strength by around 4 MPa in this case. This increase can be explained by the crystallinity of the polymer, in that the crystalline phase has stronger intermolecular interactions than the amorphous phase [202]. Plotting the tensile strength against the crystallization showed the linear relation between to parameters (Figure 3.4). Also, increasing the nozzle temperature showed more strength in this direction, which is also justified by the increase in the crystalline phase. A comparison of the results obtained from tensile strength in direction 90° indicated the dependency of these results on the nozzle speed. As mentioned, anisotropy has been one of the most important challenges in the fabricated parts by this process and studies have always

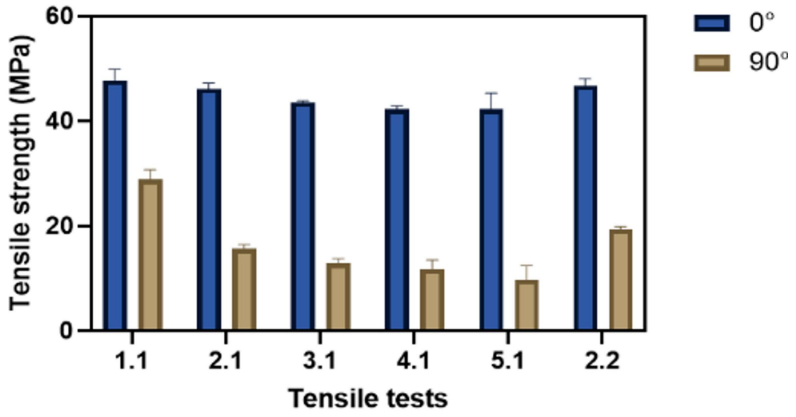

FIGURE 3.3 – Tensile strength of specimens printed with raster angles of 0^{o} and 90^{o} in nozzle speeds of 210 and 230 °C

tried to reduce this parameter. The difference in tensile strength in this direction is related to the welding between the layers. It should be noted that molecular diffusion has been one of the effective parameters in this field that is related to the mobility of polymer chains. Given that, as mentioned, reducing the nozzle velocity reduces the time range of mobility of polymer chains, which can lead to reduced molecular penetration and reduced tensile strength. Anisotropy always has been one of the important mechanical properties considered for selecting materials. By the following equation anisotropy can be calculated: DA where D_a represents the degree of anisotropy in tensile strength and is the tensile strength. Figure 3.4 shows the tensile strength of specimens printed with raster angles of 0^{o} and 90^{o} in nozzle speeds of 210 and 230 °C. According to the equation, reducing the nozzle speed from 60 to 18 mm/s led to reducing the 33% in anisotropy.

3.1.3 Dynamic mechanical properties

Dynamic mechanical properties of PLA printed parts were analyzed by the DMA method in this section. To more consideration of interlayer, the tests were done on the samples that printed at 90°. The nozzle's speed was 10 to 60 mm/s to fabricate the samples at a nozzle temperature of 210 °C in a bed temperature of 60°. Dynamic Mechanical Analysis (DMA) is a method that involves subjecting a sample to an oscillating load to measure its mechanical properties with respect to both elastically (storage modulus) and viscously (loss modulus). The storage modulus, denoted as G' represents the maximum amount of energy that can be stored during one cycle of oscillation and reflects the material's

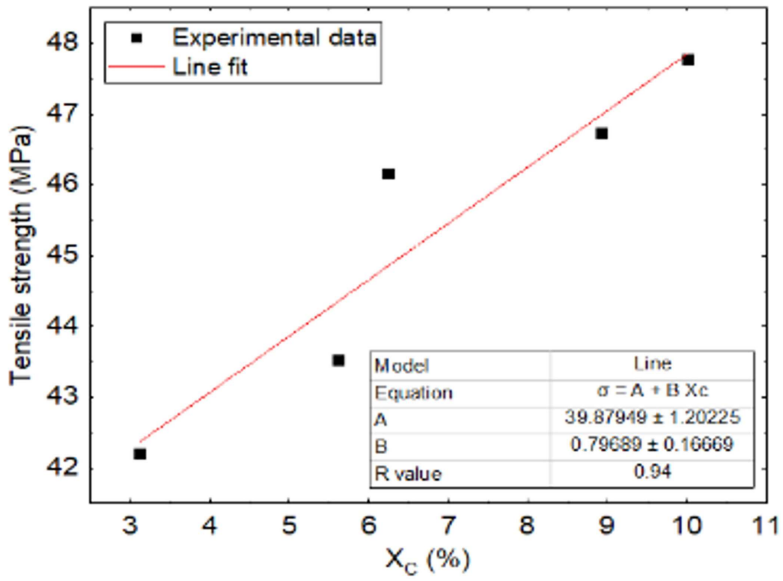

FIGURE 3.4 – Tensile strength with a raster angle of 90^{o} against the degree of crystallinity at nozzle temperature of 210 °C

stiffness. The loss modulus, denoted as G", reflects the amount of energy dissipated by the material due to internal friction. The ratio of the loss modulus to the storage modulus is known as the damping factor or $\tan(\delta)$, where δ is the phase angle between the strain and the response of the sample. The damping factor provides insight into the material's energy dissipation capacity and is related to the degree of molecular mobility, which influences the material's strength [203]. Figure 3.5 shows the storage modulus against the temperature at different frequencies for various printing parameters. Increasing the temperature is accompanied by reducing the storage modulus. Such that the rate of this decrease, rises dramatically after the glass transition of the sample corresponding to the frequency of the test. This observation is referred to the increasing mobility and chain relaxation at higher temperatures that lead to a decrease in the polymer's stiffness or storage modulus [204]. The tendency of loss factor with temperature is shown in Figure 3.6 As can be seen, this parameter first increases slowly and then significantly rises. The maximum value is corresponding to the glass transition and increases the frequency pushing these peaks to higher points. The free volume fraction and polymer chain mobility are related in that the free volume in a polymer matrix provides space for the polymer chains to move and rearrange themselves. Free volume in polymers can be attributed to the volume of total mass which is not engaged through the polymer chains. This leads to an increase in polymer chain mobility, which

can have a significant effect on the material's mechanical and physical properties. Free volume refers to the spaces between the polymer chains that are not occupied by polymer molecules. These spaces are often created during the polymerization process or by thermal or mechanical stresses. When a polymer chain is confined within a matrix, its movement is limited by the surrounding chains. However, the free volume in the matrix provides space for the polymer chains to move and reorganize themselves, which increases the mobility of the chains. As the free volume fraction increases, the polymer chains can move more freely and the material becomes more ductile and less brittle. This is because the free volume acts as a lubricant, reducing the stress concentration in the material and allowing the polymer chains to move more easily. On the other hand, when the free volume fraction is reduced, the polymer chains become more constrained and their mobility is limited. This can lead to an increase in the material's stiffness and strength, as well as a decrease in ductility. Analyzing this parameter with nozzle speeds to show the importance of the effect of process parameters on the chain mobility of the interlayer was done in this section. One can note that when increasing frequency, the α-transition temperature, T_α (related to T_g) has an increasing trend to high temperatures. The visco-elastic behavior of polymers is affected by the frequency of applied loading. This relationship between temperature and viscosity is directly proportional to frequency. Furthermore, Williams-Landel-Ferry (WLF) equation describes the correlation between temperature and the molecular relaxation times of glass-forming substances at the glass transition temperature (T_g). The equation is as follows:

$$Ln\frac{f}{f_R} = \frac{C_1(T - T_g)}{C_2 + (T - T_g)} \tag{3.1}$$

where f and f_r are frequency and reference frequency (1 Hz), respectively. T indicates temperature and T_g is reference temperature. C_1 and C_2 are the characteristic constants of the material that are associated with the free volume fraction and are given by:

$$C_1 = \frac{B}{2.303\ f_g} \tag{3.2}$$

$$C_2 = \frac{fg}{\Delta\alpha} \tag{3.3}$$

f_g is corresponding to the volume fraction at the glass transition state. B is constant near 1, $\Delta\alpha$ shows the expansion coefficient. Figure 3.6 shows the frequency ratio natural logarithm as a function

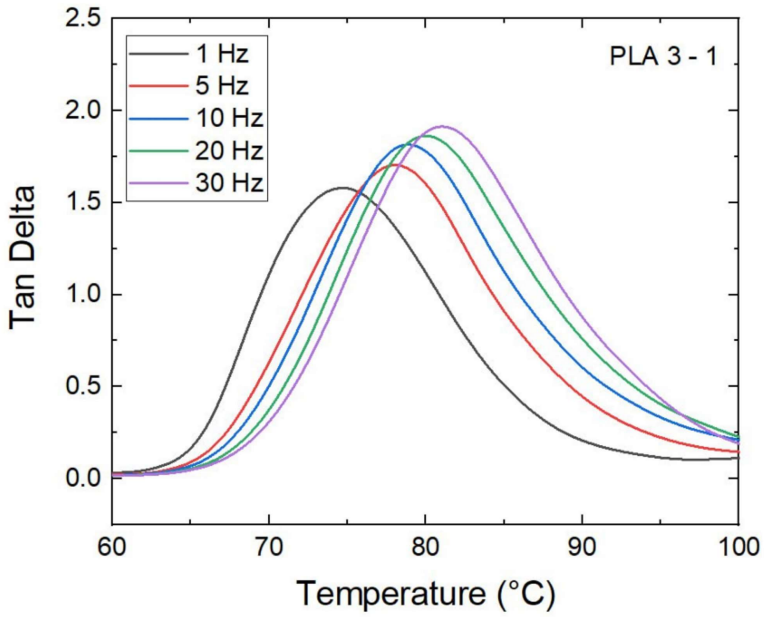

FIGURE 3.5 – Increase of glass transition temperature during multi-frequency DMA tests

TABLE 3.2 – The results of fitting from volume fraction

Equation	y = a + b × x				
Plot	1-1	1-2	1-3	1-4	1-5
a	-2.22	-0.56	-0.68	-0.14	-0.14
b	28.33	11.81	12.26	5.21	3.37
R-square	0.92	0.99	0.99	0.99	0.97

of temperature difference inverse. The linear regression of the experimental results with a correlation of more than 0.98, the slope of the straight-line plot is referred to as the ratio of C_1 to C_2. According to the results, the f_g by reducing the speed of the nozzle will be increased. It can be said that reducing the free volume fraction provides better mobility of the chains that are accompanied by better filament adhesion.

3.2 Interfacial bonding: Formation of interface and interphase investigation

The interlayer bond interface has a critical role in the mechanical properties of FFF parts. Studies have mentioned the anisotropy of the FFF parts as a challenge in this process which is related to the properties of the interlayer bonds. The process of bonding between the filament can involve three

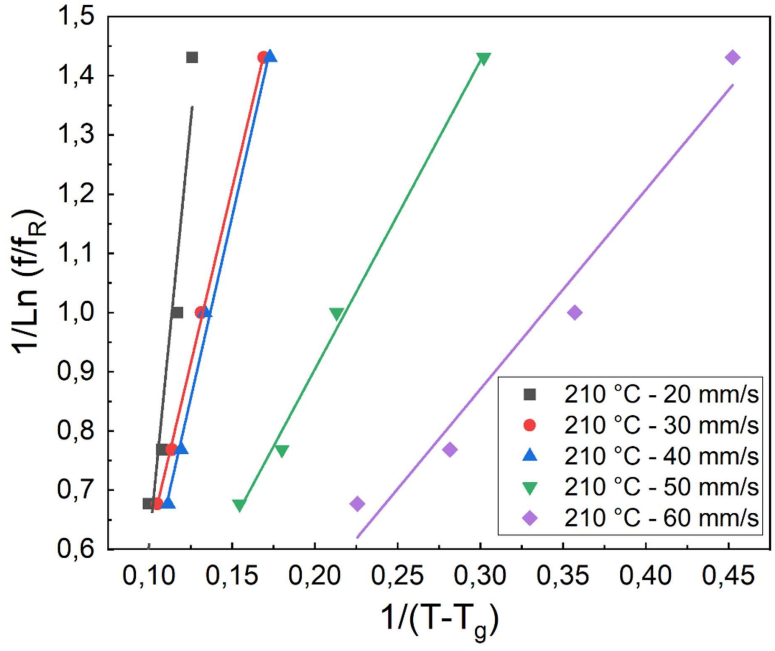

FIGURE 3.6 – WLF diagram obtained from multifrequency testing by DMA

mechanisms of surface contact, neck growth driven by surface tension, and molecular diffusion and entanglement across the inter-filament interface. Studies have tried to reduce the anisotropy by focusing on increasing the diffusion of the polymer chains in the interface of neighboring. It should be noted that the intermolecular penetration of polymer chains follows the power law, which is affected by the welding time. In other words, the welding time is the determining factor in the formation of the appropriate interlayer, so less welding time indicates more suitable mobility of the polymer chains to penetrating. Considering the relationship between the relaxation time and welding time, offline rheology analyses were performed on printed parts. Due to the non-isothermal conditions during the FFF process, the shift factor, α(T), by using time-temperature-superposition [205] which is calculated through William-Landel-Ferry (WLF) equation [206], should be determined:

$$\eta_0(T) = exp\left(\frac{-C_1(T-T_0)}{C_2+(T-T_0)}\right) \tag{3.4}$$

where T is the temperature for determination of α(T) in this temperature, T_0 represents the reference temperature, C_1 and C_2 are the constant fitted parameters. According to the studies number

average relaxation time, τ_n, can be considered approximately as the reptation time:

$$\tau_d(T) \cong \tau_n(T) = \frac{\eta_0(T)}{G_N^0} \tag{3.5}$$

where η_0 and G_N^0 represent the zero-shear viscosity and plateau modulus, respectively. Considering the relaxation time and temperature established the welding time has been defined as follows:

$$\tau_w = \frac{\tau_d(T)}{M_{corr}} \tag{3.6}$$

M_{corr} refers to a constant that converts the measured reptation time to τ_{weld} and according to the literature can be determined to 18. Offline rheological measurements were performed to transform the non-isothermal temperature profiles into an isothermal weld time. In this regard, the shift factors from the oscillatory shear experiments across a broad range of temperatures were determined to be related to the relaxation times across a wide range of temperatures. Figure 3.7a shows the storage and loss modulus for the range of frequency from 1 to 100 Hz at different temperatures, the complex viscosity in this condition has been shown in Figure 3.7b.

The study investigated two critical parameters, namely the zero-shear viscosity (η_0) and the plateau modulus (G_N^0). The Cross-WLF model was employed to calculate the zero-shear viscosity by examining the viscosity as a function of shear rate and temperature. The plateau modulus corresponds to the storage modulus (G) at the frequency where the loss modulus (G") reaches a minimum. The plateau modulus was defined as the G value at the second G-G" crossover, following established literature. Figure 3.8 presents the calculation of G_N^0 and η_0 based on a time-temperature-superposition master curve at 220 °C. According to the results, G_N^0 was determined at the frequency of 3 MHz equal to 0.19 MPa.

The term quantifies the fraction of diffusion across layers (x/x_∞) that can be calculated from total welding time as follows [4]:

$$\frac{x}{x_\infty} = \sqrt{6}\left(\int_0^t \frac{1}{\tau_w(T)}dt\right)^{0.25} \tag{3.7}$$

Where x and x_∞ indicate the interlayer penetration distance of diffusion between layers and inter-penetration depth of the chain length at maximum values which are related to full-strength samples,

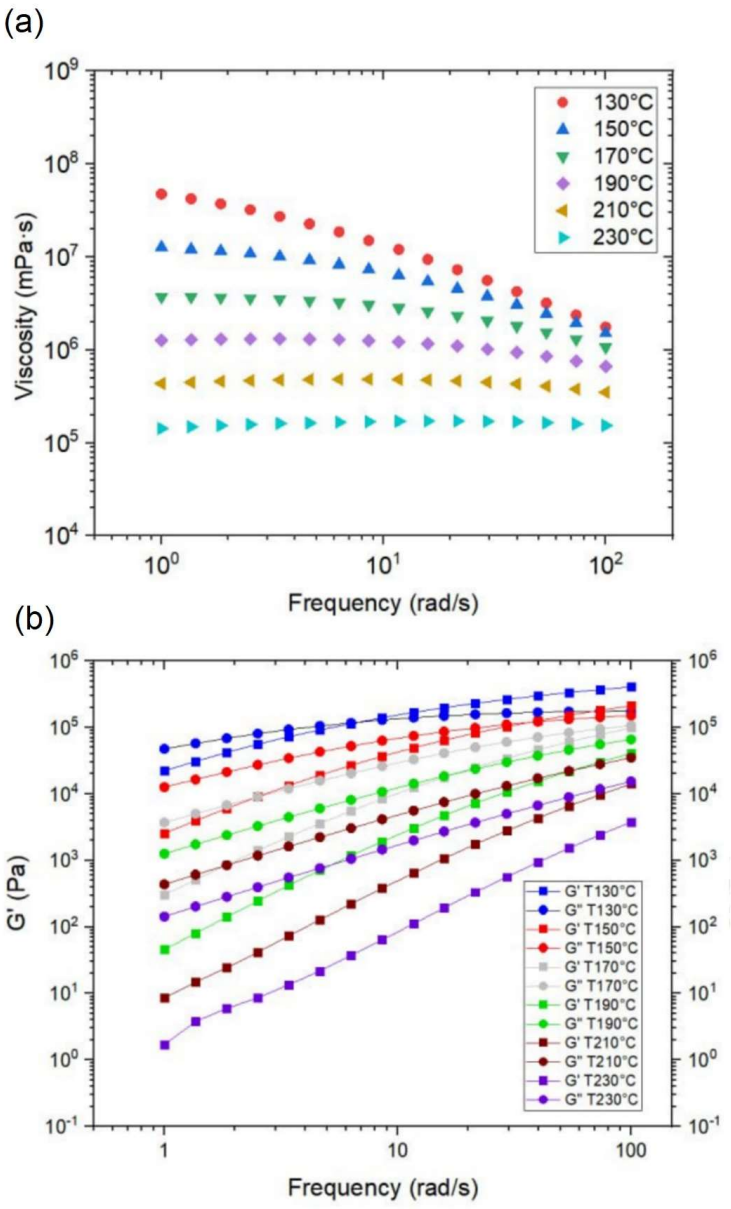

FIGURE 3.7 – (a) Storage and loss modulus and (b) complex viscosity for the range of frequency from 1 to 100 Hz at different temperatures

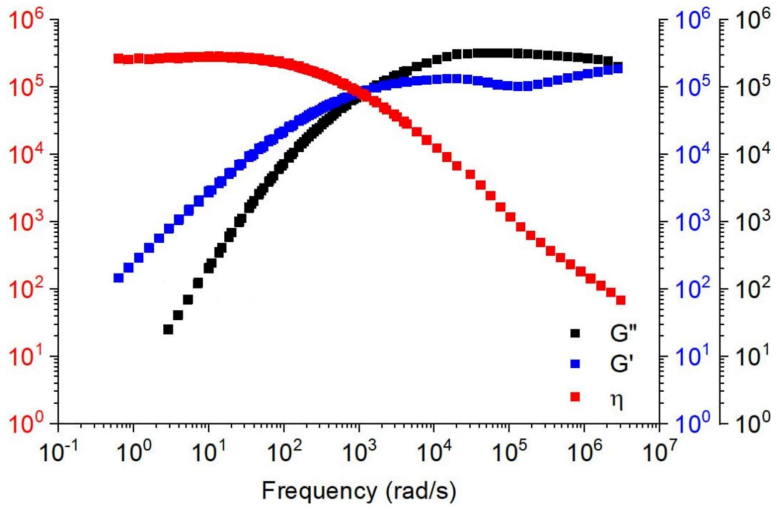

FIGURE 3.8 – Time-temperature-superposition master curve at 220 °C

respectively. Interlayer diffusion can be obtained from the above equation by considering x_∞ equal to 1 nm, which refers to entanglement length or Kuhn segment for many common polymers. In addition, t indicates the time during the diffusion which is from the start of printing up to the crystallization temperature (Analyzing the heat transfer in transient conditions is a subject that will be explained in the next section). The Tc was selected to limit chain diffusion at the interlayer, and this fact follows from the studies that demonstrate the creation of spherulites in the weld zone with an extreme effect on filament adhesion. The results, show the weld inter-penetration thickness from 9.35 to 9.91 nm depending on the different process parameters.

The results of welding time according to Equation B.22 are shown in Figure 3.9. As can be seen, increasing the temperature is accompanied by reducing the welding time. It can be said that a longer time provides better molecular diffusion and entanglement at the weld interface. The effect of welding time on mechanical properties has been analyzed with respect to the different process parameters of temperature and speed of the nozzle.

3.2.1 Heat transfer during filament deposition

The studies have highlighted the vital role of temperature in the bonding between previously and currently deposited filaments in FFF-printed parts. As the filament exits the nozzle and makes

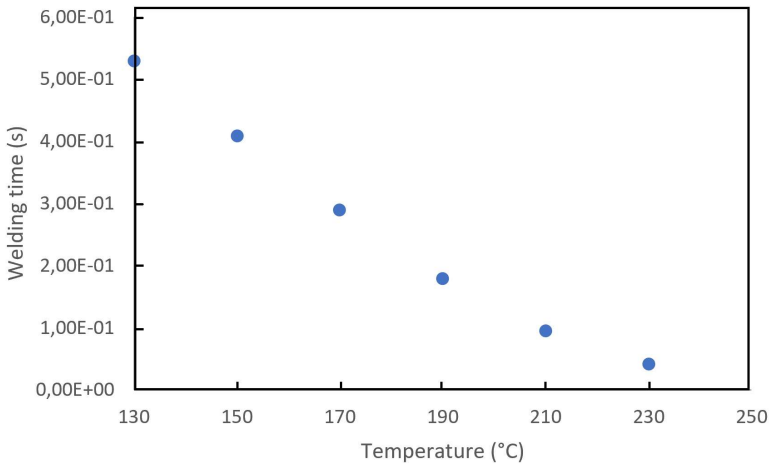

FIGURE 3.9 – Welding time against the temperature

contact with the previous layer, interlayer diffusion initiates and continues throughout the cooling process. As the temperature drops below the glass transition temperature (Tg), the rate of diffusion decreases progressively until it eventually finishes. This section of this thesis investigates experimental measurements of layer temperature and models the profile of this temperature during printing time based on the heat loss by convection with the environment. The expression for the thermal variation of the interface is as follows [141]:

$$\frac{\partial T}{\partial t} = b(T_\infty - T) \tag{3.8}$$

T_∞ and T are attributed to the plateau temperature and nozzle temperature, and b is a constant, that has a direct relation with convective heat transfer coefficient (h_{conv}) and the specific area (A_s), and inverse relation with density (ρ), deposited filament volume (V) and specific heat (C_p), which as follows:

$$b = \frac{h_{conv} A_s}{\rho V C_p} \tag{3.9}$$

The specific deposited filament area and filament volume were directly observed by optical microscopy. Regarding, the printed samples with different process parameters were polished and analyzed with ImageJ software. Figure 3.10 shows the optical microscopy of polished printed samples.

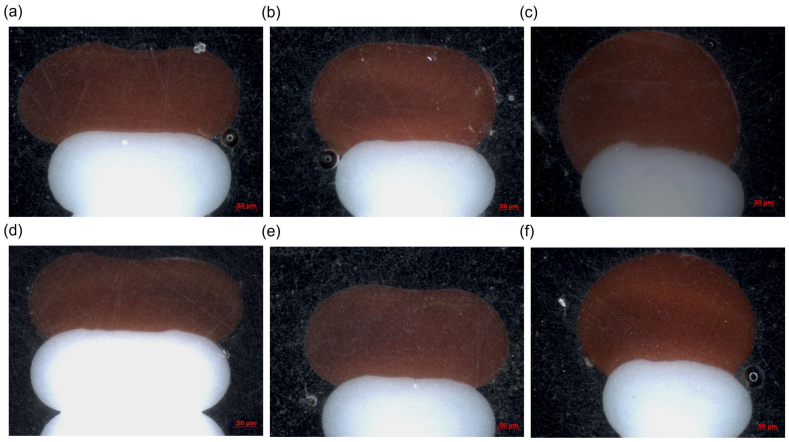

FIGURE 3.10 – Optical microscopy from printed samples : (a, b and c) printed speed of 8 mm/s and nozzle temperature of 210, 220 and 230 °C, respectively, (d, e and f) printed speed of 33 mm/s and nozzle temperature of 210, 220 and 230 °C, respectively.

Figure 3.11 shows the experimental temperature evolution of interfaces at the top layer printed compared to the model. As can be seen, the model can fit the experimental data well. Figure 3.12 shows the temperature profile with respect to the different temperatures and speeds of the nozzle. It should be noted that the volume of printed filament was measured at 0.1 s of the printed sample.

3.2.2 Microstructural analysis of interlayer

Atomic force microscopy (AFM) images from the polished cross-section of the FFF printed sample near the interlayer area (Figure 3.13). According to the results, the weld interface can be indicated from the images. This area can be related to the interphase between each polymeric layer that can involve about 4 µm. This interphase is caused by the intermolecular diffusion of chains in each neighbor layer. To analyze the effect of process parameters in this area, microscopical images were obtained.

By deposition of two polymeric layers during printing, the interphase will be formed between two molten polymers. This interphase is a transitional region where the properties of two polymers gradually blend, resulting in a zone of partially mixed materials that lie between the bulk of each polymer. The interphase region can significantly impact the strength and durability of the bond that forms between two polymers. The resulting bond will be strong and durable if the interphase is well-formed and exhibits strong adhesion between the two polymers. However, if the interphase is weak or

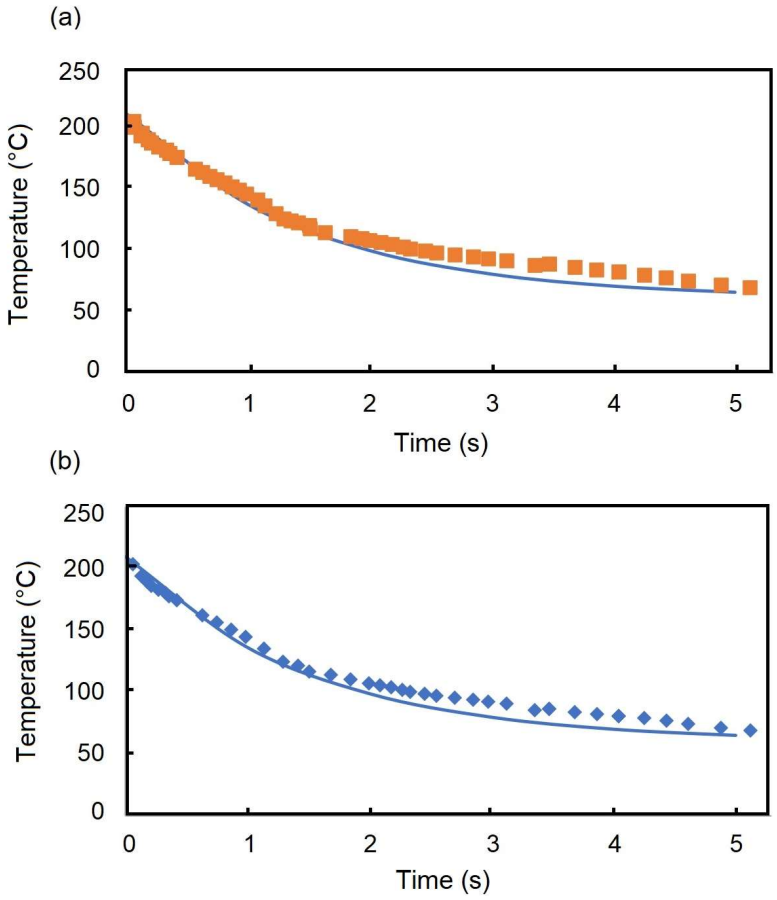

FIGURE 3.11 – Comparing experimental and modeled temperature evolution during fused filament fabrication process at 210 °C nozzle temperature, temperature bed of 60 °C and nozzle speed of (a) 8 mm/s and (b) 33 mm/s.

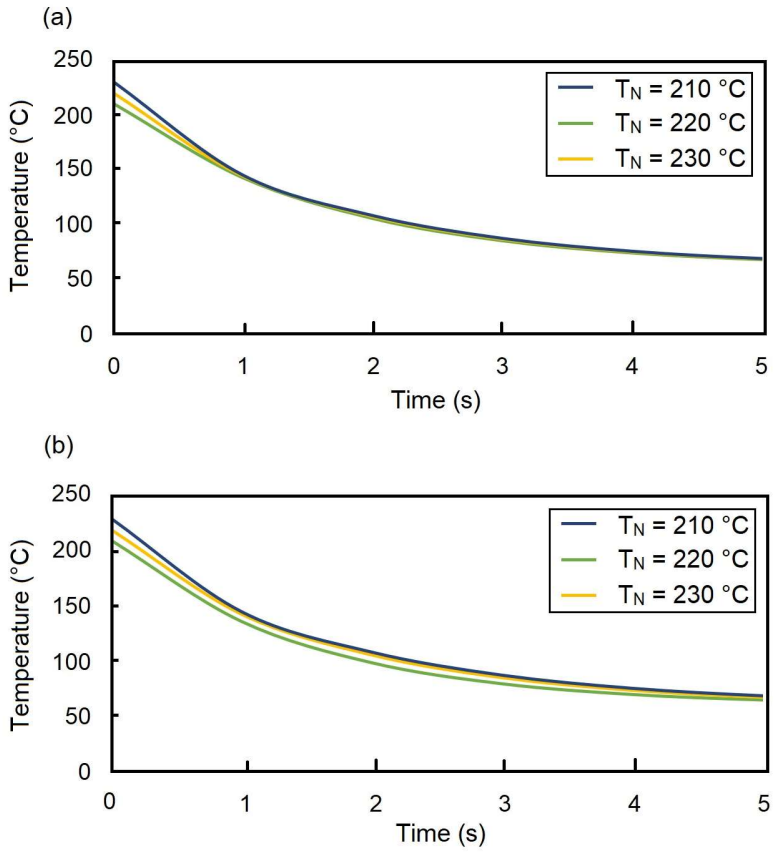

FIGURE 3.12 – Modeled temperature profile during fused filament fabrication process at temperature bed of 60 °C and nozzle speed of (a) 8 mm/s and (b) 33 mm/s in different temperatures of the nozzle.

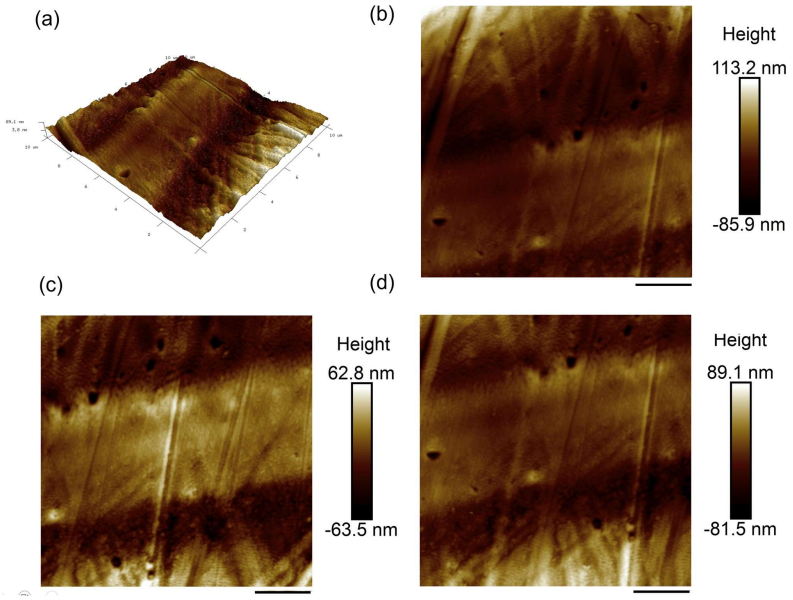

FIGURE 3.13 – AFM images obtained from the polished cross-section of FFF-printed sample at the weld area. The black scale bar indicates 2 µm.

poorly formed, the bond will be weaker and more susceptible to failure. Therefore, understanding and controlling the interphase during polymer welding is critical for achieving strong and durable bonds between different polymers. This can be achieved through careful control of process parameters, such as nozzle temperature, nozzle speed, and bed temperature that lead to the different welding times, viscosity, and pressure. The interphase between two polymeric layers was analyzed through optical microscopy. Figure B.15 shows the microscopical images from the single and two-color thin walls. As can be seen, the interphase cannot be seen in a single-color mode that is show the aim to use two colors for printing the samples.

Figure B.15 shows the interphase distance between two polymeric layers against the different parameter processes including temperature and speed of the nozzle. The results show increasing this distance by increasing the nozzle temperature and decreasing the nozzle speeds. Considering the mechanical results from the micro tensile test it can be said that the quality of interphase can play a more important role compared to the welding line with respect to the temperature and speed of the nozzle.

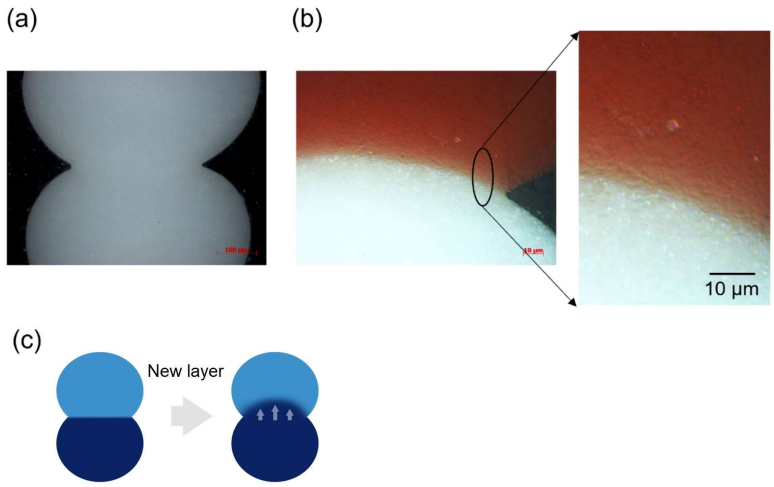

FIGURE 3.14 – (a) Microscopic image of single-color thin wall, (b) a Microscopic image of a two-color thin wall, and (c) a schematic of the interphase between two polymeric layer

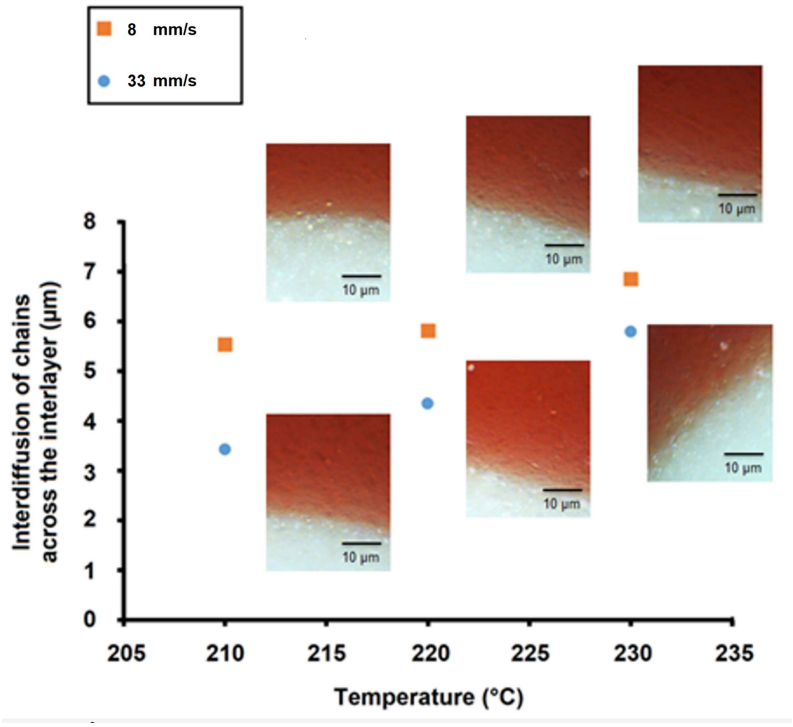

FIGURE 3.15 – Interphase between two polymeric layers against the different parameter process

3.2.3 Interlayer mechanical behavior

Thanks to the micro traction test, mechanical behavior between two printed layers was analyzed. Figure 3.16 shows the strain-stress curves from this test. According to the results, a nozzle temperature of 22O °C at a speed of 8 mm/s showed a UTS of about 13.3 MPa which was better than the two other nozzle temperatures at this speed. It can be said that, first increasing the temperature from 210 to 220 °C is accompanied by improving the UTS, but after this temperature, the UTS starts to decrease. Improving the interlayer strength by raising the temperature can be explained by time welding, such that decreasing the time welding by increasing the temperature and in addition reducing the viscosity can provide a better condition for the adhesion of adjacent filaments. The effect of welding time was studied by Qi et al [207]. The results showed a reduction in the anisotropy of PA-FFF printed parts by reducing time welding.

3.3 Interlayer bonding improvement and optimization of printing parameters

Regarding the high rotational speed that was required to provide the proper pressure in the compressor, PPS was used as a high-performance polymer for manufacturing the impeller. To acquire an in-depth understanding of the mechanical anisotropy induced by the FFF technique, the effect of nozzle temperatures and nozzle speed on the mechanical properties of FFF printed parts was investigated. In addition, annealing of the samples at different times was chosen as a post-processing method to improve the mechanical properties. The optimized conditions through the highest value were selected by analyzing the Gray Relational Grade (GRG) values in the 16th trial using ANOVA and S/N investigation. It is found that increasing nozzle temperature gives rise to a decrease in crystallinity, slightly improving the tensile strength of the PPS parts with the deposited strands parallel to the loading direction (i.e. raster angle=90°). Finally, manufacturing an impeller with optimized parameters was investigated by probing the surface through SEM and analyzing the geometrical accuracy from a 3D scanner.

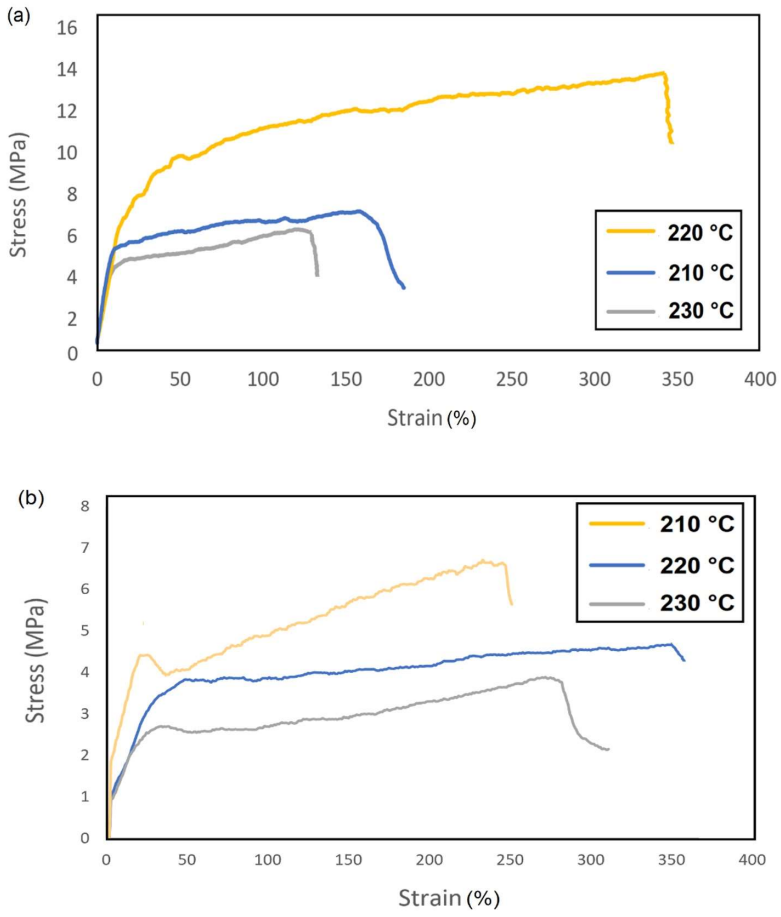

FIGURE 3.16 – Stress-strain curve from the micro tensile test: (a) at nozzle speed of 100 and (b) at nozzle speed of 35 mm/s

3.3.1 Gray relational analysis

Normalizing the experimental data was performed through the GRA method. Response results consisting of UTS, Young's modulus, and Crystallization have been analyzed. According to the expected quality characteristics of different responses, this value can be divided into three criteria for optimization in this method. "Larger-is-better", "smaller-is-better", and "normal-is-better" are shown in Equations B.23, B.24, and B.25, respectively.

$$X^*(p) = \frac{X_i\,(p) - Min(X_i\,(p))}{Max(X_i\,(p)) - Min(X_i\,(p))} \tag{3.10}$$

$$X^*(p) = \frac{Max(X_i\,(p)) - X_i\,(p)}{Max(X_i\,(p)) - Min(X_i\,(p))} \tag{3.11}$$

$$X^*\,(p) = 1 - |Xip - OB| Max[Max(Xip) - OB, OB - Min(Xip)] \tag{3.12}$$

- Max(Xi(p)): highest value of Xi(p)
- Min(Xi(p)): minimum value of Xi(p)
- OB: the target value
- X* (p): is the GRG value
- i: denote the number of trials
- Xi(p): response value of the target experiment

The UTS, Young's modulus, and crystallization are normalized using the "larger-is-better" rule. The sequence of deviations was calculated from Equation 3.13:

$$\Delta_{oi} \;= ||X_0\,(p) \;- X_i\,(p)\,|| \tag{3.13}$$

Where $\Delta_{oi}(p)$ represents the deviation sequence and X0(p) is the reference sequence which is equal to one. Following the deviation sequence, the Gray Relational Coefficient reflects the link between ideal and normal experimental results (GRC). Equation B.27 determines the Grey connection coefficient for each normalized data.

$$X^{*}(p) = 1 - \frac{\Delta_{min} + \zeta.\Delta_{max}}{\Delta_{oi}(p) + \zeta.\Delta_{max}} \tag{3.14}$$

Where ζ is the identification coefficient and is between 0 and 1 and is typically considered 0.5 and ζi (p) defines the gray relation coefficient. Additionally, the values of Δ oi (p) for min and max are max and min respectively. The multi-response qualities are typically evaluated using the gray relational grade (GRG). On the other hand, GRG is calculated using Equation B.28, the average total of the GRC.

$$\gamma_i = \frac{1}{n}\sum_{i=1}^{n}\zeta(p) \tag{3.15}$$

Where n is the number of process parameters, a higher GRG denotes a closer fit of the process parameter combination to the ideal. Following that, all experimental experiments were sorted according to GRG values between 1 and 16, with the most excellent GRG value designating the Optimum run, regarded as being in the first place. The 9th trial, which has the most excellent GRG value, has the best qualities compared to the other trials.

3.3.2 ANOVA and S/N ratio model fitting

Analysis of variance (ANOVA) and signal-to-noise ratio (S/N) tests were performed one at a time on the experimentally obtained data. All of the data were analyzed with MINITAB® 19.0. The Taguchi technique is used to examine the impact of a large number of parameters on a particular response. Figure 3.17 shows the stress-strain curves with respect to the different printing and post-processing conditions of the mechanical behaviors of the samples.

The signal-to-noise (S/N) ratio is used to analyze the effects of each parameter on response and optimize process parameters. As a result, a larger S/N ratio denotes ideal circumstances. Using MINITAB®19.0, analysis of variance (ANOVA) and signal-to-noise ratio were utilized to examine the data from the GRG. The Taguchi method was used to analyze the impact of GRG on the results. Larger-is-better was employed to maximize the GRG to optimize the process parameters since the higher GRG value, the better the intended answers. Figures 3.18a and b show various levels for each parameter against the mean S/N ratio. According to the results, ideal process parameters for producing the highest GRG can be achieved at the printing temperature of 340 °C, annealing time of 6 h,

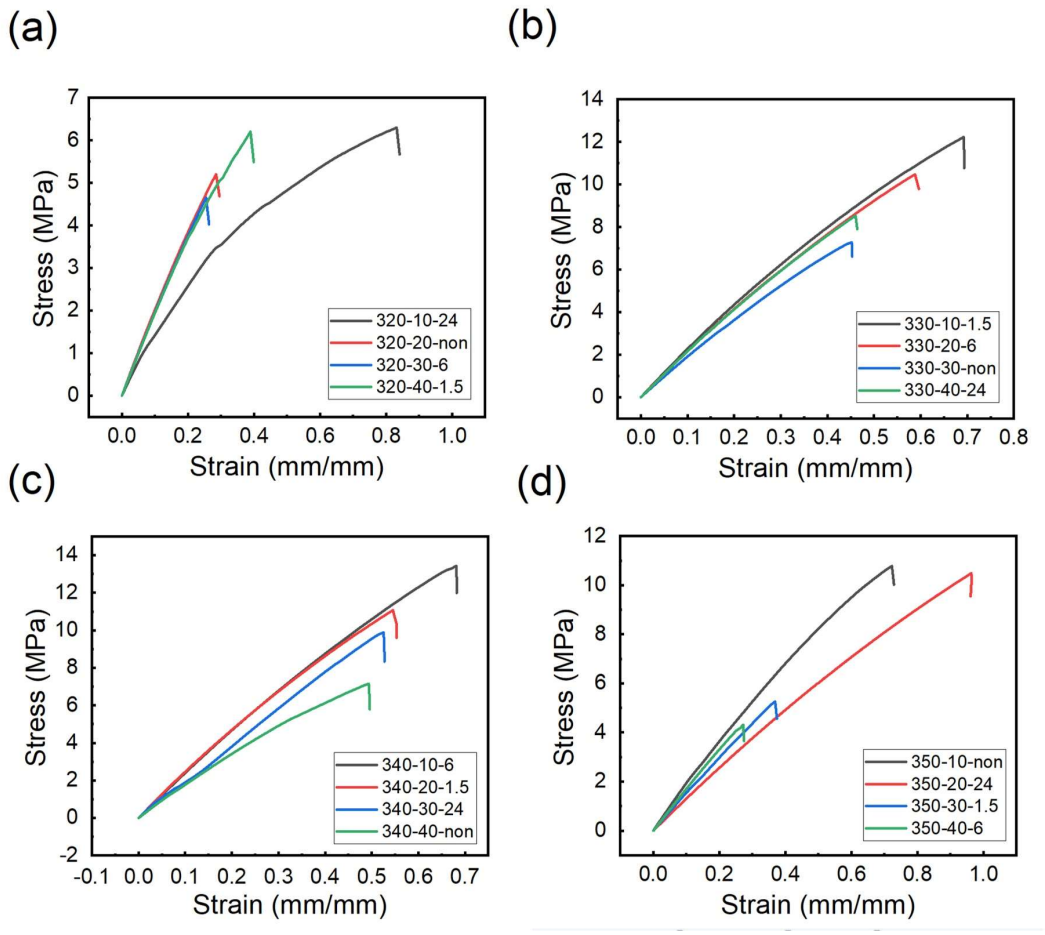

FIGURE 3.17 – Stress–strain curve of samples in different print and annealing conditions

TABLE 3.3 – Process Parameters of FFF Printed rotors

Source	DF	Adj SS	Adj MS	F-Value	P-Value
A	3	0.03263	0.010876	2.94	0.121
B	3	0.10802	0.036007	9.72	0.010
C	3	0.06816	0.022719	6.14	0.029
Error	6	0.02222	0.003703		
Total	15	0.23102			

and print speed of 20 mm/min.

The ANOVA method was used to assess the effects of each process parameter on the response variables. Table 3.3 displays the ANOVA results. Using Equation B.29, the adjusted sum of squares (Adj SS) was obtained.

$$s_T = \sum_{i=1}^{n} (\eta_i - \eta_j)^2) \tag{3.16}$$

In this formula, i stands for the average S/N ratio, j for the total mean S/N ratio, and n for the total number of experiments. It was found that print speed, annealing time, and printing temperature have the most significant effects on the amount of GRG, respectively, by examining the F-value mentioned in Table 3.3. and taking into account the rule that higher value, greater effect of related parameters.

Surface and contour diagrams, which are visual representations of the regression equation, are shown in Figures3.19 and 3.20, respectively. They were created by MINITAB 19.0 software and depicted the interactions between two separate process parameters on GRG. These figures demonstrate that the maximum GRG value is between 330 and 340 °C at the highest annealing temperatures and lowest print speeds.

3.3.3 Confirmation test

In the last step, a confirmation experiment was performed using optimum levels of process parameters to verify this parameter obtained from the GRA and also to evaluate the improvement in responses. To ensure the repeatability of the results, five tensile test parts with optimal parameters were fabricated by the FFF 3D printer. And the predicted Grey relational grade value or $Y_{predicted}$ is compared to the mean value of the grey relational grade obtained from the confirmation Equation B.30 and is used to calculate the predicted GRG value for optimal parameters.

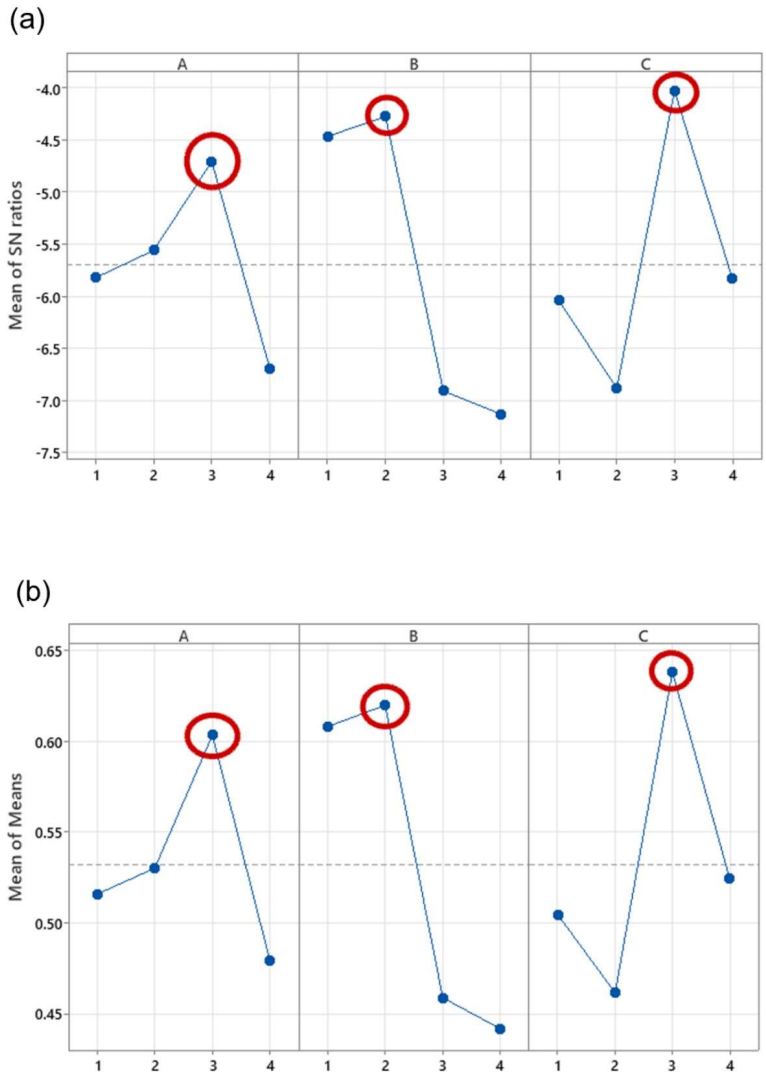

FIGURE 3.18 – Main Effects Plot for (a) S/N ratios GRG and (b) means GRG

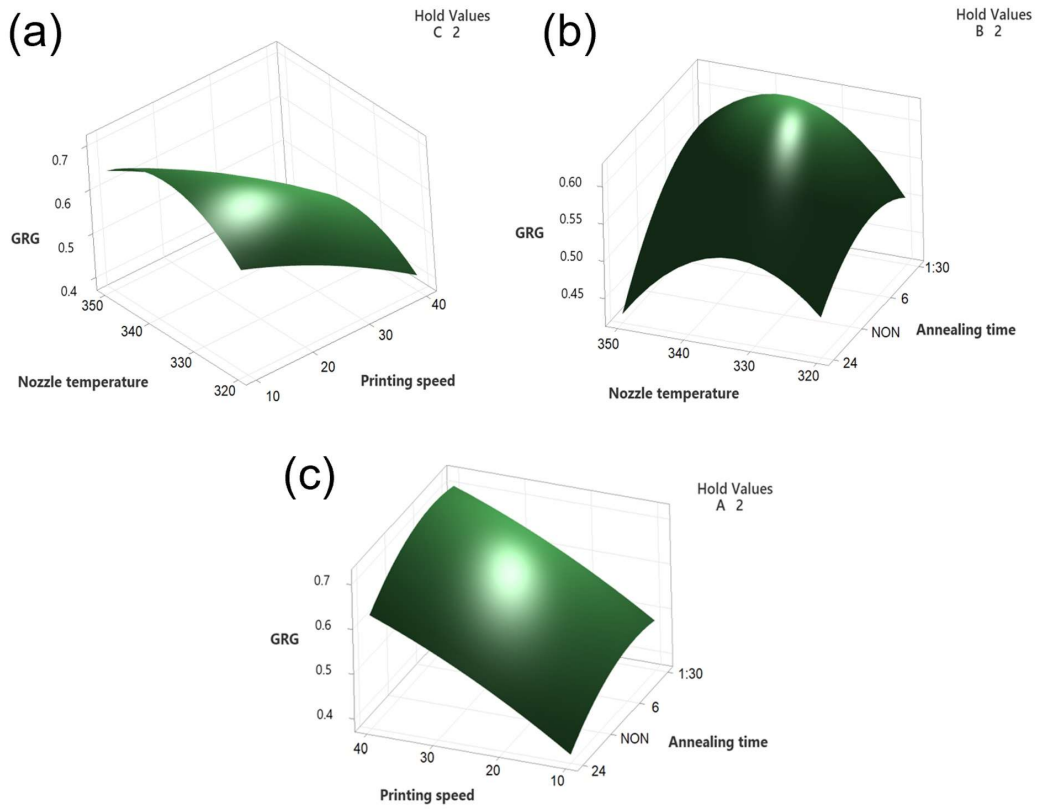

FIGURE 3.19 – GRG Surface plots. (a) print speed and nozzle temperature, (b) nozzle temperature and annealing time, (c) annealing time and print speed on GRG

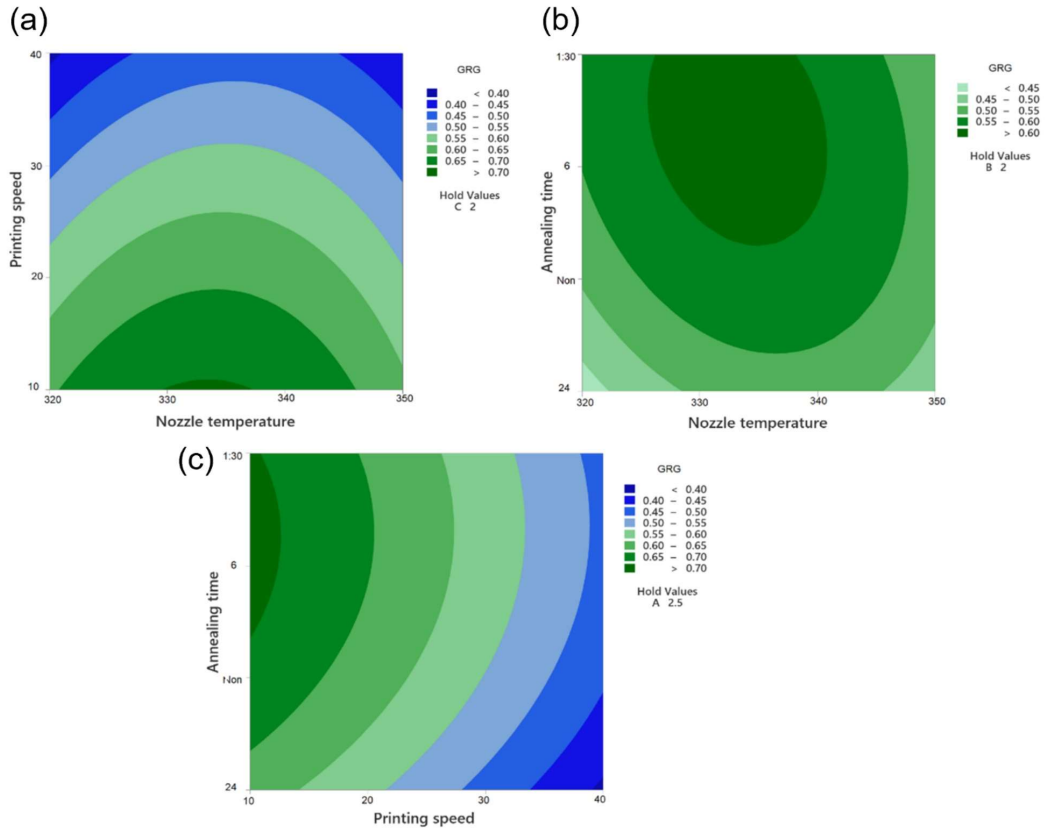

FIGURE 3.20 – GRG contour plots. The effect of; (a) print speed and nozzle temperature, (b) nozzle temperature and annealing time, (c) annealing time and print speed on GRG

TABLE 3.4 – Measured values of responses

	Initial parameter setting	Optimal parameter	
		Predicted	Experimental
Setting Level	Experimental No. 9 (340-10-6)	Sample code (340-20-6)	Sample code (340-20-6)
Young's modulus (MPa)	2432.6		3153.6
Ultimate tensile strength (MPa)	13.3		11.7
Crystallinity (%)	26.6		27.1
GRG	0.660	0.796	0.757

$$Y_{Predicted} = y_m + \sum_{i=1}^{n} (y_i - y_m) \tag{3.17}$$

$$Error(\%) = [\frac{GRG_{Predicted} - GRG_{Experimental}}{GRG_{Experimental}}] * 100 \tag{3.18}$$

$$Improvment(\%) = [GRG_{Experimental} - GRG_{Intitial}] * 100 \tag{3.19}$$

Where y_m represents the total mean of the GRG, y_i refers to the average GRG at the optimal level, and n is the number of chosen process parameters. Then a compression test was applied to the parts to evaluate the strength and Young's modulus of PPS parts. After calculating the experimental GRG the improvement in GRG is evaluated by percentage error between the predicted GRG and the experimental GRG. All the measured values of GRG are shown in Table 3.4, and by comparing the initial GRG and the GRG obtained from the experiment and using Equation B.31, it was found that the optimum GRG value has improved by 10%. So the results show that the values of the optimal parameters obtained from the GRA method have improved all the intended responses. Also, by comparing the predicted GRG and the GRG of the experiment (Equation B.32), it was found that the error rate is equal to 5 and it can be said that there is a good correlation between these values.

3.3.4 Effect of process parameters

The results showed the rank of impact process parameters from printing speed, extrusion temperature to annealing. Proper welding in the FFF parts can be mentioned as an important parameter that

impacts the final mechanical properties of the samples. Such that, enhancing the quality of the welding zone is followed by the improvement of mechanical properties. For the semi-crystalline polymers, nucleation and growth of spherulites can be introduced as a parameter that strongly impacts the chain molecular diffusion between two filaments that could be continuous until T_g. In fact, the creation of the spherulites after chain diffusion between two layers can improve the mechanical behavior of the parts, otherwise, increasing the crystallization in the parts such that the previous layers would be a good place for germination cannot improve the mechanical performance and have a negative effect [144]. The model fitting results from section 3.2.3 showed the improvement of mechanical properties and increased the degree of crystallization in higher printing temperatures and less speed at an annealing time of from 90 min to 6h. Figure 3.21 shows the DSC results from printed samples without annealing consisting of one exothermic peak around 122 °C and one endothermic from 250 to 285 °C. The exothermic peak refers to the cold crystallization that can correspond to the ordering of molecular chains in the crystalline PPS lamellae and is associated with heating. Yang et al. [84] studied the effect of thermal processing on the crystallization of 3D-printed PEEK samples. They showed an increase in the crystallization by reducing the nozzle temperature which was attributed to the incomplete melting result of the crystalline region in the nozzle with a lower and nonuniformity temperature inside. The DSC results from Figure 3.21 show the change in enthalpy of cold crystallization by changing the process parameters, such that the minimum of this value ($\approx$0.85 J/g) was reported for an extrusion temperature of 350 °C with a nozzle speed of 10 mm/min without a post-heating process. It can be said that higher temperature with lower speeds provides better melting during the printing.

Figure 3.22 shows scanning electron analysis (SEM) of samples without load and after printing. Fractographic analysis of specimens constructed at different layer thicknesses is illustrated. According to the results surface of samples printed with optimized parameter show better coalescence between the polymeric layers and fewer voids compared to the other samples.

3.3.5 Compressor impeller manufacturing

The fabrication of polymeric impellers has been at the center of a lot of attention. The impellers in the case of compressors can provide the proper fluid pressure through certain rotational speeds. Using FFF is a good method for the fabrication of these parts regarding their geometry complexity. Figure 3.23 shows a fabricated impeller with an optimized process of parameters. Considering the importance

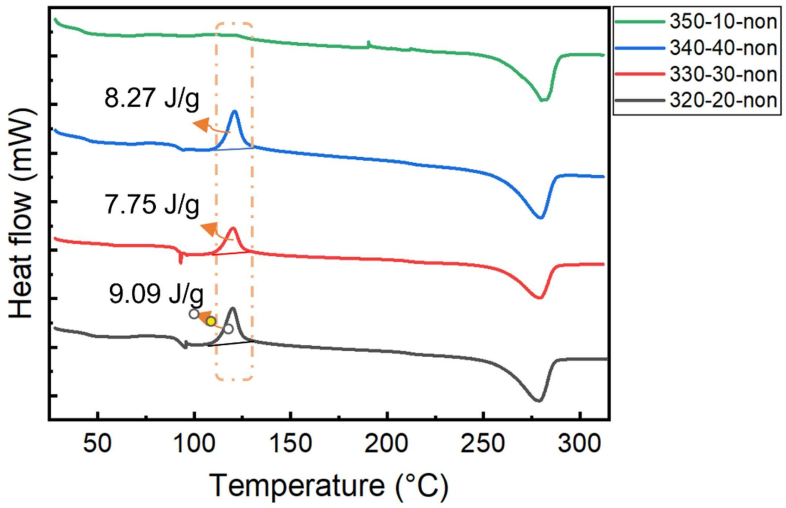

FIGURE 3.21 – DSC results of samples without annealing conditions

of coalescence between the polymeric layers on the final performance of the compressor, the surface of the blades was probed by SEM. The microscopical images show good welding between the layers, however, porosity is visible between some layers.

The geometrical accuracy of the fabricated impeller is another parameter that should be considered with respect to the method of fabrication [208, 209]. Considering the layer-by-layer manufacturing of parts in FFF method, depending on the precision of the technique, different geometric accuracies can be obtained. The layer height during manufacture has been considered an important parameter that can have an impact on the final surface roughness [210, 211]. Figure 3.24a shows the surface scan of the impeller from the scanner that was analyzed to investigate the geometrical accuracy. The deviations from the surface normals as this deviation is referred to as errors during the manufacturing process shown in Figure 3.24b and c. The average error across all distance measurements was -46 µm with a standard deviation of ±0.09 µm, respectively, (Figure 3.24d). According to the results, 81.2% of the surface deviation error was in the range of -0.1 to 0.1 mm.

3.3.6 Conclusions

In this section, the relation between the manufacturing process and properties of FFF parts has been shown. Different methods of characterization to show the importance of process parameters on

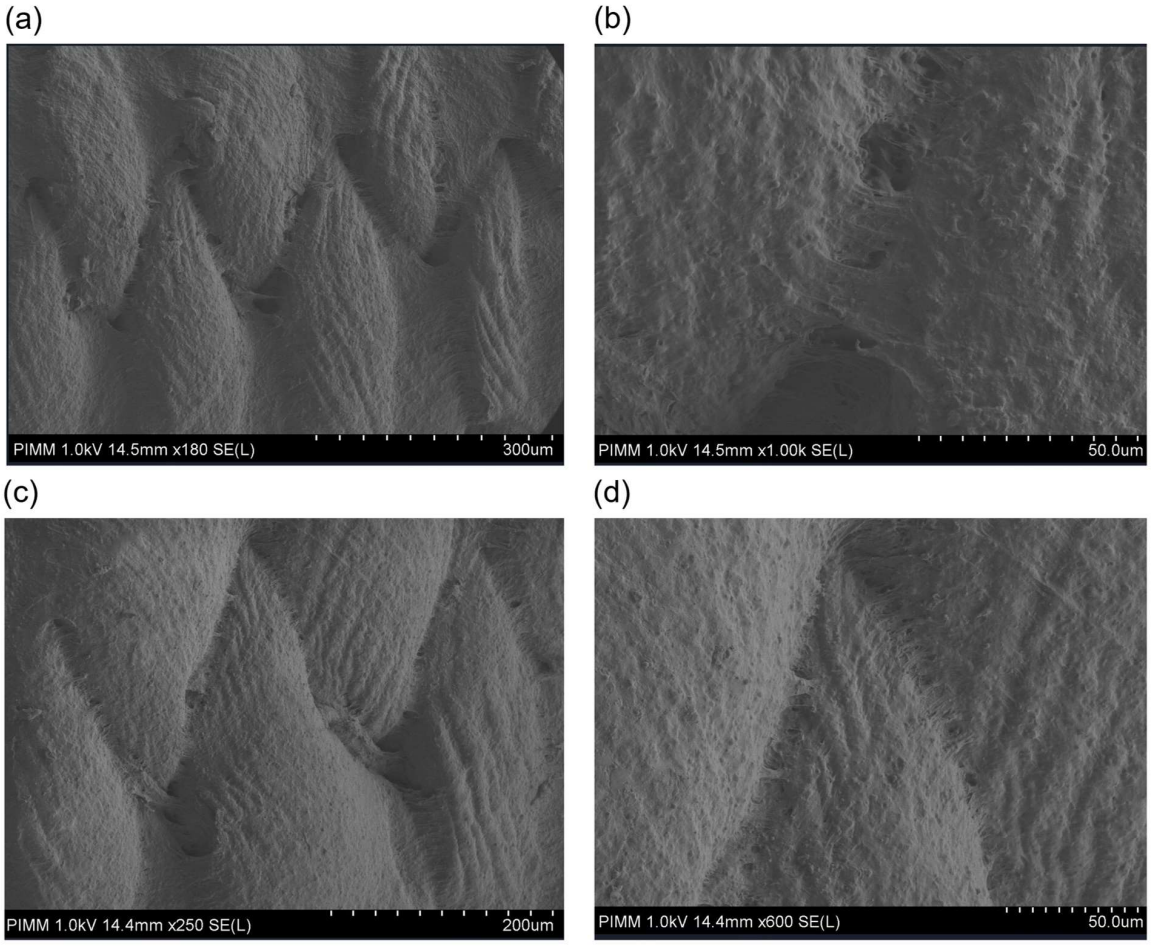

FIGURE 3.22 – Scanning electronic analysis of samples in different magnifications: (a and b) sample of 340–40–non and (c and d) optimized parameters (340-20-6h)

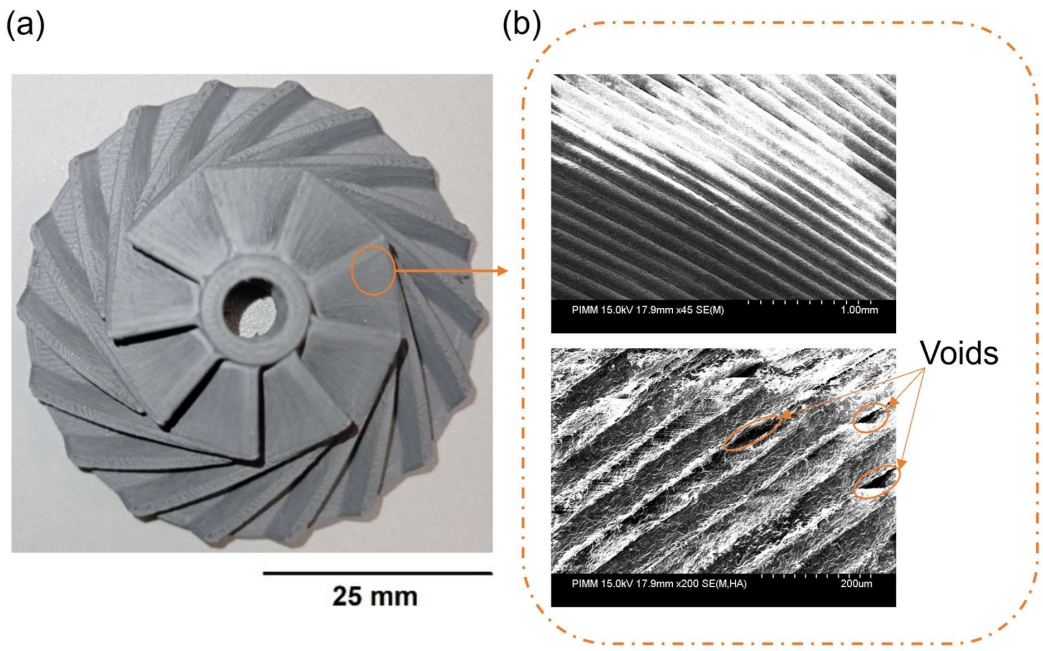

FIGURE 3.23 – (a) 3D printed impeller and (b) SEM images with different magnification on the impeller blade

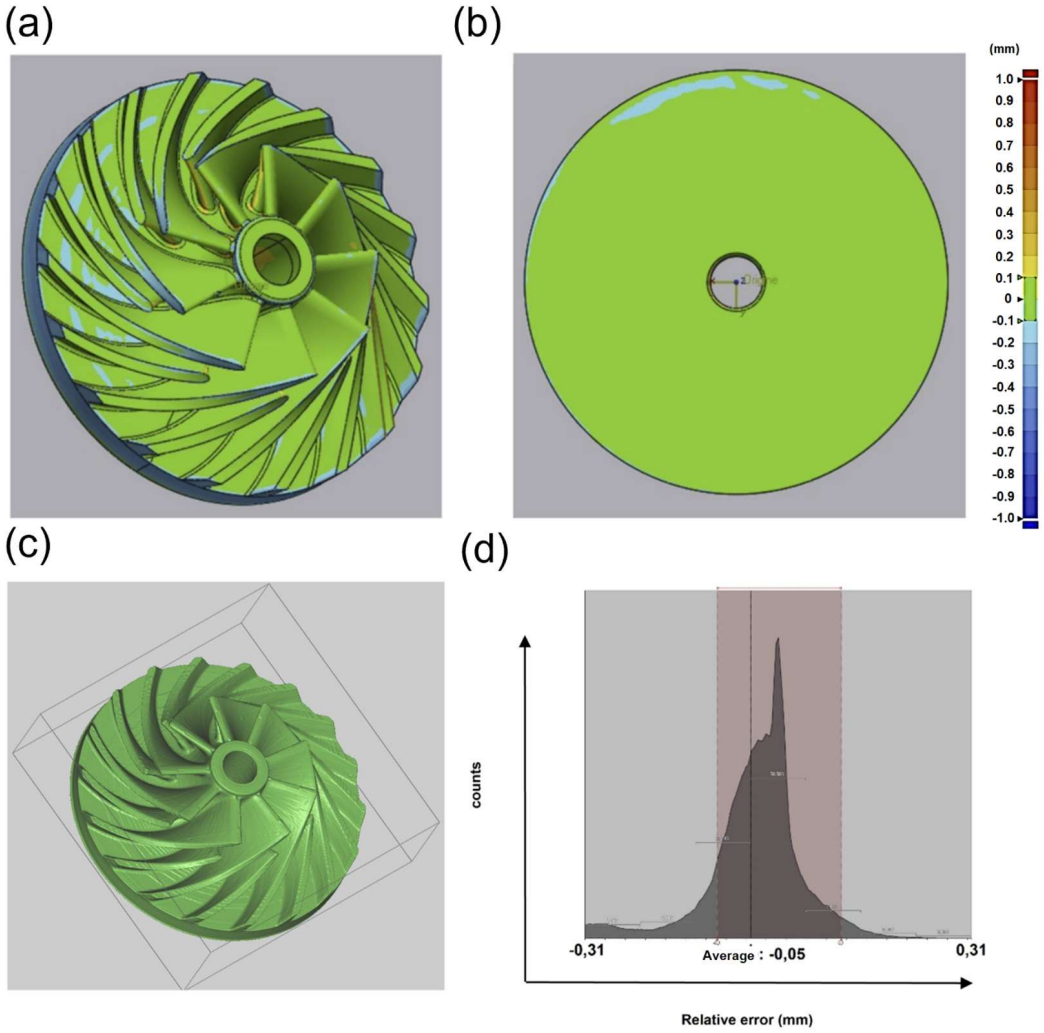

FIGURE 3.24 – (a and b) Local comparison of best fit freeform inductor data against nominal CAD geometry, (c) surface scanned of the impeller, and (d) deviation of discrete data points from the free-form inductor

physicochemical and mechanical properties were used. The interphase between two polymeric layers was analyzed through the optical microscope. In addition, the effect of two process parameters of nozzle speed and nozzle temperature, and time of annealing as a post-processing method on the mechanical behavior of interlayer and crystallization percentage of printed parts were investigated. Polyphenylene sulfide was selected as a high-performance polymer during this study. The parameters were optimized through multi-response optimization utilizing the GRA method. Process parameters and annealing time have been three variations as input parameters to achieve the best mechanical interlayer properties and high crystallization percentage. Analyzing the GRG data by ANOVA and S/N showed the optimal process parameters of nozzle temperature and speed of 340 and 20 mm/s, respectively, annealed at 200 °C for 6h. Microscopic results show the importance of parameters on suitable coalescence between the printed layers that impact the mechanical and Physico-chemical properties. Optimized parameters were used to manufacture an impeller of a compressor and fabricated parts were probed through SEM and a 3D scanner.

Chapitre 4

Relation between the manufacturing process and properties in SLA approach

Content

4.1 Effect of process and post-process parameters on thermal and physicochemical properties

4.1.1 Thermogravimetric analysis

To investigate the thermal stability of samples thermogravimetric analysis (TGA) was performed. Figure B.24 shows the TGA analysis for resin, green and post-cured samples. Figure B.24a Shows derivative thermogravimetric curves for each sample. According to the results, higher thermal stability of crosslinked polymers compared to the net one was shown which is in good agreement with the literature [212]. The results showed a different number of decomposition stages for resin compared to the green and post-cured samples. Loss weight for the resin showed a 2-stage decomposition whereas in other samples was happen in 3 stages. The stages of resin decomposition were accrued in 102.9, 352.9, and 438.20 °C which in each step resin lost was 23.4, 44.2, and 34.2%, respectively. The first decomposition step is related to the evaporation of volatile components acrylate groups at 102.9 °C. The second and third steps of the resin degradation have coincided with the temperature of the first and second degradation stag of green and post-cured samples. As mentioned, in general, all the resin which used in SLA method can be cured by heating in a certain range. So, the resin will be cured by increasing the temperature during the TGA analysis which can be led to the approximately same decomposition temperature compared to the other samples. Green sample and post-cured samples showed more thermal resistance compared to the resin which represents the important role of cross-links on thermal behavior. The first weight loss in the samples was at 352.9 °C which was accompanied by 52.5% weight loss. This weight loss can be attributed to the trapped volatile materials that are released. The next step happened at 438.20 °C that represented the completion decrosslinking and thermal degradation. The weight loss of this step was 47.5% and this reduction can be attributed to the decomposition of aromatic structures [213, 214]. TRT 80 °C showed the best thermal behavior among the other samples which is related to the density of cross-links in these samples compare to the others.

4.1.2 Effect of post-processing on polymerization

The effect of post-curing on the polymerization of the samples was studied by using FTIR and DSC in this study. Regarding, the FTIR results, absorption changes in the functional groups were

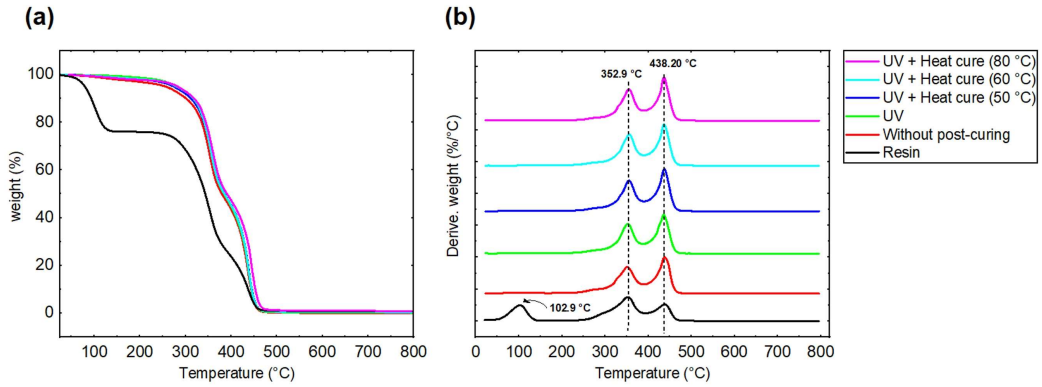

FIGURE 4.1 – Thermal stability of resin, without post cure and post cured: (a) thermogravimetry weight loss and (b) derivative thermogravimetric curve

investigated. Figure 4.2 shows the FTIR results related to the green, UV, and UV with heat curing at different temperatures in the range of 40 - 80 °C for 0°-printed samples. The absorption bands related to the methacrylate function, amide II vibration, and the C-O-C have appeared at the peaks of 1637, 1535, and 1100-1245 cm^{-1}, respectively [215, 216]. The absorption peak in 1701 cm^{-1} is corresponding to the C=O bond for urethane dimethacrylate [217]. Two absorption peaks of C=C at 1630 cm^{-1} and amide II at 1532 cm^{-1} (I1630 cm^{-1}/I1532 cm^{-1}) were considered as an index for the calculation of residual unpolymerized monomers [215, 218]. The ratio obtained for the green sample was considered to control which ratio shows the 100% residual of unpolymerized monomers. Consequently, residual unpolymerized monomers for post-cured samples according to the control ratio were calculated. According to the intensity ratio, the percentage of residual UDMA for UV, UV with heat 40 °C, UV with heat 50 °C, UV with heat 60 °C, and UV with heat 80 °C post-cured samples were 83.77, 82.36, 79.36, 76.01, and 67.37%, respectively. Curing the resin in stereolithography can be divided into two mechanisms of photocuring and thermal curing [219]. The photocuring mechanism in (meth)acrylate-based resin performs by the radical system which consists of radical generation, initiation, and propagation of radicals or the first step of this mechanism, radical generation occurs by converting photolytic energy into a reaction for the initiation of polymerization [151]. On the other hand, thermal curing is another mechanism in that polymerization is started by photoinitiators with temperature (all of the stereolithography resins have photoinitiators for curing with temperature) [220]. For investigation of curing mechanisms, studies have analyzed two peaks of C=C bands at 810

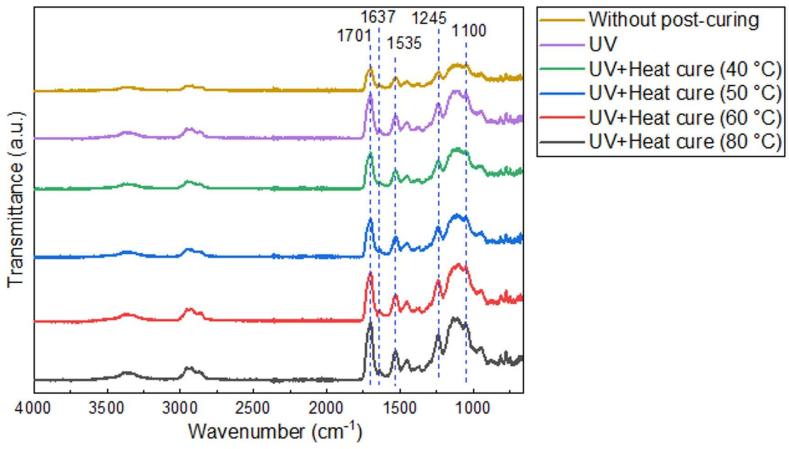

FIGURE 4.2 – FTIR spectrum of samples in a green and post-cured condition

and 1632 cm-1 that are related to the acrylate group [214, 221]. Changes in the absorption of these peaks represent the polymerization of monomers during the crosslinking reaction [222–224]. Figure shows the ratio of I1701 cm^{-1}/I810 cm^{-1} against the temperature. The Figure B.26 showed the linear relation with a threshold in the 50 °C ($R > 0.98$). First, the polymer main chain crosslinking reaction is dominant. On the other hand, It can be mentioned that the second slop is related to the side photochemical reactions of the macromolecular chain groups. According to the temperature range used in post-curing, it can be said that the mechanism of polymerization was the only photocured mechanism because according to the DSC results, thermal cured happened in the temperature range of 110 to 200 °C.

The thermal properties of the liquid resin and samples considering the different post-curing conditions were analyzed by DSC. According to the results, by the following equation, the cure degree of the samples which indicates the polymerization of the samples after post-curing was investigated [148]:

Degree of cure (%) = (1 -$\Delta H_{sample}/\Delta H_{resin}$) × 100

where ΔH_{sample} and ΔH_{resin} are the heat release energy from samples and resin, respectively. Figure 4.4 shows the heat flow against the temperature for resin. For measuring the ΔH_{resin}, the heat flow from the liquid resin was analyzed and heat release energy was measured equal to 99.34 J/g.

The obtained results of DSC for the green and post-cured samples are indicated in Figure 4.5. All obtained DSC heating plots show endothermic peaks corresponding to glass transition and one

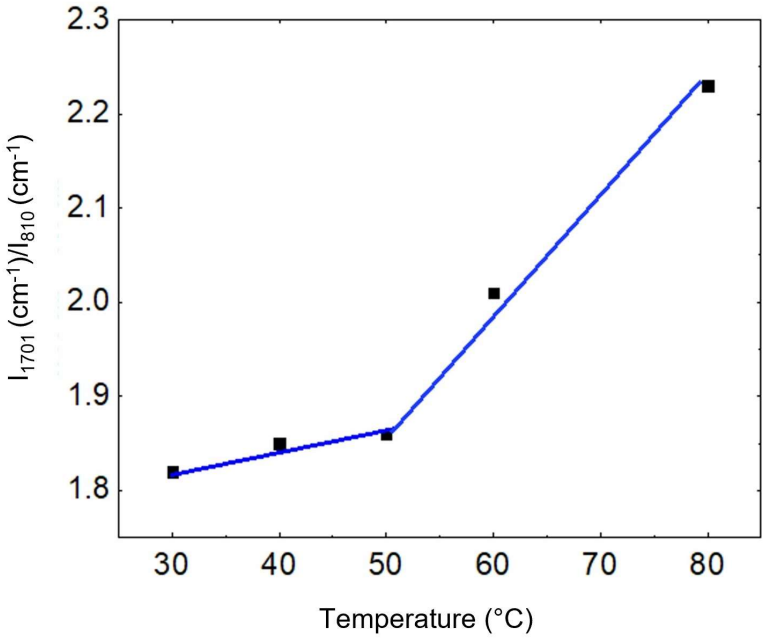

FIGURE 4.3 – The obtained I1701 cm^{-1}/I810 cm^{-1} ratio of absorption from FTIR for post-cured samples in the temperature range of 30 - 80 °C

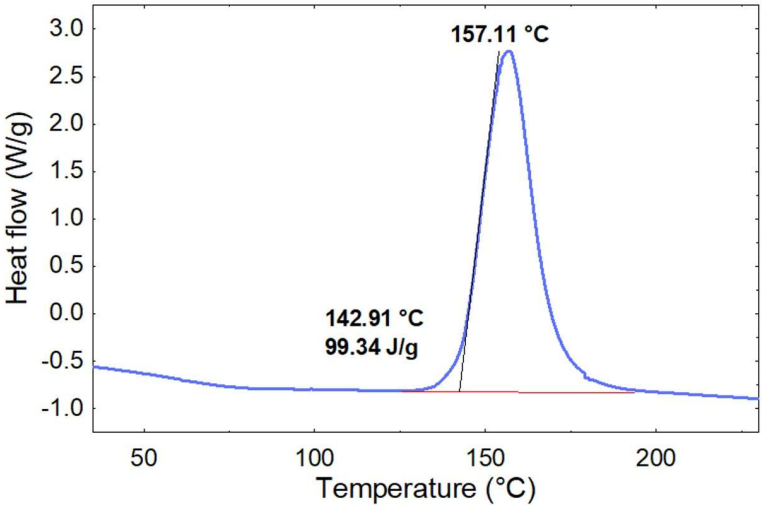

FIGURE 4.4 – The DSC heat flow plot for liquid resin

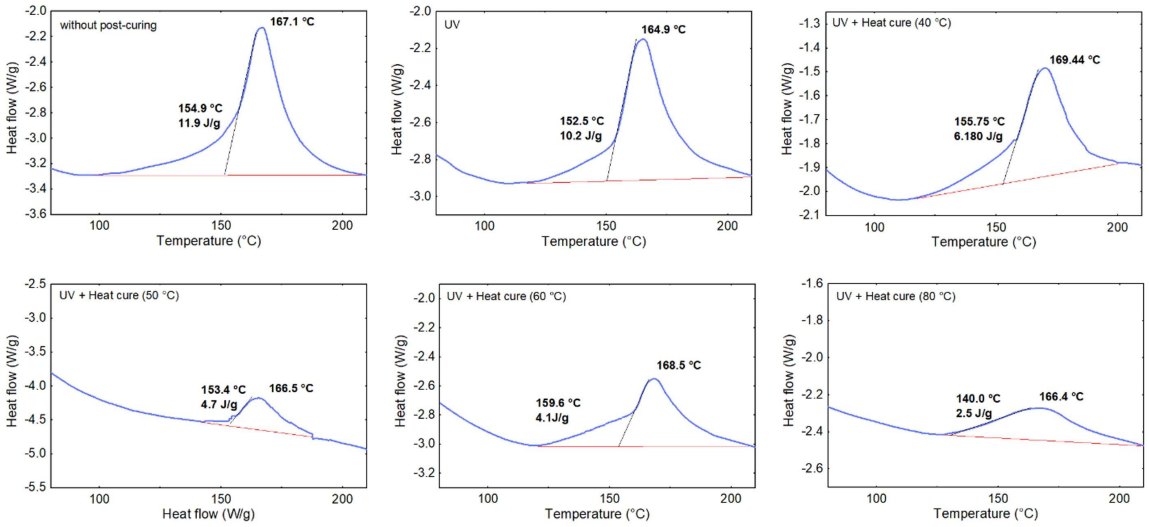

FIGURE 4.5 – The results of DSC for the samples

exothermic peak corresponding to thermal curing. According to this figure, curing was performed in the range of 110 to 200 °C. The maximum and minimum enthalpy was 11.87 and 2.51 J/g which related to the sample without post-curing and post-cured sample by UV with the heat presence of 80 °C, respectively. According to the cure degree results, the green sample was 88% cured whereas post-curing by using the light and the 80 °C increased the degree of cure of the samples up to 98%. As a result, increasing the temperature from 40 to 80 °C leads to increasing the polymerization during the post-curing, which can be attributed to the increasing the mobility of the polymer chain by increasing the temperature. Thus, increasing the temperature leads to an increase in the chain mobility, and by increasing the polymer network mobility, the chain transfer reaction will be increased [225, 226].

4.1.3 Thermomechanical behavior characterization

Dynamic mechanical thermal analysis (DMTA) in flexion mode was used to investigate the thermo-mechanical behavior of fabricated samples. Green and post-cured 0°-printed samples were selected for this purpose. Figure 4.6. shows the storage modulus and tan δ without post-cured samples in different frequencies of 1, 3, and 10 Hz. According to Figure 4.6a, a shift toward a higher temperature of the peak of tan δ was observed by increasing the frequency. Tan δ value is attributed to the phase displacement of the sinusoidal movement of the clamps compared to the responded movement of the

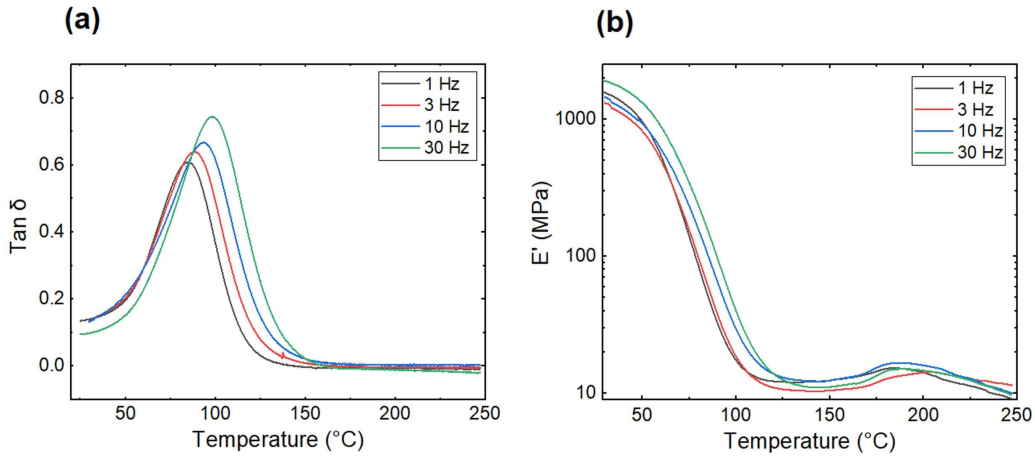

FIGURE 4.6 – a) Flexion storage modulus (E) and (b) tan for green parts in frequencies of 1, 3,10 and 30 Hz

samples [227]. The maximum of this displacement which is displayed as a peak can be seen near the T_g caused by the segmental movement of polymer chains [228]. Increasing the frequency during the test is accompanied by decreasing the segmental molecular motions [229]. So, the segmental motions which have an important role in changing the transition from glassy to the rubbery state become restricted and cause to increase of the T_g [230]. Figure 4.6b shows the storage modulus against the temperature for different frequencies. Decreasing in E was observed by Increasing the temperature up to 150 °C which is related to the increasing the mobility of polymeric segments during heating. In the range of 150 to 250 °C modulus was increased and then was reduced again. In this range of temperature residual resins can be cured and subsequently modulus will be increased and again by increasing the temperature E was reduced.

Figure 4.7 shows the storage modulus and tan δ for post-cured samples at a frequency of 10 Hz. According to the results of Figure 8(a), the lowest T_g was related to the UV-cured sample, and then in the other samples, the T_g was increased with increasing the curing temperature the highest T_g was for heat curing at 80 °C with UV. Considering the critical role of segmental motions on T_g and reducing these motions by increasing the polymerization, increasing the glass transition is directly related to the polymerization of parts during post-treatment. According to Figure 4.7b, storage modulus at room temperature for UV and UV+Heat curing at 80 °C showed the lowest and highest with 1795.9 and 2307.7 MPa, respectively. All the samples showed a reduction in modulus with increasing temperature

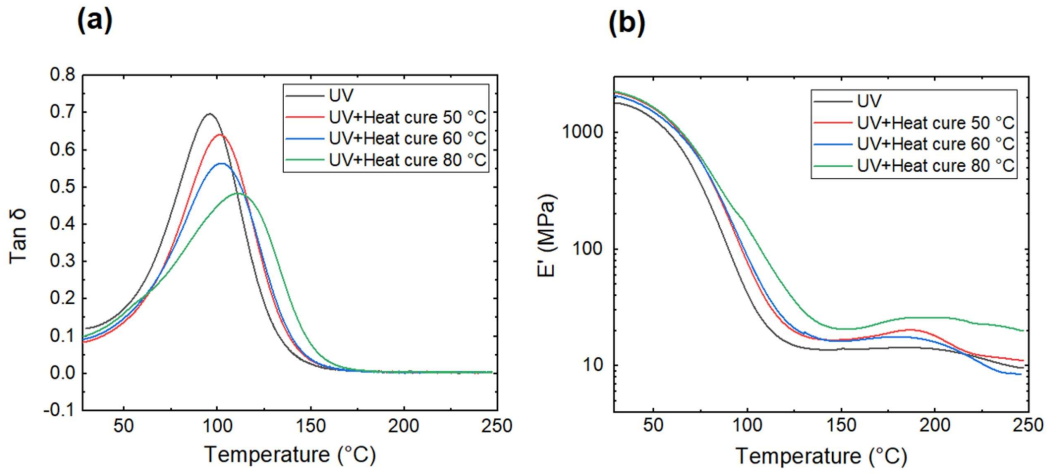

FIGURE 4.7 – (a) Flexion storage modulus (E) and (b) tan δ for post-cured samples in frequencies 10 Hz

TABLE 4.1 – Measured values of responses

Sample name	Frequency (Hz)	Tg (°C)
Without post-curing	1	85.4
Without post-curing	3	89.0
Without post-curing	10	94.46
Without post-curing	30	99.19
UV	10	96.59
UV+Heat cure 50 °C	10	102.34
UV+Heat cure 60 °C	10	104.34
UV+Heat cure 80 °C	10	113.99

which this reduce was performed by a lower rate for UV+Heat cure 80 °C compared to another. Also, changes in the modulus from 150 to 210 °C show the incomplete cured in the samples, and in this range of temperature residual resin was cured. Glass transition of samples is presented in Table 4.1.

4.2 Mechanical characterization

4.2.1 Effect of build orientation

The results from tensile tests are shown in Figure 4.8 These results show the stress-strain curve of samples concerning the sub-build orientation and different post-curing conditions. For investigation of the printing orientation effect on mechanical properties, each printed group in 0°, 45°, and 90° were

compared together. Various directions of printing show the different mechanical behavior of samples. This fact shows the anisotropy of fabricated parts and also can impact the steps up to break in the stress-strain curves. The stress-strain curves for 0°-printed show the linearly elastic, nonlinearly ascending, yield-like (peak) behavior, strain softening, and then plastic flow. These samples indicate the most percentage of elongation compared to the other printed samples in different directions. Literature has shown the plasticizer effect of unreacted monomers on the final product. Also, considering the DSC results that were discussed in the previous section, the amount of residual resin in the samples was shown. So considering the direction of tension, which has been in the direction of the printed plate, it can be said that the elongation of the samples has reached its maximum value. After stretching the material up to the special ratio that is called the "natural draw ratio", necking will be stopped, and through the new material at the neck and shoulders, this part starts to grow. This phenomenon, "drawing", continues until spans the full gauge length of the specimen. Considering the strengthened microstructure during this process, it can be said that failure occurs when new materials are unable to transform outside the neck [231]. Ductile Stress-strain curves were observed for 45°-printed samples. According to this figure, the results show the linear elastic and then the plastic flow of samples during the tensile test. The percentage of elongation was less than the 0°-printed samples, while the value of maximum stress at break was increased compared to the other two groups. Considering the direction of printed plates with tensile direction in this group it can be said that material transfer has not occurred in the neck area. This fact caused decreasing elongation. Curves in the group of 90°-printed samples were rigid. This sub-build direction showed the least value in %elongation around 2% and maximum stress at break. In general, the results show that maximum stress at the break for printed samples can be ranked as follows: 45°>0°>90°. This fact shows the important effect of sub-build on printing the parts.

4.2.2 Effect of post-curing: UV radiation and temperature

In this section importance of post-curing temperature with UV was analyzed on the samples printed with different build orientations. Figure 4.9 shows the values of Young's modulus obtained from the mechanical tests. Results showed the important effect of temperature during the post-curing on the mechanical behavior, such that Young's modulus of the samples was increased by increasing the temperature. The maximum mechanical strength was achieved at 80 °C + UV post-treatment in

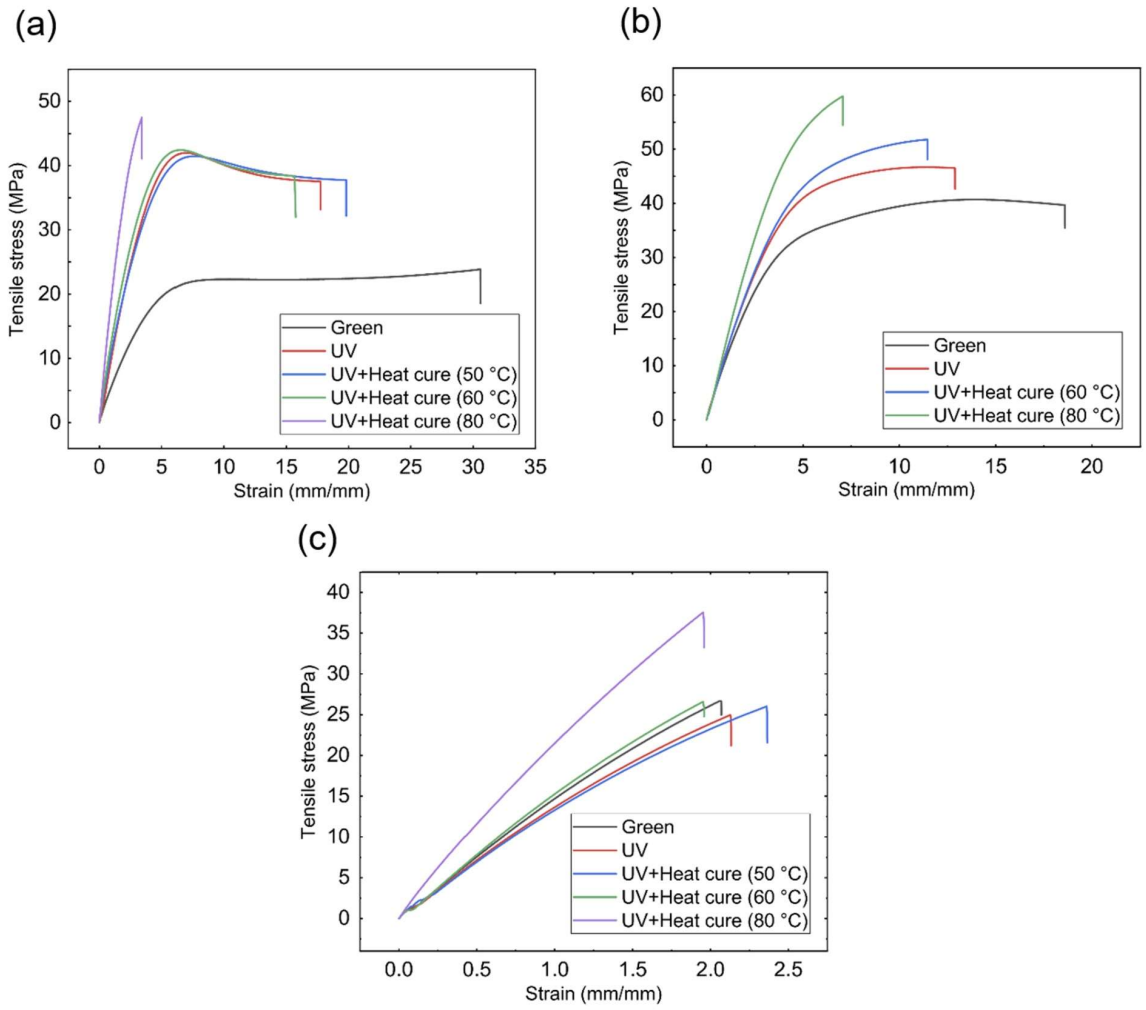

FIGURE 4.8 – Stress-strain curves with different post-curing conditions: (a) 0°-printed, (b) 45°-printed and (c) 90°-printed

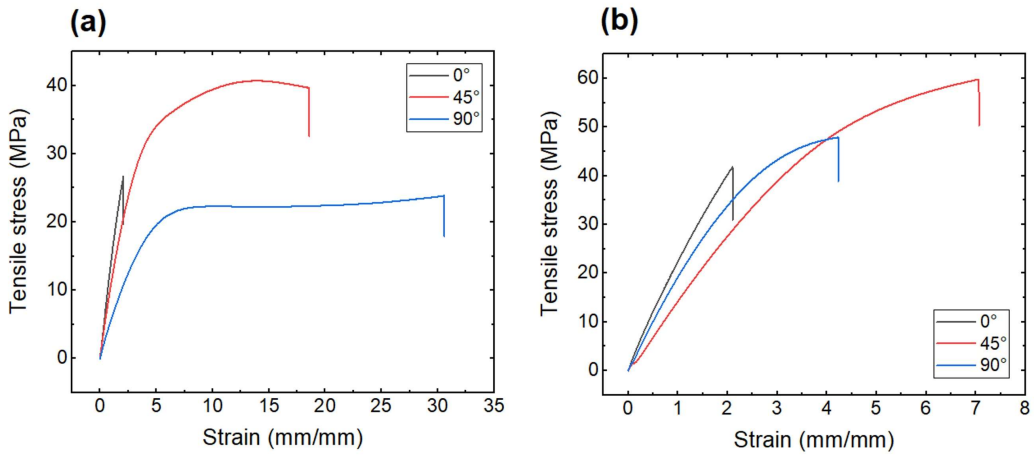

FIGURE 4.9 – Stress-strain curve of samples in different print orientations: (a) without post-curing and (b) post-cured at 80 °C

all the printing orientations. This increase can be attributed to the increasing curing percentage at high temperatures post-curing. The more curing percentage at higher temperatures is related to the better mobility of polymeric chains. Also, according to the results from Figure 4.10, the key role of temperature on the shape of stress-strain curves can be observed. In this figure, the strain softening effect was reduced by increasing the temperature during the tensile test, especially in the samples printed at 45°. This observation can be explained by the plasticizer effect of residual resin during the test. In addition, increasing the cross-link density can lead to less ability of chains to the movement leading to the reduction of the strain softening. The mechanical properties of green and post-cured samples were analyzed for the different sub-build orientations. The maximum tensile strength and elongation results were considered for competing for the mechanical properties of the samples. Figures 4.10a and b show the stress–strain curve for different orientation printed samples without and post-cured at 80 °C, respectively. According to Figure 4.9a, maximum tensile stress without post-cured samples for 0°, 45° and 90° were 25, 20, and 40 MPa, respectively. Also, the maximum strain was for 90°, 45°, and then 0°. Figure 4.11b shows the stress against the strain for UV+Heat cure 80 °C for different orientations printed samples. The maximum stress at break was 55, 44 and 50 MPa for 0°, 45°, and 90°, respectively. In addition, the 45°-printed part showed a higher strain at break compared to the 0° and 45°-printed parts.

Figures 4.10a and b are shown the maximum tensile strength and %elongation, respectively. The

results showed a significant effect of post-curing on the tensile strength and %elongation of samples. In general, post-curing led to a decrease in the %elongation of the samples. Increases in the maximum tensile strength of the samples by post-curing can be referred directly to the amount of polymerization of samples. It should be mentioned that uncured resin which is between the layers, or the surface of the parts known as a place with poor mechanical properties, which leads to a reduction in the mechanical properties of the part [152, 232, 233]. So, improvement of the mechanical properties can be expected by increasing the amount of polymerization in the samples. In addition, in a study by Salmoria et al. [149] the release of internal stress concentration in the samples during the post-curing as one of the important factors in improving the mechanical properties has been considered. Therefore, polymerization and release of the internal stress can well explain the increase in mechanical properties by increasing the temperature in the post-curing for the samples. As mentioned, the mechanical properties of the fabricated parts were also examined in different sub-build orientations. According to the results, the maximum tensile strength can be ranked as follows: $90^\circ < 0^\circ < 45^\circ$. So that the samples without heat treatment showed 0°, 45°, and 90° maximum elongation equal to 2.83, 12.37, and 30.96%, respectively. According to the results, the maximum tensile strength was achieved for the orientation of 45°. It is related to the angle of the layers at an angle to the force direction. Also, according to Saini et al. [234] it was shown that the elastic modulus of the samples printed by the SLA method at an angle of 45° showed a higher elastic modulus than the sample of other printed angles which is referred to the elastic properties in this orientation. As can be seen from the results the maximum tensile strength was reduced by increasing the angle orientation from 45° to 90°. On the other hand, by increasing the angle orientation from 45° to 90°, % elongation was increased. The microstructure of the fabricated parts by SLA can be divided into three regions: over-cured resin, cured resin, and non-cured resin. The region of the non-cured resin is between the layers or on the surface of the samples [152, 232]. In a study by Asmussen et al. [235]they introduced the non-reacted monomer as a plasticizing parameter on the polymer which can impact the physical and mechanical properties. Given that the 90° and 45° samples were tensioned in the direction of the layers it can seem that the plasticizing effect of residual resin was maximum. However, due to the angle of the layers with the direction of tension, this effect can be insignificant for the angle of 0°.

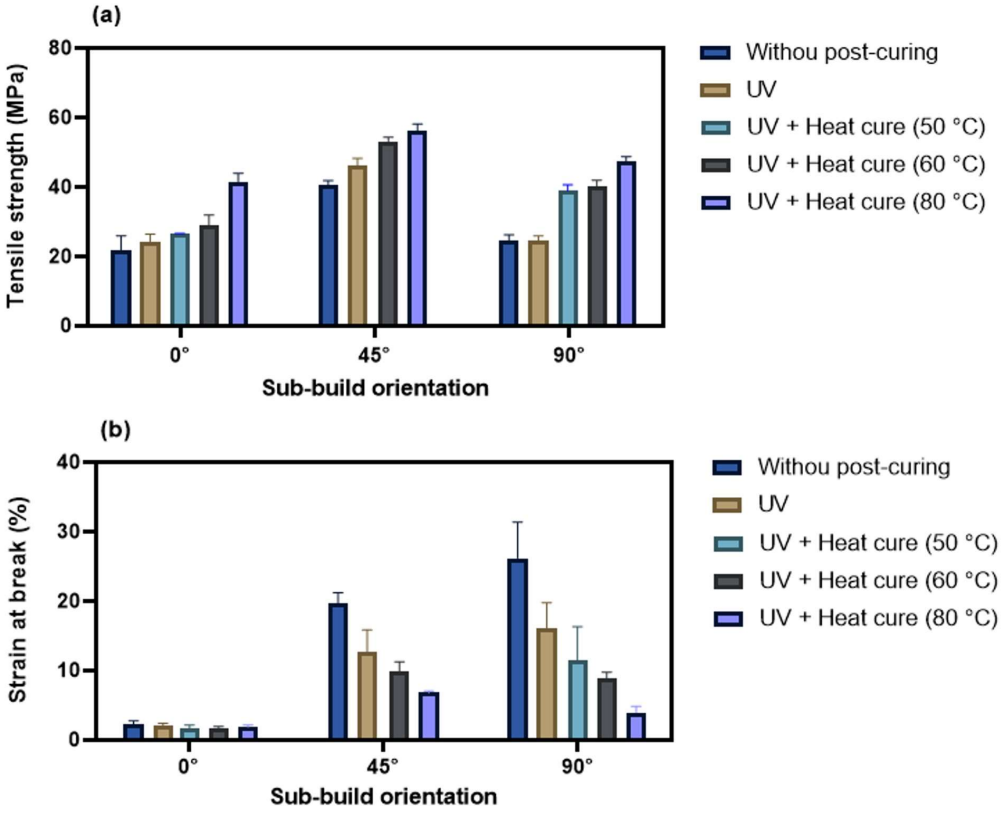

FIGURE 4.10 – (a) Maximum tensile strength and (b) %elongation for green and post-cured samples

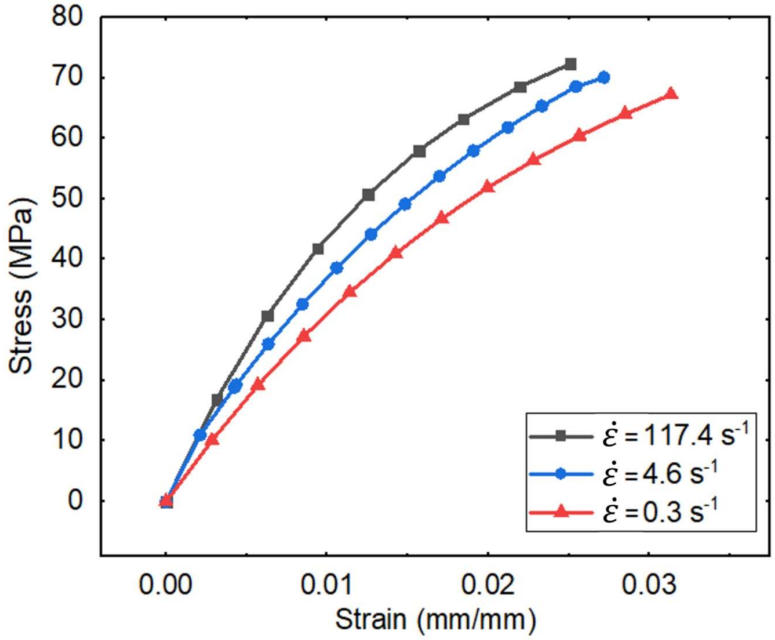

FIGURE 4.11 – Stress-strain curves at different strain rates

4.2.3 Effect of strain rate on tensile loading: 45°, post-cured

Investigation of strain rate was carried out on the samples of 45°-printed that were post-cured at 80 °C in the presence of UV for 30 min. Figure 4.11 shows strain-stress curves of this test at different rates from 0.3 to 117.4 s-1. According to the results, the ultimate tensile strength was increased by increasing the rate. Such that, these values for rates of 117.4, 4.6, and 0.3 s^{-1} were 73, 68.8, and 67.5 MPa, respectively. The different zones of these curves consisted of an initial linear elasticity domain, followed by a yielding domain and then a moderate increase of stress. In addition, the stress-strain curves did not show a significant change in the slope of the elastic zone, indicating Yang's modulus is independent of rates. Stress-strain curve of the similar sample in static condition (0.001 s^{-1}) shows ductile deformation with large straining and a low increase of stress. The maximum value of ultimate tensile stress and the strain at break were 59.1 MPa and 6.8%, respectively. So, dynamic loading on the samples significantly reduced strain at break and increased the ultimate tensile stress.

Furthermore, a threshold in the ultimate stress and strain was considered that corresponds to the first non-linearity behavior. This point can be referred to as a transition from passing linear to

TABLE 4.2 – Parameters from the Backofen equation

Parameters of power function	C	K	m	R^2
Threshold	10.54	34.56	0.03	0.99
Ultimate stress (MPa)	43.46	20.10	0.11	0.92

nonlinear properties and can be caused by the initial microfracture. Increasing the force during the test the initial microfracture growth and leads to fracture. Figure 4.12 presents the stress and strain threshold results. According to this figure, stress and strain thresholds were decreased by increasing the rate that is described increasing the rate is accompanied by going to the non-linear stage with less strain and stress. On the other hand, a decrease in the rate can cause a delay of this transition in the samples which means a delayed damage onset. It seems that at a high rate, increasing the rate can cause an increase in the crack density, whereas decreasing the rate can provide more crack propagation. In addition, the results show a direct relation between modulus and strain rate, such that a higher modulus follows at more strain rates. Also, for investigation of the failure mechanism and dynamic analysis properties concerning the effect of strain rate on the stress, strain rate sensitivity "m" was considered. Regarding, this parameter was evaluated from the Backofen equation which is an empirical power-law function, as follows [236]:

$$\sigma = C + K\dot{\varepsilon}^m \tag{4.1}$$

Where σ is stress, $\dot{\varepsilon}$ indicates the strain rate, C and K are the constants that refer to the experimental conditions and microstructure of materials, and m shows the SRS index. It can be said that by increasing the SRS index, the sensitivity of the material with strain rate will be raised. Threshold and ultimate stress were considered for investigating the effect of different rates on the different steps of failure. That sensitivity index from the Threshold can correspond to the linear zone, whereas the index from the equation respected to the ultimate stress can refer to the non-linear step. The results from the fitting are shown in Table 4.2. According to the results, the samples showed more rate sensitivity in the non-linear stage compared to the linear step. This can be attributed to the visco damage behavior of the samples during the test. After the linear stage, the mechanism of the damage will be active which accompanies the creation of cracks in the samples and is more sensitive to strain rate.

According to the results, a greater m index for ultimate stress compared to the yield stress can show more sense of the sample with strain rate after yield stress, which is located in the zone of

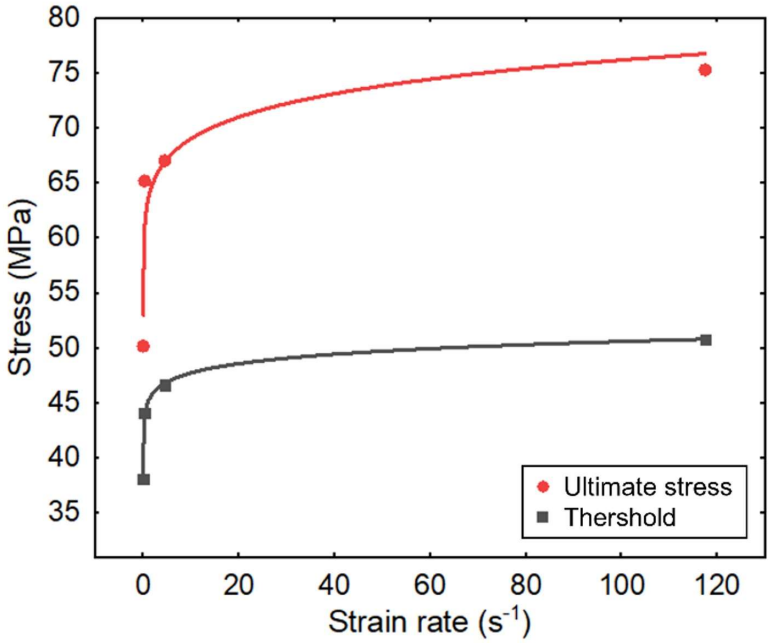

FIGURE 4.12 – Strain rate sensitivity for threshold and ultimate stress

non-linear. So, it can be said that the non-linearity stage is more sensitive to strain rate compared to the linear step in the stress-strain curve.

4.2.4 Microstructure analysis related to the printed samples

Figures 4.13a and b show micrographs of the fracture surface of a 90° printed sample that post-cured at 60 °C with respect to the different magnifications after the tensile test. Plastic deformation area along with another region of brittle failure can be observed in the fractured surface of Figure 4.13a. The plastic deformation region can be attributed to the chain slippage which flaw propagation speed is reduced by the stress release. In addition, the fractured surface of Figure 4.13b shows a region with layer forms that can indicate the layered nature of parts printed by this method. In other regions of this figure, the failure is not observed layer by layer which seems to be the fact that the curing has been done completely in this area [149].

To investigate the effect of different strain rates on damage, surface fractures of samples 45°-printed post-cured at 80 °C were observed. Figure 4.14 shows the SEM of fractured samples in the strain rates of 0.3, 4.6, and 117.4 s-1 at different magnifications. The figures show the brittle fracture containing

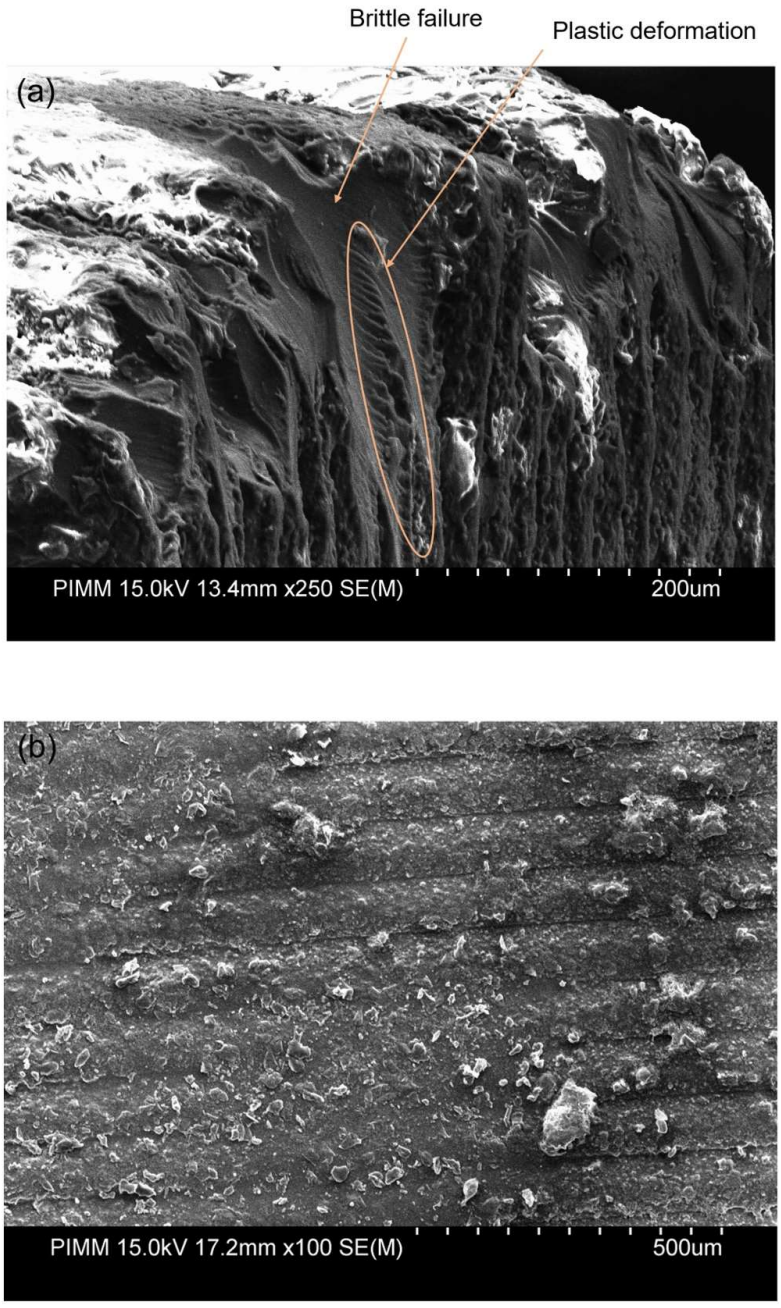

FIGURE 4.13 – Fracture surface of 0° printed sample and post-cured at 60 °C with respect to the (a) more magnification and (b) lower magnification

the plastic region which this region will be decreased by increasing the strain rate, such that surface fracture at the strain rate of 117.4 s^{-1} did not show the plastic deformation. Figures 4.14a and b are attributed to the strain rate of 0.3 s^{-1}, as can be seen, the cracks have grown more compared to the other strain rates. In addition, according to the shear and cavitation evidence in the plastic area, it can seem the chain slippage mechanics is a failure mechanism. This mechanism can occur when the propagation speed is reduced by the stress release.

4.2.5 Conclusions

In this section, the effect of post-curing at different temperature ranges at a certain time on the mechanical properties of urethane dimethacrylate resin was investigated. The mechanical properties of green and post-cured samples were analyzed for the different sub-build orientations. Physico-chemical, thermal, and mechanical properties were investigated by DSC, FTIR, TGA, DMA, and tensile analysis. The obtained result explained the curing mechanism of the samples in the post-curing and the value of residual resin was calculated. The key role of residual resin in the parts on thermal and mechanical analysis was explained. This effect was investigated on the glass transitions of the samples so that post-curing caused the increasing the glass transition. According to the results, an increase in the post-curing temperature process increased the tensile strength so that the post-curing at 80 °C caused an increase in the polymerization up to 98%. Finally, results showed the maximum tensile strength in the rank of $90° < 0° < 45°$. In addition, the mechanical properties of the materials were considered under the quasi-static and high strain rate tensile loading. Following some points can be concluded:

• The importance of post-curing on final mechanical behavior was shown in the post-processing method. Post-curing was accompanied by reducing the residual monomer, such that by increasing the polymerization in the parts elongation was reduced. DSC Results show the maximum cure degree of the samples up to 98% during the post-treatment with UV at 80 °C.

• The mechanical behavior of the samples in quasi-static conditions shows the sensibility with build orientation. Such that, the most value of stress at break was attributed to the 45°-printed parts, then for 0° and finally for 90°. In addition, different shapes in the stress-strain curve consist of brittle, ductile, and curve with softening effects.

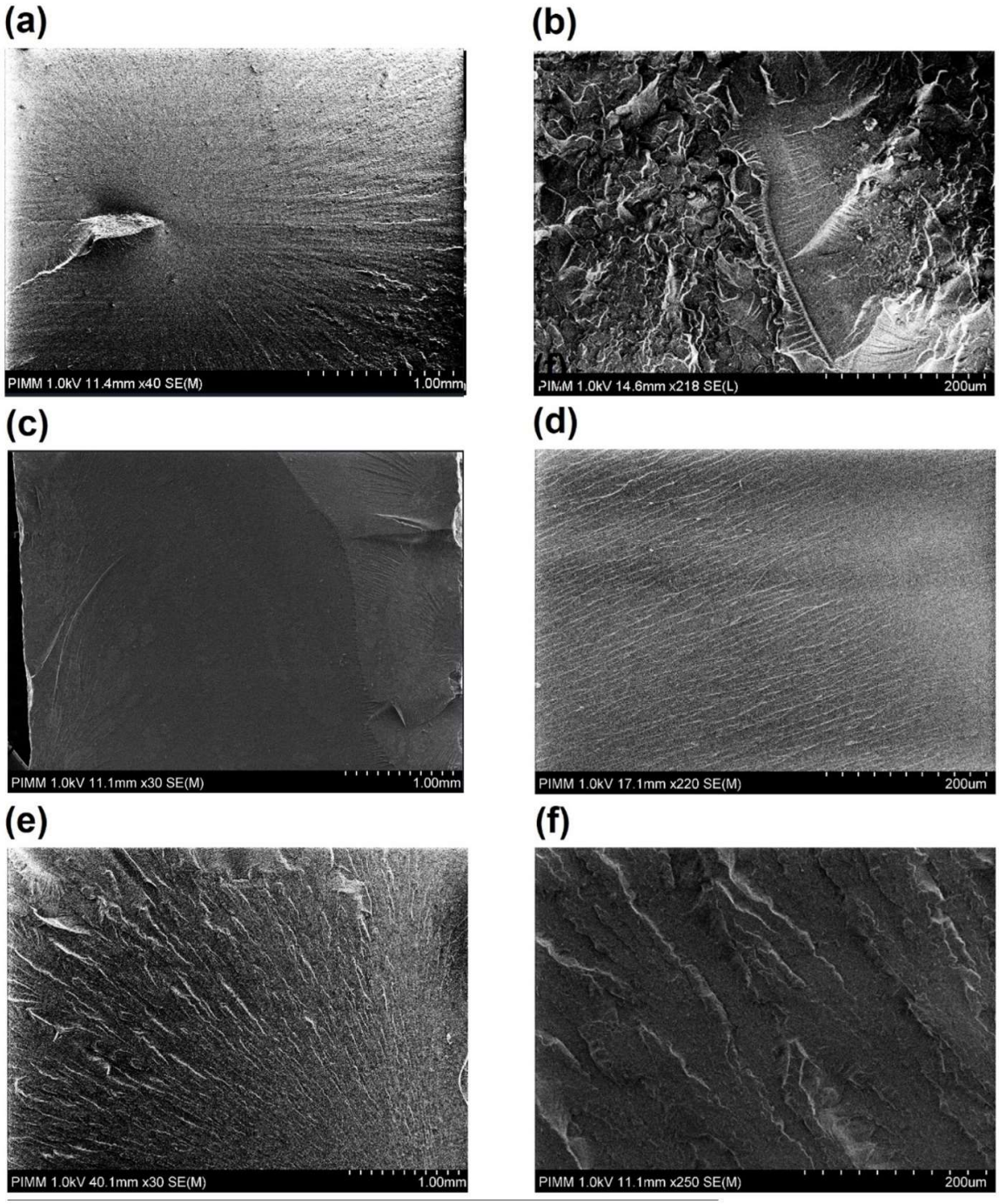

FIGURE 4.14 – Surface electron microscopic analysis in different magnifications for failure surface at different strain rates: (a and b) 0.3 s^{-1}, (c and d) 4.6 s^{-1}, and (e and f) 117.4 s^{-1}

• Results of high strain rate from 0.001 to 117.4 s^{-1} on the mechanical behavior show the important role of strain rate on the mechanism of failure. The samples showed more sensibility in the nonlinearity zone compared to the linear step of the stress-strain curves.

Chapitre 5

Numerical simulation and validation: Performance of structural part

Content

5.1 Analysis of strength distribution of the impeller

5.1.1 Finite elements analysis

Numerical analyses for parts designed considering the working conditions have been one of the most critical steps in the study of materials [165]. When it comes to wheels, there is no exception to this, and numerical evaluations have always been one of the essential steps in the study of materials for this component. In other words, numerical analytics can be seen as a tool to balance performance and reliability during product development and design. In this section, the numerical analysis of centrifugal impellers and compressor rotors will be discussed. As mentioned, properties such as modulus of elasticity, thermal expansion, fracture toughness, fatigue resistance, thermal conductivity, specific heat capacity, corrosion resistance and thermal stability have been among the parameters taken into account in the selection of materials for the manufacture of wheels and rotors. of compressors [167]. It should be mentioned that centrifugal stress due to rotational forces, bending stress due to fluid pressure and momentum change, and thermal stresses due to thermomechanical loading are the properties that have been considered as properties. effective factors in the simulations. Thus, by examining the materials under the mentioned forces, the authority of the material will be tested in simulation [168]. Structural analysis is the most common application of finite element analysis which is used to study different types of loads including stress, strain, and deformation. The fundamental formula for rotational load acting on a disc and related to stress is shown below (Equation 5.1):

$$F = \rho r \omega^2 \tag{5.1}$$

According to this equation, the centrifugal force (F) can vary depending on the density of the material (ρ), the radius of the wheel (r) and the angular velocity (ω). In order to analyze the stress distribution in simple terms, axisymmetric problems must be taken into account. In this regard, there are two stress components: radial tensile stress rr and tangential tensile stress . Their distribution on a disc can be seen in Figure 5.1. These radial (σrr) and tangential ($\sigma\theta\theta$) tensile stresses can be defined using the following differential equation:

$$\frac{\partial \sigma_{rr}}{\partial \sigma_{\theta\theta}} + \frac{1}{r}(\sigma_{rr} - \sigma_{\theta\theta}) = - \rho r \omega^2 \tag{5.2}$$

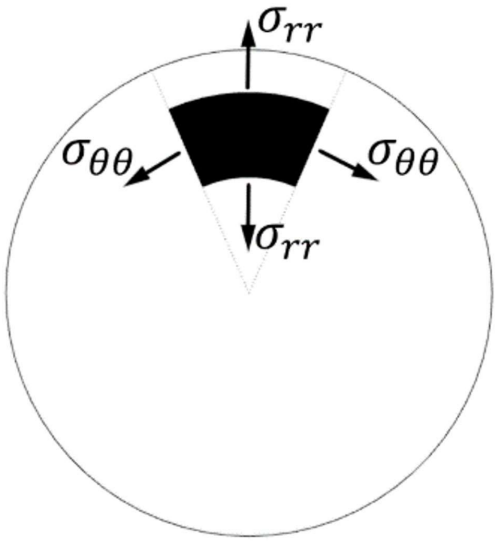

FIGURE 5.1 – Stress distribution scheme

And the radial (ϵrr) and tangential ($\epsilon\theta\theta$) strains can be expressed by the following equation:

$$\epsilon_{rr} = \frac{\partial u_r}{\partial r} \qquad \text{and} \qquad \epsilon_{\theta\theta} = \frac{u_r}{r} \tag{5.3}$$

Based on Hooke's law, the dependencies between stress and strain can be obtained as follows:

$$\epsilon_{rr} = \frac{1}{E}\left[\sigma_{rr} - \nu\sigma_{\theta\theta}\right] \qquad \text{and} \qquad \epsilon_{\theta\theta} = \frac{1}{E}\left[\sigma_{\theta\theta} - \nu\sigma_{rr}\right] \tag{5.4}$$

Where E is Young's modulus and ν indicates Poisson's ratio. After substitution and simplification of Equation 5.4, the following deformation formula (Equation 5.5) can be obtained:

$$u_r = C_1 r + C_2\frac{1}{r} - \frac{1}{8}\frac{1-\nu^2}{E}\rho r^3\omega^2 \tag{5.5}$$

The boundary conditions for hollow discs were defined using Equation 5.6:

$$\sigma_{rr}(a) = 0 \qquad \text{and} \qquad \sigma_{rr}(b) = 0 \tag{5.6}$$

Where a is the inside diameter and b is the outside diameter, and introducing two constants A, C (Equation 5.7):

TABLE 5.1 – Measured values of responses

Material	Young's modulus (MPa)	Poisson ratio	Density (kg/m3)
PPS	1800	0.38	1280
SLA	9600	0.3	1630

$$A = \frac{-EC_2}{1+\nu} = -\frac{1}{8}(3+\nu)\ \rho\omega^2 a^2 b^2 \tag{5.7}$$

,

$$C = \frac{EC_1}{2(1-\nu)} = \frac{1}{16}(3+\nu)\ \rho\omega^2(a^2+b^2) \tag{5.8}$$

The system of equations **??** describing radial tensile stresses, tangential tensile stresses, and strain in the radial direction is obtained.

$$\sigma_{rr}(r) = \frac{3+\nu}{8}\rho\omega^2\left[a^2+b^2-r^2-\frac{a^2b^2}{r^2}\right] \tag{5.9}$$

$$\sigma_{\theta\theta}(r) = \frac{3+\nu}{8}\rho\omega^2\left[a^2+b^2-\frac{1+3\nu}{3+\nu}r^2-\frac{a^2b^2}{r^2}\right] \tag{5.10}$$

$$u(r) = \frac{3+\nu}{8}\rho\omega^2\frac{1-\nu}{E}\left[a^2+b^2-\frac{1+\nu}{3+\nu}r^2+\frac{1+\nu}{1-\nu}\frac{a^2b^2}{r^2}\right] \tag{5.11}$$

Based on the finite element method (FEM) using ABAQUS, stresses of the impeller that mainly depend on mass and rotational speed were analyzed.

5.1.2 Numerical model and boundary conditions

In order to evaluate the strength properties of the developed impeller disc, made of different materials and at different rotational speeds, finite element method (FEM) calculations were carried out. The purpose of the calculations was first of all to check the maximum stresses and deformations of the compressor disc. Two materials, with the designations PPS and SLA, were taken into account in the calculations. The data for these materials, which were used in the strength calculations, are given in Table 5.1.

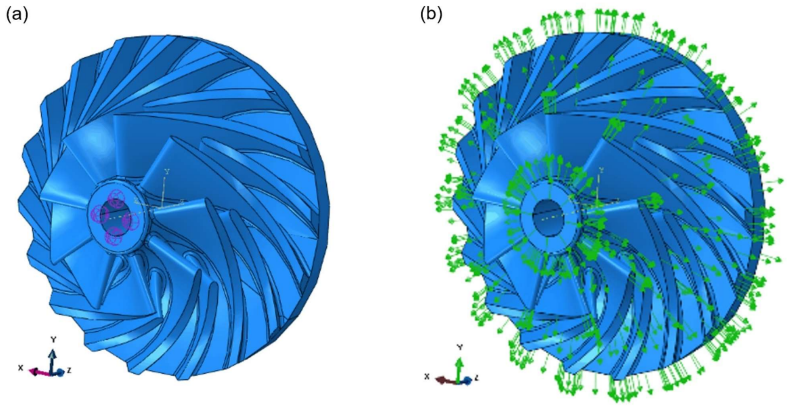

FIGURE 5.2 – (a) 3D model of compressor impeller disc, on which the support points (b) and the load caused by the centrifugal force are marked

The numerical model was developed using the Abaqus CAE software and the strength calculations were carried out in the Abaqus/Standard program. A geometric model, previously developed for CFD analysis and 3D printing, was used to develop the FEM model. The complex three-dimensional geometry of the impeller disc was divided into simpler solids in order to create additional edges and points to facilitate discretization and the modeling of boundary conditions. The 3D model with the boundary conditions and the load is shown in Figure 5.2. To ensure that the restraint of the impeller disc does not cause an increase in stress, it was fixed at eight points located on the edge of the central hole, using additional spring elements (which connect points to the ground). These elements restrict movement in three perpendicular directions and have a stiffness of 1,000 N/m in each direction. Four attachment points for the spring elements can be seen in Figure 5.2a and the other four are located on the other side of the impeller disc. This method of restraint does not introduce any additional stresses. The entire body (the disc) was subjected to a centrifugal force (Figure 5.2b), the magnitude of which corresponded to a speed of 52 krpm or 90 krpm, depending on the calculation case. The disc was therefore only loaded by a centrifugal force, which means that the calculations did not take into account other loads, which may occur due to, for example, the flow of the compressor's working fluid or disc unbalance.

The three-dimensional geometry of the model was then divided into finite elements. Due to the very complex geometry and the irregular shapes of the blades, a decision was made to use tetrahedral

TABLE 5.2 – Measured values of responses

Model Number	Approx. size of elements (mm)	Number of elements	Number of DOF	Calculation time (s)	Maximum stress (MPa)	Maximum displacement (mm)
1	0.7	413.769	1796.487	20.787	28.45	0.1132
2	1.4	108.465	495.831	1.231	29.07	0.1129
3	2.8	27.794	137.535	202	30.88	0.1146

elements (C3D10). These are 10-node finite elements that are used to perform three-dimensional stress analyses with second-order shape functions. In order to choose the proper number of elements for this analysis, a check was made to see the effect of the size and number of finite elements on the calculation results. For this purpose, three FEM models were developed, which differ only in size and number of finite elements. A summary of the basic data for these models is presented in Table 5.3. FEM mesh verification calculations were carried out for the PPS material at a speed of 52 krpm.

Based on the calculations carried out, it can be concluded that doubling the size of the elements (from 0.7 mm to 1.4 mm) resulted in an almost fourfold decrease in the number of finite elements and degrees of freedom (DOF) of the model. This also caused an almost seventeenfold reduction in calculation time, from 20,787 seconds to 1,231 seconds (about 20 minutes). The error in determining stresses using a model with fewer degrees of freedom was 2.18%, and the error in determining displacements was only 0.27%. By further increasing the finite element to 2.8 mm, a further (six-fold) reduction in computation time (to 202 seconds) could be achieved, but this came at the expense of calculation accuracy. In this case, the error in determining stresses was as high as 8.54%, and the error in determining displacements was 1.24%. Based on these results, a decision was made to use a FEM model with an approximate size of elements of 1.4 mm for further analysis. This model was able to significantly reduce the calculation time compared to the most accurate model while achieving an acceptable level of computational accuracy. The FEM model of the compressor impeller disc, selected for further analysis, is presented in Figure 5.3.

Strength calculations were carried out for two different rotational speeds, namely 52 krpm and 90 krpm, with two materials (PPS and SLA), as mentioned in the previous subsection. Selected calculation results of stress and displacement distributions for the PPS material, obtained for a rotational speed of 52 krpm, are shown in Figure 5.4. In Figure 5.4b, it can be seen that the highest stresses in the impeller disc occur at the edge of the central hole. In this area, the reduced stresses calculated according to the

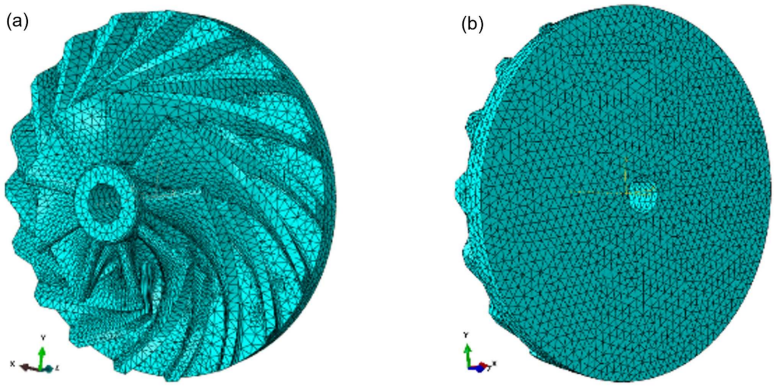

FIGURE 5.3 – (a) FEM model of compressor impeller disc: blade side view and (b) disc side view

von Mises hypothesis reached a value of 29.07 MPa. This is due to the stretching of the material in the circumferential direction at the edge of the disc hole, which is caused by the centrifugal force. In the other part of the disc, the reduced stresses were lower and did not exceed 20 MPa. The maximum stress value obtained from the calculations is lower than the experimentally obtained tensile strength of the samples made of PPS material, which was 29.4 MPa. On the other hand, based on Figure 5.4, it can be concluded that the largest displacements on the impeller disc occurred at the edges of the blades, where they reached a value of 0.1129 mm.

5.1.3 Calculation results

Similar calculations were carried out for a speed of 90 krpm. In this case, the maximum stress reached 87.54 MPa, which far exceeds the tensile strength of the PPS material. The maximum displacement in this case was 0.3404 mm. Since the stress and displacement distributions at a higher speed were of the same nature as at 52 krpm, and the changes were only visible in the stress and displacement values, these results are not presented in graphical form. A summary of the most important results for the two materials and two rotational speeds is shown in Table 5.3.

As regards the compressor impeller disc made of the SSL material, the maximum reduced stress at a speed of 52 krpm was 36.40 MPa, and at 90 krpm increased to 109.40 MPa. The increase in stress compared to the disc made of PPS material was due to the higher density of the SLA material. For this material, the tensile strength determined through experiments was higher and amounted to 79.5 MPa. Therefore, the disc with the analyzed geometry can safely operate at 52 krpm and even

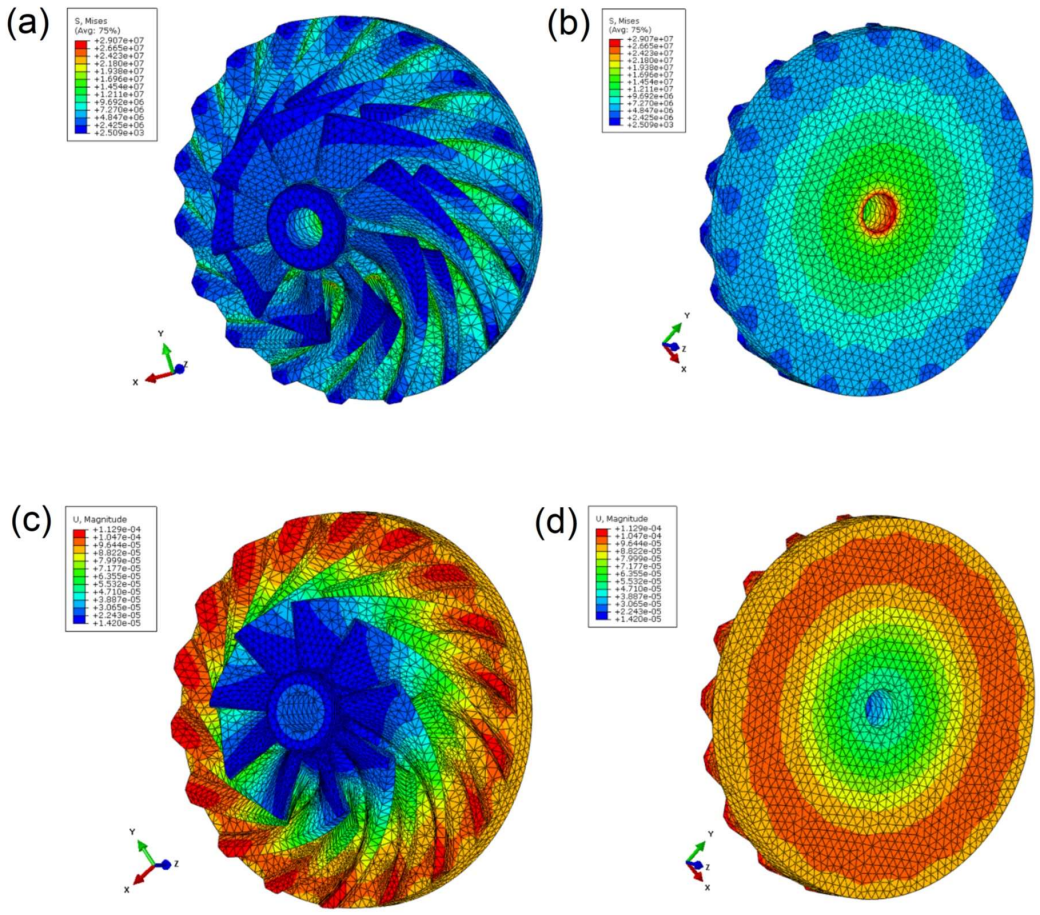

FIGURE 5.4 – (a and b) reduction in stress distribution and (c and d) displacement distribution of the compressor wheel at a speed of 52 krpm for the PPS wheel

TABLE 5.3 – Measured values of responses

Material	Rotational speed (rpm)	Maximum reduced stress (MPa)	Maximum displacement (mm)
PPS	52000	29.07	0.1129
PPS	90000	87.54	0.3404
SLA	52000	36.40	0.0294
SLA	90000	109.40	0.0877

at higher speeds. On the other hand, the strength of this material is too low for the impeller disc to operate at 90 krpm. The displacements of the blade tips of the disc made of SLA were significantly smaller than those of PPS, due to the several times higher Young's modulus. These displacements were observed to be below 0.1 mm, even at 90 krpm. Based on the strength calculations carried out, it can be concluded that the impeller disc with a flow-optimized geometry is not suitable for operation at a speed of 90 krpm. At the lower analyzed speed (52 krpm), in the impeller disc made of PPS material, reduced stresses similar to the tensile strength of this material (which are 29.07 MPa and 29.40 MPa, respectively) occur. As for the disc made of SLA, the maximum stresses at 52 krpm are significantly lower than the tensile strength of this material (they are 36.40 MPa and 79.5 MPa, respectively). A disc made of this material can therefore operate at higher speeds, but in both cases, further optimization of the disc geometry is required before a speed of 90 krpm can be achieved. Apart from the new geometry, target calculations must also take into account all loads acting on the disc during operation and the effect of the operating temperature on the material properties.

5.2 Performance of the finished part: microstructure, geometric accuracy and flow analysis

5.2.1 Effect of optimized process parameters on the microstructure of the fabricated parts

Figure 5.5 shows the microscope optic images from the surface of the impellers. As can be seen, the layers of printing can be observed for the printed impellers that are related to the nature of producing from this technique. According to this figure, FDM wheels show the gaps between their layers which are related to the not enough diffusion of molecular chains deposited in each layer of polymeric filament on other layers. According to the figure the gap between the filaments of PPS-340 is reduced compared to the PPS-320. As mentioned one of the differences between the process parameters of these two impellers was the nozzle temperature. Increasing the nozzle temperature in PPS-340 caused better adhesion between the filament which is referred to as the time welding during printing. Such that increasing the time welding can increase the mobility of chains and molecular diffusion and re-entanglement [4, 6]. Figures 5.5 e and f show the image from the impeller of Rigid 10 k printed with SLA. The images do show not the inter-layer voids for this impeller. It can be said that one of the bold differences between the wheels was related to the surface of the parts, such that the printed-SLA wheel showed a better surface and interlayer adhesion compared to the FDM parts.

Presence the of gaps and voids between the layers can act as a place for passing the fluid that is accompanied by reducing the performance of the compressor. Weiß et al. [1] studied the potential of additive manufacturing in an Organic Rankine Cycle micro turbo-expanders. In their study, internal leakages were mentioned as a major loss for the compressor with a nylon Selective laser sintering wheel. The big difference between the performance of the impeller of PPS 320 compared to the PPS 340 and Rigid 10 k can be referred to as the interlayer quality. Considering the key role of the weld interface on the final performance of the compressor, printed impellers were probed using SEM to investigate the influence of method and process parameters on the weld interface. Figure 5.5 shows the SEM images for PPS 320, PPS 340 and Rigid 10k. For FFF-printed impellers, increasing the printing temperature from 320 °C (for PPS 320) to 340 °C (for PPS 340) on the weld interface led to fewer amounts of triangle inter-filament voids. Figure 5.6e and f indicate the surface of Rigid 10k, as can be seen, complete coalescence between adjacent layers during the fabrication was achieved from SLA.

5.2.2 Effect of optimized process parameters on geometric accuracy of the fabricated parts

Studies have shown the important effect of surface roughness on the performance of centrifugal compressors [119]. Liu et al. [120] studied the effect of blade surface roughness on compressor performance in a turbocharger. In their study, nine different blades with various surface roughness were considered and numerically analyzed. The results showed the inverse effect of surface roughness on performance. This parameter can induce the mechanism of compressor performance degradation, such that, by increasing the surface roughness the reverse flow near the leading edge of blades was more severe, which means the compressor flow is influenced by roughness. Considering the layer-by-layer fabrication of parts through additive manufacturing, depending on the precision of technic different geometrical accuracy can be achieved. Layer heights during the fabrication have been considered an important parameter that can impact the final surface roughness. For example, printing a cylindrical shape with respect to its central axis parallel to the x-direction is accompanied by less surface roughness compared to the inclined direction between x and y. To investigate the effect of the technique of printing on surface roughness, the deviation between the parts and the designed file was analyzed. Regarding, printed PPS 2 and Rigid 10 K were scanned, then stl. file from scanning was fitted on the CAD file. Geomagic software was used to this end, which minimizes the residual error to ensure direct comparison. Figure 5.7 shows the deviations of surface normals and it was used for comparison due

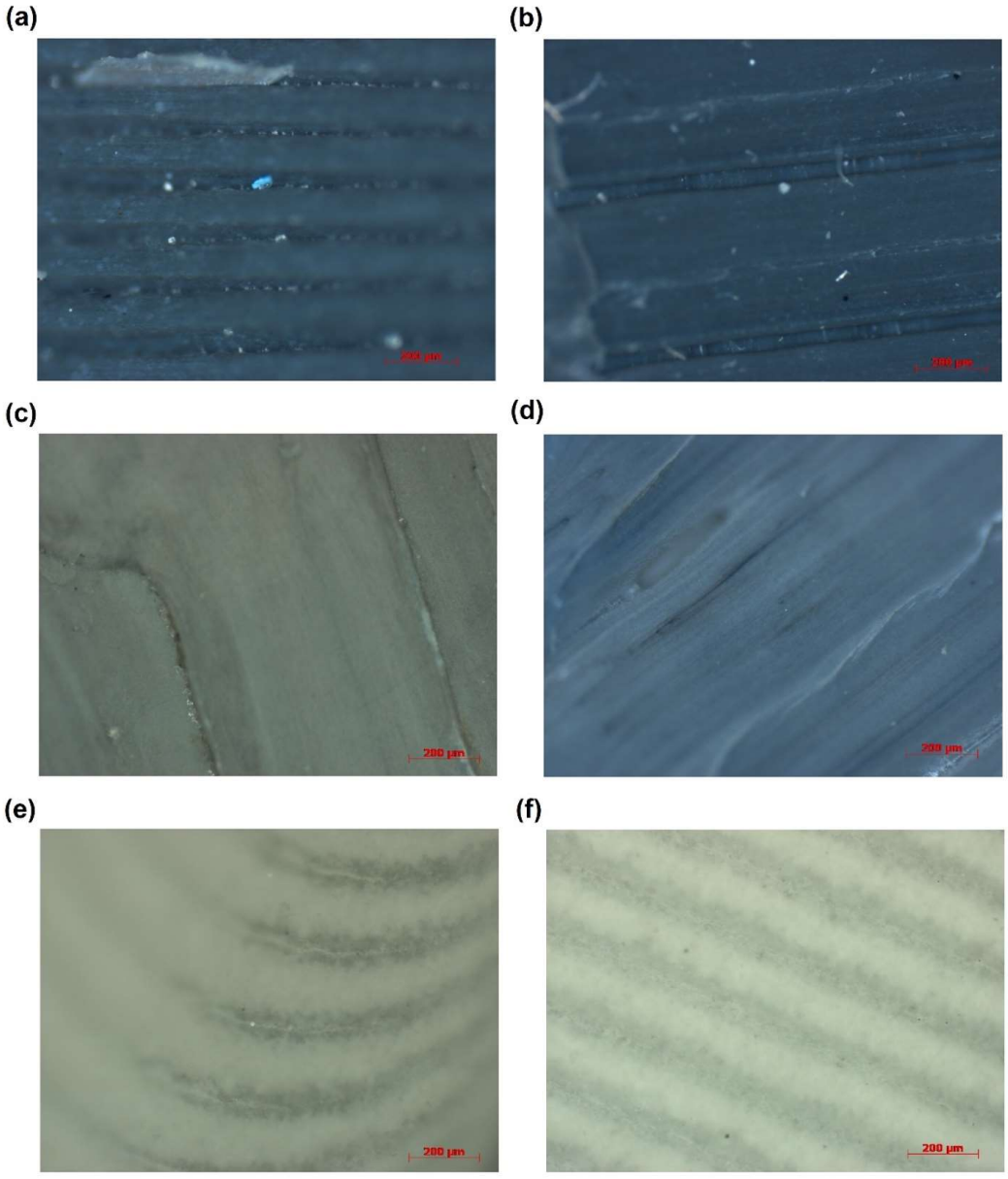

FIGURE 5.5 – (a and b) reduction in stress distribution and (c and d) displacement distribution of the compressor wheel at a speed of 52 krpm for the PPS wheel

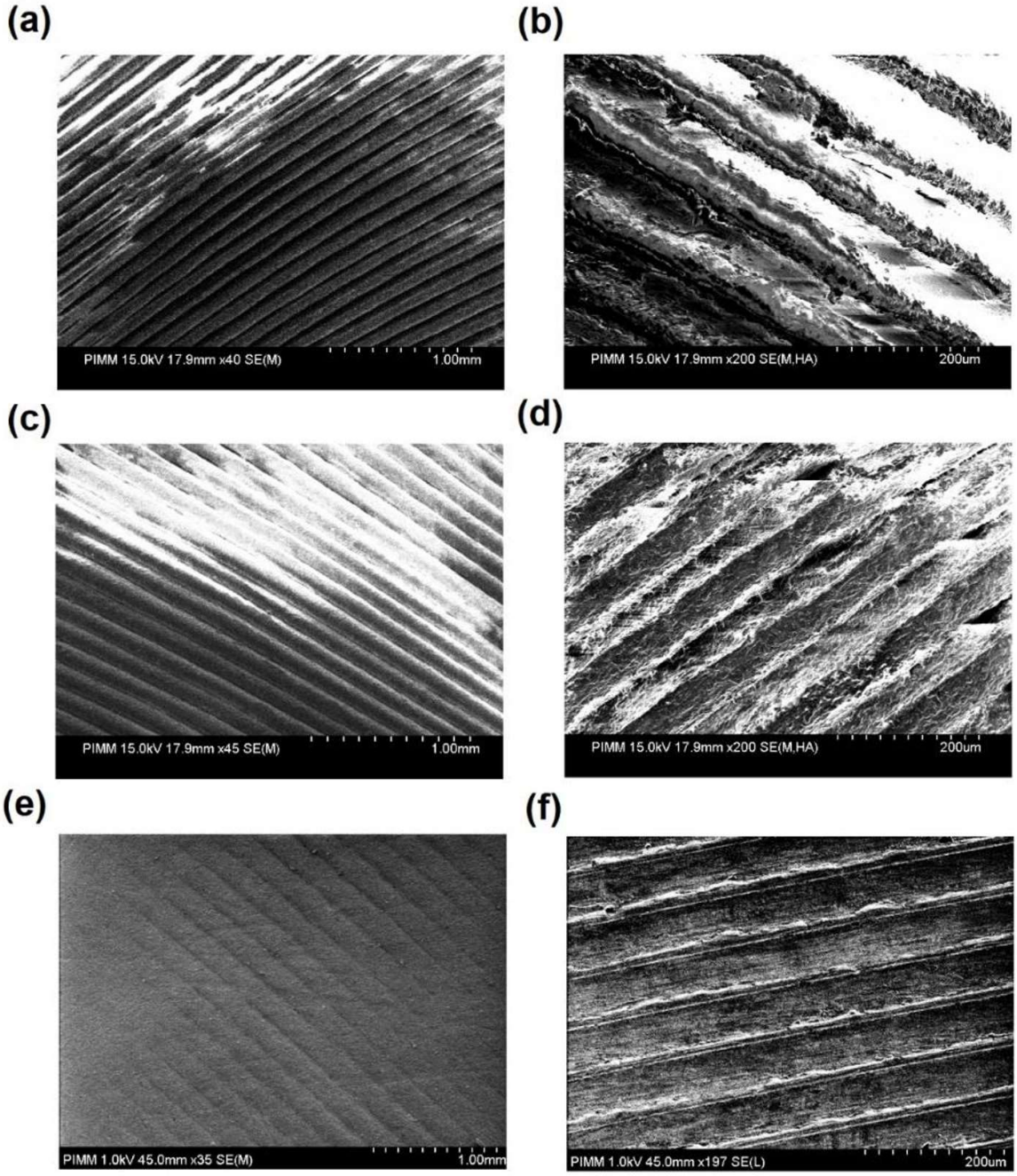

FIGURE 5.6 – SEM des roues (à partir de la pale): (a et b) PPS-320, (c et d) PPS-340 et (e et f) Rigide 10k

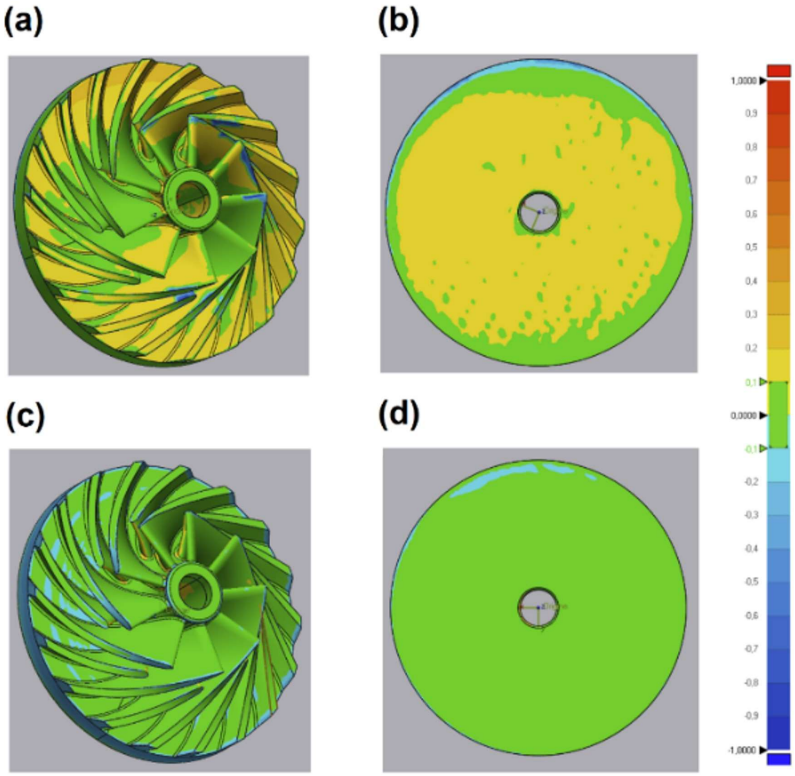

FIGURE 5.7 – Local comparison of best fit of freeform inductor data to nominal CAD geometry

to the complexity of the surface. The mean error across all measurements of distance for PPS 1 and Rigid 10k were -46 and 92 μm (undersized) with a standard deviation of $\pm$0.09 and $\pm$0.16 μm, respectively, presented in Figure 5.8. As can be seen in this figure, Rigid 10k shows a more homogeneous distribution error compared to PPS 1. It should be mentioned that considering the use of the support during the impeller fabrication, the separation of the support was accompanied by the creation of holes in the sample. Also, to increase the mechanical properties Rigid 10k was post-cured, and this post-processing can induce the shrinkage in the sample due to the changing the bonding between the residual monomer and other polymer chains from Van der Waals to covalence bonding. According to the results of the performance of the compressor up to the rotational speed of 52000 rpm, PPS 1 shows a more efficient performance compared to the Rigid 10 which can be said that increasing the deviation error of the rotor decreased the efficiency.

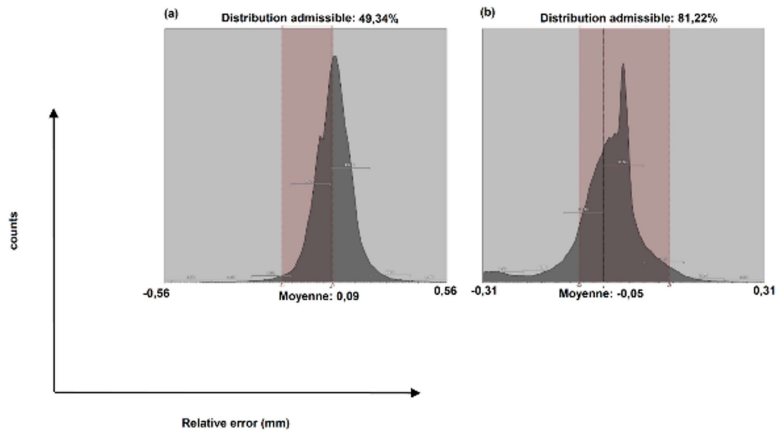

FIGURE 5.8 – Deviation of discreet data points compared to the free form inductor (all construction plates)

5.2.3 Flow analysis of compressor regarding the different process parameters

The three FFF and SLA printed centrifugal compressor rotors, described previously, were experimentally evaluated. The characteristic curves of each rotor are taken at different speeds. However, at speeds above 70 krpm, the FFF-printed rotor was a failure due to excessive stress caused by centrifugal force. Figure 5.9 shows the compression rate obtained by the three printed rotors for a speed of 52 krpm from experimental and CFD simulation. The blue line is the characteristic curve of the compressor using the PPS-320 rotor, while the green line represents PPS-340 rotor.

It is seen that the PPS-320 rotor gives a lower compression ratio, while the other two rotors give equivalent results closer to the CFD simulation. In addition, for PPS-340, the operating range has significantly lower rotor mass flow rates than other rotors and CFD simulation results. This means that this rotor generates a lot of losses. One of the reasons for these losses can be the leakage of the airflow inside the rotor. If this is the case, this is explained by the specificity of the FFF process for which the material is deposited layer by layer. When the pressure difference between the surfaces of the rotor increases, the leakage flux inside the rotor appears and gradually increases. This leak impedes the flow of air inside the blade passages, thus reducing the performance of the rotor. The size of the voids depends on the different process parameters such as nozzle temperature, speed of molten filament deposition, layer thickness, and filling pattern [110]. However, an increasing percentage of filling is

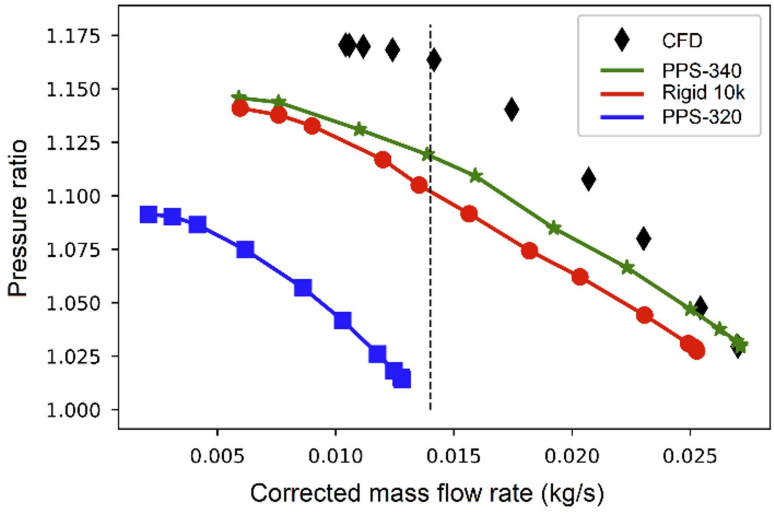

FIGURE 5.9 – Pressure ratio against the corrected mass flow rate for different printed rotors

accompanied by reducing the porosity of the parts. Indeed, the PPS-340 rotor presents significantly improved or even slightly better performances than those of the Rigid10k rotor. This can be explained as follows: when the rotor rotates at high speed, due to the properties of PPS used in the FFF method, it can elongate (about 4%) under the action of centrifugal force in the radial direction which leads to an increase the Euler work of the rotor. In addition, there are still impression ridges on the surfaces of the blade casing which partially prevent leakage flows. However, Rigid10K rotor has lower elongation (about 1%) so the effect of centrifugal force does not affect compressor performance. The performance of the system from each of the 3D-printed wheels is shown in Figure 5.10. According to the results of the PPS-320 rotor, the throughput was between 0.002 and 0.012 kg/s. The maximum value of the compression ratio was 1.09. The performance of this rotor showed values from 5 to 20%, and the maximum efficiency was 22% at a compression ratio of 1.06. The results obtained for the PPS 340 showed an increase in yield compared to the PPS-320. The maximum efficiency was about 64% for this rotor. The rotor manufactured by SLA has an efficiency between PPS-320 and PPS-340. The flow rate at 52 krpm was between 0.006 and 0.024 with a maximum compression ratio of 1.14. This rotor has a maximum efficiency of about 62%. However, the experimental measurements compared to the results of the CFD simulation are quite different (about a 10% difference).

Figure 5.11 shows the aerodynamic power of the compressor against the corrected mass flow rate

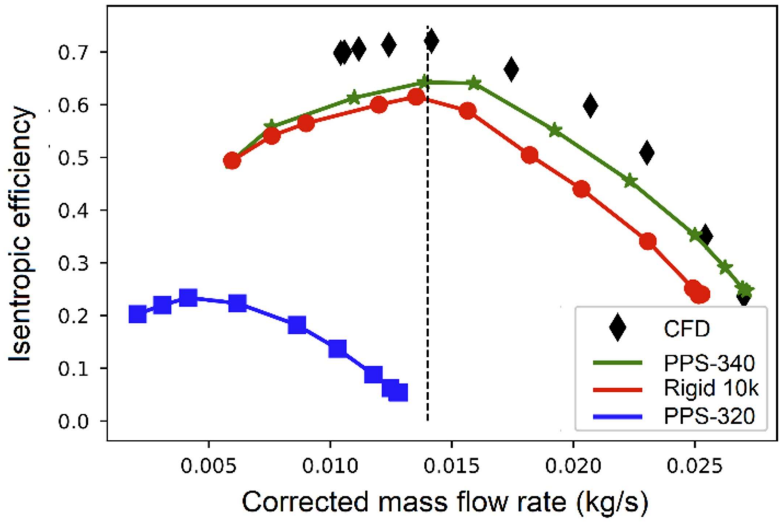

FIGURE 5.10 – Compressor isentropic efficiency comparison between rotors

concerning numerical and experimental results. PPS-320 rotor has higher power consumption due to the high losses, so efficiency is low. The other two rotors give quite comparable results but still show a difference from the CFD results. Furthermore, the aerodynamic power of the compressor is related to the temperature of the compressed air flow, as shown in Figure 5.12. PPS-320 rotor generates a much higher temperature than other rotors, which once again proves that the rotor has aerodynamic losses due to leakage flows hindering the air circulation inside of the rotor. This obstruction causes localized vortex areas which increase the friction between the air streams as well as the friction of the air with the rotor surface. As a result, the temperature and power of the airflow increased considerably while efficiency decreases rapidly. Both PPS-340 and Rigid10k rotors give almost identical results to CFD results.

5.3 Conclusions

This section presents the structural aspect of the compressor rotor was analyzed through a numerical model. Experimental measurements were done to investigate the aerodynamic performance. A high-performance thermoplastic (polyphenylene sulfide) and a resin (Rigid 10k) were selected to produce the rotors. Additive manufacturing was chosen as the manufacturing method. The parts were

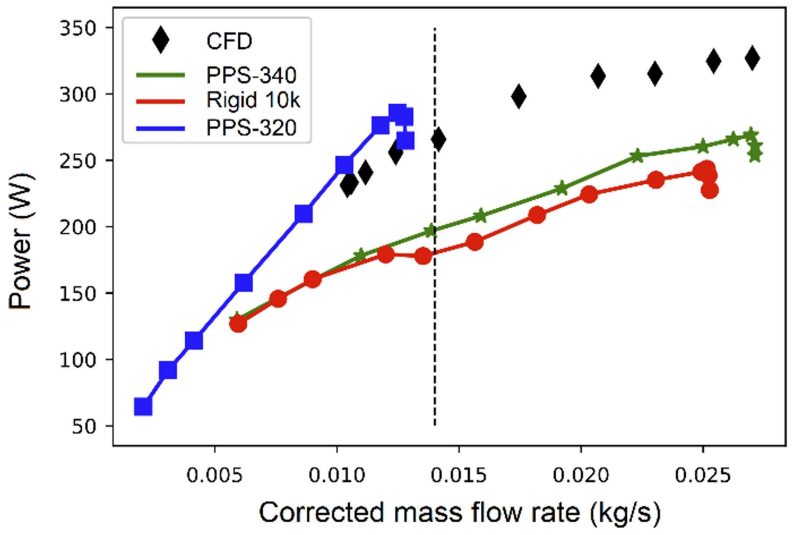

FIGURE 5.11 – Power of compressor on the shaft for different printed impellers

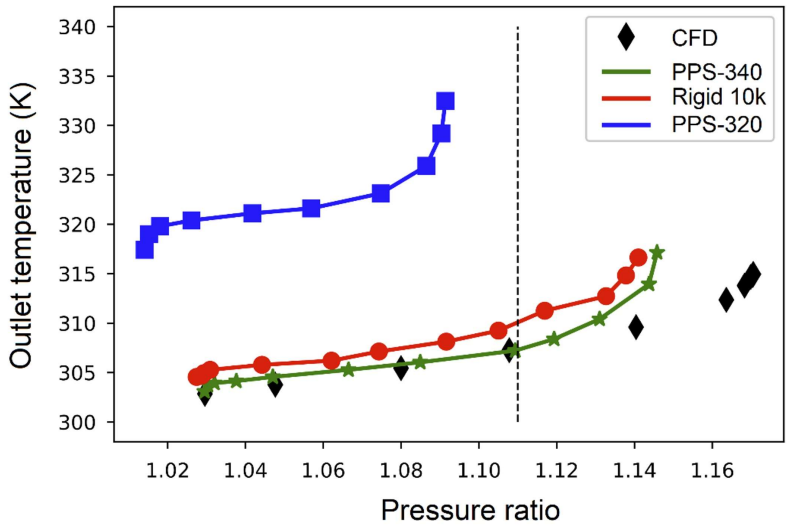

FIGURE 5.12 – Output temperature against the pressure ratio for different rotors

obtained by FFF and SLA. The main conclusions of this section are as follows:

• The rotor fabricated by FFF with PPS can reach speeds of 60 krpm without failure while the rotor made by the SLA method can reach higher speeds. We, therefore, recommend that FFF-printed rotors by PPS do not exceed this speed.

• The printed impeller was shown to respond adequately and withstand centrifugal forces and bending stresses at a rotational speed of 52,000 rpm. Returns optimum for each of the materials can be classified as follows: PPS-320 $<$ Rigid 10k $<$ PPS-340.

• The results show the key role of coalescence between adjacent layers during fabrication. Reducing the inter-layer adhesion can significantly reduce performance. The analysis of this parameter was made by microscopic observation and the improvement of the spacer between the layers made it possible to increase the yield from 22% to 64% for the rotors manufactured by FFF.

Chapitre 6

Conclusions and perspectives

6.1 Conclusions

This thesis was carried out between two laboratories, LIFSE and PIMM, at Arts et Métiers Institute of Technology to use polymer instead of metals for manufacturing the compressor part. This purpose was realized in two aspects of numerical and experimental analysis. Two main scientific and technical locks must be distinguished:

• The need to understand the relation between the microstructure of the material and the final performance of the compressor through a multi-physic and multi-scale study and by considering the physical, chemical, and mechanical properties of the samples with respect to the process parameters.

• The lack of modeling allows a reliable structural and fluidal simulation of compressors regarding the additive manufacturing parts for compressors. Indeed, many models and simulations are available in the literature, but validations based on experimental tests are missing.

A centrifugal compressor is designed based on iterative calculations of a 0D model in combination with loss models. The model can provide a preliminary geometry of the compressor according to the specifications. Then, the 3D geometry of the compressor was optimized through the Computational Fluid Dynamics (CFD) calculation to find the best geometry and predict its performance. In addition, the structural aspect of the compressor rotor was analyzed through a numerical model. The microstructure of materials using different methods of analysis and characterization was studied. In addition, the influence of the process parameters on this microstructure on the one hand and on the performance (mechanical and functional) of the part was investigated. A high-performance thermoplastic (polyphenylene sulfide) and a resin (Rigid 10k) were selected to produce the rotors. Additive manufacturing was chosen as the manufacturing method. The parts were obtained by FFF and SLA. The results show the key role of coalescence between adjacent layers during fabrication. Reducing the inter-layer adhesion can significantly reduce performance. The analysis of this parameter was made by microscopic observation and the improvement of the spacer between the layers made it possible to increase the yield from 22% to 64% for the rotors manufactured by FFF. The developed healing model provided reasonable predictions for bond strength by including diffusion terms as well as the

temperature within the printed part. The interface healing model developed based on the reptation theory was successfully applied to polymer welding experiments. The results of accurate bond strength based on their rheological properties and prospective processing conditions on polylactic acid can provide insight into the priori information about the material's properties and the processing conditions. The effect of two process parameters of nozzle speed and nozzle temperature, and time of annealing as a post-processing method on the mechanical behavior of interlayer and crystallization percentage of printed parts were investigated. Polyphenylene sulfide was selected as a high-performance polymer during this study. The parameters were optimized through multi-response optimization utilizing the GRA method. Process parameters and annealing time have been three variations as input parameters to achieve the best mechanical interlayer properties and high crystallization percentage. Analyzing the GRG data by ANOVA and S/N showed the optimal process parameters of nozzle temperature and speed of 340 and 20 mm/min, respectively, annealed at 200 °C for 6h. Microscopical results show the importance of parameters on good coalescence between the printed layers that impact the mechanical and Physico-chemical properties. Studying the physical, chemical, and mechanical studies of urethane dimethacrylate resin in stereolithography approach. The mechanical properties of green and post-cured samples were analyzed for the different sub-build orientations. The obtained result explained the curing mechanism of the samples in the post-curing and the value of residual resin was calculated. The key role of residual resin in the parts on thermal and mechanical analysis was explained. This effect was investigated on the glass transitions of the samples so that post-curing caused the increasing the glass transition. According to the results, an increase in the post-curing temperature process increased the tensile strength so that the post-curing at 80 °C caused an increase in the polymerization up to 98%. Finally, results showed the maximum tensile strength in the rank of $90° < 0° < 45°$. Numerical simulation has been performed for structural analysis of the additive-manufactured impeller. The numerical analysis provides the category of material selection at different centrifugal forces corresponding to the different rotational speeds. Finally, the importance of microstructure and process parameters on the final performance of the compressor was shown.

6.2 Perspectives

The perspective of this work can include two main parts:

1. Materials and processes: Fused filament fabrication (FFF) and Stereolithography (SLA), are

poised to revolutionize compressor element design and production. To further advance this area of study, future investigations can focus on exploring advanced material development for additive manufacturing, aiming to tailor novel materials with optimized microstructural characteristics for enhanced mechanical properties and superior compressor performance. Additionally, researchers can delve into in-depth material microstructure control by studying the influence of FDM and SLA process parameters on microstructural evolution, enabling fine-tuning of printing settings for optimal performance. Combining multiscale material characterization techniques and Design for Additive Manufacturing principles, future studies can unlock innovative compressor element designs with lightweight structures and material grading, while in-situ monitoring and control systems can ensure consistent microstructures during the additive manufacturing process. Furthermore, research endeavors can explore post-processing techniques for microstructural refinement and validation of additive manufacturing components ultimately paving the way for environmentally sustainable practices in compressor element manufacturing.

2. Computational Modeling and Simulation:

Incorporating sophisticated computational modeling and simulation approaches can significantly complement the experimental findings of this thesis. Finite Element Analysis (FEA), molecular dynamics simulations, and machine learning algorithms can be utilized to predict the mechanical properties, performance characteristics, and failure mechanisms of compressor elements with different microstructures and under varying operating conditions. In addition, calculating the performance of the compressor through computational fluid dynamics by considering the surface roughness and thermal expansion of polymeric 3D-printed impellers would be interesting.

Bibliographie

[1] A. P. Weiß, V. Novotný, T. Popp, P. Streit, J. Špale, G. Zinn, and M. Kolovratník, "Customized ORC micro turbo-expanders - From 1D design to modular construction kit and prospects of additive manufacturing," *Energy*, vol. 209, p. 118407, 2020. [Online]. Available: https://www.sciencedirect.com/science/article/pii/S0360544220315140

[2] H. Vanaei, "Etude et modélisation de la rhéologie des polymères au cours du procédé fdm (fabrication additive)," Ph.D. dissertation, Paris, HESAM, 2021.

[3] J. E. Seppala, S. H. Han, K. E. Hillgartner, C. S. Davis, and K. B. Migler, "Weld formation during material extrusion additive manufacturing," *Soft matter*, vol. 13, no. 38, pp. 6761–6769, 2017.

[4] T. J. Coogan and D. O. Kazmer, "Prediction of interlayer strength in material extrusion additive manufacturing," *Additive Manufacturing*, vol. 35, p. 101368, 2020.

[5] A. Andrearczyk, P. Bagiński, and P. Klonowicz, "Numerical and experimental investigations of a turbocharger with a compressor wheel made of additively manufactured plastic," *International Journal of Mechanical Sciences*, vol. 178, p. 105613, 2020.

[6] J. T. Gravdahl and O. Egeland, *Compressor surge and rotating stall: Modeling and control*. Springer Science Business Media, 2012.

[7] H. P. Bloch and J. J. Hoefner, *Reciprocating compressors:: operation and maintenance*. Elsevier, 1996.

[8] M. Stewart, "8 - Dynamic compressors," in *Surface Production Operations*, M. Stewart, Ed. Boston: Gulf Professional Publishing, 2019, pp. 527–653.

[9] D. Japikse, *Centrifugal compressor design and performance.* Concepts Eti, 1996.

[10] D. Gerada, A. Mebarki, N. L. Brown, C. Gerada, A. Cavagnino, and A. Boglietti, "High-speed electrical machines: Technologies, trends, and developments," *IEEE transactions on industrial electronics*, vol. 61, no. 6, pp. 2946–2959, 2013.

[11] Y. Y. Sun, P. Wang, S. L. Lu, L. Q. Li, M. L. S. Nai, and J. Wei, "Laser welding of electron beam melted Ti-6Al-4V to wrought Ti-6Al-4V: Effect of welding angle on microstructure and mechanical properties," *Journal of Alloys and Compounds*, vol. 782, pp. 967–972, 2019.

[12] D. Hagelstein, K. Hillewaert, R. A. Van den Braembussche, A. Engeda, R. Keiper, and M. Rautenberg, "Experimental and numerical investigation of the flow in a centrifugal compressor volute," *J. Turbomach.*, vol. 122, no. 1, pp. 22–31, 2000.

[13] S. Peng, T. Li, X. Wang, M. Dong, Z. Liu, J. Shi, and H. Zhang, "Toward a sustainable impeller production: Environmental impact comparison of different impeller manufacturing methods," *Journal of Industrial Ecology*, vol. 21, no. S1, pp. S216–S229, 2017.

[14] M. P. Boyce, *Centrifugal compressors: a basic guide.* PennWell Corporation, 2003.

[15] H. González-Barrio, A. Calleja-Ochoa, A. Lamikiz, and L. N. López de Lacalle, "Manufacturing Processes of Integral Blade Rotors for Turbomachinery, Processes and New Approaches," *Applied Sciences*, vol. 10, no. 9, p. 3063, 2020.

[16] A. Andrearczyk, B. Konieczny, and J. Sokołowski, "Additively Manufactured Parts Made of a Polymer Material Used for the Experimental Verification of a Component of a High-Speed Machine with an Optimised Geometry—Preliminary Research," *Polymers*, vol. 13, no. 1, p. 137, 2021.

[17] S. Agarwal and K. M. High, "Newer-generation ventricular assist devices," *Best Practice Research Clinical Anaesthesiology*, vol. 26, no. 2, pp. 117–130, 2012.

[18] H. Bozorgasareh, J. Khalesi, M. Jafari, and H. O. Gazori, "Performance improvement of mixed-flow centrifugal pumps with new impeller shrouds: Numerical and experimental investigations," *Renewable Energy*, vol. 163, pp. 635–648, 2021.

[19] T. Novaković, M. Ogris, and J. Prezelj, "Validating impeller geometry optimization for sound quality based on psychoacoustics metrics," *Applied acoustics*, vol. 157, p. 107013, 2020.

[20] M. M. C. Dhere, A. M. Badadhe, A. S. Patil, M. B. Bankar, and A. K. Tarange, "Design, Analysis Material Optimization of Submersible Pump Impeller by FEA Experimentation."

[21] J. Sun, S. Chen, Y. Qu, and J. Li, "Review on stress corrosion and corrosion fatigue failure of centrifugal compressor impeller," *Chinese Journal of Mechanical Engineering*, vol. 28, no. 2, pp. 217–225, 2015.

[22] I. Hernandez-Carrillo, C. J. Wood, and H. Liu, "Advanced materials for the impeller in an ORC radial microturbine," *Energy Procedia*, vol. 129, pp. 1047–1054, 2017.

[23] L. A. Martynyuk, D. V. Afanasiev, L. V. Bykov, A. D. Ezhov, and M. A. Mezintsev, "The study of the applicability of polymer composite materials for the manufacture of the impeller of a centrifugal compressor," in *IOP Conference Series: Materials Science and Engineering*, vol. 1060, no. 1. IOP Publishing, 2021, p. 12026.

[24] S. Fernández, M. Jiménez, J. Porras, L. Romero, M. M. Espinosa, and M. Dominguez, "Additive manufacturing and performance of functional hydraulic pump impellers in fused deposition modeling technology," *Journal of Mechanical Design*, vol. 138, no. 2, p. 24501, 2016.

[25] R. K. Upadhyay, A. K. Mishra, and A. Kumar, "Mechanical degradation of 3D printed PLA in simulated marine environment," *Surfaces and Interfaces*, vol. 21, p. 100778, 2020.

[26] G. Zywica, T. Z. Kaczmarczyk, E. Ihnatowicz, P. Baginski, and A. Andrearczyk, "Application OF a heat resistant plastic IN a high-speed microturbine designed for the domestic ORC system," 2019.

[27] R. Maier, S. VINTILĂ, R. Mihalache, V. Vilag, M. Sima, and V. Dragan, "Decreasing the Mass of Turbomachinery Subansamblies Using Advanced Polymer Composites," *MATERIALE PLASTICE*, vol. 56, no. 4, pp. 687–692, 2019.

[28] N. K. Kar, Y. Hu, N. J. Kar, and R. J. Kar, "Failure analysis of a polymer centrifugal impeller," *Case Studies in Engineering Failure Analysis*, vol. 4, pp. 1–7, 2015.

[29] C. Jiang, "Investigating Impeller Wear and Its Effect on Pump Performance Using Soft Materials," 2019.

[30] T. Gebäck and A. Heintz, "A Pore Scale Model for Osmotic Flow: Homogenization and Lattice Boltzmann Simulations," *Transport in Porous Media*, vol. 126, no. 1, pp. 161–176, 2019.

[31] J. Škorpík, "15. SHAPES OF PARTS AND MATERIALS OF TURBOMACHINES."

[32] S. E. Gad, "Polymers," in *Encyclopedia of Toxicology (Third Edition)*, third edit ed., P. Wexler, Ed. Oxford: Academic Press, 2014, pp. 1045–1050. [Online]. Available: https://www.sciencedirect.com/science/article/pii/B978012386454300912X

[33] J. M. Jafferson and D. Chatterjee, "A review on polymeric materials in additive manufacturing," *Materials Today: Proceedings*, vol. 46, pp. 1349–1365, 2021.

[34] P. K. Mallick, "Thermoplastics and thermoplastic–matrix composites for lightweight automotive structures," in *Materials, design and manufacturing for lightweight vehicles*. Elsevier, 2021, pp. 187–228.

[35] O. Ogorodnyk and K. Martinsen, "Monitoring and control for thermoplastics injection molding a review," *Procedia Cirp*, vol. 67, pp. 380–385, 2018.

[36] S. Garzon-Hernandez, D. Garcia-Gonzalez, A. Jérusalem, and A. Arias, "Design of FDM 3D printed polymers: An experimental-modelling methodology for the prediction of mechanical properties," *Materials Design*, vol. 188, p. 108414, 2020.

[37] D. Drummer, D. Rietzel, and F. Kühnlein, "Development of a characterization approach for the sintering behavior of new thermoplastics for selective laser sintering," *Physics Procedia*, vol. 5, pp. 533–542, 2010.

[38] G. S. Ponticelli, F. Tagliaferri, S. Venettacci, M. Horn, O. Giannini, and S. Guarino, "Re-Engineering of an Impeller for Submersible Electric Pump to Be Produced by Selective Laser Melting," *Applied Sciences*, vol. 11, no. 16, p. 7375, 2021.

[39] E. Umaras, A. Barari, and M. S. G. Tsuzuki, "Tolerance analysis based on Monte Carlo simulation: a case of an automotive water pump design optimization," *Journal of Intelligent Manufacturing*, pp. 1–15, 2020.

[40] D. Garlotta, "A literature review of poly (lactic acid)," *Journal of Polymers and the Environment*, vol. 9, no. 2, pp. 63–84, 2001.

[41] S. Olivera, H. B. Muralidhara, K. Venkatesh, K. Gopalakrishna, and C. S. Vivek, "Plating on acrylonitrile–butadiene–styrene (ABS) plastic: a review," *Journal of materials science*, vol. 51, no. 8, pp. 3657–3674, 2016.

[42] V. R. Sastri, "8 - High-Temperature Engineering Thermoplastics: Polysulfones, Polyimides, Polysulfides, Polyketones, Liquid Crystalline Polymers, and Fluoropolymers," in *Plastics in Medical Devices (Second Edition)*, second edi ed., V. R. Sastri, Ed. Oxford: William Andrew Publishing, 2014, pp. 173–213.

[43] G. Dolzyk and S. Jung, "Tensile and fatigue analysis of 3D-printed polyethylene terephthalate glycol," *Journal of Failure Analysis and Prevention*, vol. 19, no. 2, pp. 511–518, 2019.

[44] P. Latko-Durałek, K. Dydek, and A. Boczkowska, "Thermal, rheological and mechanical properties of PETG/RPETG blends," *Journal of Polymers and the Environment*, vol. 27, no. 11, pp. 2600–2606, 2019.

[45] D. Garcia-Gonzalez, M. Rodriguez-Millan, A. Rusinek, and A. Arias, "Investigation of mechanical impact behavior of short carbon-fiber-reinforced PEEK composites," *Composite Structures*, vol. 133, pp. 1116–1126, 2015.

[46] I. Hernandez-Carrillo, C. Wood, and H. Liu, "Development of a 1000 W organic Rankine cycle micro-turbine-generator using polymeric structural materials and its performance test with compressed air," *Energy Conversion and Management*, vol. 190, pp. 105–120, 2019.

[47] A. Pavlović, M. Šljivić, M. Kraisnik, J. Ilić, and J. Anić, "Polymers in additive manufacturing: The case of a water pump impeller," *FME Transactions*, vol. 45, no. 3, pp. 354–359, 2017.

[48] M. Polák, "Behaviour of 3D printed impellers in performance tests of hydrodynamic pump," in *Proceedings of the 7th International Conference on Trends in Agricultural Engineering, Prague, Czech Republic*, 2019, pp. 17–20.

[49] T. M. Premkumar, V. Pushpak, K. V. Krishna, D. G. Reddy, N. S. Kumar, V. Hariram, S. Serala-

than, and R. S. Nakandhrakumar, "Design and fusion deposit modelling of radial flow centrifugal pump," *Materials Today: Proceedings*, vol. 33, pp. 3497–3503, 2020.

[50] J. Jang, K. Cho, and G.-H. Yang, "Design and experimental study of dragonfly-inspired flexible blade to improve safety of drones," *IEEE Robotics and Automation Letters*, vol. 4, no. 4, pp. 4200–4207, 2019.

[51] T. Li, B. Wen, Y. Tian, Z. Li, and S. Wang, "Numerical simulation and experimental analysis of small drone rotor blade polarimetry based on RCS and micro-Doppler signature," *IEEE Antennas and Wireless Propagation Letters*, vol. 18, no. 1, pp. 187–191, 2018.

[52] N. Zirak, M. Shirinbayan, S. Farzaneh, and A. Tcharkhtchi, "Effect of molecular weight on crystallization behavior of poly (lactic acid) under isotherm and non-isotherm conditions," *Polymers for Advanced Technologies*, 2021.

[53] U. Kyzyrov and D. Turgali, "Performance Enhancement of a Centrifugal Pump by Impeller Retrofitting," 2019.

[54] R. Kopparapu, S. Mathew, E. Siciliano, G. Stasick, and M. Dias, "Designing a Centrifugal Pump System for High Altitude Water Crises," 2017.

[55] M. T. Birosz, M. Andó, and S. Jeganmohan, "Finite Element Method modeling of Additive Manufactured Compressor Wheel," *Journal of The Institution of Engineers (India): Series D*, vol. 102, no. 1, pp. 79–85, 2021.

[56] A. Machalski, J. Skrzypacz, P. Szulc, and D. Błoński, "Experimental and numerical research on influence of winglets arrangement on vortex pump performance," in *Journal of Physics: Conference Series*, vol. 1741, no. 1. IOP Publishing, 2021, p. 12019.

[57] A. Odetti, M. Altosole, G. Bruzzone, M. Caccia, and M. Viviani, "Design and construction of a modular pump-jet thruster for autonomous surface vehicle operations in extremely shallow water," *Journal of Marine Science and Engineering*, vol. 7, no. 7, p. 222, 2019.

[58] A. V. Huynh, P. Stein, and E. D. Buhr, "3D-printed assistive pipetting system for gel electrophoresis for technicians with low acuity vision," *BioTechniques*, vol. 70, no. 1, pp. 49–53, 2020.

[59] X. Ling, X. Jing, C. Zhang, and S. Chen, "Polyether Ether Ketone (PEEK) Properties and Its Application Status," in *IOP Conference Series: Earth and Environmental Science*, vol. 453, no. 1. IOP Publishing, 2020, p. 12080.

[60] D. K. Platt, *Engineering and high performance plastics market report: a Rapra market report*. iSmithers Rapra Publishing, 2003.

[61] K. Pedersen, "Analysis of copper corrosion in compacted bentonite clay as a function of clay density and growth conditions for sulfate-reducing bacteria," *Journal of applied microbiology*, vol. 108, no. 3, pp. 1094–1104, 2010.

[62] K. Pedersen, A. F. Bengtsson, J. S. Edlund, and L. C. Eriksson, "Sulphate-controlled diversity of subterranean microbial communities over depth in deep groundwater with opposing gradients of sulphate and methane," *Geomicrobiology Journal*, vol. 31, no. 7, pp. 617–631, 2014.

[63] J. Gotro and R. B. Prime, "Thermosets," *Encyclopedia of Polymer Science and Technology*, pp. 1–75, 2002.

[64] J.-P. Pascault and R. J. J. Williams, "Overview of thermosets: structure, properties and processing for advanced applications," in *Thermosets*. Elsevier, 2012, pp. 3–27.

[65] X. Li, X. Zhang, J. Chen, L. Huang, and Y. Lv, "The mechanical properties and creep behavior of epoxy polymer under the marine environment: A molecular dynamics investigation," *Materials Today Communications*, vol. 28, p. 102737, 2021.

[66] M. J. Mullins, D. Liu, and H.-J. Sue, "Chapter 2 - Mechanical properties of thermosets," Q. B. T. T. S. E. Guo, Ed. Elsevier, 2018, pp. 35–68. [Online]. Available: https://www.sciencedirect.com/science/article/pii/B9780081010211000022

[67] Y. Sano, R. Matsuzaki, M. Ueda, A. Todoroki, and Y. Hirano, "3D printing of discontinuous and continuous fibre composites using stereolithography," *Additive Manufacturing*, vol. 24, pp. 521–527, 2018. [Online]. Available: https://www.sciencedirect.com/science/article/pii/S2214860418303282

[68] W. Hao, Y. Liu, H. Zhou, H. Chen, and D. Fang, "Preparation and characterization of 3D printed continuous carbon fiber reinforced thermosetting composites," *Polymer Testing*,

vol. 65, pp. 29–34, 2018. [Online]. Available: https://www.sciencedirect.com/science/article/pii/S0142941817314149

[69] M. Biron, *Thermosets and composites: material selection, applications, manufacturing and cost analysis*. Elsevier, 2013.

[70] V. N. Matveev, L. S. Shabliy, and A. V. Krivcov, "Application of stereolithography prototypes for gas dynamic tests and visualization," in *Journal of Physics: Conference Series*, vol. 803, no. 1. IOP Publishing, 2017, p. 12097.

[71] R. C. Paul, B. Ramachandran, G. Sushma, K. H. A. Harshavardhan, and I. Rohith, "An empirical research on areca fiber polymer composite for automotive components in modern industry," *Materials Today: Proceedings*, vol. 33, pp. 4493–4497, 2020.

[72] R.-M. Wang, S.-R. Zheng, and Y. G. Zheng, *Polymer matrix composites and technology*. Elsevier, 2011.

[73] R. Kaundal, "Role of process variables on solid particle erosion of polymer composites: a critical review," *Silicon*, vol. 9, no. 2, pp. 223–238, 2017.

[74] V. Mallick, "Thermoplastic composite based processing technologies for high performance turbomachinery components," *Composites Part A: Applied Science and Manufacturing*, vol. 32, no. 8, pp. 1167–1173, 2001. [Online]. Available: https://www.sciencedirect.com/science/article/pii/S1359835X01000641

[75] Q. Li, J. Piechna, and N. Mueller, "Static, Dynamic and Failure Behavior of a Novel Axial Composite Impeller for Water Chiller," in *ASME International Mechanical Engineering Congress and Exposition*, vol. 44298, 2010, pp. 81–87.

[76] D. Chung, *Carbon fiber composites*. Elsevier, 2012.

[77] D. Berry, "Use of Victrex® PEEK™ Thermoplastic to Drive New Designs, Processing Flexibility, and Cost Reduction in Aerospace Components," *SAE Transactions*, pp. 426–431, 2002.

[78] A. Rashedi, I. Sridhar, and K. J. Tseng, "Multi-objective material selection for wind turbine blade and tower: Ashby's approach," *Materials & Design*, vol. 37, pp. 521–532, 2012.

[79] M. Patil and N. Müller, "Structural analysis of continuous fiber wound composite impellers of a multistage high-speed counter rotating axial compressor for compressing water vapor (R-718) as refrigerant using Finite Element Analysis," *Materials Design*, vol. 50, pp. 683–693, 2013.

[80] D. Goerke, A.-L. Le Denmat, T. Schmidt, F. Kocian, and E. Nicke, "Aerodynamic and mechanical optimization of CF/PEEK blades of a counter rotating fan," in *Turbo Expo: Power for Land, Sea, and Air*, vol. 44731. American Society of Mechanical Engineers, 2012, pp. 21–33.

[81] D. Wu, Y. Liu, D. Li, X. Zhao, and C. Li, "Effect of materials on the noise of a water hydraulic pump used in submersible," *Ocean Engineering*, vol. 131, pp. 107–113, 2017.

[82] B. Henriques, D. Fabris, J. Mesquita-Guimarães, A. C. Sousa, N. Hammes, J. C. M. Souza, F. S. Silva, and M. C. Fredel, "Influence of laser structuring of PEEK, PEEK-GF30 and PEEK-CF30 surfaces on the shear bond strength to a resin cement," *Journal of the Mechanical Behavior of Biomedical Materials*, vol. 84, pp. 225–234, 2018.

[83] R. Kumar, R. Singh, and I. P. S. Ahuja, "Investigations of mechanical, thermal and morphological properties of FDM fabricated parts for friction welding applications," *Measurement*, vol. 120, pp. 11–20, 2018.

[84] C. Yang, X. Tian, D. Li, Y. Cao, F. Zhao, and C. Shi, "Influence of thermal processing conditions in 3D printing on the crystallinity and mechanical properties of PEEK material," *Journal of Materials Processing Technology*, vol. 248, pp. 1–7, 2017.

[85] B. Suresha, B. N. Ramesh, K. M. Subbaya, and G. Chandramohan, "Mechanical and three-body abrasive wear behavior of carbon-epoxy composite with and without graphite filler," *Journal of Composite Materials*, vol. 44, no. 21, pp. 2509–2519, 2010.

[86] D. B. Shah, K. M. Patel, S. J. Joshi, B. A. Modi, A. I. Patel, and V. Pariyal, "Thermo-mechanical characterization of carbon fiber composites with different epoxy resin systems," *Thermochimica Acta*, vol. 676, pp. 39–46, 2019.

[87] Y. Ming, S. Zhang, W. Han, B. Wang, Y. Duan, and H. Xiao, "Investigation on process parameters of 3D printed continuous carbon fiber-reinforced thermosetting epoxy composites," *Additive Manufacturing*, vol. 33, p. 101184, 2020.

[88] E. Pérez-Pacheco, J. I. Cauich-Cupul, A. Valadez-González, and P. J. Herrera-Franco, "Effect of moisture absorption on the mechanical behavior of carbon fiber/epoxy matrix composites," *Journal of materials science*, vol. 48, no. 5, pp. 1873–1882, 2013.

[89] K. Uhlig, A. Spickenheuer, L. Bittrich, and G. Heinrich, "Development of a highly stressed bladed rotor made of a cfrp using the tailored fiber placement technology," *Mechanics of Composite Materials*, vol. 49, no. 2, pp. 201–210, 2013.

[90] Y. Liu, Y. Guo, J. Zhao, X. Chen, H. Zhang, G. Hu, X. Yu, and Z. Zhang, "Carbon fiber reinforced shape memory epoxy composites with superior mechanical performances," *Composites Science and Technology*, vol. 177, pp. 49–56, 2019.

[91] J. F. Gu¨ lich, "Effect of Reynolds number and surface roughness on the efficiency of centrifugal pumps," *J. Fluids Eng.*, vol. 125, no. 4, pp. 670–679, 2003.

[92] A. Caggiano, "Machining of fibre reinforced plastic composite materials," *Materials*, vol. 11, no. 3, p. 442, 2018.

[93] M. D. Mentzos, A. P. Markopoulos, N. I. Galanis, D. P. Margaris, and D. E. Manolakos, "Design, Numerical Analysis and Manufacture of Radial Pump Impellers with Various Blade Geometries," *Drag Reduction and Velocity Profiles Distribution of Crude Oil Flow in Spiral Pipes*, p. 104, 2015.

[94] F. J. Quail, T. Scanlon, and M. Strickland, "Development of a regenerative pump impeller using rapid manufacturing techniques," *Rapid Prototyping Journal*, 2010.

[95] W. Shi, L. Zhou, W. Lu, B. Pei, and T. Lang, "Numerical prediction and performance experiment in a deep-well centrifugal pump with different impeller outlet width," *Chinese Journal of Mechanical Engineering*, vol. 26, no. 1, pp. 46–52, 2013.

[96] M. R. Khosravani and S. Nasiri, "Injection molding manufacturing process: Review of case-based reasoning applications," *Journal of Intelligent Manufacturing*, vol. 31, no. 4, pp. 847–864, 2020.

[97] J.-M. Kim, S.-H. Chai, M.-H. Yoon, and J.-P. Hong, "Plastic injection molded rotor of concentrated flux-type ferrite magnet motor for dual-clutch transmission," *IEEE Transactions on Magnetics*, vol. 51, no. 11, pp. 1–4, 2015.

[98] K. Bari, "Experimental and simulation performance for fan extraction system," *Global Journal of Research In Engineering*, 2017.

[99] C. Fernandes, A. J. Pontes, J. C. Viana, and A. Gaspar-Cunha, "Modeling and Optimization of the Injection-Molding Process: A Review," *Advances in Polymer Technology*, vol. 37, no. 2, pp. 429–449, 2018.

[100] M. U. Rosli, S. N. A. A. Termizi, C. Y. Khor, M. A. M. Nawi, A. A. Omar, and M. I. Ishak, "Optimisation of Process Parameters in Plastic Injection Moulding Simulation for Blower Impeller's Fan Using Response Surface Methodology," in *Intelligent Manufacturing and Mechatronics*. Springer, 2021, pp. 309–318.

[101] Z. Shen, J. Zheng, D. Hu, W. Meng, and Z. Jiao, "Intelligent Mold Tooling Design with Plastic Injection, CFD and Structural Simulation."

[102] M. Arifin, B. Wahono, E. Junianto, and A. D. Pasek, "Process manufacture rotor radial turboexpander for small scale organic Rankine cycles using selective laser melting machine," *Energy Procedia*, vol. 68, pp. 305–310, 2015.

[103] J. I. A. Dejun, L. I. Fanchun, and Y. ZHAnG, "3D-printing process design of lattice compressor impeller based on residual stress and deformation," *Scientific reports*, vol. 10, no. 1, pp. 1–11, 2020.

[104] H. P. Tang, Q. B. Wang, G. Y. Yang, J. Gu, N. Liu, L. Jia, and M. Qian, "A honeycomb-structured Ti-6Al-4V oil–gas separation rotor additively manufactured by selective electron beam melting for aero-engine applications," *JOM*, vol. 68, no. 3, pp. 799–805, 2016.

[105] X. Tan, Y. Kok, S. B. Tor, and C. K. Chua, "Application of electron beam melting (EBM) in additive manufacturing of an impeller," in *Proceedings of the 1st International Conference on Progress in Additive Manufacturing (Pro-AM 2014)*, 2014, pp. 327–332.

[106] N. Zirak, M. Shirinbayan, M. Deligant, and A. Tcharkhtchi, "Toward Polymeric and Polymer Composites Impeller Fabrication," *Polymers*, vol. 14, no. 1, p. 97, 2022.

[107] I. J. Solomon, P. Sevvel, and J. Gunasekaran, "A review on the various processing parameters in FDM," *Materials Today: Proceedings*, vol. 37, pp. 509–514, 2021.

[108] F. Quail, M. Stickland, and T. Scanlon, "Rapid manufacturing technique used in the development of a regenerative pump impeller," 2009.

[109] G. Priyanka and M. V. Rao, "Design and Additive Manufacturing of Pump Impeller using 3D Printing Technology," *International Journal of Scientific Research in Science, Engineering and Technology*, vol. 4, no. 1, pp. 2394–4099, 2018.

[110] X. Gao, S. Qi, X. Kuang, Y. Su, J. Li, and D. Wang, "Fused filament fabrication of polymer materials: A review of interlayer bond," *Additive Manufacturing*, p. 101658, 2020.

[111] R. Badarinath and V. Prabhu, "Integration and evaluation of robotic fused filament fabrication system," *Additive Manufacturing*, vol. 41, p. 101951, 2021. [Online]. Available: https://www.sciencedirect.com/science/article/pii/S2214860421001160

[112] V. Dikshit, G. D. Goh, A. P. Nagalingam, G. L. Goh, and W. Y. Yeong, "Recent progress in 3D printing of fiber-reinforced composite and nanocomposites," *Fiber-Reinforced Nanocomposites: Fundamentals and Applications*, pp. 371–394, 2020.

[113] G. Budzik, "Properties of made by different methods of RP impeller foundry patterns," *Archives of Foundry Engineering*, vol. 7, no. 2, pp. 83–86, 2007.

[114] W. Przybylski and S. Dzionk, "Impeller pump development using rapid prototyping methods," *Advances in manufacturing science and technology*, vol. 35, no. 1, pp. 15–23, 2011.

[115] A. Manthiram, X. Zhao, and W. Li, "Developments in membranes, catalysts and membrane electrode assemblies for direct methanol fuel cells (DMFCs)," in *Functional materials for sustainable energy applications*. Elsevier, 2012, pp. 312–369.

[116] M. Mieloszyk, A. Andrearczyk, K. Majewska, M. Jurek, and W. Ostachowicz, "Polymeric structure with embedded fiber Bragg grating sensor manufactured using multi-jet printing method," *Measurement*, vol. 166, p. 108229, 2020.

[117] S. Bettermann, R. Stuhr, H.-U. Moritz, and W. Pauer, "Customizable 3D-printed stirrers for investigation, optimization and scale-up processes of batch emulsion copolymerizations," *Chemical Engineering Science*, vol. 206, pp. 50–62, 2019.

[118] A. Çelik, D. Linsky, R. Miezner, A. Kleiman, B. Leizeronok, M. Palman, S. Acarer, and B. Cukurel, "Design Methodology and Concept Demonstration of Preassembled Additively Manufactured Turbomachinery Systems: Case Study of Turbocharger Based Medical Ventilators," *Journal of Engineering for Gas Turbines and Power*, vol. 144, no. 12, p. 121010, 2022.

[119] J. P. Bons, "A review of surface roughness effects in gas turbines," 2010.

[120] C. Liu, Y. Cao, S. Ding, W. Zhang, Y. Cai, and A. Lin, "Effects of blade surface roughness on compressor performance and tonal noise emission in a marine diesel engine turbocharger," *Proceedings of the Institution of Mechanical Engineers, Part D: Journal of Automobile Engineering*, vol. 234, no. 14, pp. 3476–3490, 2020.

[121] P. R. Gradl, D. C. Tinker, J. Ivester, S. W. Skinner, T. Teasley, and J. L. Bili, "Geometric feature reproducibility for laser powder bed fusion (L-PBF) additive manufacturing with Inconel 718," *Additive Manufacturing*, vol. 47, p. 102305, 2021.

[122] E. Umaras and M. S. G. Tsuzuki, "Additive manufacturing-considerations on geometric accuracy and factors of influence," *IFAC-PapersOnLine*, vol. 50, no. 1, pp. 14 940–14 945, 2017.

[123] R. Paul and S. Anand, "Optimal part orientation in Rapid Manufacturing process for achieving geometric tolerances," *Journal of Manufacturing Systems*, vol. 30, no. 4, pp. 214–222, 2011.

[124] G. Budzik, J. Woźniak, A. Paszkiewicz, Ł. Przeszłowski, T. Dziubek, and M. Dębski, "Methodology for the quality control process of additive manufacturing products made of polymer materials," *Materials*, vol. 14, no. 9, p. 2202, 2021.

[125] T. D. Ngo, A. Kashani, G. Imbalzano, K. T. Q. Nguyen, and D. Hui, "Additive manufacturing (3D printing): A review of materials, methods, applications and challenges," *Composites Part B: Engineering*, vol. 143, pp. 172–196, 2018.

[126] S. A. M. Tofail, E. P. Koumoulos, A. Bandyopadhyay, S. Bose, L. O'Donoghue, and C. Charitidis, "Additive manufacturing: scientific and technological challenges, market uptake and opportunities," *Materials today*, vol. 21, no. 1, pp. 22–37, 2018.

[127] P. Chennakesava and Y. S. Narayan, "Fused deposition modeling-insights," in *Proceedings of the*

international conference on advances in design and manufacturing ICADM, vol. 14, 2014, p. 1345.

[128] K. Özsoy, "A Comparative Finite Element Stress Analysis Of Isotropic Matrix And 3D Printed PLA Material," in *Proceedings on 2nd International Conference on Technology and Science*, 2019.

[129] J. Butt and R. Bhaskar, "Investigating the effects of annealing on the mechanical properties of FFF-printed thermoplastics," *Journal of Manufacturing and Materials Processing*, vol. 4, no. 2, p. 38, 2020.

[130] N. Vidakis, M. Petousis, L. Tzounis, A. Maniadi, E. Velidakis, N. Mountakis, and J. D. Kechagias, "Sustainable additive manufacturing: Mechanical response of polyamide 12 over multiple recycling processes," *Materials*, vol. 14, no. 2, p. 466, 2021.

[131] S. C. Daminabo, S. Goel, S. A. Grammatikos, H. Y. Nezhad, and V. K. Thakur, "Fused deposition modeling-based additive manufacturing (3D printing): techniques for polymer material systems," *Materials today chemistry*, vol. 16, p. 100248, 2020.

[132] B. N. Turner, R. Strong, and S. A. Gold, "A review of melt extrusion additive manufacturing processes: I. Process design and modeling," *Rapid prototyping journal*, vol. 20, no. 3, pp. 192–204, 2014.

[133] A. E. Tontowi, L. Ramdani, R. V. Erdizon, and D. K. Baroroh, "Optimization of 3D-printer process parameters for improving quality of polylactic acid printed part," *International Journal of Engineering and Technology*, vol. 9, no. 2, pp. 589–600, 2017.

[134] R. Wool and K. M. O'connor, "A theory crack healing in polymers," *Journal of applied physics*, vol. 52, no. 10, pp. 5953–5963, 1981.

[135] R. P. Wool, B. Yuan, and O. J. McGarel, "Welding of polymer interfaces," *Polymer Engineering Science*, vol. 29, no. 19, pp. 1340–1367, 1989.

[136] L. J. Bastien and J. W. Gillespie Jr, "A non-isothermal healing model for strength and toughness of fusion bonded joints of amorphous thermoplastics," *Polymer Engineering Science*, vol. 31, no. 24, pp. 1720–1730, 1991.

[137] F. Yang and R. Pitchumani, "Healing of thermoplastic polymers at an interface under nonisothermal conditions," *Macromolecules*, vol. 35, no. 8, pp. 3213–3224, 2002.

[138] J. Yin, C. Lu, J. Fu, Y. Huang, and Y. Zheng, "Interfacial bonding during multi-material fused deposition modeling (FDM) process due to inter-molecular diffusion," *Materials & Design*, vol. 150, pp. 104–112, 2018.

[139] T. J. Coogan and D. O. Kazmer, "Healing simulation for bond strength prediction of FDM," *Rapid Prototyping Journal*, 2017.

[140] Y. S. Ko, D. Herrmann, O. Tolar, W. J. Elspass, and C. Brändli, "Improving the filament weld-strength of fused filament fabrication products through improved interdiffusion," *Additive Manufacturing*, vol. 29, p. 100815, 2019.

[141] X. Lacambra-Andreu, X. P. Morelle, A. Maazouz, J.-M. Chenal, and K. Lamnawar, "Rheological investigation and modeling of healing properties during extrusion-based 3D printing of poly (lactic-acid)," *Rheologica Acta*, vol. 62, no. 1, pp. 31–44, 2023.

[142] X. Gao, S. Qi, X. Kuang, Y. Su, J. Li, and D. Wang, "Fused filament fabrication of polymer materials: A review of interlayer bond," *Additive Manufacturing*, vol. 37, p. 101658, 2021.

[143] N. von Windheim, D. W. Collinson, T. Lau, L. C. Brinson, and K. Gall, "The influence of porosity, crystallinity and interlayer adhesion on the tensile strength of 3D printed polylactic acid (PLA)," *Rapid Prototyping Journal*, vol. 27, no. 7, pp. 1327–1336, 2021.

[144] D. W. Collinson, N. von Windheim, K. Gall, and L. C. Brinson, "Direct evidence of interfacial crystallization preventing weld formation during fused filament fabrication of poly (ether ether ketone)," *Additive Manufacturing*, vol. 51, p. 102604, 2022.

[145] A. Andrearczyk and G. Żywica, "A concept of a test stand for the investigation of a 3d printed turbochargers and selected fluid-flow machinery," *Transactions of the Institute of Fluid-Flow Machinery*, no. 133, pp. 3–11, 2016.

[146] A. Andrearczyk, P. Bagiński, and P. Klonowicz, "Numerical and experimental investigations of a turbocharger with a compressor wheel made of additively manufactured plastic," *International Journal of Mechanical Sciences*, vol. 178, p. 105613, 2020.

[147] K. M. Khalil, S. Mahmoud, and R. K. Al- Dadah, "Experimental and numerical investigation of blade height effects on micro-scale axial turbines performance using compressed air open cycle," *Energy*, vol. 211, p. 118660, 2020. [Online]. Available: https://www.sciencedirect.com/science/article/pii/S0360544220317680

[148] J. Y. H. Fuh, L. Lu, C. C. Tan, Z. X. Shen, and S. Chew, "Processing and characterising photosensitive polymer in the rapid prototyping process," *Journal of Materials Processing Technology*, vol. 89, pp. 211–217, 1999.

[149] G. V. Salmoria, C. H. Ahrens, M. Fredel, V. Soldi, and A. T. N. Pires, "Stereolithography somos 7110 resin: mechanical behavior and fractography of parts post-cured by different methods," *Polymer Testing*, vol. 24, no. 2, pp. 157–162, 2005.

[150] C. Decker, "High-speed curing by laser irradiation," *Nuclear Instruments and Methods in Physics Research Section B: Beam Interactions with Materials and Atoms*, vol. 151, no. 1-4, pp. 22–28, 1999.

[151] A. Bagheri and J. Jin, "Photopolymerization in 3D printing," *ACS Applied Polymer Materials*, vol. 1, no. 4, pp. 593–611, 2019.

[152] G. V. Salmoria, C. H. Ahrens, V. E. Beal, A. T. N. Pires, and V. Soldi, "Evaluation of post-curing and laser manufacturing parameters on the properties of SOMOS 7110 photosensitive resin used in stereolithography," *Materials Design*, vol. 30, no. 3, pp. 758–763, 2009.

[153] Y. Deng, J. Li, Z. He, J. Hong, and J. Bao, "Urethane acrylate-based photosensitive resin for three-dimensional printing of stereolithographic elastomer," *Journal of Applied Polymer Science*, vol. 137, no. 42, p. 49294, 2020.

[154] C. M. Cheah, A. Y. C. Nee, J. Y. H. Fuh, L. Lu, Y. S. Choo, and T. Miyazawa, "Characteristics of photopolymeric material used in rapid prototypes Part I. Mechanical properties in the green state," *Journal of Materials Processing Technology*, vol. 67, no. 1-3, pp. 41–45, 1997.

[155] J. Martín-Montal, J. Pernas-Sánchez, and D. Varas, "Experimental Characterization Framework for SLA Additive Manufacturing Materials," *Polymers*, vol. 13, no. 7, p. 1147, 2021.

[156] R. Hague, S. Mansour, N. Saleh, and R. Harris, "Materials analysis of stereolithography resins for use in rapid manufacturing," *Journal of materials science*, vol. 39, no. 7, pp. 2457–2464, 2004.

[157] D. S. Kumar, M. J. Shukla, K. K. Mahato, D. K. Rathore, R. K. Prusty, and B. C. Ray, "Effect of post-curing on thermal and mechanical behavior of GFRP composites," in *IOP conference series: materials science and engineering*, vol. 75, no. 1. IOP Publishing, 2015, p. 12012.

[158] A. C. Uzcategui, A. Muralidharan, V. L. Ferguson, S. J. Bryant, and R. R. McLeod, "Understanding and improving mechanical properties in 3D printed parts using a dual-cure acrylate-based resin for stereolithography," *Advanced engineering materials*, vol. 20, no. 12, p. 1800876, 2018.

[159] J. Zhao, Y. Yang, and L. Li, "A comprehensive evaluation for different post-curing methods used in stereolithography additive manufacturing," *Journal of Manufacturing Processes*, vol. 56, pp. 867–877, 2020.

[160] Y. Yang, T. Wang, S. Wang, X. Cong, S. Zhang, M. Zhang, J. Luan, and G. Wang, "Strong Interface Construction of Carbon Fiber–reinforced PEEK Composites: An Efficient Method for Modifying Carbon Fiber with Crystalline PEEK," *Macromolecular rapid communications*, vol. 41, no. 24, p. 2000001, 2020.

[161] R. Gauvin, Y.-C. Chen, J. W. Lee, P. Soman, P. Zorlutuna, J. W. Nichol, H. Bae, S. Chen, and A. Khademhosseini, "Microfabrication of complex porous tissue engineering scaffolds using 3D projection stereolithography," *Biomaterials*, vol. 33, no. 15, pp. 3824–3834, 2012.

[162] B. Wang, G. Ding, K. Chen, S. Jia, J. Wei, Y. Wang, R. He, and Z. Shao, "A physical and chemical double enhancement strategy for 3D printing of cellulose reinforced nanocomposite," *Journal of Applied Polymer Science*, vol. 137, no. 39, p. 49164, 2020.

[163] A. Chiappone, F. Bella, J. R. Nair, G. Meligrana, R. Bongiovanni, and C. Gerbaldi, "Structure–performance correlation of nanocellulose-based polymer electrolytes for efficient quasi-solid DSSCs," *ChemElectroChem*, vol. 1, no. 8, pp. 1350–1358, 2014.

[164] M. P. Watters and M. L. Bernhardt, "Curing parameters to improve the mechanical properties of stereolithographic printed specimens," *Rapid Prototyping Journal*, 2018.

[165] D. Mourtzis, M. Doukas, and D. Bernidaki, "Simulation in manufacturing: Review and challenges," *Procedia Cirp*, vol. 25, pp. 213–229, 2014.

[166] D. S. Delhelay, "Nonlinear finite element analysis of the coupled thermomechanical behaviour of turbine disc assemblies," 2001.

[167] P. Dowson, D. Bauer, and S. Laney, "Selection of materials and material related processes for centrifugal compressors and steam turbines in the oil and petrochemical industry," in *Proceedings of the 37th turbomachinery symposium*. Texas AM University. Turbomachinery Laboratories, 2008.

[168] R. M. Hannun, H. I. Radhi, and N. A. Essi, "The types of mechanical and thermal stresses on the first stage rotor blade of a turbine," *Revista Innovaciencia*, vol. 7, no. 1, pp. 1–11, 2019.

[169] N. A. Essi, R. M. Hunnun, and H. I. Radhi, "Prediction of mechanical stresses of single rotor blade of low pressure of Nasiriya power plant steam turbine," *University of Thi-Qar Journal for Engineering Sciences*, vol. 10, no. 1, pp. 71–78, 2019.

[170] X. Zheng and C. Ding, "Effect of temperature and pressure on stress of impeller in axial-centrifugal combined compressor," *Advances in Mechanical Engineering*, vol. 8, no. 6, p. 1687814016653547, 2016.

[171] F.-K. Benra, H. J. Dohmen, J. Pei, S. Schuster, and B. Wan, "A comparison of one-way and two-way coupling methods for numerical analysis of fluid-structure interactions," *Journal of applied mathematics*, vol. 2011, 2011.

[172] S. B. Pope, "Turbulent flows," 2001.

[173] E. M. V. Siggeirsson and S. Gunnarsson, "Conceptual design tool for radial turbines," *Printed by Chalmers University of Technology Repro-service Gothenburg, Sweden*, 2015.

[174] T. Gresh, *Compressor performance: aerodynamics for the user*. Butterworth-Heinemann, 2018.

[175] K. C. Thin, M. M. Khaing, and K. M. Aye, "Design and performance analysis of centrifugal pump," *World Academy of Science, Engineering and Technology*, vol. 46, no. 1, pp. 422–429, 2008.

[176] M. Mojaddam and S. A. M. Torshizi, "Design and optimization of meridional profiles for the impeller of centrifugal compressors," *Journal of Mechanical Science and Technology*, vol. 31, no. 10, pp. 4853–4861, 2017.

[177] J. Li, L. Tang, and Y. Zhang, "The influence of blade angle on the performance of plastic centrifugal pump," *Advances in Materials Science and Engineering*, vol. 2020, 2020.

[178] R. DiPippo, "Chapter 8 - Binary Cycle Power Plants," in *Geothermal Power Plants (Fourth Edition)*, fourth edi ed., R. DiPippo, Ed. Oxford: Butterworth-Heinemann, 2016, pp. 193–239. [Online]. Available: https://www.sciencedirect.com/science/article/pii/B9780081008799000082

[179] S. Sharma, A. Broatch, J. García-Tíscar, J. M. Allport, and A. K. Nickson, "Acoustic characterisation of a small high-speed centrifugal compressor with casing treatment: An experimental study," *Aerospace Science and Technology*, vol. 95, p. 105518, 2019.

[180] J. Sun, Z. Zuo, Q. Liang, X. Zhou, W. Guo, and H. Chen, "Theoretical and experimental study on effects of Humidity on Centrifugal compressor performance," *Applied Thermal Engineering*, vol. 174, p. 115300, 2020.

[181] N. T. Quyet, "Evaluation of spring-mass-damping models of mistuned turbomachine impellers to analyse vibration and fatigue life," , vol. 24, no. 4 (153), 2020.

[182] O. Matsushita, M. Tanaka, H. Kanki, M. Kobayashi, and P. Keogh, *Vibrations of rotating machinery*. Springer, 2017.

[183] K. C. More, S. Dongre, and G. P. Deshmukh, "Experimental and numerical analysis of vibrations in impeller of centrifugal blower," *SN Applied Sciences*, vol. 2, no. 1, pp. 1–14, 2020.

[184] S. Barone, P. Neri, A. Paoli, and A. V. Razionale, "Low-frame-rate single camera system for 3D full-field high-frequency vibration measurements," *Mechanical Systems and Signal Processing*, vol. 123, pp. 143–152, 2019.

[185] G. Mousmoulis, N. Karlsen-Davies, G. Aggidis, I. Anagnostopoulos, and D. Papantonis, "Experimental analysis of cavitation in a centrifugal pump using acoustic emission, vibration measurements and flow visualization," *European Journal of Mechanics-B/Fluids*, vol. 75, pp. 300–311, 2019.

[186] L. W. McKeen, *Fatigue and tribological properties of plastics and elastomers.* William Andrew, 2016.

[187] S. Kumar and K. K. Singh, "Tribological behaviour of fibre-reinforced thermoset polymer composites: A review," *Proceedings of the Institution of Mechanical Engineers, Part L: Journal of Materials: Design and Applications*, vol. 234, no. 11, pp. 1439–1449, 2020.

[188] S. Abazariyan, R. Rafee, and S. Derakhshan, "Experimental study of viscosity effects on a pump as turbine performance," *Renewable Energy*, vol. 127, pp. 539–547, 2018.

[189] S. Jia, D. Yu, Y. Zhu, Z. Wang, L. Chen, and L. Fu, "Morphology, crystallization and thermal behaviors of PLA-based composites: wonderful effects of hybrid GO/PEG via dynamic impregnating," *Polymers*, vol. 9, no. 10, p. 528, 2017.

[190] B. Monge Brenes, "Design of supercritical carbon dioxide centrifugal compressors," 2014.

[191] R. H. Aungier, "Mean streamline aerodynamic performance analysis of centrifugal compressors," 1995.

[192] J. E. Coppage and F. Dallenbach, "Study of supersonic radial compressors for refrigeration and pressurization systems," Tech. Rep., 1956.

[193] W. Jansen, "A method for calculating the flow in a centrifugal impeller when entropy gradient are present," *Inst. Mech. Eng. Internal Aerodynamics*, 1970.

[194] J. P. Johnston and R. C. Dean Jr, "Losses in vaneless diffusers of centrifugal compressors and pumps: analysis, experiment, and design," 1966.

[195] J. W. Daily and R. E. Nece, "Chamber dimension effects on induced flow and frictional resistance of enclosed rotating disks," 1960.

[196] H. W. Oh, E. S. Yoon, and M. K. Chung, "An optimum set of loss models for performance prediction of centrifugal compressors," *Proceedings of the Institution of Mechanical Engineers, Part A: Journal of Power and Energy*, vol. 211, no. 4, pp. 331–338, 1997.

[197] F. Kawai, "Polylactic acid (PLA)-degrading microorganisms and PLA depolymerases," in *Green Polymer Chemistry: Biocatalysis and Biomaterials.* ACS Publications, 2010, pp. 405–414.

[198] A. J. Müller, M. Avila, G. Saenz, and J. Salazar, "Crystallization of PLA-based Materials," *Poly (lactic acid) science and technology: processing, properties, additives and applications*, vol. 2015, 2015.

[199] A. Gregorova, "Application of differential scanning calorimetry to the characterization of biopolymers," *Applications of Calorimetry in a Wide Context-Differential Scanning Calorimetry, Isothermal Titration Calorimetry and Microcalorimetry*, pp. 3–20, 2013.

[200] J. R. Riba, J. Cailloux, R. Cantero, T. Canals, and M. L. Maspoch, "Multivariable methods applied to FTIR: A powerful technique to highlight architectural changes in poly (lactic acid)," *Polymer Testing*, vol. 65, pp. 264–269, 2018.

[201] R. Xu, J. Xie, and C. Lei, "Influence of melt-draw ratio on the crystalline behaviour of a polylactic acid cast film with a chi structure," *RSC advances*, vol. 7, no. 63, pp. 39 914–39 921, 2017.

[202] M. F. Talbott, G. S. Springer, and L. A. Berglund, "The effects of crystallinity on the mechanical properties of PEEK polymer and graphite fiber reinforced PEEK," *Journal of Composite Materials*, vol. 21, no. 11, pp. 1056–1081, 1987.

[203] W. Brostow, "Dynamic Mechanical Analysis: a practical introduction," 2007.

[204] M. Rubinstein and R. H. Colby, *Polymer physics*. Oxford university press New York, 2003, vol. 23.

[205] C. McIlroy and P. D. Olmsted, "Deformation of an amorphous polymer during the fused-filament-fabrication method for additive manufacturing," *Journal of Rheology*, vol. 61, no. 2, pp. 379–397, 2017.

[206] M. L. Williams, R. F. Landel, and J. D. Ferry, "The temperature dependence of relaxation mechanisms in amorphous polymers and other glass-forming liquids," *Journal of the American Chemical society*, vol. 77, no. 14, pp. 3701–3707, 1955.

[207] S. Qi, X. Gao, Y. Su, X. Dong, D. Cavallo, and D. Wang, "Correlation between welding behavior and mechanical anisotropy of long chain polyamide 12 manufactured with fused filament fabrication," *Polymer*, vol. 213, p. 123318, 2021.

[208] L.-C. Chuang and H.-T. Young, "Integrated rough machining methodology for centrifugal impeller manufacturing," *The International Journal of Advanced Manufacturing Technology*, vol. 34, no. 11, pp. 1062–1071, 2007.

[209] H.-T. Young, L.-C. Chuang, K. Gerschwiler, and S. Kamps, "A five-axis rough machining approach for a centrifugal impeller," *The International Journal of Advanced Manufacturing Technology*, vol. 23, no. 3, pp. 233–239, 2004.

[210] A. Boschetto and L. Bottini, "Accuracy prediction in fused deposition modeling," *The international journal of advanced manufacturing technology*, vol. 73, no. 5, pp. 913–928, 2014.

[211] S. Singh, S. Ramakrishna, and R. Singh, "Material issues in additive manufacturing: A review," *Journal of Manufacturing Processes*, vol. 25, pp. 185–200, 2017.

[212] M. Lebedevaite, J. Ostrauskaite, E. Skliutas, and M. Malinauskas, "Photoinitiator free resins composed of plant-derived monomers for the optical μ-3d printing of thermosets," *Polymers*, vol. 11, no. 1, p. 116, 2019.

[213] D. Kunwong, N. Sumanochitraporn, and S. Kaewpirom, "Curing behavior of a UV-curable coating based on urethane acrylate oligomer: the influence of reactive monomers," *Sonklanakarin Journal of Science and Technology*, vol. 33, no. 2, p. 201, 2011.

[214] A. Barkane, O. Platnieks, M. Jurinovs, and S. Gaidukovs, "Thermal stability of UV-cured vegetable oil epoxidized acrylate-based polymer system for 3D printing application," *Polymer Degradation and Stability*, vol. 181, p. 109347, 2020.

[215] Q. Alsandi, M. Ikeda, Y. Arisaka, T. Nikaido, Y. Tsuchida, A. Sadr, N. Yui, and J. Tagami, "Evaluation of Mechanical and Physical Properties of Light and Heat Polymerized UDMA for DLP 3D Printer," *Sensors*, vol. 21, no. 10, p. 3331, 2021.

[216] T. Zhao, R. Yu, X. Li, Y. Zhang, X. Yang, X. Zhao, and W. Huang, "A comparative study on 3D printed silicone-epoxy/acrylate hybrid polymers via pure photopolymerization and dual-curing mechanisms," *Journal of Materials Science*, vol. 54, no. 6, pp. 5101–5111, 2019.

[217] T. Buruiana, V. Melinte, L. Stroea, and E. C. Buruiana, "Urethane dimethacrylates with car-

boxylic groups as potential dental monomers. synthesis and properties," *Polymer journal*, vol. 41, no. 11, pp. 978–987, 2009.

[218] F. L. B. Amaral, V. Colucci, R. G. PALMA-DIBB, and S. A. M. Corona, "Assessment of in vitro methods used to promote adhesive interface degradation: a critical review," *Journal of Esthetic and Restorative Dentistry*, vol. 19, no. 6, pp. 340–353, 2007.

[219] O. Konuray, J. M. Salla, J. M. Morancho, X. Fernández-Francos, M. García-Alvarez, and X. Ramis, "Curing kinetics of acrylate-based and 3D printable IPNs," *Thermochimica Acta*, vol. 692, p. 178754, 2020.

[220] C. Mendes-Felipe, D. Patrocinio, J. M. Laza, L. Ruiz-Rubio, and J. L. Vilas-Vilela, "Evaluation of postcuring process on the thermal and mechanical properties of the Clear02™ resin used in stereolithography," *Polymer Testing*, vol. 72, pp. 115–121, 2018.

[221] S. Gaidukovs, A. Medvids, P. Onufrijevs, and L. Grase, "UV-light-induced curing of branched epoxy novolac resin for coatings." *Express Polymer Letters*, vol. 12, no. 10, 2018.

[222] D. Kunwong, N. Sumanochitraporn, and S. Kaewpirom, "Curing behavior of a UV-curable coating based on urethane acrylate oligomer: the influence of reactive monomers," *Sonklanakarin Journal of Science and Technology*, vol. 33, no. 2, p. 201, 2011.

[223] Z. Li, X. Yang, L. Wu, Z. Chen, Y. Lin, K. Xu, and G. Q. Chen, "Synthesis, characterization and biocompatibility of biodegradable elastomeric poly(ether-ester urethane)s based on poly(3-hydroxybutyrate-co-3- hydroxyhexanoate) and poly(ethylene glycol) via melting polymerization," *Journal of Biomaterials Science, Polymer Edition*, vol. 20, no. 9, pp. 1179–1202, 2009.

[224] H. Pelletier, N. Belgacem, and A. Gandini, "Acrylated vegetable oils as photocrosslinkable materials," *Journal of applied polymer science*, vol. 99, no. 6, pp. 3218–3221, 2006.

[225] C. Dall'Argine, A. Hochwallner, N. Klikovits, R. Liska, J. Stampf, and M. Sangermano, "Hot-Lithography SLA-3D Printing of Epoxy Resin," *Macromolecular Materials and Engineering*, vol. 305, no. 10, p. 2000325, 2020.

[226] K. Yang, Y. Wu, and F. Huang, "Numerical simulations of microcrack-related damage and ignition behavior of mild-impacted polymer bonded explosives," *Journal of hazardous materials*, vol. 356, pp. 34–52, 2018.

[227] A. Ji, S. Zhang, S. Bhagia, C. G. Yoo, and A. J. Ragauskas, "3D printing of biomass-derived composites: application and characterization approaches," *RSC Advances*, vol. 10, no. 37, pp. 21 698–21 723, 2020.

[228] R. P. White and J. E. G. Lipson, "Polymer free volume and its connection to the glass transition," *Macromolecules*, vol. 49, no. 11, pp. 3987–4007, 2016.

[229] G. Li, P. Lee-Sullivan, and R. Thring, "Determination of activation energy for glass transition of an epoxy adhesive using dynamic mechanical analysis," *Journal of thermal analysis and calorimetry*, vol. 60, no. 2, pp. 377–390, 2000.

[230] D. Bird, E. Caravaca, J. Laquidara, K. Luhmann, and N. M. Ravindra, "Formulation of Curable Resins Utilized in Stereolithography," in *TMS 2019 148th Annual Meeting Exhibition Supplemental Proceedings*. Springer, 2019, pp. 1575–1587.

[231] D. Ambrosio, X. Gabrion, P. Malecot, F. Amiot, and S. Thibaud, "Influence of manufacturing parameters on the mechanical properties of projection stereolithography–manufactured specimens," *The International Journal of Advanced Manufacturing Technology*, vol. 106, no. 1, pp. 265–277, 2020.

[232] J. R. C. Dizon, A. H. Espera Jr, Q. Chen, and R. C. Advincula, "Mechanical characterization of 3D-printed polymers," *Additive Manufacturing*, vol. 20, pp. 44–67, 2018.

[233] Z. Weng, Y. Zhou, W. Lin, T. Senthil, and L. Wu, "Structure-property relationship of nano enhanced stereolithography resin for desktop SLA 3D printer," *Composites Part A: Applied Science and Manufacturing*, vol. 88, pp. 234–242, 2016.

[234] J. S. Saini, L. Dowling, J. Kennedy, and D. Trimble, "Investigations of the mechanical properties on different print orientations in SLA 3D printed resin," *Proceedings of the Institution of Mechanical Engineers, Part C: Journal of Mechanical Engineering Science*, vol. 234, no. 11, pp. 2279–2293, 2020.

[235] S. V. Asmussen, G. F. Arenas, and C. I. Vallo, "Enhanced degree of polymerization of methacrylate and epoxy resins by plasmonic heating of embedded silver nanoparticles," *Progress in Organic Coatings*, vol. 88, pp. 220–227, 2015.

[236] H.-n. Zhang, H. Chang, X.-j. Li, X.-g. Wu, and Q.-w. He, "The effect of strain rate on compressive behavior and failure mechanism of CMDB propellant," *Defence Technology*, vol. 18, no. 3, pp. 467–475, 2022.

Annexe A

List of the publications

Related to thesis

• **Zirak N**, Shirinbayan M, Deligant M, Tcharkhtchi A. Toward polymeric and polymer composites impeller fabrication. Polymers. 2021 Dec 28;14(1):97.

• **Zirak N**, Benfriha K, Shakeri Z, Shirinbayan M, Fitoussi J, Tcharkhtchi A. Interlayer bonding improvement and optimization of printing parameters of FFF polyphenylene sulfide parts using GRA method. Progress in Additive Manufacturing. 2023 Jun 18:1-2.

• **Zirak N**, Shirinbayan M, Benfriha K, Deligant M, Tcharkhtchi A. Stereolithography of (meth) acrylate-based photocurable resin: thermal and mechanical properties. Journal of Applied Polymer Science. 2022 Jun 10;139(22):52248.

• Shirinbayan M, **Zirak N**, Saddaoui O, Mammeri A, Azzouz K, Benfriha K, Tcharkhtchi A, Fitoussi J. Effect of build orientation and post-curing of (meth) acrylate-based photocurable resin fabricated by stereolithography on the mechanical behavior from quasi-static to high strain rate loadings. The International Journal of Advanced Manufacturing Technology. 2022 Nov;123(5-6):1877-87.

• **Zirak N**, Nguyen V T, Deligant M, Shirinbayan M, Danlos A, Żywica G, Henner M, Benevides R, Bakir F, Tcharkhtchi A. Numerical and experimental investigation of a centrifugal compressor: prospects of polymer additive manufacturing. Journal of Process Mechanical Engineering, Part E. Revised.

Other articles

• **Zirak N**, Tcharkhtchi A. Fatigue life prediction for amorphous glassy polymers based on cumulative evolution of micro-defects. International Journal of Fatigue. 2023 Feb 1;167:107360.

• Tcharkhtchi A, Villalonga S, **Zirak N**, Lucas A, Farzaneh S, Shirinbayan M. Optimal dome design for 700 bar hydrogen tank type IV: hyperelliptic functions and shape factor. Energy Storage.:e469.

• Tcharkhtchi A, Abbasnezhad N, Seydani MZ, **Zirak N**, Farzaneh S, Shirinbayan M. An overview of filtration efficiency through the masks: Mechanisms of the aerosols penetration. Bioactive materials. 2021 Jan 1;6(1):106-22.

• **Zirak N**, Maadani AM, Salahinejad E, Abbasnezhad N, Shirinbayan M. Fabrication, drug delivery kinetics and cell viability assay of PLGA-coated vancomycin-loaded silicate porous microspheres. Ceramics International. 2022 Jan 1;48(1):48-54.

• Abbasnezhad N, **Zirak N**, Shirinbayan M, Tcharkhtchi A, Bakir F. On the importance of physical and mechanical properties of PLGA films during drug release. Journal of Drug Delivery Science and Technology. 2021 Jun 1;63:102446.

Congress

Zirak N, Nguyen V T, Deligant M, Shirinbayan M, Tcharkhtchi A. Etude préliminaire de l'influence du procédé et des paramètres d'impression 3D sur la précision et la tenue mécanique d'un rotor de compresseur centrifuge. 25ème Congrès Français de Mécanique, Nantes, France.

Annexe B

Résumé de thèse

Optimisation de la réalisation d'un élément de compresseur / Etude de l'interaction entre la microstructure du matériau, le procédé de transformation et la performance du produit fin

B.1 Introduction

En particulier, la fonction d'un compresseur peut être définie comme un système pour comprimer et augmenter la pression du liquide de travail. Fournir de l'air pour la combustion, l'air comprimé pour l'application dans les outils pneumatiques, le processus de transport du liquide par les pipelines et un certain processus pour le processus de circulation du fluide parmi les objectifs de l'utilisation de compresseurs sont mentionnés. Les moteurs de turbojet utilisés dans la propulsion aérospatiale, la production d'électricité utilisant des turbines à gaz industrielles, la turbocompresseur de moteurs à combustion interne et la pressurisation du gaz et des fluides dans l'industrie des processus sont les exemples qui ont attiré beaucoup d'attention parmi les études [3]. Généralement, les compresseurs

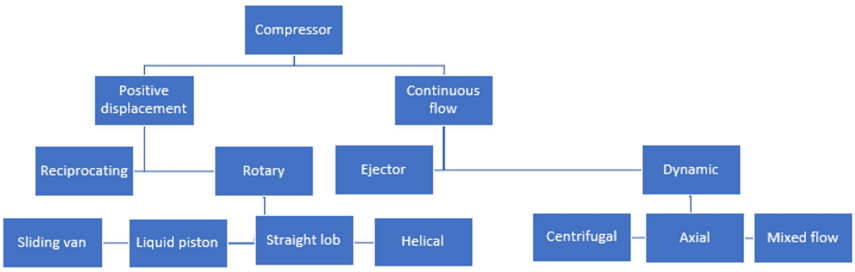

FIGURE B.1 – Catégories de compresseurs

peuvent être divisés en deux catégories de déplacement positif et d'écoulement continu. Les différentes catégories de compresseurs sont présentées dans la figure B.1. Les compresseurs de déplacement positifs sont des compresseurs dans lesquels un ou plusieurs volumes diminuent et augmentent cinématiquement. En d'autres termes, dans ces compresseurs, la limitation successive du volume de fluide augmente la pression du fluide qui peut être utilisée pour l'écoulement intermittent dans un espace fermé. Les compresseurs de déplacement positifs ont été divisés en deux types: soit alternatif ou rotatif. La pression dans le compresseur alternatif a augmenté en alternant le mouvement d'un piston dans le cylindre. Dans les compresseurs de déplacement positifs rotatifs, la compression et le déplacement se produisent par des éléments rotatifs. La galette coulissante, le piston liquide, le lobe droit et le lobe hélicoïdal sont les subdivides de déplacement positif rotatif [4].

Les compresseurs de type à flux continu sont les compresseurs avec la capacité de convertir la vitesse du mélange de liquide d'entrée fermé par un gaz ou un jet à vapeur à grande vitesse en pression dans le diffuseur pour comprimer le fluide. Les compresseurs dynamiques et éjecteurs sont la classe de cette catégorie. Dans un compresseur dynamique augmentant la pression fourni en convertissant la vitesse du fluide qui a été causée par un élément de rotation à la pression. Le centrifuge, le flux axial

et le flux mixte sont répertoriés dans cette catégorie de compresseurs. Il convient de noter que le type de gaz d'écoulement créé dans le flux centrifuge, axial et mixte est radial, et axial et combine certaines caractéristiques de l'écoulement centrifuge et axial, respectivement [5]. Comme mentionné, il existe de nombreuses catégories de compresseurs existants et la sélection de compresseurs en fonction de la situation sera différente. Les coûts de maintenance faibles, la taille compacte et le poids approprié sont parmi les propriétés importantes du compresseur centrifuge qui a conduit à sa différenciation des autres compresseurs. En général, les compresseurs à débit axial sont utilisés pour fournir des débits élevés et des rapports à basse pression. L'efficacité des compresseurs à flux axial est plus que celle des compresseurs centrifuges; Cependant, les compresseurs axiaux ont montré une région de fonctionnement plus petite. Les compresseurs centrifuges sont utilisés à des débits moyens et à des ratios à haute pression qui sont très efficaces dans cette situation. Dans les débits faibles et les ratios à haute pression, le rotatif et la récipient, les compresseurs sont généralement appliqués [5,6]. Les compresseurs centrifuges ont été l'un des compresseurs les plus applicables de l'industrie. Certaines des propriétés importantes de ce type sont données ci-dessous:

- Un fonctionnement en douceur,
- Grande tolérance pour les fluctuations de processus,
- Fiabilité plus élevée par rapport aux autres types de compresseurs,
- Capacité à travailler avec des gaz avec un faible poids moléculaire.

La pression de sortie des compresseurs centrifuges jusqu'à 70 MPa a été signalée. Généralement, l'entraînement de ce type de turbine à gaz compresseur ou de moteur électrique qui, dans certains

cas, tel que les applications en aval, les turbines à vapeur ou les turboexpanders peut être utilisée. La vitesse de fonctionnement dans les compresseurs centrifuges peut être constituée de divers sondages, par exemple dans le cas des applications d'aéronefs et d'espace se situe entre 50 000 à 100 000 tr / min. Dans le cas des demandes de transmission de gaz, 8 000 à 14 000 tr / min ont été signalés [7].

Les roues à aubes sont considérées comme un élément clé des turbomachines [1]. La roue en rotation rapide peut forcer le fluide de travail en convertissant la vitesse du fluide en pression [2]. Compte tenu de l'utilisation des roues dans différents systèmes de machines rotatives, elles ont été utilisées comme l'une des pièces les plus importantes pour diverses applications dans des domaines tels que l'aérospatiale [3], l'automobile [4] et le médical [5]. L'amélioration de l'efficacité du système par les roues a fait l'objet de nombreuses études [6]. A cette fin et de manière générale, des études basées sur l'optimisation de la géométrie, utilisant des matériaux hautes performances et un procédé de fabrication adapté ont été tentées pour améliorer le système. L'utilisation de matériaux plus légers à haute résistance avec une grande capacité de résistance aux forces pendant le travail est considérée comme une étape essentielle pour augmenter l'efficacité [7] du compresseur. Les matériaux métalliques [8], polymères [9] et composites [10] sont les principales catégories de matériaux qui ont été utilisés pour la fabrication de rotors et de roues. Le poids élevé des métaux, qui entraîne une diminution de l'efficacité, a été l'un des principaux inconvénients de ceux-ci. De plus, le coût élevé des matières premières métalliques et la prise en compte des méthodes de fabrication courantes conduisent à augmenter le coût de fabrication. De plus, le coût de maintenance élevé des rotors métalliques est un autre inconvénient. Citons également la fissuration par corrosion sous contrainte et les ruptures par fatigue ont toujours été associées aux rotors

métalliques [8]. Tous ces problèmes conduisent à ce que les polymères et les composites polymères soient au centre de l'attention des études. En ce qui concerne, l'utilisation de ces matériaux en raison de leur faible poids, de leur bonne résistance chimique et de leur bonne résistance constitue un bon choix pour une utilisation en place et lieu des composants métalliques [11]. En outre, l'utilisation de ces matériaux dans la fabrication peut impliquer des méthodes qui impliqueront des coûts beaucoup plus faibles par rapport aux méthodes traditionnelles de production de pièces métalliques telles que le forgeage et le moulage. En général, les polymères thermoplastiques et les polymères thermodurcissables font partie des polymères qui ont été utilisés pour fabriquer les rotors. Dans les polymères thermoplastiques, l'acrylonitrile butadiène styrène (ABS) [9], l'acide polylactique (PLA) [12], le polyéther éther cétone (PEEK) [13] sont les exemples qui ont été utilisés pour la fabrication des roues. D'autre part, les composites ont été employés dans des situations où un matériau avec une résistance plus élevée est requise [10]. Dans ce rapport, les polymères et composites polymères qui ont été pris en compte pour la fabrication de roues dans différentes applications ont été étudiés. En raison de l'importance des méthodes de fabrication et de leur effet sur le produit final, différents procédés de fabrication tels que la fabrication additive, le moulage par injection et la fabrication de turbines conventionnelles ont été expliqués. De plus, l'importance de la dynamique des fluides computationnels pour la simulation et de l'interaction fluide - structure par rapport aux contraintes principales a été discutée. Enfin, des tests de performance pour l'évaluation des roues fabriquées ont été mentionnés.

B.1.1 Matériaux utilisés pour la fabrication des roues

Compte tenu du rôle primordial des matériaux utilisés dans la fabrication des composants rotatifs, en ce qui concerne la production des différents composants et les conditions de travail, la sélection et la fabrication des matériaux ont été parmi les plus importantes. Une bonne résistance aux contraintes, à la fatigue, à l'érosion et un rapport élevé entre résistance mécanique et densité du matériau font partie des propriétés exemplaires des matériaux utilisés dans la fabrication des compresseurs et ont toujours été déterminantes dans les choix [14]. En outre, le coût des matériaux et la livraison sont d'autres paramètres qui comptent parmi les critères de choix de la matière. Dans cette section, les matériaux utilisés dans la construction des rotors et des roues sont expliqués. Dans le cas du cycle micro-organique de Rankine qui est l'un des systèmes importants pour la gestion des sources de combustibles fossiles (gaz de combustion et chaleur résiduelle) et des énergies renouvelables, le remplacement des rotors en polymère et composite au lieu du métal a été mentionné comme un facteur important à traiter avec l'utilisation limitée de ces turbines en raison de leur coût peu économique [9]. Les inconvénients mentionnés ont conduit à ce que le polymère et les composites soient au centre de l'attention de nombreuses études.

B.1.2 Méthodes de fabrication des turbines polymères et composites polymères

L'effet important de la méthode de fabrication peut être clairement indiqué par la consommation d'énergie pendant le processus et les performances de la roue [1,3]. La capacité de production en série, l'obtention de propriétés mécaniques appropriées et d'une bonne surface, une haute précision pour des géométries complexes et une efficacité économique font partie des critères de sélection du processus de

fabrication des roues. La fabrication additive, le fraisage et le moulage par injection ont été envisagés parmi les méthodes de fabrication des roues polymères et composites.

B.1.2.1 Fabrication additive (FA)

La fabrication additive (FA) est un procédé de fabrication basé sur la fabrication de pièces par assemblage de matériaux, directement à partir d'un modèle 3D. Depuis 1980, étant donné que, selon certaines sources, la pièce fabriquée a été produite directement à partir d'un fichier de données correctement formaté, couche par couche, elle peut être considérée comme la date de naissance du processus de FA. Au cours des dernières années, en raison de l'augmentation significative des propriétés mécaniques obtenues par la production de FA, cette méthode a été introduite comme une méthode souhaitable et fiable pour la production de pièces. La technologie FA peut être classée dans les systèmes de polymère liquide, de particules discrètes, de matériau fondu et de blindage solide. L'utilisation de la FA pour les fabrications de rotors et de turbines ne fait pas exception et a attiré l'attention dans de nombreuses études. La fusion sélective au laser (SLM) [95,96], la stéréolithographie (SLA), la modélisation par dépôt par fusion (FDM) et la technique d'impression multiJet (MJP) sont les méthodes FA qui ont été utilisées pour le rotor et la roue. L'une des méthodes les plus courantes et les moins coûteuses parmi le processus FA est la modélisation par dépôt en fusion (FDM). Dans ce procédé, en faisant fondre le filament thermoplastique dans une buse à une certaine vitesse, des pièces peuvent être ainsi réalisées. Dans plusieurs études, le FDM a été utilisé pour produire les roues du compresseur et de la pompe. Caille et al. [97] a étudié la roue de la pompe par la méthode FDM. La roue avait un diamètre de 75 mm de et une épaisseur de 1,3 mm. La roue a été fabriquée pour être utilisée dans une pompe

alimentée par un moteur à induction de 3 kW et une vitesse de rotation de 3000 tr/min. Les résultats ont montré que la roue réalisée par cette méthode a répondu aux critères de qualité, de résistance, de performances et de cadence de fabrication. Dans une étude menée par Fernandez et al, [11] une roue fabriquée par FDM à des fins de pompe a été analysée. Leur étude a montré que la roue ainsi réalisée avait une performance similaire à la roue d'origine de la pompe hydraulique rotodynamique. De plus, compte tenu de l'effet important de la rugosité de la roue sur les performances des compresseurs et des pompes, la rugosité inhérente des surfaces externes de la roue n'a pas affecté les résultats de la courbe de débit de la pompe. Dans une autre étude de Priyanka et Varaprasada Rao [98], ils concluent que pour une roue produite par FDM cette technique peut être présentée comme une méthode méritante qui peut remplacer les procédés traditionnels de fabrication. Cependant, la différence de propriétés mécaniques dans diverses directions (anisotropie) a été l'un des problèmes qui a toujours existé dans les pièces fabriquées par le procédé FDM [99]. Badarinath et al. [100] ont étudié le développement et caractérisé les performances d'un système FDM robotisé à la place des machines FDM basées sur le mécanisme de portique à trois axes. La roue fabriquée par cette méthode présentait des régions de remplissage et de chevauchement du périmètre dans la base exemptes de vides et de sur-dépôt. Les résultats ont également indiqué que le dépôt était uniforme dans les régions de changements de direction dans les pièces à géométrie complexe. Cette méthode peut donc être retenue pour la fabrication de pièces aux géométries complexes. La stéréolithographie (SLA) est une technique selon laquelle la polymérisation d'un monomère liquide photodurcissable d'une manière spatialement sélective se produira en utilisant la lumière ultraviolette (ou un laser). La structure 3D est obtenue en alternant les films

liquides minces et les étapes de photopolymérisation spatialement contrôlées [101]. Généralement, les roues fabriquées par cette méthode sont utilisées dans deux buts : directement comme rotor ou roue ou indirectement dans les méthodes de coulée [102]. Dans un cas industriel, Dans l'étude d'Isaias et al. [9], la méthode FA a été appliquée pour la fabrication d'une roue pour la microturbine radiale à cycle organique de Rankine (ORC). Dans cette étude, une roue thermoplastique (ABS) d'un diamètre de 49 mm a été utilisée pour la rotation à une vitesse de 36.000 tr/min. Les résultats de leur étude ont montré que le rotor fabriqué par cette méthode pouvait rivaliser avec celui en aluminium. De plus, cette dernière caractéristique aidant à minimiser le déséquilibre, la fatigue de l'arbre et l'endommagement du carter en cas de défaillance figuraient parmi les avantages obtenus par cette méthode. L'impression MultiJet (MJP) est un processus d'impression AM qui permet de fabriquer couche par couche une résine plastique photodurcissable par un processus d'impression piézo. La haute précision de cette méthode pour fabriquer les géométries complexes est l'une des caractéristiques principales de cette technique. Des études ont présenté cette technique comme une méthode performante pour la fabrication de rotors et de roues. Andrearczyk and Żywica [103] ont fabriqué la roue d'un compresseur et la roue d'une turbine par MJP dans le but de les utiliser dans un turbocompresseur. Selon leur étude, la plage de pression du compresseur était comprise entre 0 et 1,6 MPa. De plus, compte tenu de la résistance à la traction de ce photopolymère qui mentionnait environ 65 MPa et de la température de fonctionnement de 88 °C, ce procédé par ce type de photopolymère était une méthode viable pour la fabrication des pièces mentionnées du turbocompresseur. Artur Andrearczyk et al. [7] utilisant le MJP ont étudié les champs d'application de cette méthode en considérant les aspects conception, tests

et optimisation des éléments des machines à écoulement de fluide. Dans leur étude, le rotor fabriqué en polymère présentait un diamètre de 42,5 mm à l'entrée du compresseur du turbocompresseur (les turbocompresseurs sont les machines à écoulement de fluide avec l'une des vitesses de rotation nominales les plus élevées). La plage de température allait de 50 à 150 °C pour l'air d'admission de cette machine. La vitesse de rotation jusqu'à 100.000 tr/min a été utilisée dans cette expérience. Il convient de mentionner que les résultats ainsi obtenus à partir des roues de compresseur, qui ont été fabriquées en polymère et en aluminium, ont montré qu'à 90.000 tr/min, la roue en polymère peut fonctionner tout aussi bien que la roue en aluminium.

B.1.2.2 Une introduction sur FDM

Toutes les industries ont changé leur concentration, des méthodes de fabrication traditionnelles aux procédures de prototypage rapide (RP) pour réduire les temps de cycle de fabrication de pièces tout en conservant des propriétés mécaniques essentielles. Cela aide à maintenir les industries compétitives sur le marché. Les processus RP ont été établis pour la première fois dans les années 1980, connus sous le nom de fabrication additive (AM), de fabrication de couches, de processus additifs, de fabrication de formes libres et de techniques additives. Cette technologie construit des objets en ajoutant du matériel au format Laa yered avec l'utilisation de la conception assistée par ordinateur (CAD) [123]. La méthode de fabrication additive (AM) comprend plusieurs techniques qui permettent le développement d'objets tridimensionnels avec des géométries complexes. L'AM a été utilisée dans la construction et la construction, le secteur automobile, l'aérospatiale, l'art, l'industrie alimentaire [124]. L'extrusion de matériaux (ME), le jet de matériau (MJ), la fusion de lit de poudre (PBF), la feuille de feuille (SL),

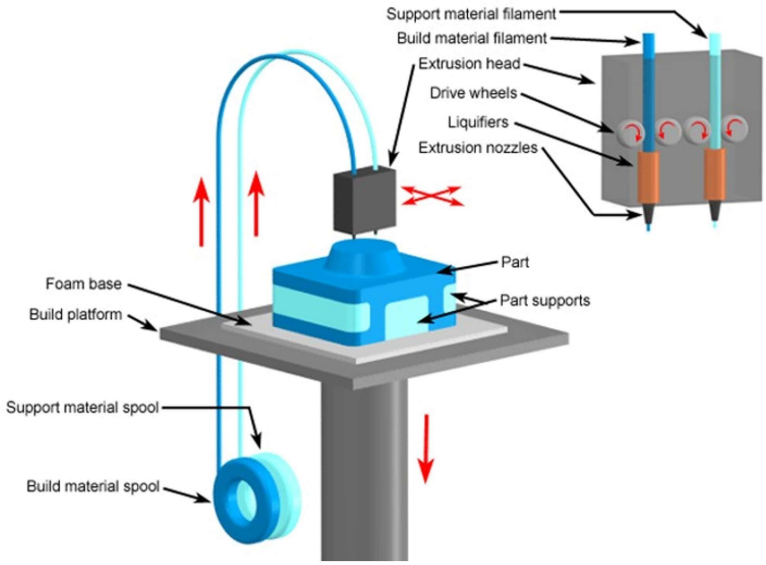

FIGURE B.2 – Imprimante FFF 3D; a) Imprimante allemande Reprap X500®3D (FFF), b) sch ema de l'imprimante FFF 3D [133].

le jet de liant (BJ), la polymérisation photo de la cuve (VP) et le dépôt d'énergie réalisé (DED) sont sept types des méthodes AM qui ont été développées au fil des ans [125]. Dans le processus FFF, un polymère est fourni dans un liquéfier, qui extrude un filament tout en se déplaçant dans des plans X-Y successifs le long de l'axe Z pour construire un objet 3D [126]. Différentes parties de l'imprimante FFF 3D sont illustrées à la figure 1.6 [127].

B.1.2.3 Adhésion des couches en FFF

La formation de liaisons pendant l'impression peut être divisée en trois processus en contact de surface, la croissance du cou entraînée par la tension en surface et la diffusion moléculaire, et l'enchevêtrement à travers l'interface inter-filament. L'historique thermique et la pression d'extrusion pendant la fabrication peuvent entraîner le processus de soudage. La formation d'une interface entre

deux polymères peut s'expliquer par la guérison des polymères par la laine et l'O'Connor [133]. Selon cette théorie, différents stades de guérison consistent en 5 étapes, y compris (1) le réarrangement de surface, (2) l'approche de surface, (3) le mouillement, (4) la diffusion et (5) la randomisation. Cela, la diffusion intermoléculaire dans la zone mouillée conduit à l'augmentation de cette interface. Les emplacements aléatoires dans la zone mouillée dans une certaine zone sont le lieu de nucléation de la diffusion intermoléculaire. La théorie de Wool et al. [134] peut expliquer le soudage à une interface polymère concernant la structure dépendant du temps de l'interface de soudage qui est déterminée en termes de dynamique moléculaire des chaînes polymères. La dynamique moléculaire des chaînes polymères a été modélisée par la théorie de la réputation. Dans cette théorie, les chaînes de polymères sont supposées être dans un tube selon les contraintes topologiques. Ce tube peut configurer la chaîne polymère, qui est considérée comme une plage pour le mouvement de la chaîne polymère. La figureB.3 montre schématiquement cette configuration avec des moments différents d'une chaîne à l'état fondu. Temps passant dans cet état, la chaîne par mouvement brownien peut aller-retour dans le tube. Le temps dont la chaîne a besoin de désengagement du tube ou de détente est appelé tr. Cela, moins que cette époque est conduit à un mouvement de chaîne mineure.

Après cette théorie, l'interdiffusion moléculaire à l'interface de deux polymères en considérant le mouillage instantané peut être expliqué. La figureB.4 montre schématiquement l'interdiffusion moléculaire entre deux surfaces de polymères mouillés. T = 0 indique le contact moléculaire, et après cela, le temps de passage s'accompagne de chaînes réparties au hasard dans l'espace.

Selon la théorie de la reptation, la relation entre la longueur des chaînes mineures avec le temps

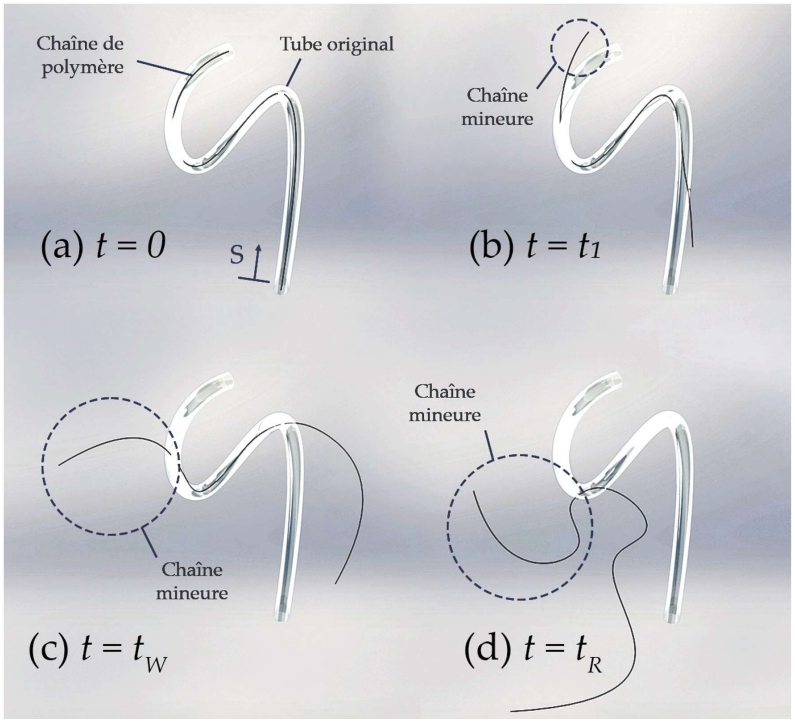

FIGURE B.3 – Schéma du modèle de reptation pour la guérison

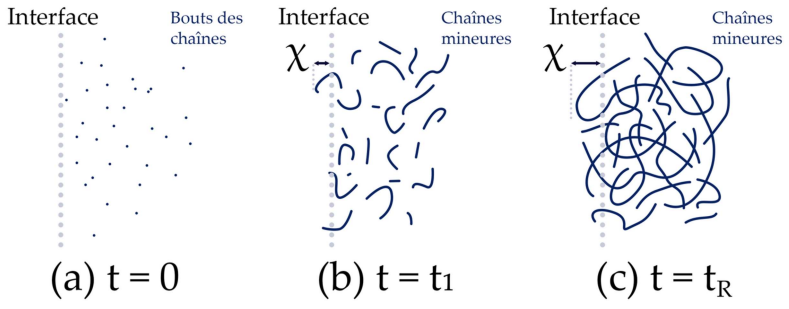

FIGURE B.4 – Dynamique de reptation à travers une interface polymère / polymère

qui a une corrélation de racine carrée peut être réalisée comme suit:

$$\frac{l}{L} = (\frac{t}{T_r})^{0.5} \tag{B.1}$$

Afin d'enquêter sur l'interdiffusion des chaînes pour la distance X, l'équation suivante peut être appliquée:

$$\frac{x}{x_\infty} = (\frac{t}{T_r})^{0.25} \tag{B.2}$$

Yang et Pitchumani [136] ont développé un modèle pour le processus de guérison dans des conditions non isothermes basées sur la théorie de la reptation des chaînes de polymère. On peut dire que le modèle a été modifié à partir du modèle Bastien et Gillespie en considérant les gradients de température plus petits. La dépendance de la résistance aux liaisons via l'historique de la température et le temps de soudage a été étudiée dans leur étude. Par le modèle analytique présenté, le degré de guérison, qui est attribué au terme de quantification de la fraction de diffusion à travers les couches, le temps est le suivant:

$$D_h(t) = \left[\int_0^t \frac{1}{t_w(T)} dt\right]^{0.25} \tag{B.3}$$

Le soudage temporel, tw, a été calculé en ajustant le modèle Arrhenius sur les différents résultats des échantillons de cisaillement fabriqués dans des conditions isothermes à différentes températures. L'étude de l'interface dans la zone de soudure de FFF imprimée basée sur la théorie de la reptation

a été extrêmement utilisée dans des études récentes [2,139]. Lacambra-Andreu et al. [140] ont étudié la diffusion moléculaire intercouche de poly (d, l-lactic acide) (pdlla) pendant le processus FFF par théorie de la reptation. À cette fin, le profil de température a été prédit par transfert de chaleur dans des conditions transitoires, la caractérisation rhéologique a été analysée pour estimer la viscosité et le temps de relaxation. Selon les résultats, la diffusion du polymère à l'interphase a été prédite en influençant le degré de guérison et ils ont montré l'impact de cet aspect sur la force des échantillons imprimés. La figureB.5a montre un schéma de formation de soudage dans les couches 1 et 2 sur la base de la théorie de la rétention. L'interface interfaciale contre le temps a été montrée sur la figureB.5b pour une buse de température de 190 °C à l'interface de ces couches. Les résultats ont montré une interphase avec une épaisseur de 17,2 nm à l'interface. Le rôle clé du profil de température sur le processus de guérison a été montré que l'augmentation de la température s'accompagne d'une amélioration de la guérison et d'une meilleure soudage entre les filaments adjacents.

Une introduction de la stéréolithographie La stéréolithographie (SLA) est une méthode d'impression 3D populaire qui a été développée pour la première fois dans les années 1980. Il s'agit d'une forme de fabrication additive qui utilise un matériau de résine liquide pour créer des objets 3D couche par couche. Le SLA est couramment utilisé pour produire des pièces complexes à haute résolution avec une excellente finition de surface et une précision dimensionnelle. Le processus commence par la création d'un modèle 3D de l'objet à imprimer à l'aide du logiciel de conception assistée par ordinateur (CAD). Le fichier numérique est ensuite chargé dans l'imprimante SLA et exposé au rayonnement du faisceau laser ultraviolet (UV), qui induit un processus de polymérisation localisé pour solidifier la couche de

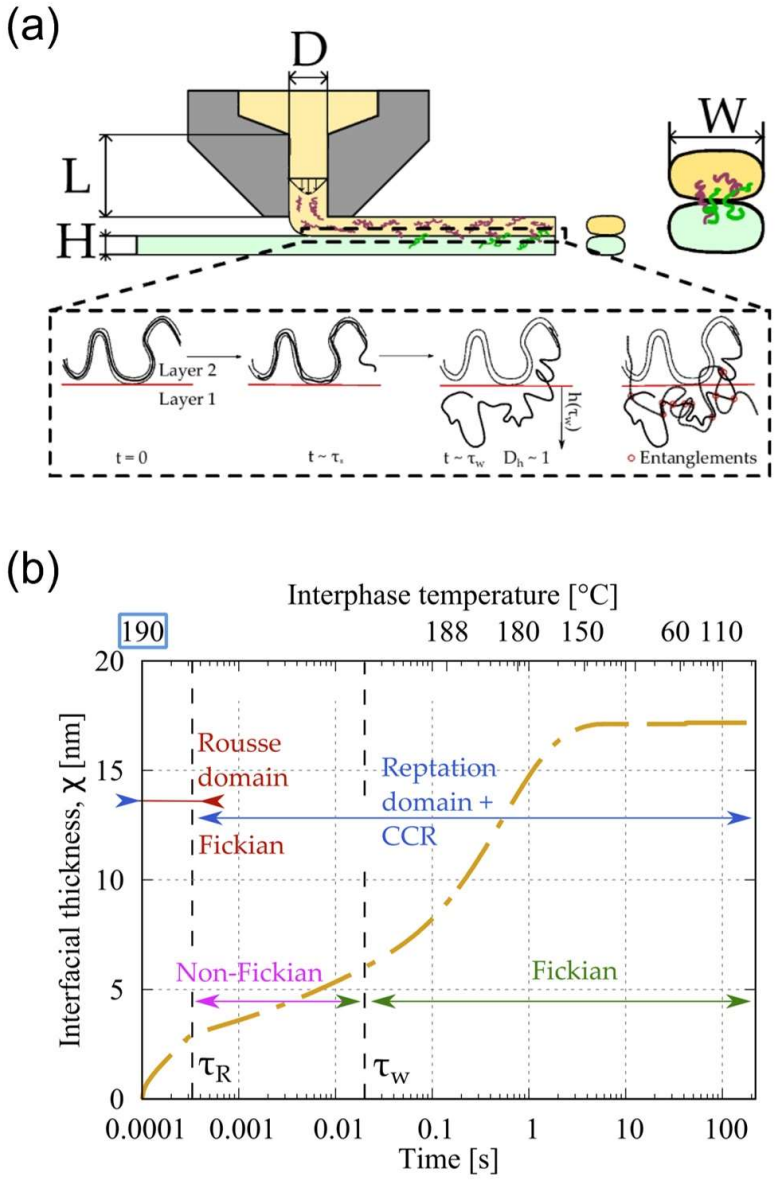

FIGURE B.5 – (a) Schéma d'un processus d'impression par interdiffusion de chaînes avec le temps de dépôt et (b) l'évolution de l'épaisseur interfaciale entre les couches 1 et 2 pendant une température de buse de 190 °C[141].

résine liquide par couche pour former des pièces fabriquées directement à partir de données informatiques 3D. Lorsque le faisceau laser scanne chaque couche de l'objet, il solidifie sélectivement la résine à des points spécifiques, suivant la forme du modèle 3D. La plate-forme d'imprimante est ensuite légèrement abaissée et le processus se répète, renforçant la couche d'objet par couche jusqu'à ce qu'elle soit terminée. Le pourcentage de polymérisation dans les pièces fabriquées peut être mentionné comme un paramètre clé qui a un impact sur les propriétés physicochimiques, mécaniques et thermomécaniques. En général, ce pourcentage peut être atteint jusqu'à 80% pour une partie verte et la méthode de post-traitement peut augmenter cette valeur à 95%. Différentes méthodes de post-traitement peuvent être trouvées dans la littérature correspondant au lavage des échantillons immédiatement après l'impression et le post-ouvrage en gardant les échantillons en présence de rayonnement UV avec ou sans température. De plus, le rayonnement micro-ondes est une autre méthode post-future pour augmenter le pourcentage de durcissement.

B.1.3 Évaluation du compresseur: numérique et expérimental

En général, les analyses numériques pour les pièces conçues, en tenant compte des conditions de travail, ont été l'une des étapes les plus critiques dans l'étude des matériaux. En ce qui concerne les composants rotatifs du compresseur, ils ne font pas exception à cela, et les évaluations numériques ont toujours été l'une des étapes vitales pour l'étude des matériaux mis en jeu [104]. En d'autres termes, l'analyse numérique peut être considérée comme un outil permettant d'équilibrer performances et fiabilité lors du développement et la conception des produits [105]. Dans cette section, l'analyse numérique des roues et rotors centrifuges des compresseurs sera discutée. Comme mentionnées, des

propriétés telles que le module d'élasticité, la dilatation thermique, la ténacité à la rupture, la résistance à la fatigue, la conductivité thermique, la capacité thermique spécifique, la résistance à la corrosion et la stabilité thermique ont été parmi les paramètres pris en compte dans la sélection des matériaux pour la fabrication des roues et des rotors. des compresseurs [106]. Il convient de mentionner que la contrainte centrifuge due à la rotation, la contrainte de flexion due à la pression du fluide et au changement de quantité de mouvement, et les contraintes thermiques dues à la charge thermomécanique sont les propriétés qui ont été considérées comme des facteurs importants dans les simulations. Ainsi, en examinant les matériaux sous des calculs par éléments finis des forces mentionnées, la viabilité du matériau sera testée en simulation [107]. L'analyse structurelle est l'application la plus courante de l'analyse par éléments finis qui permet d'étudier différents types de charges, notamment les contraintes, les déformations, etc. Les équations statiques structurelles linéaires sont les suivantes [108]:

$$\frac{\partial \sigma_x}{\partial x} + \frac{\partial \tau_{xy}}{\partial y} + \frac{\partial \tau_{xz}}{\partial z} + F_{bx} = 0 \tag{B.4}$$

$$\frac{\partial \tau_{yx}}{\partial x} + \frac{\partial \sigma_y}{\partial y} + \frac{\partial \tau_{yz}}{\partial z} + F_{by} = 0 \tag{B.5}$$

$$\frac{\partial \tau_{zx}}{\partial x} + \frac{\partial \tau_{zy}}{\partial y} + \frac{\partial \sigma_z}{\partial z} + F_{bz} = 0 \tag{B.6}$$

Avec représente la contrainte normale, la contrainte de cisaillement, Fbx, Fby et Fbz sont les forces par unité de volume agissant le long des directions x, y, and z, respectivement. En considérant les différentes charges mentionnées comme conditions aux limites sur la roue, une analyse des contraintes structurelles par éléments finis peut être effectuée. La force centrifuge par section de pale apparaît

sous forme de contraintes centrifuges qui peuvent s'écrire généralement comme suit:

$$F_C = mr\omega^2 \tag{B.7}$$

Ou FC représente la force centrifuge, *omega* est a vitesse de rotation r et m indiquent respectivement le rayon et la masse de la section considérée. Pour considérer l'influence thermique sur les pales, les équations pour les matériaux solides tridimensionnels (considérés comme élastiques linéaires et isotropes) sont les suivantes [109]:

$$\varepsilon = \ (D-1)\sigma + \alpha\Delta T \tag{B.8}$$

$$\Delta T = T - T_{Ref} \tag{B.9}$$

Ou , , TRef, D et *alpha* sont respectivement le vecteur déformation totale, le vecteur contrainte, la température de référence, la matrice de rigidité élastique du matériau et la matrice de coefficients de dilatation thermique. L'interaction fluide-structure (FSI) est l'approche utilisée pour l'analyse structurelle de la roue. Dans cette méthode, l'effet de la dynamique des fluides sur la mécanique structurelle de la roue, basée sur la dynamique des fluides computationnelle (CFD) et l'analyse structurelle par éléments finis (FEA), peut être étudié [110,111]. La résolution des équations de Navier-Stokes à moyenne de Reynolds (RANS) a été l'une des méthodes les plus utilisées en CFD [112]. Les équations sont les suivantes [109]:

$$\nabla(\rho V) = 0 \tag{B.10}$$

$$\nabla.(\rho VV) = \rho f - \nabla p + \nabla.T \tag{B.11}$$

$$\nabla.(\rho hV) = \rho f.V + \nabla.(T.V) - \nabla.q \tag{B.12}$$

Où V, f, p, T, h et q sont respectivement le vecteur vitesse du fluide, le vecteur force par unité de masse, la pression, le tenseur de contraintes visqueuses, l'enthalpie volumétrique et le vecteur flux thermique. L'interaction fluide-structure pour atteindre la condition limite de charge à partir de l'interaction du fluide et de la roue peut être calculée par la dynamique des fluides en numérique (CFD) qui est basée sur la résolution des équations de Reynolds-Averaged Navier-Stokes (RANS). Le terme de gradient de pression et les termes de diffusion dans les équations de quantité de mouvement, de continuité et de turbulence peuvent être obtenus en utilisant les fonctions de forme dans la CFD. Artur Andrearczyk et al. [7] ont étudié la roue en thermodurcissable dans une application de turbocompresseur. Dans cette expérience, le rotor a été fabriqué par la méthode d'impression 3D Multijet avec un diamètre de 42,5 mm. Pour les analyses et les calculs des forces mises en jeu, la vitesse de rotation et la température étaient respectivement de 100.000 tr/min et 55 ℃. D'après leurs résultats, la déformation maximale et la contrainte maximale sur la géométrie de la roue étaient de 192 m et 27 MPa. La figureB.6 montre les résultats de la distribution de contraintes et de déformations. De plus, les performances du compresseur ont été simulées sur la base de la résolution des RANS par ANSYS afin d'obtenir la carte des performances du compresseur. Leurs résultats ont montré les lignes de courant dans un référentiel relatif pour lequel la vitesse de rotation et le débit massique étaient respectivement de 200.000 tr/min

et 0,09 kg/s.

Isaias et al. [9] ont étudié et comparé les différentes roues polymères, composites et métalliques dans le but d'évaluer la faisabilité du développement d'un turbodétendeur simplifié. Les calculs sous différentes charges ont été examinés dans cette étude. La condition de pleine charge, le rotor bloqué qui est alimenté à plein débit (rotor arrêté), et une survitesse de 27% ont été les conditions prises en compte pour respecter les normes internationales. La vitesse de rotation était de 36000 tr/min et le diamètre de la roue de 49 mm. Leurs résultats ont montré que la contrainte obtenue montrait une sensibilité élevée à la force de rotation et à la charge en pression. La figureB.7(a, c et e) montre la contrainte équivalente sur la roue PEEK dans différentes conditions de chargement et d'après leurs résultats, la contrainte maximale sur la pale était de 10 MPa. Selon leur analyse pour 27% de survitesse, la valeur du facteur de sécurité pour l'aluminium, le PEEK renforcé avec 30% de fibre de verre et l'ABS étaient respectivement de 19,92, 22,25 et 13,32. Ces valeurs étaient supérieures à l'exigence minimale. La figure 10 (b, d et f) montre les lignes de courant, colorées en fonction de la température, dans les conditions de pleine charge, rotor bloqué et à 27% de survitesse. Compte tenu des lignes de courant, ils y avoir des contraintes supplémentaires autres que celles causées par la force centrifuge. L'efficacité simulée était respectivement de 86%, 0% et 84% pour les situations de pleine charge, rotor bloqué et 27% de survitesse.

Kar et al. [113] ont étudié une roue polymère dans des applications de pompes centrifuges. La roue avait un diamètre de 5,08 cm et fabriquée en polyétherimide. L'analyse des contraintes structurelles a été réalisée par analyse par éléments finis (FEA) dans des conditions centrifuges maximales en ce

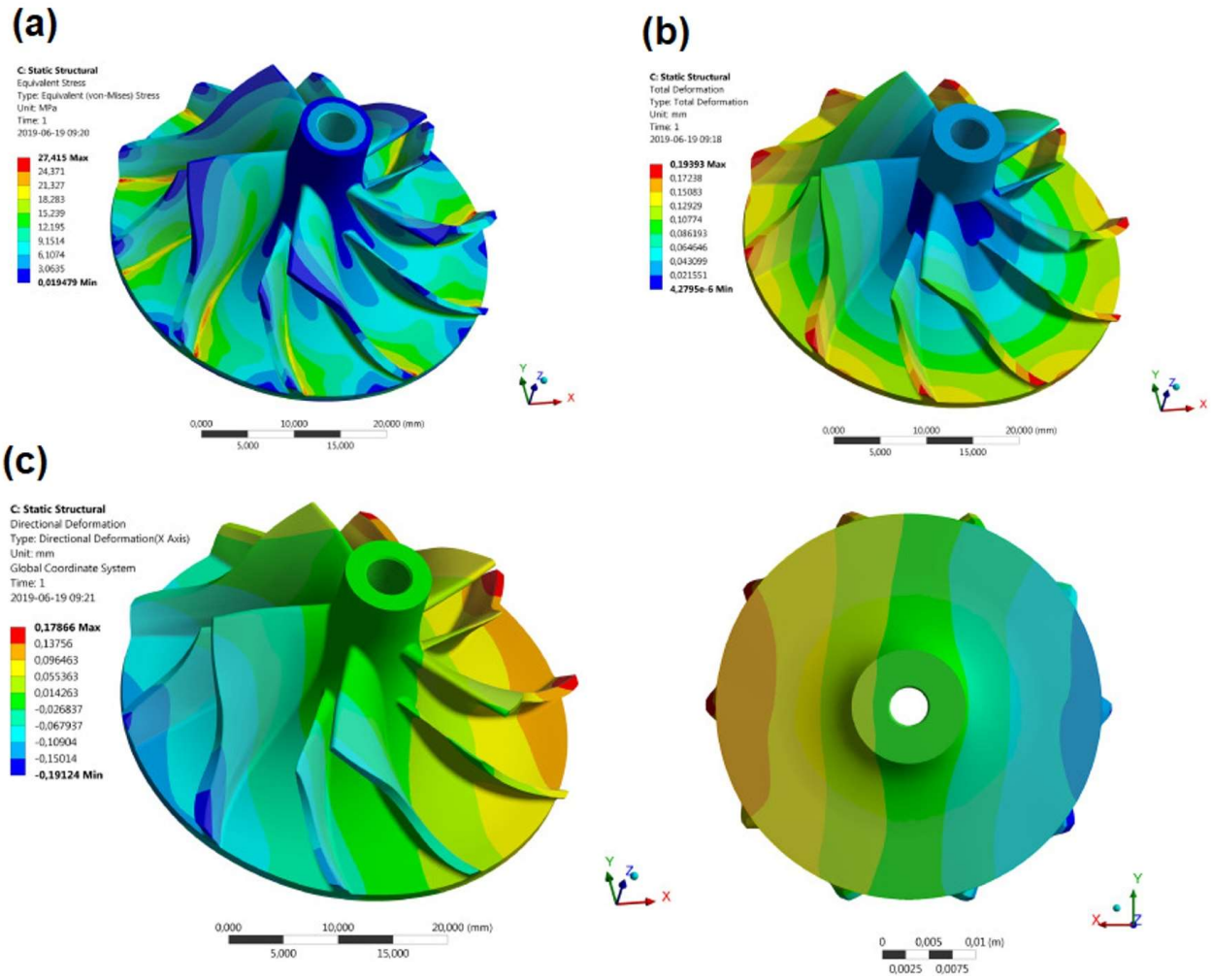

FIGURE B.6 – Distributions de contraintes (a), de déformations totales (b), de déformations directionnelles selon l'axe X en (c) et en vue de dessous sur le rotor polymère[5].

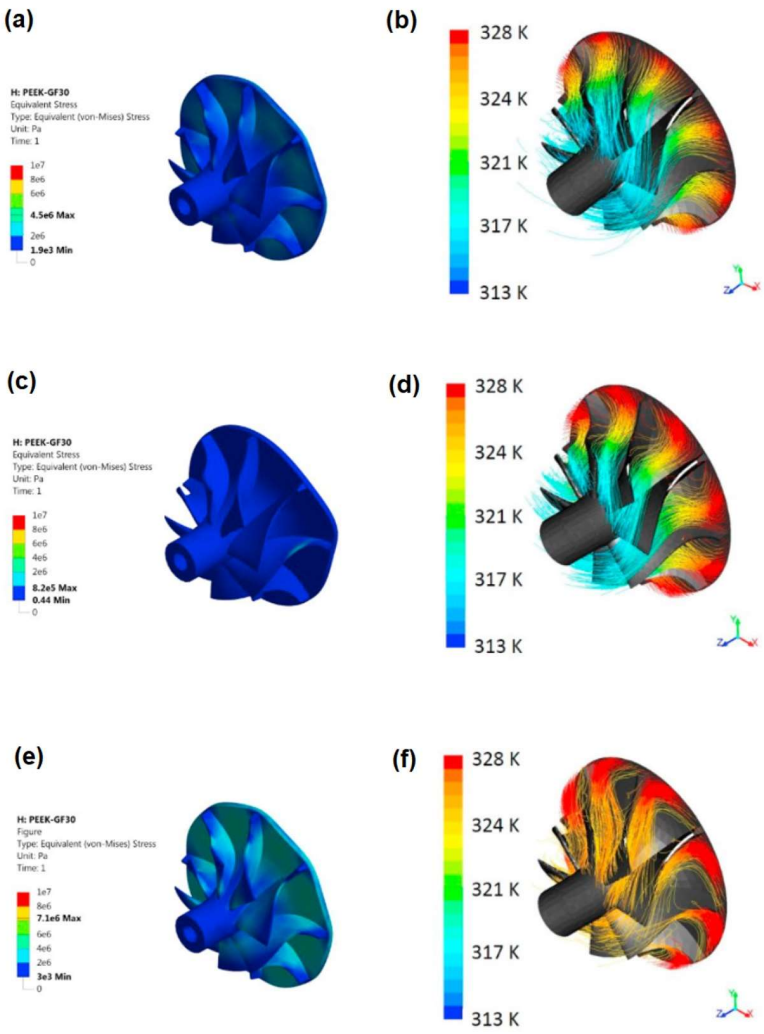

FIGURE B.7 – Contours de contrainte (Pa) pour la roue PEEK (a, c et e) et lignes de courant relatives colorées en fonction de la température totale en Kelvin (b, d et f) ; en pleine charge (a et b), rotor bloqué (c et d) et à 27% de survitesse (d et f) [9][22].

qui concerne la vitesse de rotation de 72.000 tr/min et la charge gravitationnelle. Leurs résultats ont montré que la contrainte maximale sur la roue était de 5,45 MPa.

B.1.4 Evaluation des performances

Une évaluation précise des performances de la roue dans la pompe ou le compresseur est essentielle car elle confirme la capacité de la machine à répondre aux conditions de travail ainsi qu'à une consommation d'énergie correcte. À cet égard, l'investigation sur les performances est possible grâce à l'analyse des travaux effectués sur le fluide de travail. En général, la température d'entrée, la pression d'entrée, la température de refoulement, la pression de refoulement, la vitesse de rotation, la pression différentielle à travers le débitmètre (ou traverse de Pitot), la température et la pression au débitmètre font partie des mesures permettant de déterminer les performances de la machine. De plus, une étude des vibrations a été envisagée pour confirmer les performances dynamiques. Également, le comportement tribologique de la roue dans des conditions de travail est un autre facteur qui doit être pris en compte. Selon le type d'application telle que pompe ou compresseur, l'environnement du banc d'essai sera différent. Il convient de mentionner que des tests de performances seront effectués pour atteindre la carte de fonctionnement des compresseurs ou pompes, carte qui représente le débit corrigé en fonction de la montée en pression à différentes vitesses aérodynamiques.

B.2 Dimensions du compresseur, matériaux et méthodes

B.2.1 Conception du compresseur

Pour la conception préliminaire, un modèle 0D basé sur les conditions limites a été calculé pour le rotor d'un compresseur centrifuge à rotation élevée avec une vitesse allant jusqu'à 90 000 tr/min. Les spécifications du compresseur comprenaient un taux de compression, une puissance et un débit massique de 1,4, 1,6 (KW) et 35 (g/s), respectivement. Dans cette méthode, nous effectuons un calcul préliminaire de la géométrie du rotor basé sur la courbe expérimentale de Cordier [187] par la méthode d'interpolation. Les deux paramètres les plus importants utilisés dans cette méthode sont la vitesse spécifique et le rayon spécifique :

$$\Omega = \omega \, \frac{\sqrt{\frac{\dot{m}}{\rho_1}}}{\delta h_{is}^{0.75}} \tag{B.13}$$

Le rayon spécifique :

$$R_s = 1.8031 N_s^{-0.61} \tag{B.14}$$

A partir de la valeur du rayon spécifique, le rayon du rotor est calculé par l'équation 3 :

$$r_2 \;=\; R_s \, \frac{\sqrt{\frac{\dot{m}}{\rho_1}}}{\left[\frac{\delta h_{is}}{\eta_{is}}\right]^{0.25}} \tag{B.15}$$

Ensuite, la taille de l'inducteur du rotor est calculée sur la base de la méthode de minimisation du nombre de Mach relatif en bout d'aube d'entrée pour éviter le blocage [21]. La relation entre le nombre de mach relatif et la taille de l'inducteur est montrée dans l'équation 4 :

$$M_{1s} \;=\; \frac{1}{\sqrt{\gamma \;\times\; R \;\times\; T_1}} \; \frac{\dot{m}}{\rho_1 \;\times\; \pi \;\times\; (r_{1s}^2 \;-\; r_{1h}^2) \;-\; Z \;\times\; t_b \;\times\; (r_{1s} \;-\; r_{1h})} \; \frac{1}{\cos\beta_{1s}} \tag{B.16}$$

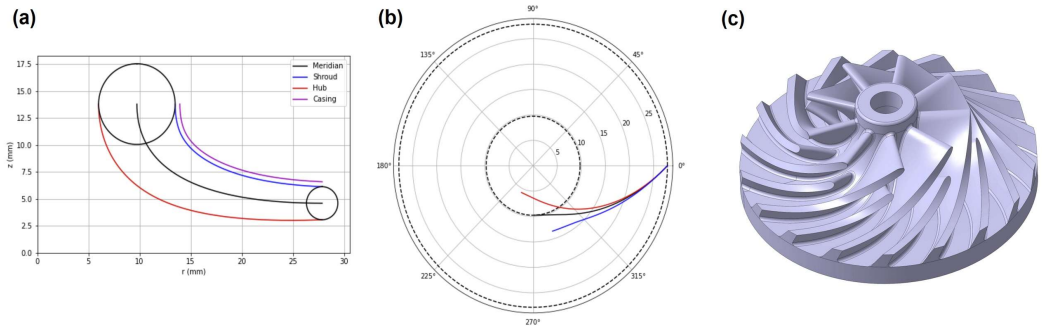

FIGURE B.8 – Géométrie de roue obtenue par la méthode de conception préliminaire

Les résultats de calculs préliminaires permettant de déterminer les dimensions détaillées de la roue sont présentés sur la figureB.8.

B.2.2 Modèle CFD

Pour évaluer au préalable les performances du rotor conçu, un modèle CFD de simulation numérique a été réalisé avec le logiciel StarCCM+ v16.02. Ce modèle est construit à partir de la taille réelle du compresseur, avec le rotor complet. Afin d'analyser les performances du compresseur, une méthode de résolution des équations RANS (Reynold-Averaged Navier-Stockes) a été utilisée. Un solveur "coupled flow" qui permet de résoudre les équations de transport simultanément avec une discrétisation de deuxième ordre par une simulation stationnaire a été appliqué. Le modèle de turbulence "k-omega SST" a été utilisé. L'interface entre les domaines fixes et tournants est directe. Le modèle de gaz utilisé est celui des gaz parfaits. Les performances du compresseur obtenues par simulation CFD sont présentées dans la figureB.9. Au point de conception, avec un débit de 35 g/s, le taux de compression est légèrement supérieur à celui attendu, tandis que le rendement isentropique est inférieur à celui attendu. Cependant, les résultats du calcul CFD montrent un écart de 5% par rapport aux spécifications. Cela

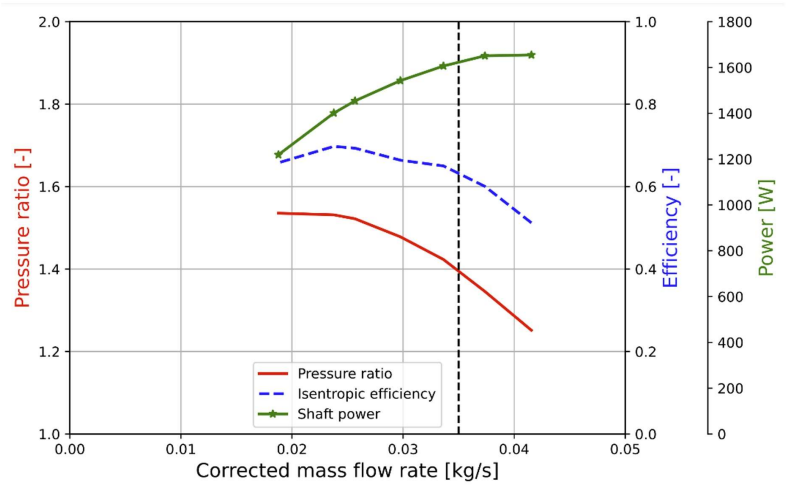

FIGURE B.9 – Compressor performance obtained by CFD simulation at 90,000 rpm

montre que le modèle de conception préliminaire répond aux exigences de conception.

La figureB.10 montre les lignes de courant de l'écoulement dans le compresseur à 90k tr/min. On peut voir qu'il n'y a pas de recirculation dans les passages des aubes du rotor ainsi que dans la volute. Cependant, des écoulements de fuite peuvent être observés en bout d'aubes du fait du jeu de fonctionnement entre le rotor et le carter.

B.2.3 Matériaux

Cette étude a sélectionné deux types de polymères thermoplastiques, l'acide polylactique (PLA) et le sulfure de polyphénylène (PPS), comme filaments d'un diamètre de 1,75 mm à utiliser dans la fabrication de filaments fondus. Une résine photodurcissable à base de diméthacrylate d'uréthane (UDMA) dilué avec les monomères de méthacrylate correspondants et d'oxyde de bis(2,-4,6-triméthylbenzoyl)phénylphosphine comme photoinitiateur a été choisie comme polymère thermodurci pour fabriquer les pièces par méthode SLA.

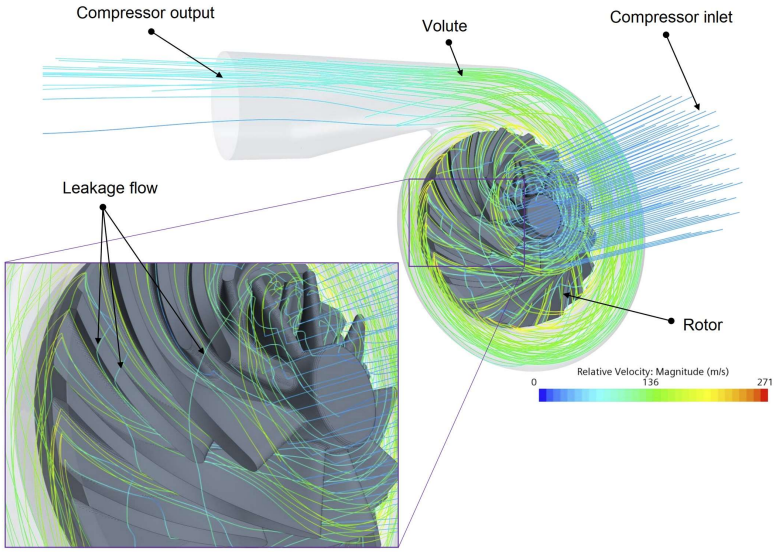

FIGURE B.10 – Lignes de courant dans les domaines de calcul

• Le PLA est un polymère thermoplastique biodégradable et biosourcé issu de ressources renouvelables telles que l'amidon de maïs ou la canne à sucre. Dans cette étude, des filaments PLA disponibles dans le commerce avec une valeur nominale. Un poids moléculaire de 37 000 g/mol a été utilisé dans les couleurs rouge et blanche. Les filaments PLA ont été achetés chez Ultrafuse.

• Le PPS est un polymère thermoplastique haute performance reconnu pour ses excellentes propriétés mécaniques et thermiques. Le filament PPS utilisé dans cette recherche a été obtenu auprès de 3DXTECH Additive Manufacturing.

• Le polymère photorésistant portant le nom commercial Black Resin (code produit : FLGPBK04)

a été acheté auprès de Formlabs (Berlin, Allemagne). Les principales caractéristiques des filaments PLA, PPS, et la résine uréthane diméthacrylate (UDMA) sont présentées dans le tableau B.1.

Le post-traitement des échantillons fabriqués par SLA, consistant en un lavage, a été effectué avec de l'alcool isopropylique d'une pureté de 99,9%.

B.2.4 Méthodes

La fabrication additive a ouvert de nouvelles perspectives dans le domaine de la production de pièces complexes et performantes. Notre projet vise à exploiter pleinement cette avancée en étudiant la relation étroite entre le procédé de fabrication, la microstructure des matériaux - tels que le PLA, le PPS et la résine photosensible - et les propriétés finales des pièces. Le Polyacide Lactique (PLA), le Polyphénylène Sulfide (PPS) et les résines photosensibles offrent des caractéristiques distinctes dans la fabrication additive. Cette section de l'étude se focalise sur l'optimisation des performances des pièces, en mettant l'accent sur la fabrication de rotors pour compresseurs. Nous explorerons deux techniques de fabrication additive : la Fused Filament Fabrication (FFF) pour le PLA et le PPS, ainsi que la Stereolithography (SLA) pour la résine photosensible. Ces techniques offrent des avantages uniques en termes de précision, de résistance et de durabilité des pièces produites. L'objectif principal réside dans

TABLE B.1 – Propriétés des polymères utilisés, selon le producteur

Caractéristiques	PLA	PPS	UDMA
Densité g/cm^3	1.24	1.28	1.09
Température de transition vitreuse (°C)	60	85	85
Température de fusion (°C)	175	285	-
Résistance à la rupture (MPa), ISO 527	37	50	38 - 65
Module d'Young (GPa), ISO 527	2.08	2.65	1.6

la compréhension approfondie de la relation entre le procédé de fabrication, la microstructure obtenue et les propriétés mécaniques finales des matériaux. En particulier, nous chercherons à optimiser la liaison interfaciale, la résistance aux contraintes mécaniques et la durabilité des rotors de compresseurs. En étudiant attentivement ces aspects, nous pourrons identifier les paramètres clés de chaque procédé, ajuster les conditions de fabrication et concevoir des structures optimales pour améliorer la performance des rotors. L'objectif ultime est de produire des pièces hautement performantes, légères et résistantes, capables de fonctionner dans des environnements exigeants.

Dans ce stade nous nous sommes efforcés de développer deux axes de recherche principaux :

• D'une part, nous étudions l'optimisation des processus FFF et SLA en utilisant l'interaction des paramètres du procédé. Cette optimisation sera réalisée dans le procédé FFF par le biais des caractéristiques rhéologiques et des mesures thermiques in situ. Dans la méthode SLA, l'interaction du processus et du post-procédé sur les propriétés mécaniques et physico-chimiques a été évaluée.

• D'autre part, nous nous sommes intéressés à l'analyse de l'effet de la microstructure et de la stabilité dimensionnelle de la roue fabriquée sur les performances finales du compresseur centrifuge.

B.3 Relation entre le procédé de fabrication et les propriétés : Liaison interfaciale dans le procédé FFF

B.3.1 Effet de la vitesse de la buse sur la cristallisation

Dans un premier temps, le matériau PLA a été utilisé pour étudier la relation entre le procédé de fabrication et les propriétés, notamment la liaison interfaciale dans le procédé FFF (Fused Filament Fabrication). Les différentes transitions, telles que la cristallisation, la transition vitreuse et la fusion

des échantillons, ont été analysées par la méthode DSC (Calorimétrie Différentielle à Balayage). Les résultats sont présentés dans le Tableau B.2). Les résultats montrent que les paramètres sélectionnés pour la fabrication des échantillons n'ont pas eu d'effet significatif sur la transition vitreuse. De plus, les résultats montrent la cristallisation à froid avec une température de départ d'environ 103 °C pour les échantillons. Il convient de mentionner que la cristallisation à froid se produit en raison d'une vitesse de refroidissement suffisamment rapide pour que le polymère ait le temps de cristalliser et de réarranger les chaînes. D'après les résultats, l'enthalpie de cristallisation à froid n'a pas montré de différence considérable compte tenu des différents paramètres d'impression, ce qui peut être justifié en considérant les mêmes conditions de refroidissement dans les échantillons. L'un des paramètres importants qui peut avoir un impact sur le Xc est la mobilité de la chaîne. L'augmentation de la mobilité de la chaîne entraîne une augmentation de la cristallinité. En raison de l'effet de la température sur la mobilité des chaînes de polymères, on peut dire que la réduction de la vitesse de la buse permet de passer plus de temps à des températures plus élevées, ce qui favorise la mobilité des chaînes. En outre, l'augmentation de la température de la buse à 230 °C a indiqué une augmentation du Xc par rapport à 210 °C à la même vitesse de buse. Étant donné que la plage de surfusion joue un rôle essentiel dans la nucléation et la croissance des cristaux, l'augmentation de la plage de surfusion peut donner plus de temps à la nucléation et à la croissance. Par conséquent, l'augmentation de la température de la buse entraîne une augmentation de la plage de surfusion qui s'accompagne d'une augmentation de Xc. Après la cristallisation à froid, deux pics de fusion sont identifiés dans la zone de fusion, ce qui indique la présence d'une morphologie cristalline différente. Les pics de fusion sont apparus à 150 et 155

TABLE B.2 – Résultats du test DSC

Échantillon	Tg (°C)	Tpeak de cristallisation à froid (°C)	Tm_1 (°C)	Tm_2 (°C)	$\Delta Hm(J/g)$	Xc (%)
Filament	60.58	117.21	153.08	160.3	20.62	1.90
1.1	59.53	114.37	152.99	159.82	25.38	10.01
2.1	60.57	110.51	152.63	159.89	21.29	8.93
3.1	59.16	113.28	152.23	158.90	21.21	6.24
4.1	60.10	109.20	151.98	159.19	19.16	5.61
5.1	61.00	116.98	158.96	159.93	13.81	3.12
2.2	59.97	111.59	152.54	159.76	23.07	9.51

°C, montrant la morphologie des sphérulites et des cristaux hexagonaux, respectivement. Les résultats ont montré une augmentation de l'entropie de fusion avec la diminution de la vitesse d'impression et l'augmentation de la température de la buse. D'autre part, une vitesse de buse plus faible a eu un effet plus important sur l'augmentation de l'entropie de fusion des sphérulites. En général, on peut dire que la diminution de la vitesse et l'augmentation de la température de la buse ont eu un effet plus important sur la cristallisation dans les formes de cristaux de sphérulite.

B.3.2 Effet de la vitesse de la buse sur les propriétés mécaniques

Pour évaluer l'effet de la vitesse d'impression sur les propriétés mécaniques des pièces, des essais de traction ont été réalisés sur des pièces imprimées en FFF avec des angles de trame de 0° et 90°. La figure 1 montre les résultats des essais mécaniques (l'expérience pour chaque échantillon consistait en trois répétitions). Les résultats montrent une différence considérable entre les échantillons à 0° et à 90°, tandis que cette différence est plus marquée pour les échantillons à 90°. La résistance à la traction des pièces à 90° pour différentes vitesses d'impression (mm/s) augmente dans l'ordre suivant : 18 > 30 > 40 > 50 > 60 mm/s. D'après les résultats de traction, l'angle de trame de 0° n'a pas montré une grande différence de résistance à la traction, mais la réduction de la vitesse de la buse a augmenté

la résistance à la traction d'environ 4 MPa dans ce cas. Cette augmentation peut s'expliquer par la cristallinité du polymère, en ce sens que la phase cristalline a des interactions intermoléculaires plus fortes que la phase amorphe. La représentation graphique de la résistance à la traction en fonction de la cristallisation a montré la relation linéaire entre les deux paramètres (Figure 1.b). En outre, l'augmentation de la température de la buse a entraîné une augmentation de la résistance dans cette direction, ce qui est également justifié par l'augmentation de la phase cristalline. Une comparaison des résultats obtenus pour la résistance à la traction dans la direction 90° a montré que ces résultats dépendaient de la vitesse de la buse. Comme nous l'avons mentionné, l'anisotropie a été l'un des défis les plus importants dans les pièces fabriquées par ce procédé et les études ont toujours essayé de réduire ce paramètre. La différence de résistance à la traction dans cette direction est liée au soudage entre les couches. Il convient de noter que la diffusion moléculaire est l'un des paramètres efficaces dans ce domaine, qui est lié à la mobilité des chaînes de polymères. Étant donné que, comme nous l'avons mentionné, la réduction de la vitesse de la buse réduit le temps de mobilité des chaînes de polymères, ce qui peut entraîner une réduction de la pénétration moléculaire et une réduction de la résistance à la traction, la différence de résistance à la traction dans cette direction est liée à la soudure entre les couches. L'anisotropie a toujours été l'une des propriétés mécaniques importantes prises en compte lors de la sélection des matériaux. La figure 1.a montre la résistance à la traction des échantillons imprimés avec des angles de trame de 0^{o} et 90^{o} à des vitesses de buse de 210 et 230 °C. Selon l'équation, la réduction de la vitesse de la buse de 60 à 18 mm/s a permis de réduire l'anisotropie de 33%.

Figure 3 Résistance à la traction (a) d'échantillons avec des angles de trame de 0^{o} et 90^{o} à des

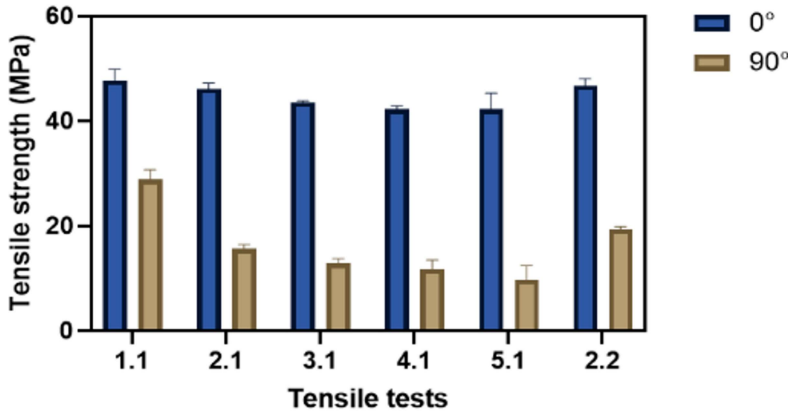

FIGURE B.11 – Résistance à la rupture d'échantillons : 0^o et 90^o à des vitesses de buse de 210 et 230 °C

vitesses de buse de 210 et 230 °C, (b) avec un angle de trame de 90^o en fonction du degré de cristallinité à une température de buse de 210 °C.

B.3.3 Liaison interfaciale dans le procédé FFF

Pour mieux prendre en compte les couches intermédiaires, les essais ont été réalisés sur les échantillons imprimés à 90°. La vitesse de la buse était de 10 à 60 mm/s pour fabriquer les échantillons à une température de buse de 210 °C dans une température de lit de 60°. L'analyse mécanique dynamique (DMA) est une méthode qui consiste à soumettre un échantillon à une charge oscillante pour mesurer ses propriétés mécaniques en ce qui concerne le comportement élastique (module de stockage) et visqueux (module de perte). Le module de stockage, noté G', représente la quantité maximale d'énergie qui peut être stockée pendant un cycle d'oscillation et reflète la rigidité du matériau. Le module de perte, noté G", reflète la quantité d'énergie dissipée par le matériau en raison du frottement interne. Le rapport entre le module de perte et le module de stockage est appelé facteur d'amortissement ou tan(),

où est l'angle de phase entre la déformation et la réponse de l'échantillon. Le facteur d'amortissement donne une idée de la capacité de dissipation d'énergie du matériau et est lié au degré de mobilité moléculaire, qui influe sur la résistance du matériau. L'augmentation de la température s'accompagne d'une réduction du module de stockage (Figure 2(a)). La vitesse de cette diminution augmente considérablement après la transition vitreuse de l'échantillon correspondant à la fréquence de l'essai. Cette observation est liée à l'augmentation de la mobilité et de la relaxation de la chaîne à des températures plus élevées, ce qui entraîne une diminution de la rigidité ou du module de stockage du polymère. La fraction de volume libre et la mobilité des chaînes de polymères sont liées en ce sens que le volume libre dans une matrice de polymères offre aux chaînes de polymères un espace pour se déplacer et se réorganiser. Le volume libre dans les polymères peut être attribué au volume de la masse totale qui n'est pas engagé par les chaînes de polymères. Il en résulte une augmentation de la mobilité des chaînes de polymères, qui peut avoir un effet significatif sur les propriétés mécaniques et physiques du matériau. Le volume libre désigne les espaces entre les chaînes de polymère qui ne sont pas occupés par des molécules de polymère. Ces espaces sont souvent créés au cours du processus de polymérisation ou par des contraintes thermiques ou mécaniques. Lorsqu'une chaîne de polymère est confinée dans une matrice, son mouvement est limité par les chaînes environnantes. Cependant, le volume libre dans la matrice offre aux chaînes de polymère un espace pour se déplacer et se réorganiser, ce qui augmente la mobilité des chaînes. Lorsque la fraction de volume libre augmente, les chaînes de polymère peuvent se déplacer plus librement et le matériau devient plus ductile et moins cassant. En effet, le volume libre agit comme un lubrifiant, réduisant la concentration de contraintes dans le matériau et permettant

aux chaînes de polymères de se déplacer plus facilement. En revanche, lorsque la fraction de volume libre est réduite, les chaînes de polymères sont davantage contraintes et leur mobilité est limitée. Cela peut entraîner une augmentation de la rigidité et de la résistance du matériau, ainsi qu'une diminution de sa ductilité. On peut noter qu'en augmentant la fréquence, la température de transition , T (liée à Tg) a une tendance à augmenter vers les hautes températures. Le comportement viscoélastique des polymères est affecté par la fréquence de la charge appliquée. Cette relation entre la température et la viscosité est directement proportionnelle à la fréquence. En outre, l'équation de Williams-Landel-Ferry (WLF) décrit la corrélation entre la température et les temps de relaxation moléculaire des substances vitreuses à la température de transition vitreuse (Tg). L'équation est la suivante :

$$Ln\frac{f}{f_R} = \frac{C_1(T - T_g)}{C_2 + (T - T_g)} \tag{B.17}$$

où f et fr sont respectivement la fréquence et la fréquence de référence (1 Hz). T indique la température et Tg est la température de référence. C1 et C2 sont les constantes caractéristiques du matériau, associées à la fraction de volume libre et données par :

$$C_1 = \frac{B}{2.303\ f_g} \tag{B.18}$$

$$C_2 = \frac{fg}{\Delta\alpha} \tag{B.19}$$

fg correspond à la fraction volumique à l'état de transition vitreuse. B est une constante proche de 1, indique le coefficient d'expansion. a) b) Figure 4 (a) Augmentation de la température de transition vitreuse au cours d'essais DMA multifréquences, (b) Diagramme WLF obtenu à partir d'essais DMA multifréquences. La figure 2(b) montre le logarithme naturel du rapport de fréquence en fonction de

l'inverse de la différence de température. La régression linéaire des résultats expérimentaux avec une corrélation de plus de 0,98, la pente du tracé de la ligne droite est appelée rapport de C1 à C2. D'après les résultats, la fg augmente en réduisant la vitesse de la buse. On peut dire que la réduction de la fraction de volume libre permet une meilleure mobilité des chaînes qui s'accompagne d'une meilleure adhésion des filaments.

B.3.4 Liaison interfaciale : Formation de l'interface et étude de l'interphase

L'interface entre les couches joue un rôle essentiel dans les propriétés mécaniques des pièces FFF. Des études ont mentionné l'anisotropie des pièces FFF comme un défi dans ce processus qui est lié aux propriétés des liaisons inter-couches. Le processus de liaison entre les filaments peut impliquer trois mécanismes : le contact de surface, la croissance du col sous l'effet de la tension de surface, et la diffusion et l'enchevêtrement moléculaires à travers l'interface inter-filament. Des études ont tenté de réduire l'anisotropie en se concentrant sur l'augmentation de la diffusion des chaînes de polymères dans l'interface de voisinage. Il convient de noter que la pénétration intermoléculaire des chaînes de polymère suit la loi de puissance, qui est affectée par le temps de soudage. En d'autres termes, le temps de soudure est le facteur déterminant dans la formation de la couche intermédiaire appropriée, de sorte que moins de temps de soudure indique une mobilité plus appropriée des chaînes de polymères pour pénétrer. Compte tenu de la relation entre le temps de relaxation et le temps de soudage, des analyses rhéologiques hors ligne ont été effectuées sur les pièces imprimées. En raison des conditions non isothermes pendant le processus FFF, le facteur de décalage, (T), en utilisant la superposition temps-température qui est calculé par l'équation de William-Landel-Ferry (WLF) doit être déterminé

:

$$\eta_0(T) = exp\left(\frac{-C_1(T-T_0)}{C_2+(T-T_0)}\right) \tag{B.20}$$

où T est la température pour la détermination de α(T) à cette température, T_0 représente la température de référence, C_1 et C_2 sont les paramètres ajustés constants. D'après les études, le temps de relaxation moyen du nombre, τ_n, peut être considéré approximativement comme le temps de relaxation:

$$\tau_d(T) \cong \tau_n(T) = \frac{\eta_0(T)}{G_N^0} \tag{B.21}$$

où η_0 et G_N^0 représentent respectivement la viscosité à cisaillement nul et le module de plateau. Compte tenu du temps de relaxation et de la température établie, le temps de soudage a été défini comme suit :

$$\tau_w = \frac{\tau_d(T)}{M_{corr}} \tag{B.22}$$

M_{corr} désigne une constante qui convertit le temps de reptation mesuré en temps de reptation. τ_{weld} et, d'après la littérature, elle peut être déterminée comme étant égale à 18. Des mesures rhéologiques hors ligne ont été effectuées pour transformer les profils de température non isothermes en un temps de soudure isotherme. À cet égard, les facteurs de décalage des expériences de cisaillement oscillatoire sur une large gamme de températures ont été déterminés et sont liés aux temps de relaxation sur une large gamme de températures. La figure B.12(a) montre le module de stockage et de perte pour la gamme de fréquences de 1 à 100 Hz à différentes températures, la viscosité complexe dans ces conditions a été montrée dans la figure B.12(b).

L'étude a porté sur deux paramètres critiques, à savoir la viscosité à cisaillement nul (η_0) et le

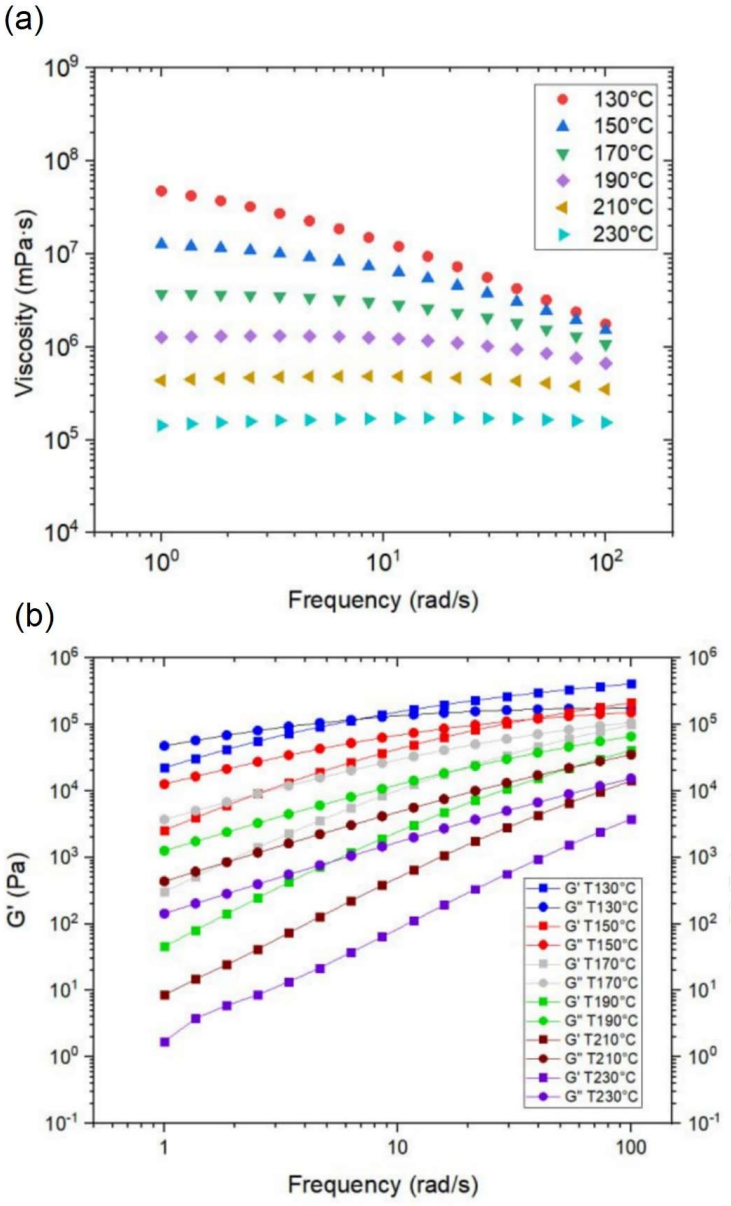

FIGURE B.12 – Viscosité complexe pour la gamme de fréquences de 1 à 100 Hz à différentes températures et (b) Module de stockage et de perte

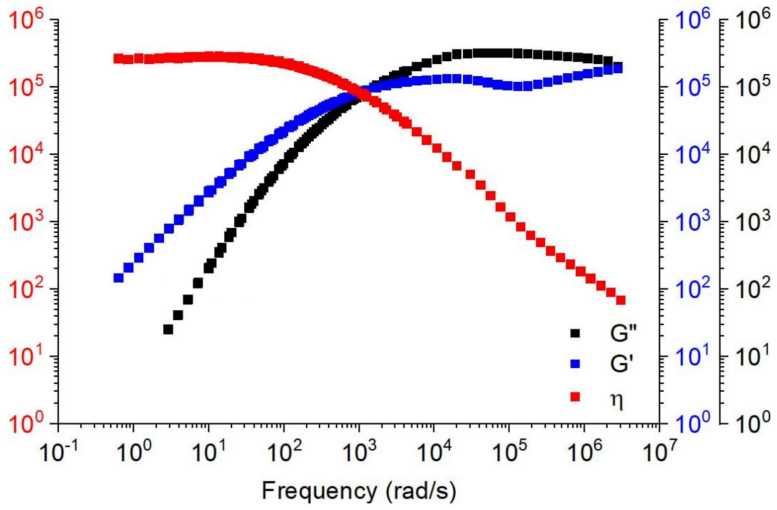

FIGURE B.13 – Courbe maîtresse temps-température-superposition à 220 °C

module de plateau (G_N^0). Le modèle Cross-WLF a été utilisé pour calculer la viscosité à cisaillement nul en examinant la viscosité en fonction du taux de cisaillement et de la température. Le module de plateau correspond au module de stockage (G) à la fréquence où le module de perte (G") atteint un minimum. Le module plateau a été défini comme la valeur G au deuxième croisement G-G", conformément à la littérature établie. La figure B.13(a) présente le calcul de G_N^0 et 0 sur la base d'une courbe maîtresse temps-température-superposition à 220 °C.

L'augmentation de la température s'accompagne d'une réduction du temps de soudage. On peut dire qu'un temps plus long permet une meilleure diffusion et un meilleur enchevêtrement des molécules à l'interface de la soudure. L'effet du temps de soudage sur les propriétés mécaniques a été analysé en fonction des différents paramètres du processus, à savoir la température et la vitesse de la buse.

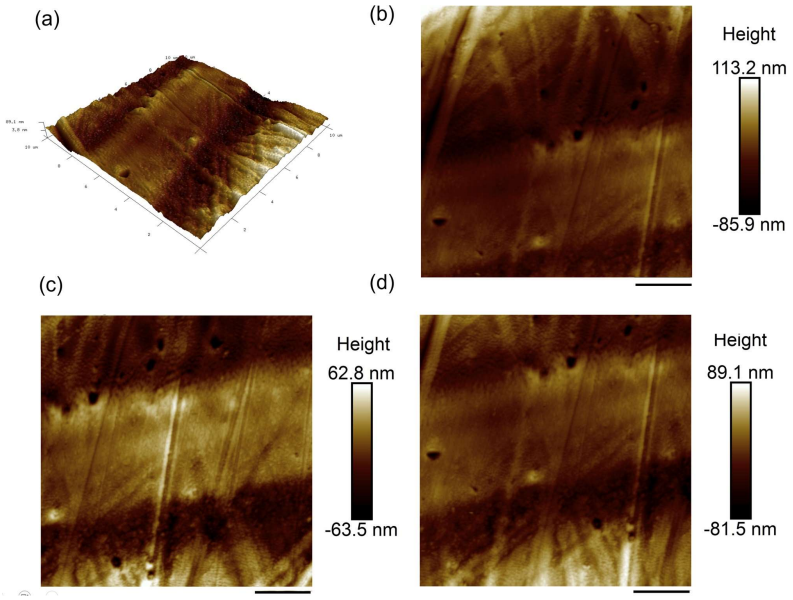

FIGURE B.14 – Images AFM : la section transversale polie de l'échantillon imprimé par FFF au niveau de la zone de soudure.

B.3.5 Analyse microstructurale de la couche intermédiaire

Images de microscopie à force atomique (AFM) de la section transversale polie de l'échantillon imprimé par FFF près de la zone intercalaire (Figure B.14). D'après les résultats, l'interface de soudure peut être indiquée sur les images. Cette zone peut être liée à l'interphase entre chaque couche polymère qui peut impliquer environ 4 µm. Cette interphase est causée par la diffusion intermoléculaire des chaînes dans chaque couche voisine. Pour analyser l'effet des paramètres du processus dans cette zone, des images microscopiques ont été obtenues.

Le dépôt de deux couches de polymères pendant l'impression entraîne la formation d'une interphase entre deux polymères fondus. Cette interphase est une région de transition où les propriétés des deux polymères se mélangent progressivement, ce qui donne une zone de matériaux partiellement mélangés

qui se trouve entre la masse de chaque polymère. La zone d'interphase peut avoir un impact significatif sur la force et la durabilité de la liaison qui se forme entre deux polymères. La liaison résultante sera forte et durable si l'interphase est bien formée et présente une forte adhérence entre les deux polymères. En revanche, si l'interphase est faible ou mal formée, la liaison sera plus faible et plus susceptible de se rompre. Il est donc essentiel de comprendre et de contrôler l'interphase pendant le soudage des polymères pour obtenir des liaisons solides et durables entre différents polymères. Cet objectif peut être atteint grâce à un contrôle minutieux des paramètres du processus, tels que la température de la buse, la vitesse de la buse et la température du lit, qui entraînent des temps de soudage, une viscosité et une pression différents. L'interphase entre deux couches de polymères a été analysée par microscopie optique. La figure 6 montre les images microscopiques de la paroi mince unicolore et bicolore. Comme on peut le voir, l'interphase n'est pas visible en mode monochrome, ce qui montre l'objectif d'utiliser deux couleurs pour l'impression des échantillons. Les résultats montrent que cette distance augmente en augmentant la température de la buse et en diminuant la vitesse de la buse. Compte tenu des résultats mécaniques de l'essai de microtraction, on peut dire que la qualité de l'interphase peut jouer un rôle plus important que la ligne de soudage en ce qui concerne la température et la vitesse de la buse.

Le test de micro-traction a permis d'analyser le comportement mécanique entre deux couches imprimées. La figure B.16 montre les courbes contrainte-déformation de ce test. D'après les résultats, la température de la buse de 22O °C à une vitesse de 500 °C a montré un UTS d'environ 13,3 MPa qui était meilleur que les deux autres températures de buse à cette vitesse. On peut dire que l'augmentation

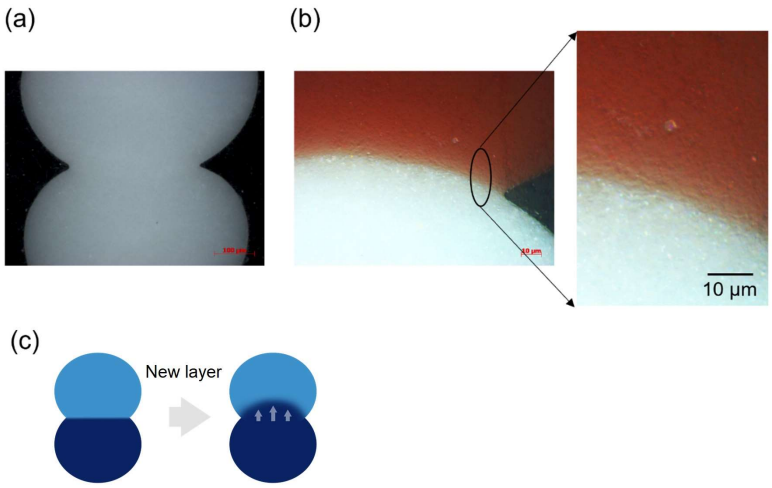

FIGURE B.15 – (a) Image microscopique d'une paroi mince unicolore, (b) image microscopique d'une paroi mince bicolore et (c) schéma de l'interphase entre deux couches de polymères.

de la température de 210 à 220 °C s'accompagne d'une amélioration de la résistance à la traction, mais qu'au-delà de cette température, la résistance à la traction commence à diminuer. L'amélioration de la résistance inter-couche par l'augmentation de la température peut s'expliquer par le temps de soudage, de sorte que la réduction du temps de soudage par l'augmentation de la température et la réduction de la viscosité peuvent offrir de meilleures conditions d'adhésion des filaments adjacents. De plus, une réduction de l'anisotropie des pièces imprimées en PA-FFF est observable en réduisant le temps de soudure.

B.3.6 Amélioration de la liaison entre les couches et optimisation des paramètres d'impression

En ce qui concerne la vitesse de rotation élevée nécessaire pour fournir la pression adéquate dans le compresseur, le PPS a été utilisé comme polymère à haute performance pour la fabrication de la roue. Pour mieux comprendre l'anisotropie mécanique induite par la technique FFF, l'effet de la température

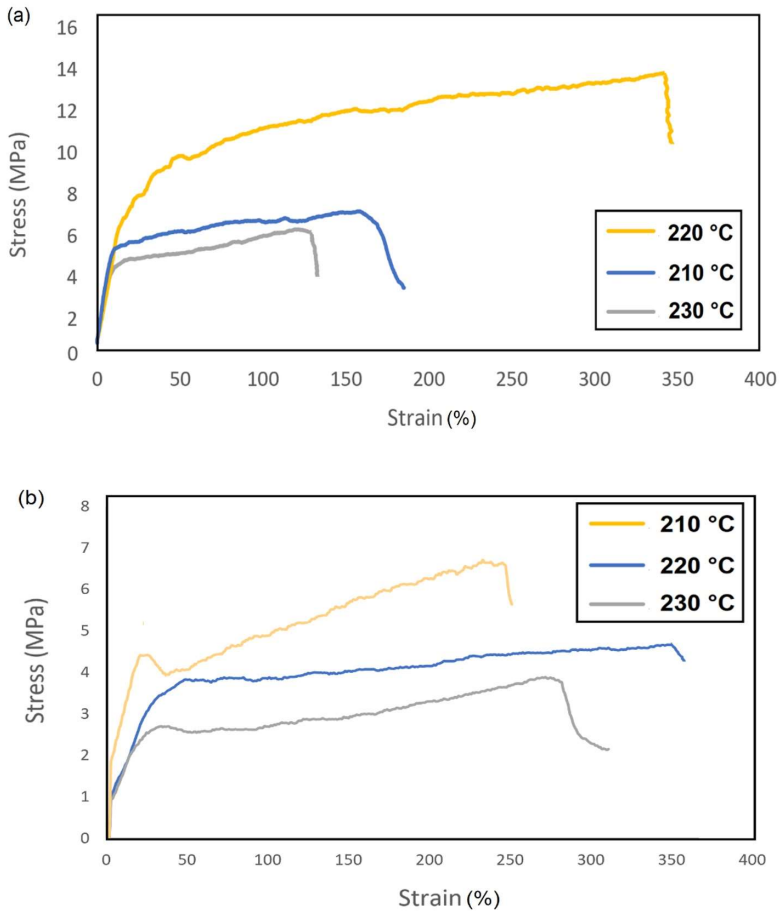

FIGURE B.16 – Courbe contrainte-déformation de l'essai de microtraction : (a) à une vitesse de buse de 500 et (b) à une vitesse de buse de 2000 mm/s

et de la vitesse des buses sur les propriétés mécaniques des pièces imprimées par FFF a été étudié. En outre, le recuit des échantillons à différents moments a été choisi comme méthode de post-traitement pour améliorer les propriétés mécaniques. Les conditions optimisées par la valeur la plus élevée ont été sélectionnées en analysant les valeurs du Gray Relational Grade (GRG) dans le 16e essai à l'aide de l'ANOVA et de l'étude S/N. On constate que l'augmentation de la température de la buse entraîne une diminution de la cristallinité, ce qui améliore légèrement la résistance à la traction des pièces en PPS avec les brins déposés parallèlement à la direction de chargement (c.-à-d. angle de trame = 90°). Enfin, la fabrication d'une roue avec des paramètres optimisés a été étudiée en examinant la surface au moyen d'un MEB et en analysant la précision géométrique à l'aide d'un scanner 3D. La normalisation des données expérimentales a été effectuée par la méthode GRA. En fonction des caractéristiques de qualité attendues des différentes réponses, cette valeur peut être divisée en trois critères d'optimisation dans cette méthode. Les équations suivantes indiquent respectivement que " plus grand est mieux ", " plus petit est mieux " et " normal est mieux " :

$$X^*(p) = \frac{X_i\,(p) - Min(X_i\,(p))}{Max(X_i\,(p)) - Min(X_i\,(p))} \tag{B.23}$$

$$X^*(p) = \frac{Max(X_i\,(p)) - X_i\,(p)}{Max(X_i\,(p)) - Min(X_i\,(p))} \tag{B.24}$$

$$X^*\,(p) = 1 - |Xip - OB|Max[Max(Xip) - OB, OB - Min(Xip)] \tag{B.25}$$

- Max(Xi (p)) : valeur la plus élevée de Xi (p)
- Min(Xi (p)) : valeur minimale de Xi (p),
- OB: la valeur cible,

- X* (p): est la valeur GRG,
- i: désigne le nombre d'essais,
- Xi(p): valeur de la réponse de l'expérience cible

La résistance à la traction, le module d'Young et la cristallisation sont normalisés en utilisant la règle " plus c'est grand, mieux c'est ". La séquence des écarts a été calculée à partir de l'équation :

$$\Delta_{oi} = ||X_0(p) - X_i(p)|| \tag{B.26}$$

Après la séquence d'écarts, le coefficient de relation de gris reflète le lien entre les résultats expérimentaux idéaux et normaux (GRC). L'équation suivante détermine le coefficient de liaison de gris pour chaque donnée normalisée :

$$X^*(p) = 1 - \frac{\Delta_{min} + \zeta.\Delta_{max}}{\Delta_{oi}(p) + \zeta.\Delta_{max}} \tag{B.27}$$

Où ζ est le coefficient d'identification et se situe entre 0 et 1 et est généralement considéré comme 0,5 et ζi (p) définit le coefficient de relation de gris. En outre, les valeurs de Δ (p) pour min et max sont respectivement Δmax et Δmin. Les qualités multiréponses sont généralement évaluées à l'aide de la note relationnelle grise (GRG). D'autre part, la GRG est calculée à l'aide de l'équation suivante, le total moyen de la GRC :

$$\gamma_i = \frac{1}{n}\sum_{i=1}^{n}\zeta(p) \tag{B.28}$$

Où n est le nombre de paramètres du processus, un GRG plus élevé indique que la combinaison des paramètres du processus est plus proche de l'idéal. Ensuite, toutes les expériences ont été triées en fonction des valeurs GRG comprises entre 1 et 16, la valeur GRG la plus excellente désignant

l'essai optimal, considéré comme étant en première position. Le 9e essai, qui a la valeur GRG la plus excellente, présente les meilleures qualités par rapport aux autres essais. L'analyse de la variance (ANOVA) et les tests du rapport signal/bruit (S/N) ont été effectués un par un sur les données obtenues expérimentalement. Toutes les données ont été analysées avec MINITAB® 19.0. La technique Taguchi est utilisée pour examiner l'impact d'un grand nombre de paramètres sur une réponse particulière. La figure B.17 montre les courbes correspondant aux différentes conditions d'impression et de post-traitement des comportements mécaniques des échantillons.

Le rapport signal/bruit (S/B) est utilisé pour analyser les effets de chaque paramètre sur la réponse et optimiser les paramètres du processus. Par conséquent, un rapport S/B plus élevé indique des circonstances idéales. En utilisant MINITAB®19.0, l'analyse de la variance (ANOVA) et le rapport signal/bruit ont été utilisés pour examiner les données du GRG. La méthode Taguchi a été utilisée pour analyser l'impact du GRG sur les résultats. L'approche " plus grand est meilleur " a été utilisée pour maximiser le GRG afin d'optimiser les paramètres du processus, car plus la valeur du GRG est élevée, meilleures sont les réponses attendues. Le figure 10 montrent différents niveaux pour chaque paramètre en fonction du rapport S/N moyen. D'après les résultats, les paramètres de processus idéaux pour produire le GRG le plus élevé peuvent être atteints à une température d'impression de 340 °C, une durée de recuit de 6 h et une vitesse d'impression de 20 mm/min.

La méthode ANOVA a été utilisée pour évaluer les effets de chaque paramètre du processus sur les variables de réponse. La somme des carrés ajustée (Adj SS) peut être obtenue par :

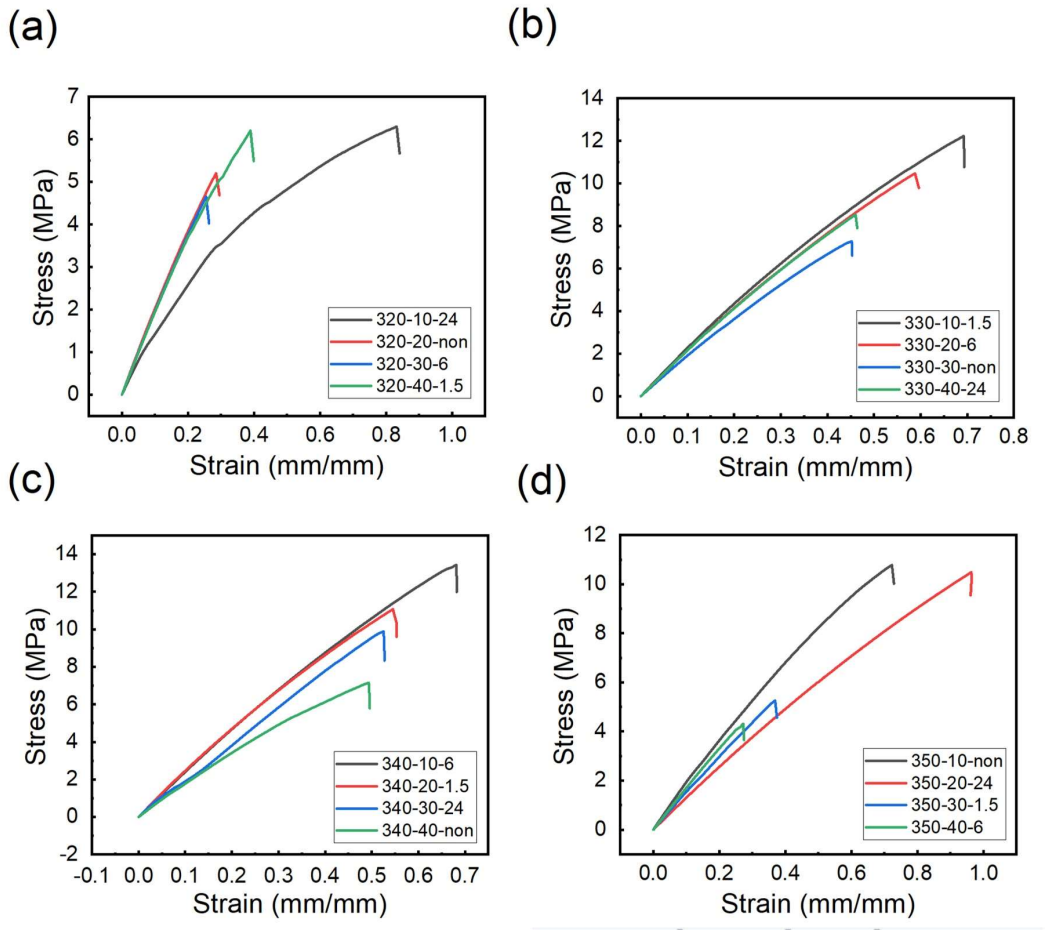

FIGURE B.17 – Courbe contrainte-déformation des échantillons dans différentes conditions d'impression et de recuit

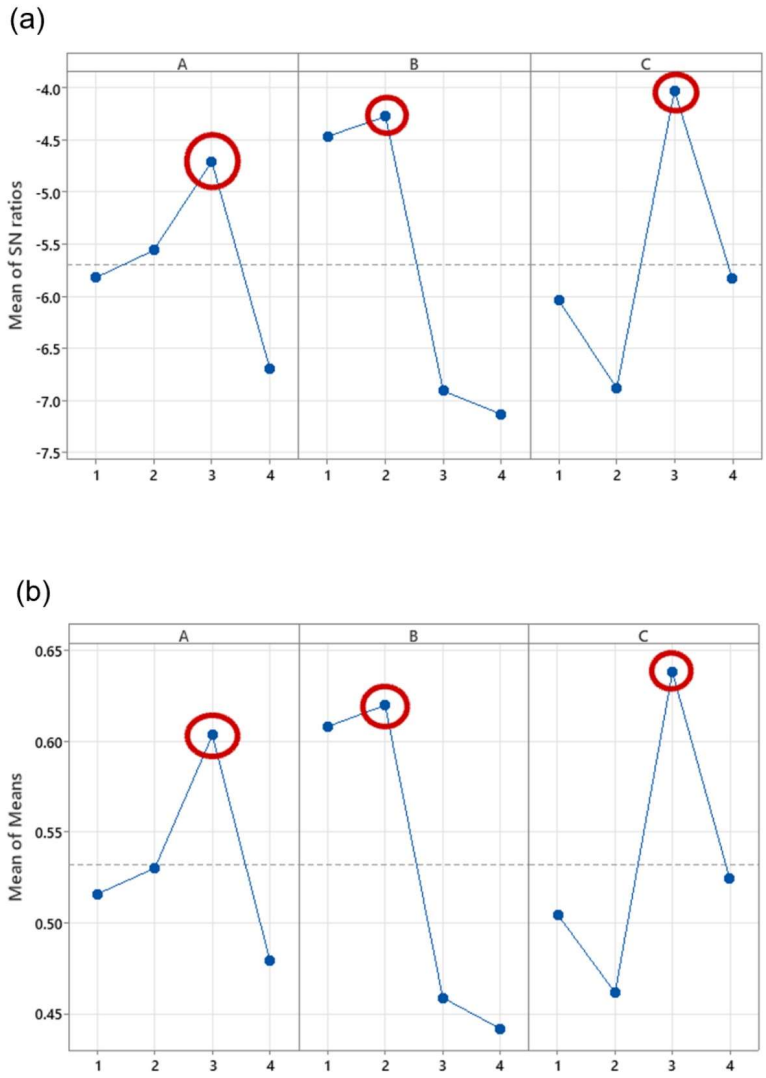

FIGURE B.18 – Graphique des effets principaux pour (a) les rapports S/N GRG et (b) les moyennes GRG

TABLE B.3 – Réponse des paramètres variables de la GRG

Source	DF	Adj SS	Adj MS	Valeur F	Valeur P
A	3	0.03263	0.010876	2.94	0.121
B	3	0.10802	0.036007	9.72	0.010
C	3	0.06816	0.022719	6.14	0.029
Error	6	0.02222	0.003703		
Total	15	0.23102			

$$s_T = \sum_{i=1}^{n} (\eta_i - \eta_j)^2) \tag{B.29}$$

Dans cette formule, i représente le rapport S/N moyen, j le rapport S/N moyen total et n le nombre total d'expériences. Il a été constaté que la vitesse d'impression, le temps de recuit et la température d'impression ont les effets les plus significatifs sur la quantité de GRG, respectivement, en examinant la valeur F mentionnée dans le Tableau B.3 et en tenant compte de la règle selon laquelle plus la valeur est élevée, plus l'effet du paramètre concerné est important.

Les diagrammes de surface et de contour, qui sont des représentations visuelles de l'équation de régression, sont présentés dans les figuresB.19 et B.20, respectivement. Ils ont été créés par le logiciel MINITAB 19.0 et décrivent les interactions entre deux paramètres de processus distincts sur le GRG. Ces figures montrent que la valeur maximale du GRG se situe entre 330 et 340 °C aux températures de recuit les plus élevées et aux vitesses d'impression les plus faibles.

Dans la dernière étape, une expérience de confirmation a été réalisée en utilisant les niveaux optimaux des paramètres du processus pour vérifier ce paramètre obtenu à partir du GRA et également pour évaluer l'amélioration dans les réponses. Pour garantir la répétabilité des résultats, cinq pièces d'essai de traction avec des paramètres optimaux ont été fabriquées par l'imprimante 3D FFF. La

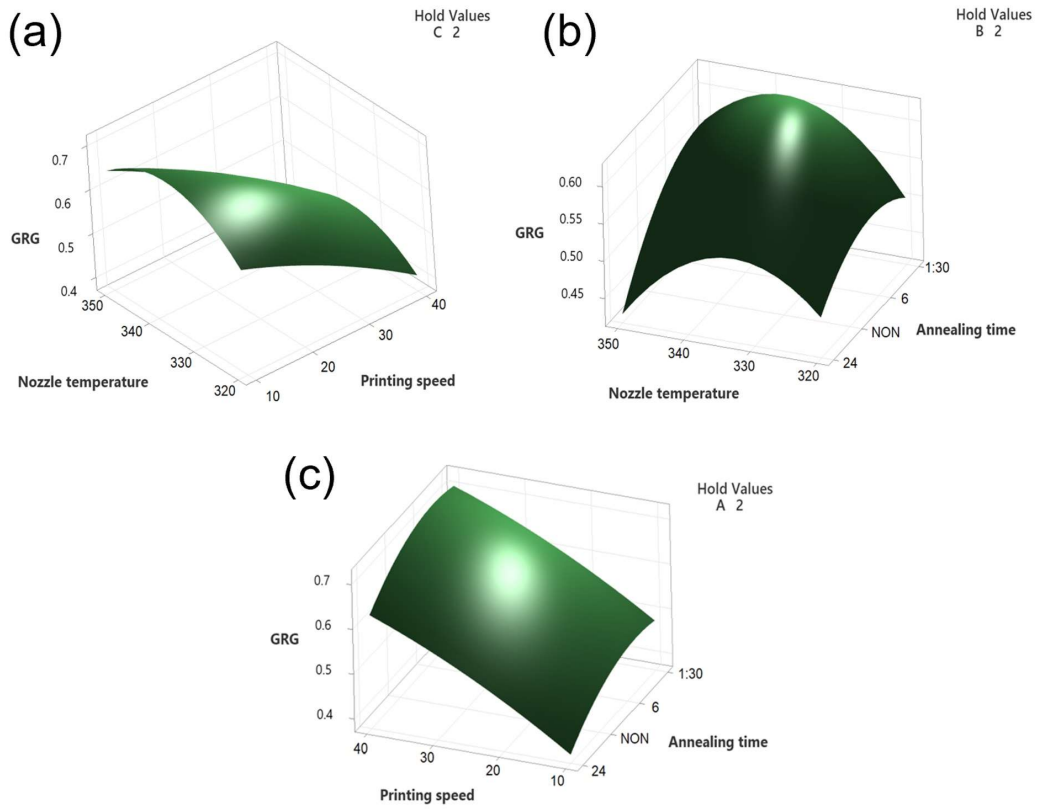

FIGURE B.19 – Tracés de surface GRG. (a) vitesse d'impression et température de la buse, (b) température de la buse et temps de recuit, (c) temps de recuit et vitesse d'impression sur GRG

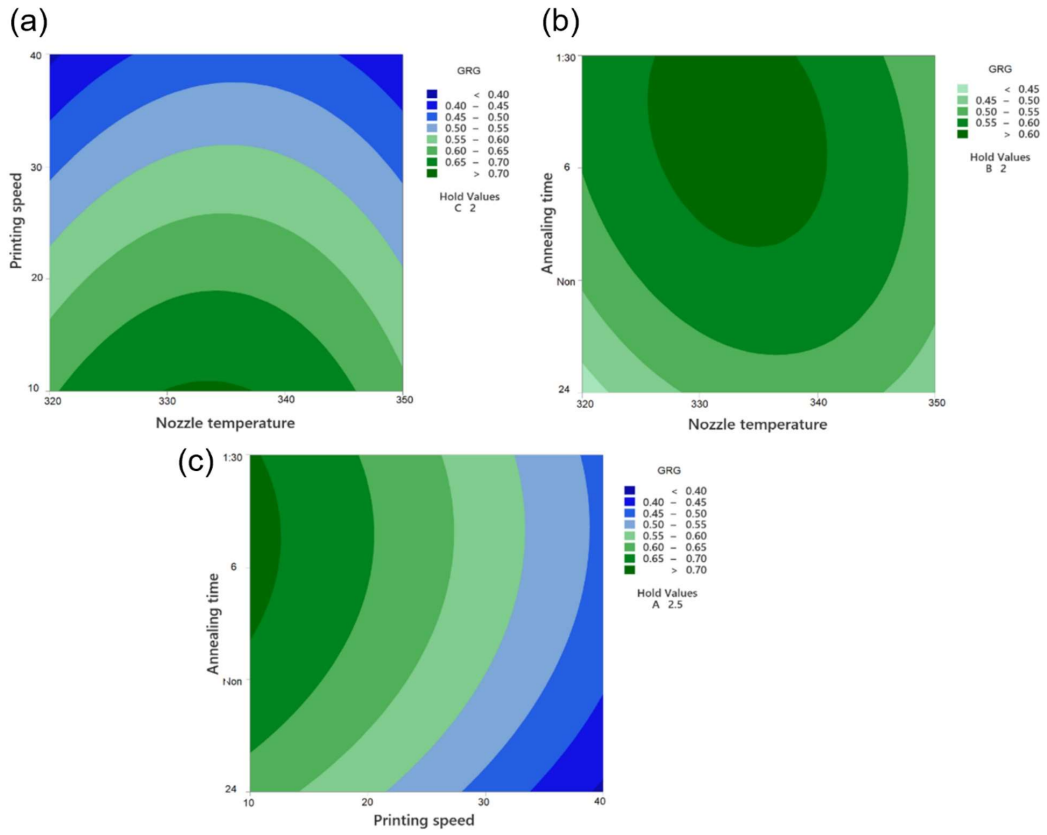

FIGURE B.20 – Tracés de contour GRG. L'effet de : (a) la vitesse d'impression et la température de la buse, (b) la température de la buse et le temps de recuit, (c) le temps de recuit et la vitesse d'impression sur le GRG

valeur prédite de la note relationnelle grise ou Yprévu est comparée à la valeur moyenne de la note relationnelle grise est utilisée pour calculer la valeur prédite de la note relationnelle grise pour les paramètres optimaux.

$$Y_{Predicted} = y_m + \sum_{i=1}^{n} (y_i - y_m) \tag{B.30}$$

$$Error(\%) = [\frac{GRG_{Predicted} - GRG_{Experimental}}{GRG_{Experimental}}] * 100 \tag{B.31}$$

$$Improvment(\%) = [GRG_{Experimental} - GRG_{Intitial}] * 100 \tag{B.32}$$

Où y_m représente la moyenne totale du GRG, yi se réfère au GRG moyen au niveau optimal, et n est le nombre de paramètres de processus choisis. Ensuite, un test de compression a été appliqué aux pièces pour évaluer la résistance et le module d'Young des pièces en PPS. Après avoir calculé le GRG expérimental, l'amélioration du GRG est évaluée par le pourcentage d'erreur entre le GRG prédit et le GRG expérimental. Toutes les valeurs mesurées du GRG sont indiquées dans le Tableau 3 Valeurs mesurées des réponses, et en comparant le GRG initial et le GRG obtenu à partir de l'expérience, il a été constaté que la valeur optimale du GRG s'est améliorée de 10%. Les résultats montrent donc que les valeurs des paramètres optimaux obtenues par la méthode GRA ont amélioré toutes les réponses prévues. De même, en comparant le GRG prédit et le GRG de l'expérience, on a constaté que le taux d'erreur est égal à 5 et on peut dire qu'il y a une bonne corrélation entre ces valeurs.

TABLE B.4 – aleurs mesurées des réponses

	Paramétrage initial	Paramètre optimal	
		Prévu	Expérimental
Niveau de réglage	N° expérimental 9 (340-10-6)	Échantillon code (340-20-6)	Échantillon code (340-20-6)
Module de Young (MPa)	2432.6		3153.6
Résistance ultime (MPa)	13.3		11.7
Cristallinité (%)	26.6		27.1
GRG	0.660	0.796	0.757

B.3.7 Effet des paramètres du procédé

Le soudage correct des pièces FFF peut être considéré comme un paramètre important qui a un impact sur les propriétés mécaniques finales des échantillons. Ainsi, l'amélioration de la qualité de la zone de soudure est suivie par l'amélioration des propriétés mécaniques. Pour les polymères semi-cristallins, la nucléation et la croissance des sphérulites peuvent être présentées comme un paramètre qui a un impact important sur la diffusion moléculaire de la chaîne entre deux filaments qui pourrait être continue jusqu'à Tg. En fait, la création de sphérulites après la diffusion de la chaîne entre deux couches peut améliorer le comportement mécanique des pièces, sinon, l'augmentation de la cristallisation dans les pièces de sorte que les couches précédentes seraient un bon endroit pour la germination ne peut pas améliorer la performance mécanique et a un effet négatif. Les résultats de l'ajustement du modèle ont montré l'amélioration des propriétés mécaniques et l'augmentation du degré de cristallisation à des températures d'impression plus élevées et à une vitesse moindre pour un temps de recuit de 90 minutes à 6 heures. La figure B.21 montre les résultats DSC des échantillons imprimés sans recuit, avec un pic exothermique autour de 122 °C et un pic endothermique entre 250 et 285 °C. Le pic

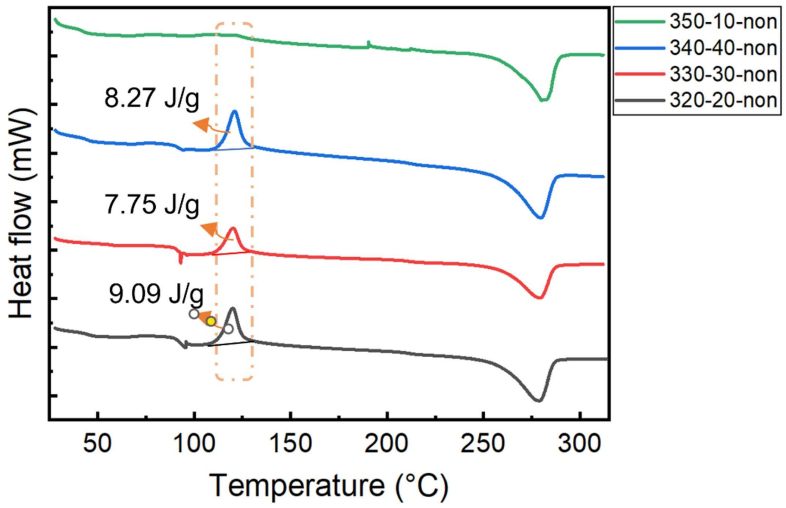

FIGURE B.21 – Résultats DSC des échantillons sans conditions de recuit

exothermique se réfère à la température d'impression et à la vitesse de recuit. Le pic exothermique fait référence à la cristallisation froide qui peut correspondre à la mise en ordre des chaînes moléculaires dans les lamelles cristallines de PPS et est associée au chauffage. Il a été démontré que l'augmentation de la cristallisation par la réduction de la température de la buse est attribuée au résultat d'une fusion incomplète de la région cristalline dans la buse avec une température plus basse et non uniforme à l'intérieur. Les résultats DSC de la figure B.21 montrent le changement de l'enthalpie de cristallisation à froid en modifiant les paramètres du procédé, de sorte que le minimum de cette valeur (0,85 J/g) a été rapporté pour une température d'extrusion de 350 °C avec une vitesse de buse de 10 mm/min sans processus de post-chauffage. On peut dire qu'une température plus élevée avec des vitesses plus faibles permet une meilleure fusion pendant l'impression.

La figure B.22 montre l'analyse électronique à balayage (MEB) d'échantillons sans charge et après impression. L'analyse fractographique des échantillons construits à différentes épaisseurs de couche est

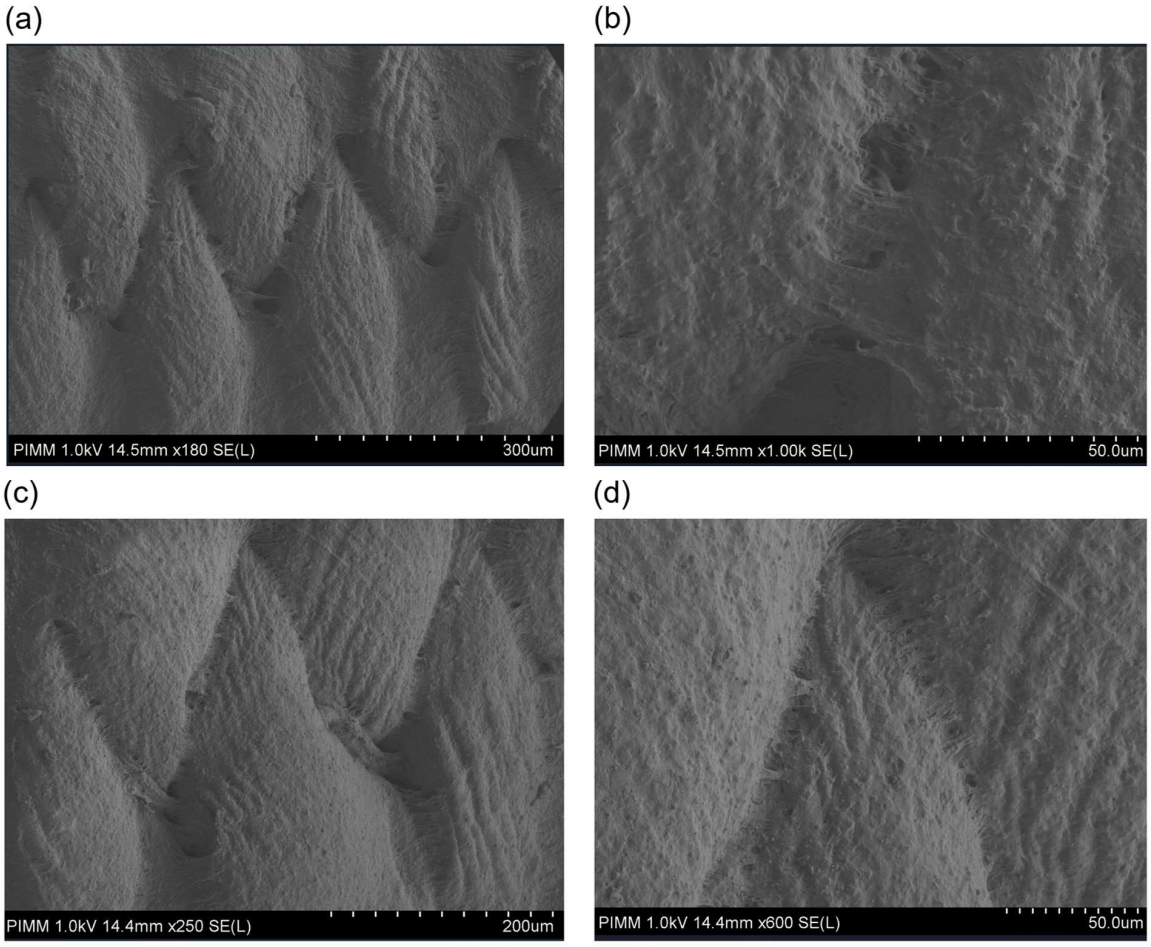

FIGURE B.22 – Analyse électronique à balayage des échantillons à différents grossissements : (a et b) échantillon de 340-40-non et (c et d) paramètres optimisés (340-20-6h).

illustrée. D'après les résultats, la surface des échantillons imprimés avec le paramètre optimisé montre une meilleure coalescence entre les couches polymères et moins de vides que les autres échantillons.

B.3.8 Fabrication de roues de compresseurs

La fabrication de roues à aubes en polymère a fait l'objet de beaucoup d'attention. Dans le cas des compresseurs, les roues à aubes peuvent fournir la pression de fluide appropriée à certaines vitesses

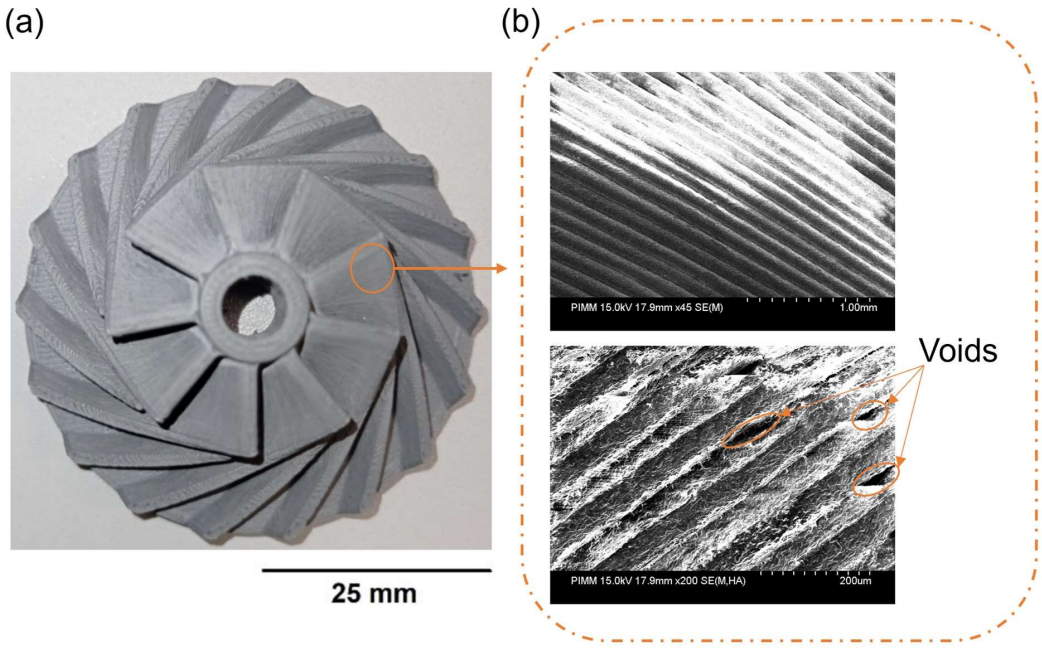

FIGURE B.23 – (a) Roue imprimée en 3D et (b) images SEM avec différents grossissements sur l'aube de la roue.

de rotation. L'utilisation de la FFF est une bonne méthode pour la fabrication de ces pièces en raison de la complexité de leur géométrie. La figure B.23 montre une roue fabriquée avec un processus de paramètres optimisé. Compte tenu de l'importance de la coalescence entre les couches polymères sur les performances finales du compresseur, la surface des pales a été examinée au microscope électronique à balayage. Les images microscopiques montrent une bonne soudure entre les couches, mais une porosité est visible entre certaines couches.

B.3.9 Conclusions

La relation entre le processus de fabrication et les propriétés des pièces FFF a été démontrée. Différentes méthodes de caractérisation ont été utilisées pour montrer l'importance des paramètres du

procédé sur les propriétés physicochimiques et mécaniques. L'interphase entre deux couches polymères a été analysée au microscope optique. En outre, l'effet de deux paramètres du procédé, à savoir la vitesse et la température de la buse, ainsi que la durée du recuit en tant que méthode de post-traitement, sur le comportement mécanique de la couche intermédiaire et le pourcentage de cristallisation des pièces imprimées ont été étudiés. Le sulfure de polyphénylène a été choisi comme polymère à haute performance pour cette étude. Les paramètres ont été optimisés par le biais d'une optimisation multiréponse utilisant la méthode GRA. Les paramètres du processus et le temps de recuit ont été trois variations en tant que paramètres d'entrée pour obtenir les meilleures propriétés mécaniques inter-couches et un pourcentage de cristallisation élevé. L'analyse des données GRG par ANOVA et S/N a montré que les paramètres optimaux du processus étaient la température de la buse et la vitesse de 340 et 20 mm/s, respectivement, avec un recuit à 200 °C pendant 6 heures. Les résultats microscopiques montrent l'importance des paramètres sur la coalescence appropriée entre les couches imprimées qui ont un impact sur les propriétés mécaniques et physico-chimiques. Les paramètres optimisés ont été utilisés pour fabriquer une roue de compresseur et les pièces fabriquées ont été examinées à l'aide d'un MEB et d'un scanner 3D.

B.4 Relation entre le procédé de fabrication SLA et les propriétés des pièces

B.4.1 Effet des paramètres de traitement et de post-traitement sur les propriétés thermiques et physicochimiques

Pour étudier la stabilité thermique des échantillons, une analyse thermogravimétrique (TGA) a été réalisée. La figure 17 montre l'analyse TGA pour la résine, les échantillons verts et les échantillons

post-cuisson. La figure 17(a) montre les courbes thermogravimétriques dérivées pour chaque échantillon. D'après les résultats, la stabilité thermique des polymères réticulés est plus élevée que celle des polymères nets. Les résultats ont montré un nombre différent de stades de décomposition pour la résine par rapport aux échantillons verts et post-cuisson. La perte de poids pour la résine a montré une décomposition en 2 étapes alors que pour les autres échantillons, elle s'est produite en 3 étapes. Les étapes de décomposition de la résine ont été accumulées à 102,9, 352,9 et 438,20 °C, ce qui a entraîné une perte de résine de 23,4, 44,2 et 34,2%, respectivement. La première étape de décomposition est liée à l'évaporation des composants volatils des groupes acrylates à 102,9 °C. Les deuxième et troisième étapes de la dégradation de la résine ont coïncidé dans la température de la première et de la deuxième étape de dégradation des échantillons verts et post-cuisson. Comme indiqué, en général, toutes les résines utilisées dans la méthode SLA peuvent être durcies par chauffage dans une certaine plage. Ainsi, la résine sera durcie en augmentant la température pendant l'analyse TGA, ce qui peut conduire à une température de décomposition à peu près identique à celle des autres échantillons. L'échantillon vert et les échantillons post-cuisson ont montré une plus grande résistance thermique par rapport à la résine, ce qui représente le rôle important des réticulations sur le comportement thermique. La première perte de poids dans les échantillons a eu lieu à 352,9 °C et s'est accompagnée d'une perte de poids de 52,5%. Cette perte de poids peut être attribuée aux matières volatiles piégées qui sont libérées. L'étape suivante s'est produite à 438,20 °C et a représenté la fin de la réticulation et la dégradation thermique. La perte de poids de cette étape était de 47,5% et cette réduction peut être attribuée à la décomposition des structures aromatiques. Le TRT 80 °C a montré le meilleur

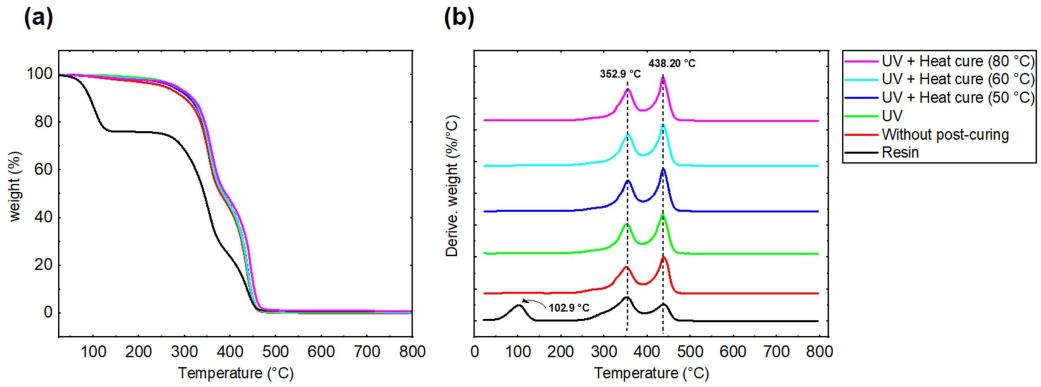

FIGURE B.24 – Stabilité thermique de la résine, sans post-cuisson et post-cuisson : (a) perte de poids par thermogravimétrie et (b) courbe thermogravimétrique dérivée.

comportement thermique parmi les autres échantillons, ce qui est lié à la densité des réticulations dans ces échantillons par rapport aux autres.

B.4.2 Effet du post-traitement sur la polymérisation

L'effet de la post-polymérisation sur la polymérisation des échantillons a été étudié à l'aide de la FTIR et de la DSC. En ce qui concerne les résultats FTIR, les changements d'absorption dans les groupes fonctionnels ont été étudiés. La figure B.25 montre les résultats FTIR liés au vert, à l'UV et à l'UV avec le durcissement à chaud à différentes températures dans la plage de 40 à 80 °C pour les échantillons imprimés à 0°. Les bandes d'absorption liées à la fonction méthacrylate, à l'amide II Les bandes d'absorption liées à la fonction méthacrylate, amide et C-O-C sont apparues aux pics de 1637, 1535, et 1100-1245 cm-1, respectivement. Le pic d'absorption à 1701 cm-1 correspond à la liaison C=O pour le diméthacrylate d'uréthane. Deux pics d'absorption de C=C à 1630 cm-1 et de l'amide II à 1532 cm-1 (I1630 cm-1/I1532 cm-1) ont été considérés comme un indice pour le calcul des monomères résiduels non polymérisés. Le rapport obtenu pour l'échantillon vert a été

considéré comme le contrôle du rapport montrant 100% de monomères non polymérisés résiduels. Par conséquent, les monomères non polymérisés résiduels pour les échantillons post-polymérisés ont été calculés en fonction du rapport de contrôle. Selon le rapport d'intensité, le pourcentage d'UDMA résiduel pour les échantillons post-polymérisation UV, UV avec chaleur 40 °C, UV avec chaleur 50 °C, UV avec chaleur 60 °C et UV avec chaleur 80 °C était respectivement de 83,77, 82,36, 79,36, 76,01 et 67,37%. La polymérisation de la résine en stéréolithographie peut être divisée en deux mécanismes : la photopolymérisation et la polymérisation thermique. Le mécanisme de photopolymérisation de la résine à base de (méth)acrylate s'effectue par le système radicalaire qui consiste en la génération, l'initiation et la propagation de radicaux ou la première étape de ce mécanisme, la génération de radicaux se produit en convertissant l'énergie photolytique en une réaction pour l'initiation de la polymérisation. Pour étudier les mécanismes de durcissement, des études ont analysé deux pics de bandes C=C à 810 et 1632 cm-1 qui sont liés au groupe acrylate. Les changements dans l'absorption de ces pics représentent la polymérisation des monomères pendant la réaction de réticulation. La figure **??** montre le rapport I1701 cm /I-1810 cm-1 en fonction de la température. La figure montre la relation linéaire avec un seuil à 50 °C ($R > 0{,}98$). Tout d'abord, la réaction de réticulation de la chaîne principale du polymère est dominante. D'autre part, on peut mentionner que la deuxième pente est liée aux réactions photochimiques latérales des chaînes macromoléculaires. D'après la plage de température utilisée pour la post-polymérisation, on peut dire que le mécanisme de polymérisation était le seul mécanisme photopolymérisé car, d'après les résultats de la DSC, la polymérisation thermique s'est produite dans la plage de température de 110 à 200 °C.

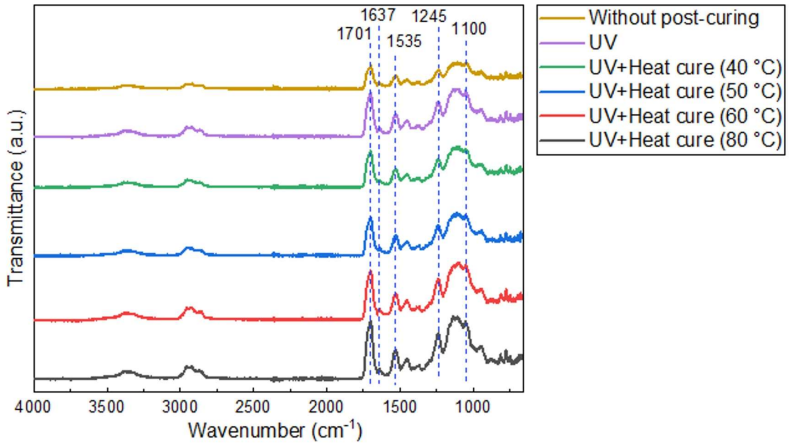

FIGURE B.25 – Spectre FTIR des échantillons à l'état vert et après durcissement

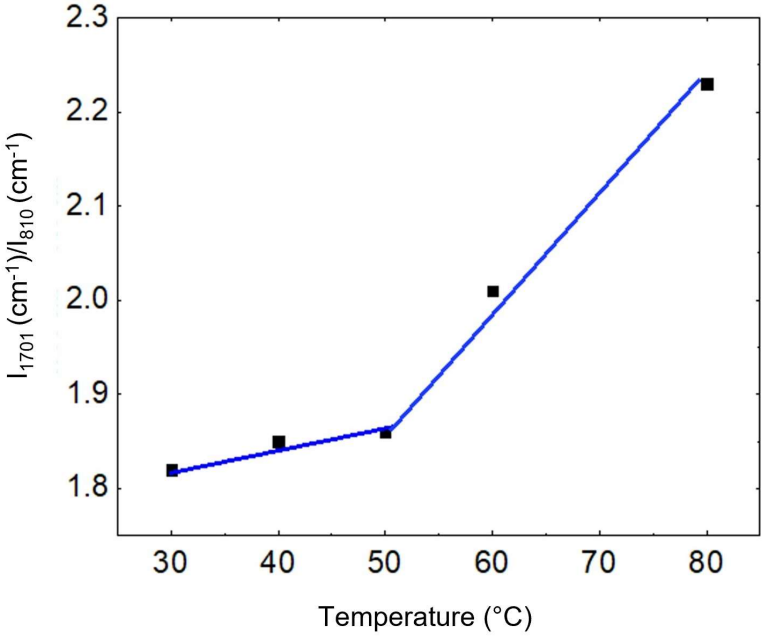

FIGURE B.26 – Rapport d'absorption I1701 cm^{-1}/I810 cm^{-1} pour les échantillons post-polymérisés.

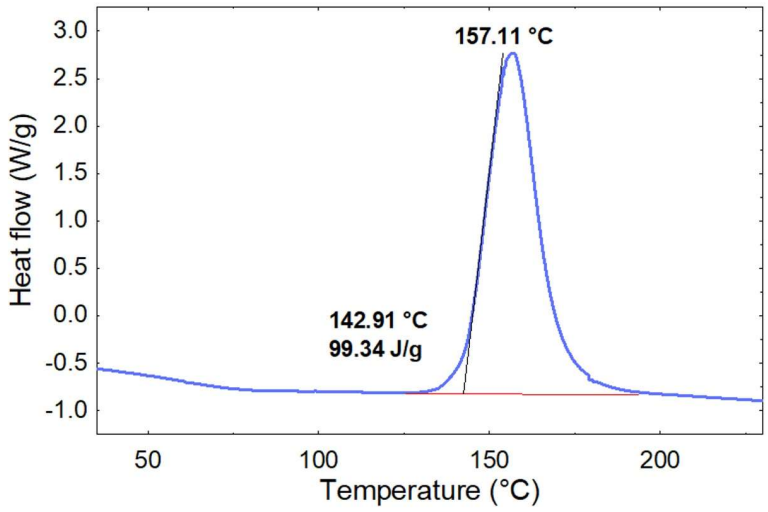

FIGURE B.27 – Tracé du flux thermique DSC pour la résine liquide

Les propriétés thermiques de la résine liquide et des échantillons dans les différentes conditions de post-polymérisation ont été analysées par DSC. Selon les résultats, l'équation suivante a permis d'étudier le degré de durcissement des échantillons qui indique la polymérisation des échantillons après la post-polymérisation :

Degré de durcissement (%) = (1 - Héchantillon/Hrésine) × 100

où Héchantillon et Hresin sont l'énergie thermique dégagée par les échantillons et la résine, respectivement. La figure B.27 montre le flux de chaleur en fonction de la température pour la résine. Pour mesurer l'énergie de dégagement de chaleur, le flux de chaleur de la résine liquide a été analysé. Hresinle flux de chaleur de la résine liquide a été analysé et l'énergie de libération de chaleur mesurée est égale à 99,34 J/g.

Les résultats obtenus par DSC pour les échantillons verts et post-cuisson sont indiqués dans la fi-

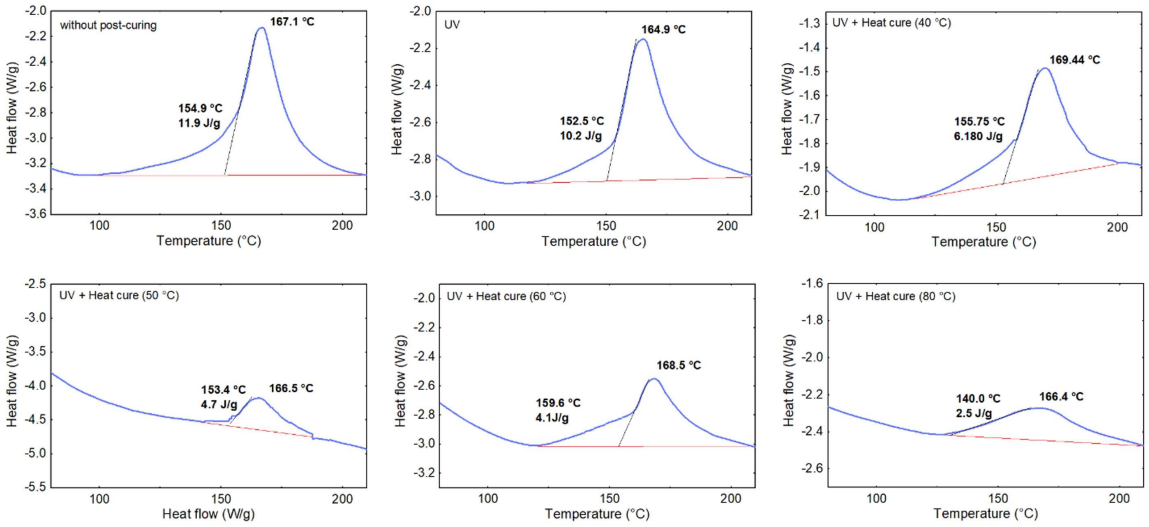

FIGURE B.28 – Les résultats de la DSC pour les échantillons

gure B.28. Tous les tracés de chauffage DSC obtenus montrent des pics endothermiques correspondant à la transition vitreuse et un pic exothermique correspondant au durcissement thermique. D'après cette figure, le durcissement a été effectué entre 110 et 200 °C. L'enthalpie maximale et minimale était de 11,87 et 2,51 J/g, ce qui correspond à l'échantillon sans post-polymérisation et à l'échantillon post-polymérisé par UV avec une présence de chaleur de 80 °C, respectivement. D'après les résultats du degré de polymérisation, l'échantillon vert était polymérisé à 88%, tandis que la post-polymérisation à l'aide de la lumière et de la température de 80 °C augmentait le degré de polymérisation des échantillons jusqu'à 98%. En conséquence, l'augmentation de la température de 40 à 80 °C entraîne une augmentation de la polymérisation pendant la post-polymérisation, ce qui peut être attribué à l'augmentation de la mobilité de la chaîne de polymère par l'augmentation de la température. Ainsi, l'augmentation de la température conduit à l'augmentation de la mobilité de la chaîne, et en augmentant la mobilité du réseau de polymères, la réaction de transfert de chaîne sera augmentée.

B.4.3 Caractérisation du comportement thermomécanique

L'analyse thermo-mécanique dynamique (DMTA) en mode flexion a été utilisée pour étudier le comportement thermo-mécanique des échantillons fabriqués. Des échantillons verts et des échantillons imprimés à 0° après polymérisation ont été sélectionnés à cette fin. La figure B.29 montre le module de stockage et le tan sans les échantillons post-polymérisés à différentes fréquences de 1, 3 et 10 Hz. D'après la figure B.29(a), un déplacement vers une température plus élevée du pic de tan a été observé en augmentant la fréquence. La valeur de Tan est attribuée au déphasage du mouvement sinusoïdal des pinces par rapport au mouvement de réponse des échantillons. Le maximum de ce déplacement qui est affiché comme un pic peut être vu près de la Tg causé par le mouvement segmentaire des chaînes de polymère. L'augmentation de la fréquence pendant le test s'accompagne d'une diminution des mouvements moléculaires segmentaires. Ainsi, les mouvements segmentaires qui jouent un rôle important dans la transition de l'état vitreux à l'état caoutchouteux sont restreints et entraînent une augmentation de la Tg. La figure B.29(b) montre le module de stockage en fonction de la température pour différentes fréquences. Une diminution de E a été observée en augmentant la température jusqu'à 150 °C, ce qui est lié à l'augmentation de la mobilité des segments polymériques pendant le chauffage. Dans la plage de 150 à 250 °C, le module a augmenté avant de diminuer à nouveau. Dans cette plage de température, les résines résiduelles peuvent être durcies et par conséquent le module augmente et de nouveau en augmentant la température E a été réduit.

La figure B.30 montre le module de stockage et le tan pour les échantillons post-polymérisation à une fréquence de 10 Hz. Le Tg le plus bas est lié à l'échantillon polymérisé aux UV, puis dans les

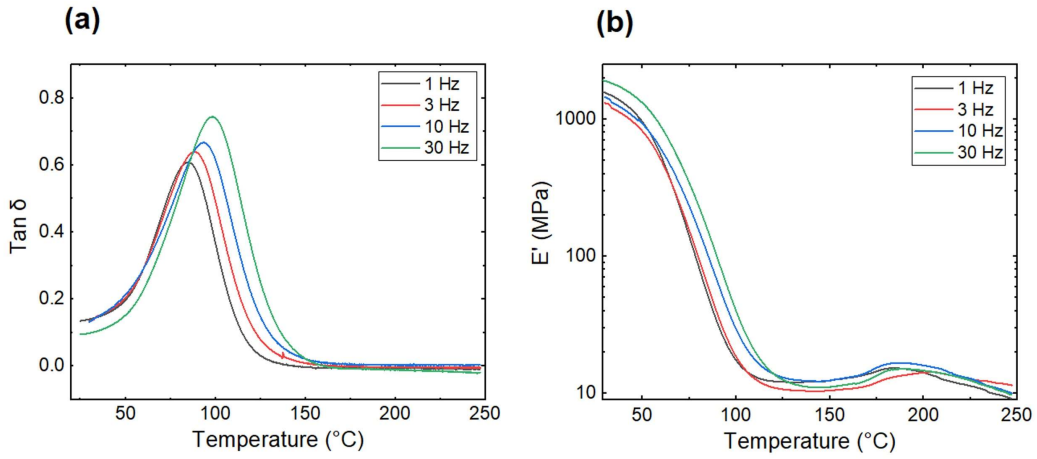

FIGURE B.29 – (a) Module de stockage en flexion (E) et (b) tan pour les pièces vertes à des fréquences de 1, 3, 10 et 30 Hz.

autres échantillons, le Tg augmente avec la température de polymérisation, le Tg le plus élevé étant celui de la polymérisation à chaud à 80 °C avec des UV. Compte tenu du rôle critique des mouvements segmentaires sur la Tg et de la réduction de ces mouvements par l'augmentation de la polymérisation, l'augmentation de la transition vitreuse est directement liée à la polymérisation des pièces pendant le post-traitement. D'après la figure B.30(b), le module de stockage à température ambiante pour la polymérisation UV et UV+chaleur à 80 °C est le plus faible et le plus élevé avec 1795,9 et 2307,7 MPa, respectivement. Tous les échantillons ont montré une réduction du module avec l'augmentation de la température. Cette réduction a été réalisée par un taux plus faible pour la polymérisation UV+chaleur à 80 °C par rapport à un autre. De même, les changements de module entre 150 et 210 °C montrent que la polymérisation des échantillons est incomplète et que, dans cette plage de température, la résine résiduelle a été polymérisée. La transition vitreuse des échantillons est présentée dans le Tableau B.5.

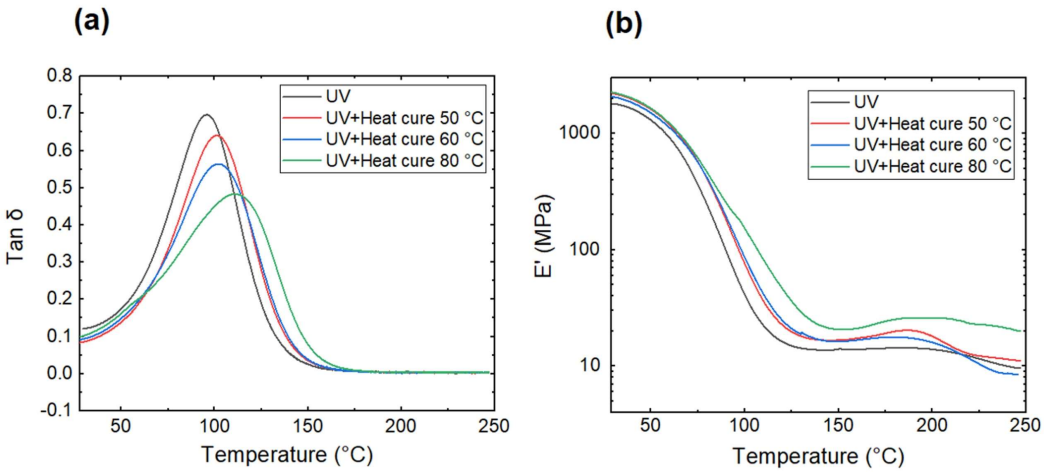

FIGURE B.30 – (a) Module de stockage en flexion (E) et (b) tan pour des échantillons post-polymérisés à des fréquences de 10 Hz.

TABLE B.5 – Valeur Tg des échantillons identifiés comme présentant un pic de tan .

Nom de l'échantillon	Fréquence (Hz)	Tg (°C)
Sans post-polymérisation	1	85.4
Sans post-polymérisation	3	89.0
Sans post-polymérisation	10	94.46
Sans post-polymérisation	30	99.19
UV	10	96.59
UV+Heat cure 50 °C	10	102.34
UV+Heat cure 60 °C	10	104.34
UV+Heat cure 80 °C	10	113.99

B.4.4 Caractérisations mécaniques

B.4.4.1 Effet de l'orientation de la construction

Les résultats des essais de traction sont présentés dans la figure B.31. Ces résultats montrent la courbe contrainte-déformation des échantillons en fonction de l'orientation de la sous-construction et des différentes conditions de post-polymérisation. Pour étudier l'effet de l'orientation de l'impression sur les propriétés mécaniques, chaque groupe imprimé à 0°, 45° et 90° a été comparé ensemble. Les différentes directions d'impression montrent les différents comportements mécaniques des échantillons. Ce fait montre l'anisotropie des pièces fabriquées et peut également avoir un impact sur les étapes jusqu'à la rupture dans les courbes contrainte-déformation. Les courbes contrainte-déformation pour les pièces imprimées à 0° montrent un comportement élastique linéaire, ascendant non linéaire, semblable au rendement (pic), un adoucissement de la déformation, puis un écoulement plastique. Ces échantillons présentent le pourcentage d'allongement le plus élevé par rapport aux autres échantillons imprimés dans différentes directions. La littérature a montré l'effet plastifiant des monomères non réagis sur le produit final. En outre, les résultats de la DSC présentés dans la section précédente montrent la quantité de résine résiduelle dans les échantillons. Ainsi, si l'on considère la direction de la tension, qui a été dans la direction de la plaque imprimée, on peut dire que l'allongement des échantillons a atteint sa valeur maximale. Après avoir étiré le matériau jusqu'au rapport spécial appelé " rapport d'étirage naturel ", l'encolure s'arrête et, grâce au nouveau matériau au niveau de l'encolure et des épaules, cette partie commence à croître. Ce phénomène, " l'étirage ", se poursuit jusqu'à ce qu'il couvre toute la longueur de la jauge de l'échantillon. Compte tenu de la microstructure renforcée au cours de ce

processus, on peut dire que la rupture se produit lorsque les nouveaux matériaux sont incapables de se transformer à l'extérieur du col. Des courbes de contrainte-déformation ductiles ont été observées pour les échantillons imprimés à 45°. D'après cette figure, les résultats montrent l'élasticité linéaire puis l'écoulement plastique des échantillons. Le pourcentage d'allongement était inférieur à celui des échantillons imprimés à 0°, tandis que la valeur de la contrainte maximale à la rupture était supérieure à celle des deux autres groupes. Si l'on considère la direction des plaques imprimées avec la direction de la traction dans ce groupe, on peut dire que le transfert de matière ne s'est pas produit dans la zone du col. Ce fait a entraîné une diminution de l'allongement. Les courbes du groupe d'échantillons imprimés à 90° étaient rigides. Cette direction de sous-construction a montré la valeur la plus faible en% d'allongement autour de 2% et la contrainte maximale à la rupture. En général, les résultats montrent que la contrainte maximale à la rupture pour les échantillons imprimés peut être classée comme suit : 45°>0°>90°. Ce fait montre l'effet important de la sous-construction sur l'impression des pièces.

B.4.4.2 Effet de la post-polymérisation : Rayonnement UV et température

Dans cette section, l'importance de la température de post-polymérisation avec les UV a été analysée sur les échantillons imprimés avec différentes orientations de construction. La figure B.32 montre les valeurs du module d'Young obtenues à partir des essais mécaniques. Les résultats ont montré l'effet important de la température pendant la post-polymérisation sur le comportement mécanique, le module d'Young des échantillons augmentant avec la température. La résistance mécanique maximale a été atteinte à 80 °C + post-traitement UV dans toutes les orientations d'impression. Cette aug-

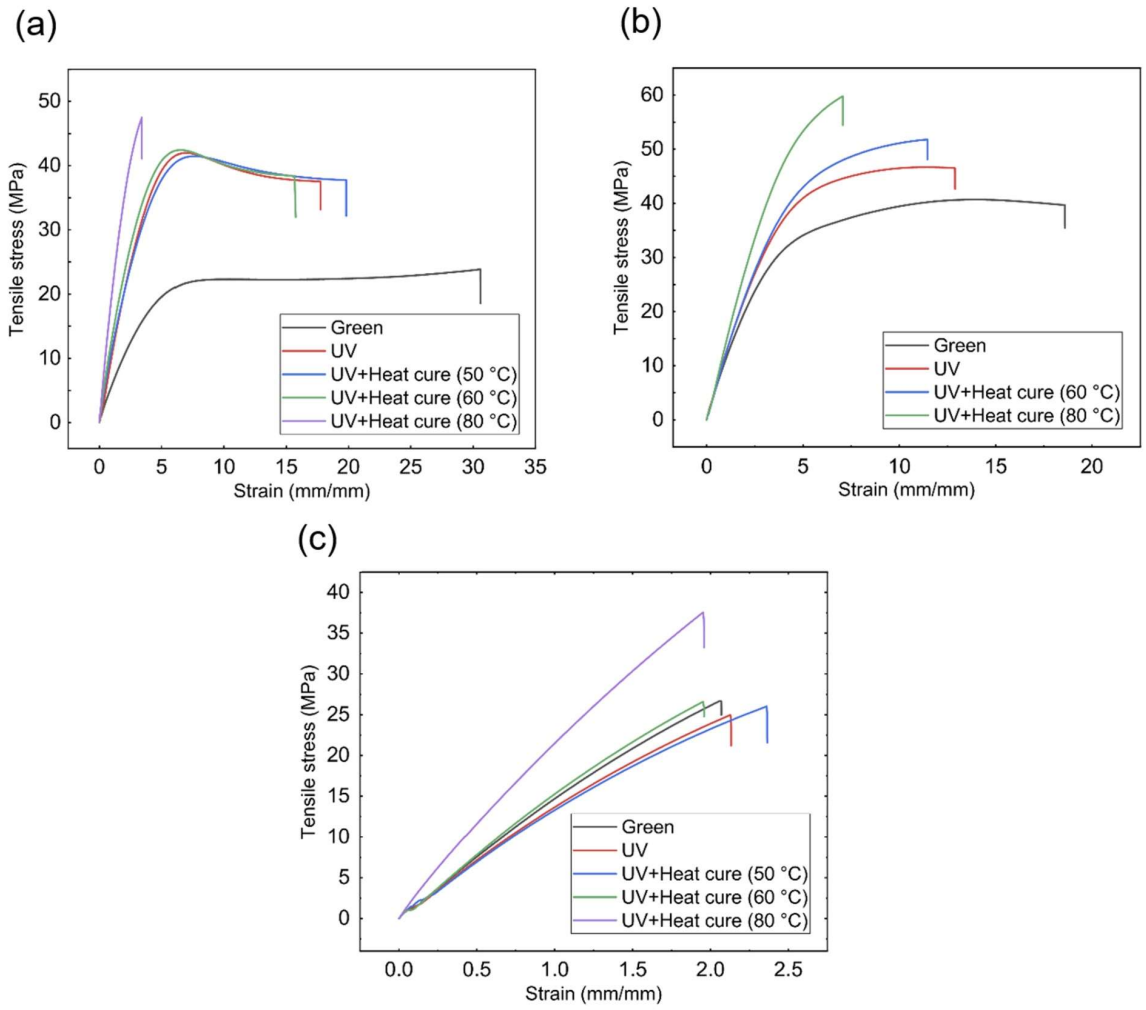

FIGURE B.31 – Courbes contrainte-déformation avec différentes conditions de post-polymérisation : (a) impression à 0°, (b) impression à 45° et (c) impression à 90°.

mentation peut être attribuée à l'augmentation du pourcentage de durcissement à des températures élevées après le durcissement. L'augmentation du pourcentage de durcissement à des températures plus élevées est liée à une meilleure mobilité des chaînes polymères. En outre, les résultats de la figure 25 montrent le rôle clé de la température sur la forme des courbes contrainte-déformation. Dans cette figure, l'effet d'adoucissement de la déformation a été réduit en augmentant la température pendant l'essai de traction, en particulier dans les échantillons imprimés à 45°. Cette observation peut s'expliquer par l'effet plastifiant de la résine résiduelle pendant l'essai. En outre, l'augmentation de la densité de réticulation peut conduire à une moindre capacité des chaînes à se déplacer, ce qui entraîne une réduction de l'assouplissement de la déformation. Les propriétés mécaniques des échantillons verts et post-cuisson ont été analysées pour les différentes orientations des sous-constructions. Les résultats de la résistance maximale à la traction et de l'allongement ont été pris en compte pour comparer les propriétés mécaniques des échantillons. La figure 25 montre la courbe contrainte-déformation pour les échantillons imprimés selon différentes orientations, sans et après polymérisation à 80 °C, respectivement. La contrainte de traction maximale des échantillons non post-polymérisés pour 0°, 45° et 90° était de 25, 20 et 40 MPa, respectivement. De même, la déformation maximale était pour 90°, 45° et ensuite 0°. La figure 25(b) montre la contrainte en fonction de la déformation pour la polymérisation UV+chaleur à 80 °C pour différentes orientations des échantillons imprimés. La contrainte maximale à la rupture était de 55, 44 et 50 MPa pour 0°, 45° et 90°, respectivement. En outre, la partie imprimée à 45° a montré une déformation à la rupture plus élevée que les parties imprimées à 0° et 45°.

Les figures B.33(a) et (b) montrent respectivement la résistance maximale à la traction et le%

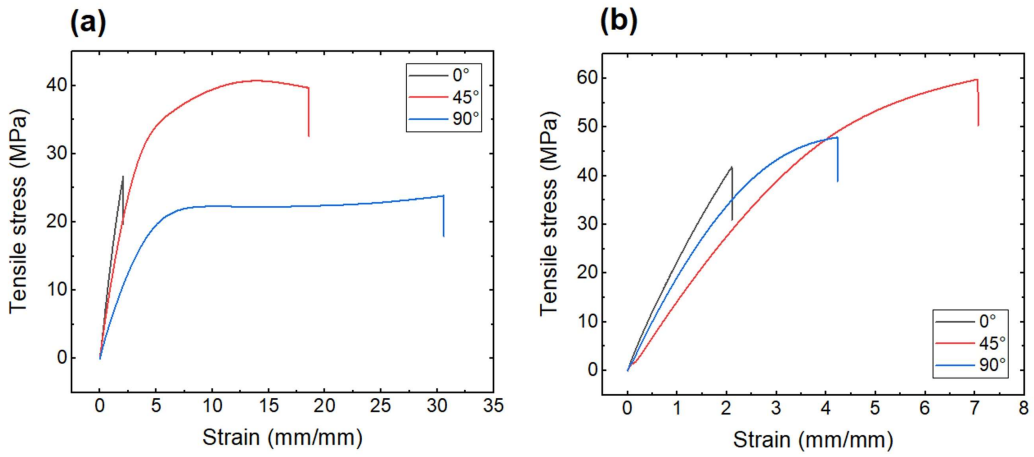

FIGURE B.32 – Courbe contrainte-déformation des échantillons dans différentes orientations d'impression : (a) sans post-cuisson et (b) post-cuisson à 80 °C.

d'allongement. Les résultats ont montré un effet significatif de la post-polymérisation sur la résistance à la traction et le% d'allongement des échantillons. En général, la post-cuisson a conduit à une diminution du% d'allongement des échantillons. L'augmentation de la résistance maximale à la traction des échantillons par post-polymérisation peut être directement liée au degré de polymérisation des échantillons. Il convient de mentionner que la résine non polymérisée qui se trouve entre les couches ou à la surface des pièces est connue comme un endroit aux propriétés mécaniques médiocres, ce qui entraîne une réduction des propriétés mécaniques de la pièce. On peut donc s'attendre à une amélioration des propriétés mécaniques en augmentant la quantité de polymérisation dans les échantillons. En outre, la libération de la concentration de contraintes internes dans les échantillons pendant la post-polymérisation a été considérée comme l'un des facteurs importants de l'amélioration des propriétés mécaniques. Par conséquent, la polymérisation et la libération de la contrainte interne peuvent expliquer l'augmentation des propriétés mécaniques par l'augmentation de la température lors de la

post-cuisson des échantillons. Comme indiqué, les propriétés mécaniques des pièces fabriquées ont également été examinées dans différentes orientations de la sous-construction. D'après les résultats, la résistance maximale à la traction peut être classée comme suit : 90° < 0° < 45°. Ainsi, les échantillons sans traitement thermique présentaient un allongement maximal de 0°, 45° et 90° égal à 2,83, 12,37 et 30,96%, respectivement. D'après les résultats, la résistance maximale à la traction a été atteinte pour l'orientation de 45°. Cela est lié à l'angle des couches par rapport à la direction de la force. De même, il a été démontré que le module élastique des échantillons imprimés par la méthode SLA à un angle de 45° montrait un module élastique plus élevé que l'échantillon des autres angles imprimés, ce qui est lié aux propriétés élastiques dans cette orientation. Comme le montrent les résultats, la résistance maximale à la traction a été réduite en augmentant l'orientation de l'angle de 45° à 90°. D'autre part, en augmentant l'orientation de l'angle de 45° à 90°, le % d'allongement a augmenté. La microstructure des pièces fabriquées par SLA peut être divisée en trois régions : résine surcuite, résine cuite et résine non cuite. La région de la résine non polymérisée se trouve entre les couches ou à la surface des échantillons. Étant donné que les échantillons à 90° et 45° ont été tendus dans le sens des couches, il peut sembler que l'effet plastifiant de la résine résiduelle soit maximal. Cependant, en raison de l'angle des couches avec la direction de la tension, cet effet peut être insignifiant pour l'angle de 0°.

B.4.4.3 Effet de la vitesse de déformation sur la charge de traction : 45°, post-cuisson

L'étude de la vitesse de déformation a été effectuée sur les échantillons imprimés à 45° qui ont été post-polymérisés à 80 °C en présence d'UV pendant 30 minutes. La figure 27 montre les courbes contrainte-déformation de cet essai à différentes vitesses de 0,3 à 117,4 s-1 . D'après les résultats, la

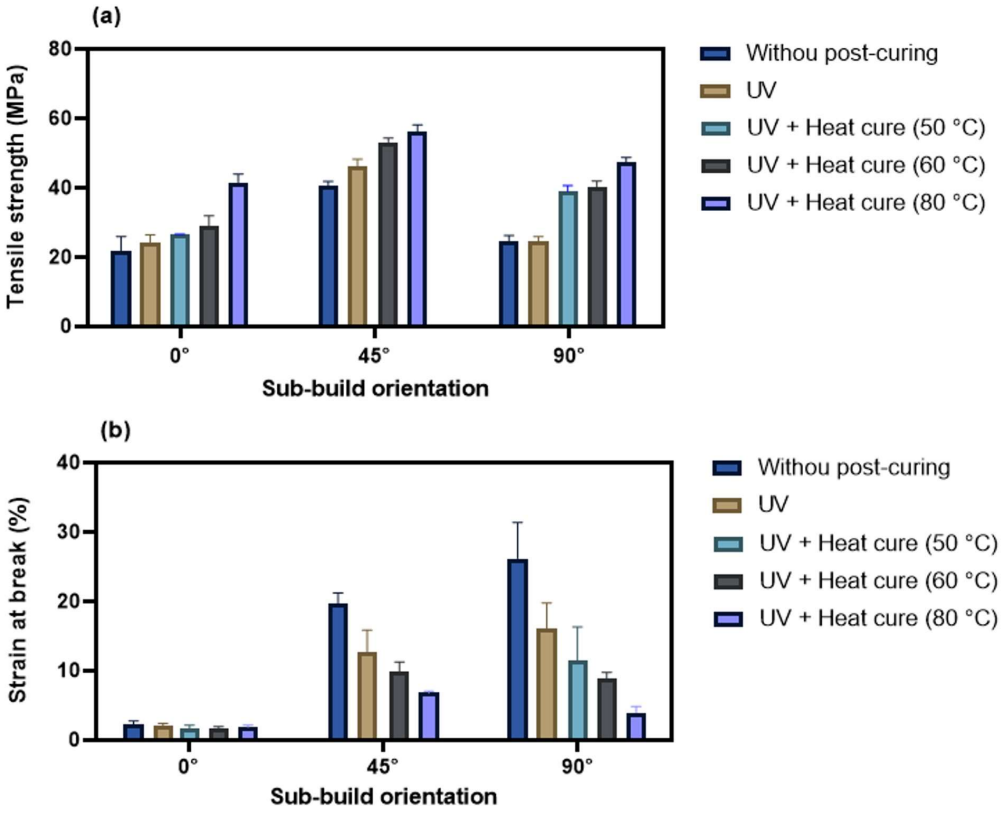

FIGURE B.33 – (a) Efort à la rupture et (b)% d'allongement pour les échantillons verts et post-polymérisés

résistance ultime à la traction a augmenté avec l'augmentation de la vitesse. Ainsi, ces valeurs pour des vitesses de 117,4, 4,6 et 0,3 s-1 étaient respectivement de 73, 68,8 et 67,5 MPa. Les différentes zones de ces courbes consistaient en un domaine d'élasticité linéaire initial, suivi d'un domaine d'élasticité et d'une augmentation modérée de la contrainte. En outre, les courbes de contrainte-déformation n'ont pas montré de changement significatif dans la pente de la zone élastique, ce qui peut indiquer que le module de Yang est indépendant des taux. La courbe contrainte-déformation de l'échantillon similaire en condition statique (0,001 s-1) montre une déformation ductile avec une déformation importante et une faible augmentation de la contrainte. La valeur maximale de la contrainte de rupture et la déformation à la rupture étaient respectivement de 59,1 MPa et de 6,8 %. Ainsi, la charge dynamique sur les échantillons a entraîné une réduction significative de la déformation à la rupture et une augmentation de la contrainte de rupture. En outre, un seuil dans la contrainte et la déformation ultimes a été considéré comme correspondant au premier comportement de non-linéarité. Les résultats des seuils de contrainte et de déformation sont présentés dans la figure B.34. D'après cette figure, les seuils de contrainte et de déformation ont diminué en augmentant la vitesse, ce qui signifie que l'augmentation de la vitesse s'accompagne d'un passage au stade non linéaire avec moins de contrainte et de déformation.

D'autre part, une diminution de la vitesse peut entraîner un retard de cette transition dans les échantillons, ce qui signifie un retard dans l'apparition des dommages. Il semble qu'à un taux élevé, l'augmentation du taux peut être causée par une augmentation de la densité des fissures, tandis que la diminution du taux peut permettre une plus grande propagation des fissures. En outre, les résultats

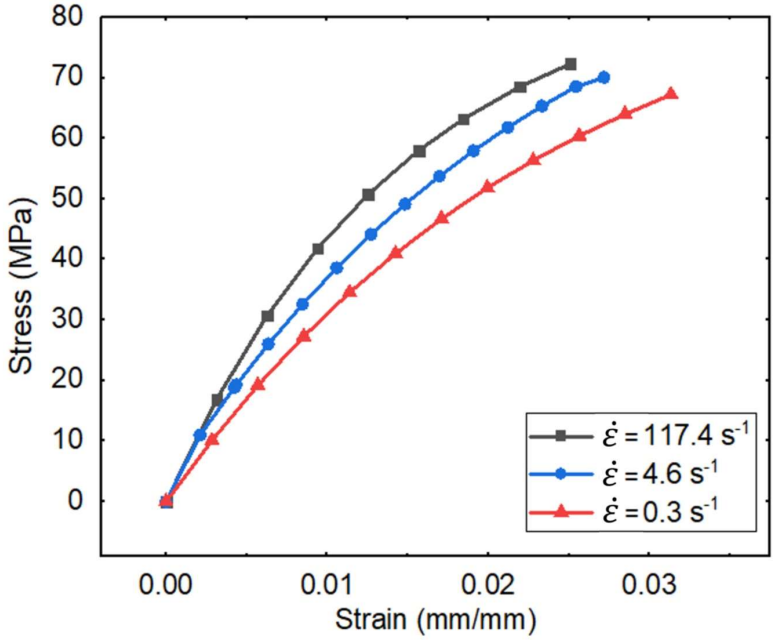

FIGURE B.34 – Courbes contrainte-déformation à différentes vitesses de déformation

montrent une relation directe entre le module et la vitesse de déformation, de sorte qu'un module plus élevé est observé à des vitesses de déformation plus élevées. En outre, pour l'étude du mécanisme de défaillance et des propriétés d'analyse dynamique concernant l'effet de la vitesse sur la contrainte, la sensibilité à la vitesse de déformation " m " a été prise en compte. Ce paramètre a été évalué à partir de l'équation de Backofen, qui est une fonction empirique de loi de puissance, comme suit :

$$\sigma = C + K\dot{\varepsilon}^m \tag{B.33}$$

Où est la contrainte, indique la vitesse de déformation, C et K sont les constantes qui se réfèrent aux conditions expérimentales et à la microstructure des matériaux, et m indique l'indice SRS. On peut dire qu'en augmentant l'indice SRS, la sensibilité du matériau à la vitesse de déformation augmente. Le seuil et la contrainte ultime ont été pris en compte pour étudier l'effet des différents taux sur les

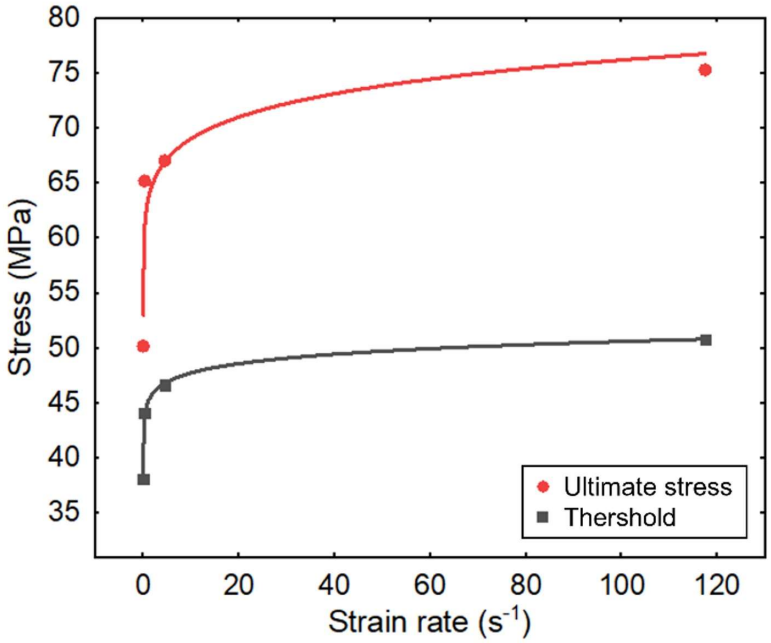

FIGURE B.35 – Sensibilité à la vitesse de déformation pour le seuil et la contrainte ultime

TABLE B.6 – Paramètres de l'équation de Backofen

Paramètres de la fonction de puissance	C	K	m	R^2
Seuil	10.54	34.56	0.03	0.99
Effort à la rupture (MPa)	43.46	20.10	0.11	0.92

différentes étapes de la rupture. L'indice de sensibilité du seuil peut correspondre à la zone linéaire, tandis que l'indice de l'équation respectée à la contrainte ultime peut se référer à l'étape non linéaire. Les résultats de l'ajustement sont présentés dans le Tableau B.6. D'après les résultats, les échantillons ont montré une plus grande sensibilité au taux dans la phase non linéaire que dans la phase linéaire. Ceci peut être attribué au comportement visco-dommageable des échantillons pendant le test. Après l'étape linéaire, le mécanisme d'endommagement sera actif et accompagnera la création de fissures dans les échantillons, et sera plus sensible à la vitesse de déformation.

D'après les résultats, un indice m plus élevé pour la contrainte ultime par rapport à la contrainte d'écoulement peut montrer plus de sens de l'échantillon avec la vitesse de déformation après la contrainte d'écoulement, qui est située dans la zone de non-linéarité. On peut donc dire que l'étape de non-linéarité est plus sensible à la vitesse de déformation que l'étape linéaire de la courbe contrainte-déformation.

B.4.4.4 Analyse de la microstructure des échantillons imprimés

La figure B.36 montre des micrographies de la surface de rupture de l'échantillon imprimé à 90° et post-polymérisé à 60 °C, avec différents grossissements, après l'essai de traction. Une zone de déformation plastique ainsi qu'une autre région de rupture fragile peuvent être observées sur la surface de rupture de la figure B.36(a). La région de déformation plastique peut être attribuée au glissement de la chaîne qui réduit la vitesse de propagation du défaut par la libération de la contrainte. En outre, la surface fracturée de la figure B.36(b) présente une région avec des formes de couches qui peuvent indiquer la nature en couches des pièces imprimées par cette méthode. Dans d'autres régions de cette figure, la rupture n'est pas observée couche par couche, ce qui semble indiquer que le durcissement a été complètement effectué dans cette zone.

Pour étudier l'effet des différentes vitesses de déformation sur les dommages, les fractures de surface des échantillons imprimés à 45° après polymérisation à 80 °C ont été observées. La figure B.37 montre le MEB d'échantillons fracturés à des vitesses de déformation de 0,3, 4,6 et 117,4 s^{-1} à différents grossissements. Les figures montrent la fracture fragile contenant la région plastique qui diminue avec l'augmentation de la vitesse de déformation, de sorte que la fracture de surface à la vitesse de

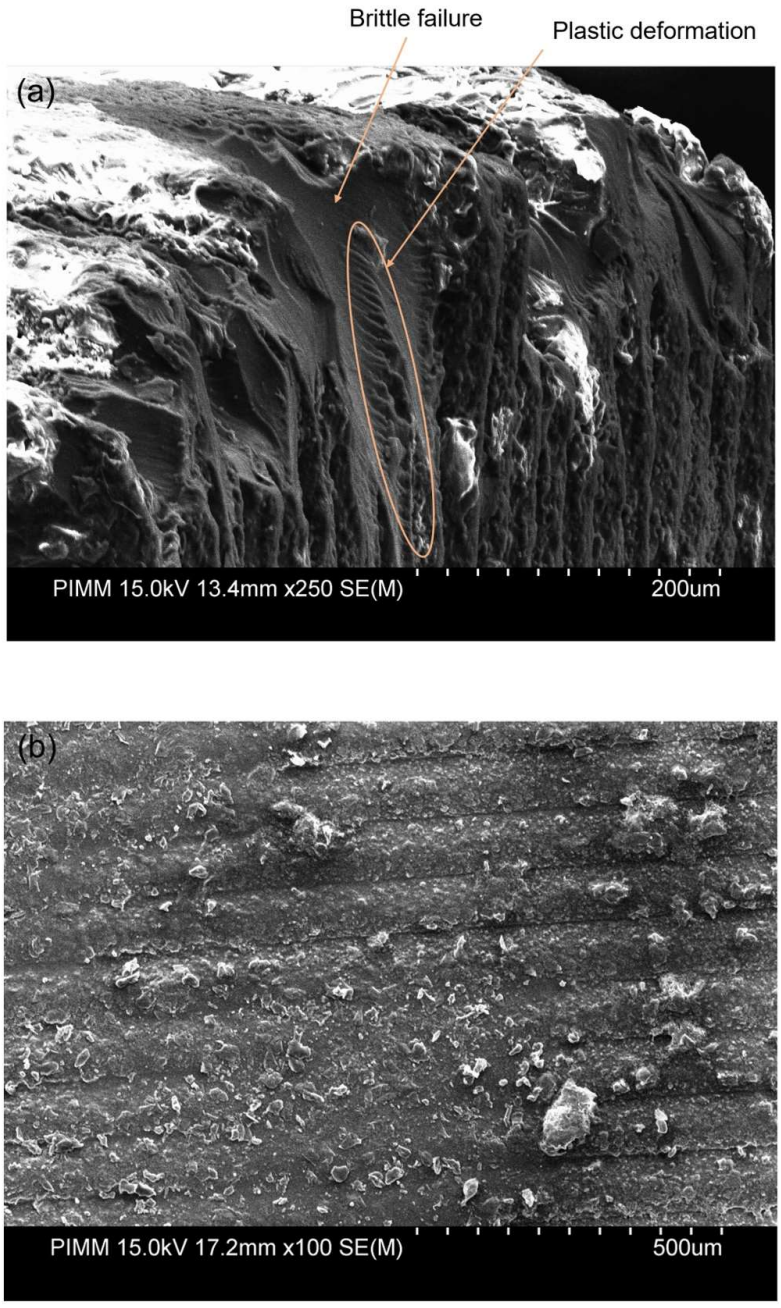

FIGURE B.36 – Surface de rupture de l'échantillon imprimé à 0° et post-polymérisé à 60 °C par rapport à (a) plus fort grossissement et (b) plus faible grossissement.

déformation de 117,4 s-1 n'a pas montré la déformation plastique. Les figures B.37(a) et (b) sont attribuées à la vitesse de déformation de 0,3 s^{-1}, comme on peut le voir, les fissures se sont agrandies davantage par rapport aux autres vitesses de déformation. En outre, d'après les preuves de cisaillement et de cavitation dans la zone plastique, il semble que le mécanisme de glissement de chaîne soit un mécanisme de rupture. Ce mécanisme peut se produire lorsque la vitesse de propagation est réduite par la libération des contraintes.

B.4.5 Conclusions

L'effet de la post-polymérisation à différentes plages de température et pendant un certain temps sur les propriétés mécaniques de la résine uréthane diméthacrylate a été étudié. Les propriétés mécaniques des échantillons verts et post-polymérisés ont été analysées pour les différentes orientations de la sous-construction. Les propriétés physico-chimiques, thermiques et mécaniques ont été étudiées par DSC, FTIR, TGA, DMA et analyse de traction. Les résultats obtenus expliquent le mécanisme de durcissement des échantillons après le durcissement et la valeur de la résine résiduelle a été calculée. Le rôle clé de la résine résiduelle dans les pièces sur l'analyse thermique et mécanique a été expliqué. Cet effet a été étudié sur les transitions vitreuses des échantillons, de sorte que la post-cuisson a entraîné une augmentation de la transition vitreuse. D'après les résultats, une augmentation de la température de post-cuisson augmente la résistance à la traction, de sorte que la post-cuisson à 80 °C entraîne une augmentation de la polymérisation jusqu'à 98 %. Enfin, les résultats ont montré que la résistance à la traction était maximale dans le rang de $90° < 0° < 45°$. En outre, les propriétés mécaniques des matériaux ont été examinées sous une charge de traction quasi-statique et à taux de déformation

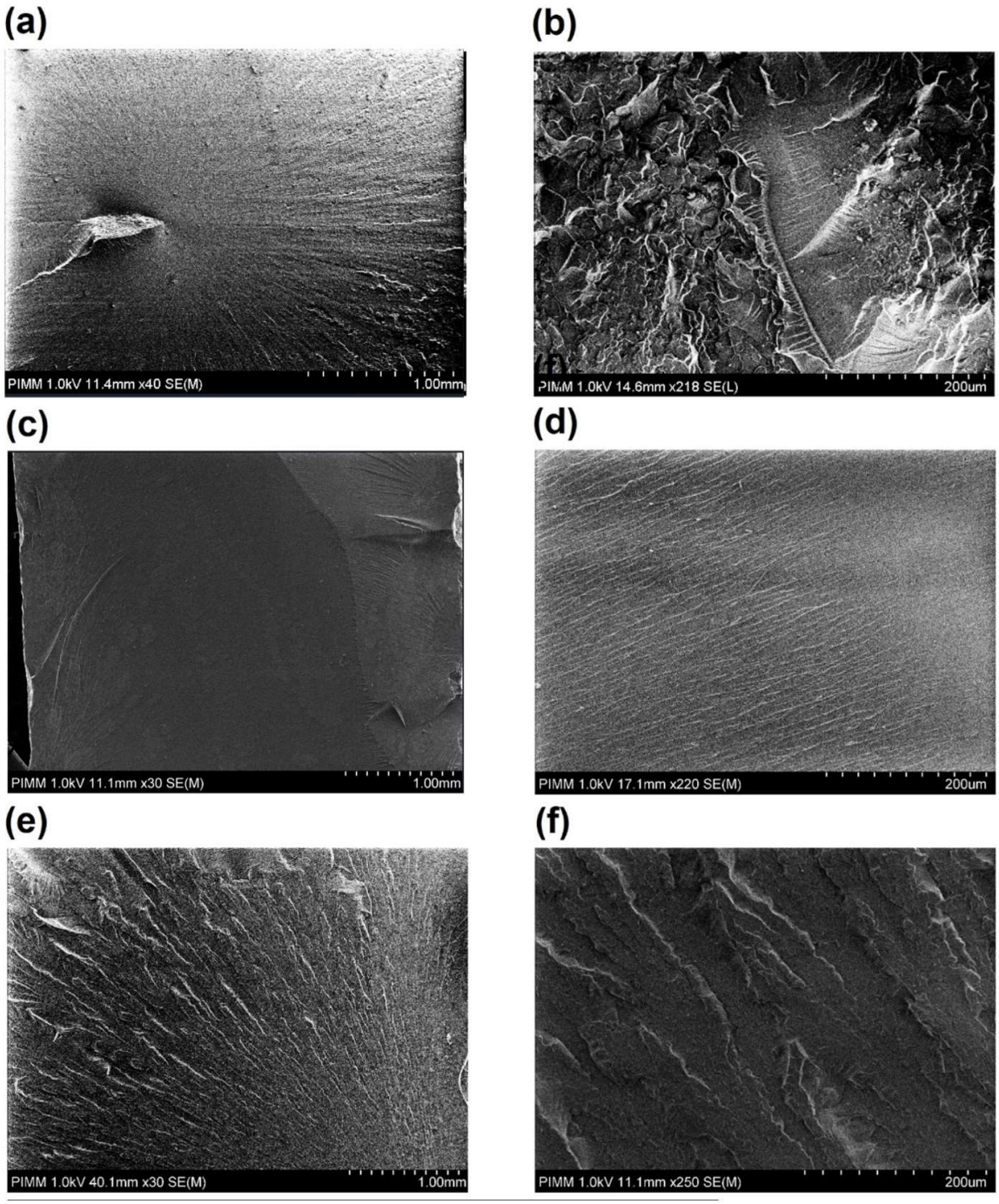

FIGURE B.37 – Analyse microscopique électronique de surface à différents grossissements pour la surface de rupture à différentes vitesses de déformation : (a et b) 0,3 s^{-1} , (c et d) 4,6 s^{-1}, et (e et f) 117,4 s^{-1}

élevé. Les conclusions suivantes peuvent être tirées : L'importance de la post-polymérisation sur le comportement mécanique final a été démontrée dans la méthode de post-traitement. La post-cuisson s'est accompagnée d'une réduction du monomère résiduel, de sorte qu'en augmentant la polymérisation dans les pièces, l'élongation a été réduite. Les résultats de la DSC montrent que le degré de polymérisation maximal des échantillons atteint 98 % pendant le post-traitement aux UV à 80 °C. Le comportement mécanique des échantillons dans des conditions quasi-statiques montre la sensibilité à l'orientation de la construction. Ainsi, la valeur la plus élevée de contrainte à la rupture a été attribuée aux pièces imprimées à 45°, puis à 0° et enfin à 90°. En outre, les différentes formes de la courbe de contrainte-déformation sont fragiles, ductiles et avec des effets d'adoucissement. Les résultats d'une vitesse de déformation élevée de 0,001 à 117,4 s^{-1} sur le comportement mécanique montrent le rôle important de la vitesse de déformation sur le mécanisme de rupture. Les échantillons ont montré une plus grande sensibilité dans la zone de non-linéarité par rapport à l'étape linéaire des courbes de contrainte-déformation.

B.5 Performance de la pièce finie : analyse structurelle, microstructure, précision géométrique et analyse de l'écoulement

B.5.1 Analyse structurelle

Dans cette section, l'analyse numérique des roues centrifuges et des rotors de compresseur sera discutée. Comme mentionné, des propriétés telles que le module d'élasticité, la dilatation thermique, la ténacité, la résistance à la fatigue, la conductivité thermique, la capacité thermique spécifique, la résistance à la corrosion et la stabilité thermique ont été parmi les paramètres pris en compte dans la

sélection des matériaux pour la fabrication des roues et rotors. des compresseurs [164]. Il convient de mentionner que les contraintes centrifuges dues aux forces de rotation, les contraintes de flexion dues à la pression du fluide et au changement de quantité de mouvement, ainsi que les contraintes thermiques dues au chargement thermomécanique sont les propriétés qui ont été considérées comme des propriétés. facteurs efficaces dans les simulations. Ainsi, en examinant les matériaux sous les forces mentionnées, l'autorité du matériau sera testée en simulation [165]. L'analyse structurelle est l'application la plus courante de l'analyse par éléments finis, utilisée pour étudier différents types de charges, notamment les contraintes, les déformations et les déformations. Les calculs de résistance ont été effectués pour deux vitesses de rotation différentes, à savoir 52 krpm et 90 krpm, avec deux matériaux (PPS et SLA), comme mentionné dans la sous-section précédente. Les résultats de calcul sélectionnés des distributions de contraintes et de déplacements pour le matériau PPS, obtenus pour une vitesse de rotation de 52 krpm, sont présentés à la figure B.38. Sur la figure B.38b, on peut voir que les contraintes les plus élevées dans le disque de la roue se produisent au bord du trou central. Dans cette zone, les contraintes réduites calculées selon l'hypothèse de von Mises ont atteint une valeur de 29,07 MPa. Cela est dû à l'étirement du matériau dans le sens circonférentiel au bord du trou du disque, provoqué par la force centrifuge. Dans l'autre partie du disque, les contraintes réduites étaient plus faibles et ne dépassaient pas 20 MPa. La valeur de contrainte maximale obtenue à partir des calculs est inférieure à la résistance à la traction obtenue expérimentalement des échantillons en matériau PPS, qui était de 29,4 MPa. D'autre part, sur la base de la figure B.38, on peut conclure que les déplacements les plus importants sur le disque de la roue se sont produits sur les bords des pales, où ils ont atteint une valeur de 0,1129

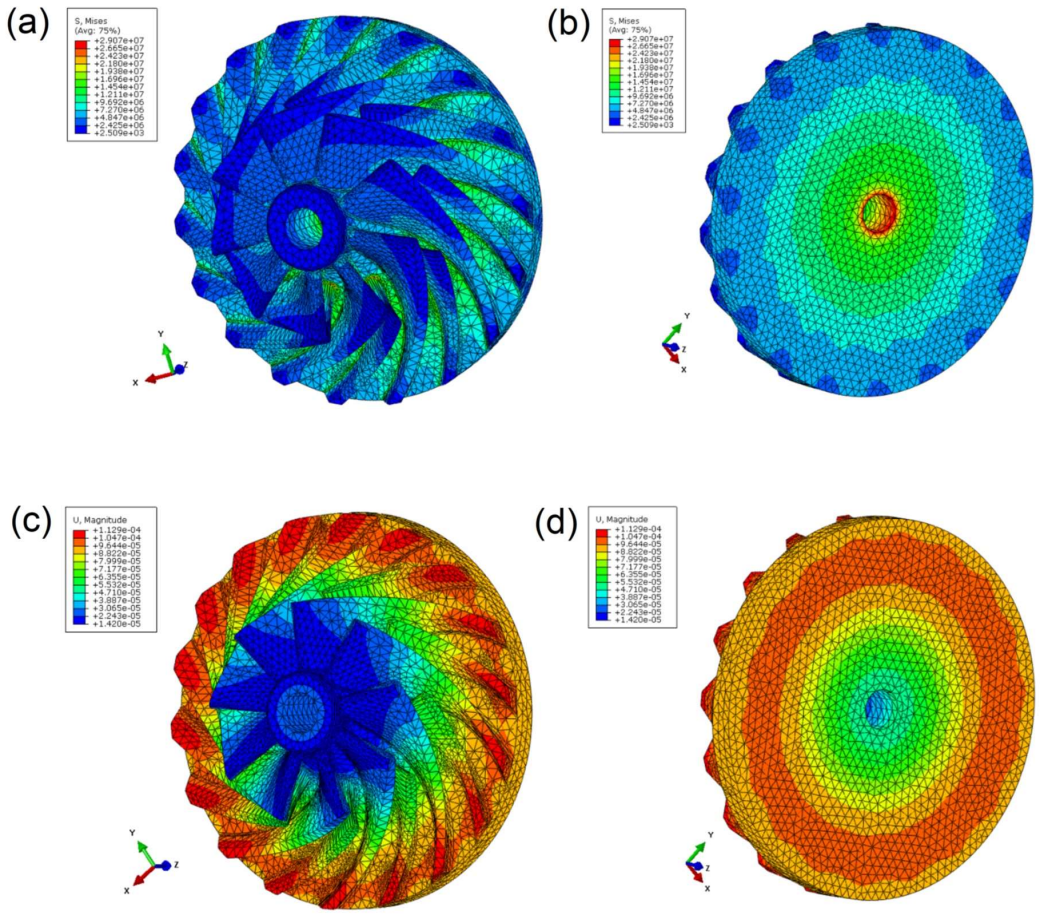

FIGURE B.38 – (a et b) réduction de la répartition des contraintes et (c et d) répartition du déplacement de la roue du compresseur à une vitesse de 52 krpm pour la roue PPS

mm.

B.5.2 Effet des paramètres optimisés du procédé sur la microstructure des pièces fabriquées

La figure B.39 montre les images optiques au microscope de la surface des roues. Comme on peut le voir, les couches d'impression peuvent être observées pour les roues imprimées, ce qui est lié à la nature de la production à partir de cette technique. D'après cette figure, les roues FDM présentent des espaces entre leurs couches qui sont liés à la diffusion insuffisante des chaînes moléculaires déposées dans

chaque couche de filament polymère sur d'autres couches. D'après la figure, l'écart entre les filaments du PPS-340 est réduit par rapport au PPS-320. Comme nous l'avons mentionné, l'une des différences entre les paramètres de traitement de ces deux roues est la température de la buse. L'augmentation de la température de la buse dans le PPS-340 a entraîné une meilleure adhérence entre les filaments, ce que l'on appelle le temps de soudure pendant l'impression. Ainsi, l'augmentation du temps de soudure peut accroître la mobilité des chaînes, la diffusion moléculaire et le réenchevêtrement. Les figureB.40 (e) et (f) montrent l'image de la roue du Rigid 10 k imprimée avec SLA. Les images ne montrent pas les vides entre les couches pour cette roue. On peut dire que l'une des différences les plus marquées entre les roues était liée à la surface des pièces, la roue imprimée SLA présentant une meilleure surface et une meilleure adhérence entre les couches que les pièces FDM. La présence d'espaces et de vides entre les couches peut servir de lieu de passage du fluide, ce qui s'accompagne d'une réduction des performances du compresseur.

Compte tenu du rôle clé de l'interface de soudure sur les performances finales du compresseur, les roues imprimées ont été examinées à l'aide du MEB pour étudier l'influence de la méthode et des paramètres du processus sur l'interface de soudure. La figure B.40 montre les images MEB pour le PPS 1, le PPS 2 et le Rigid 10k. Pour les roues imprimées par FFF, l'augmentation de la température d'impression de 320 °C (pour le PPS 1) à 340 °C (pour le PPS 2) sur l'interface de soudure a permis de réduire la quantité de vides triangulaires entre les filaments. Les figures B.40(e) et (f) montrent la surface de Rigid 10k, comme on peut le voir, la coalescence complète entre les couches adjacentes au cours de la fabrication a été obtenue à partir de SLA.

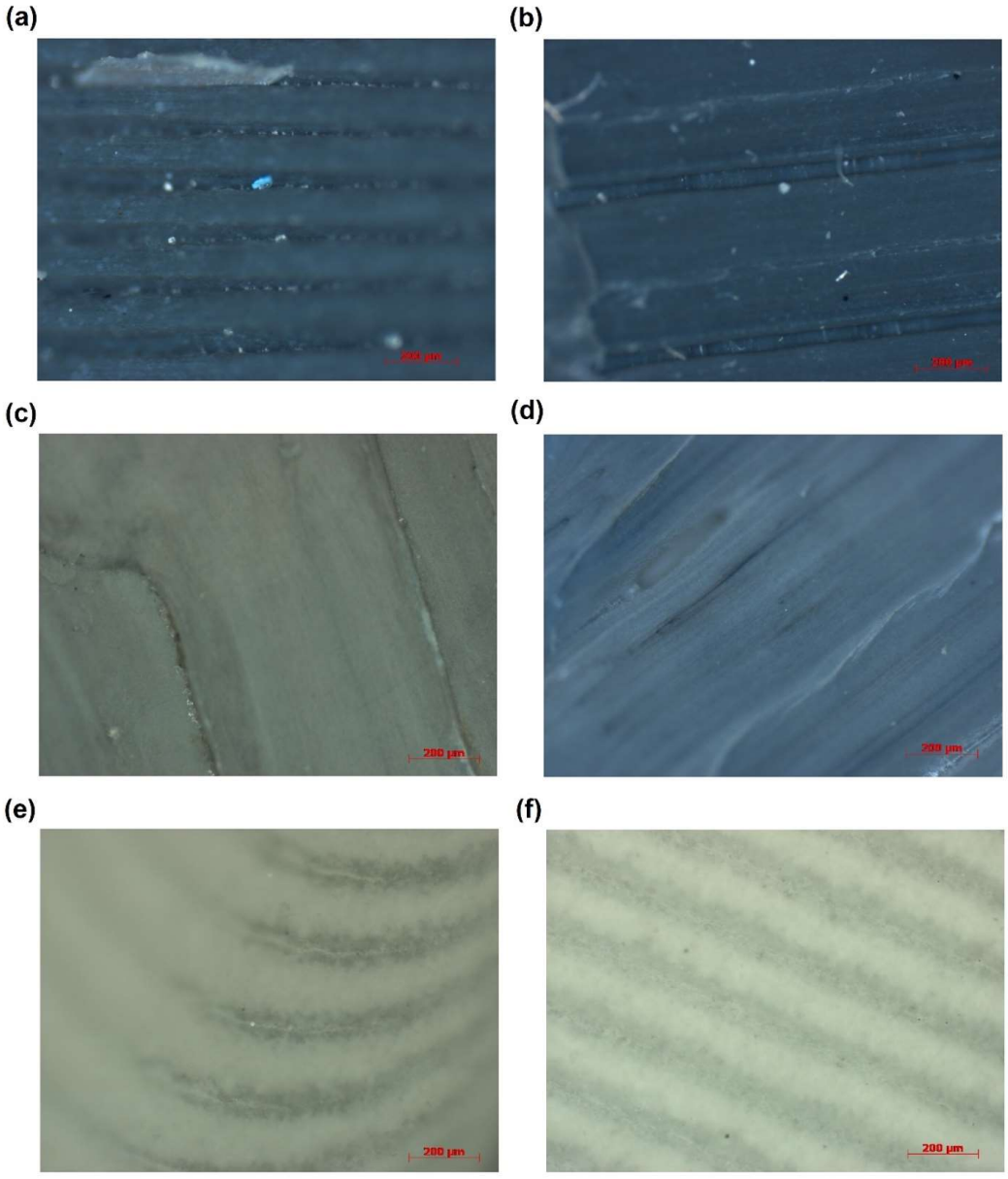

FIGURE B.39 – Microscopie optique des turbines (zone de visualisation : sur la pale de la turbine) : (a et b) PPS-320, (c et d) PPS-340 et (e et f) Rigide 10k

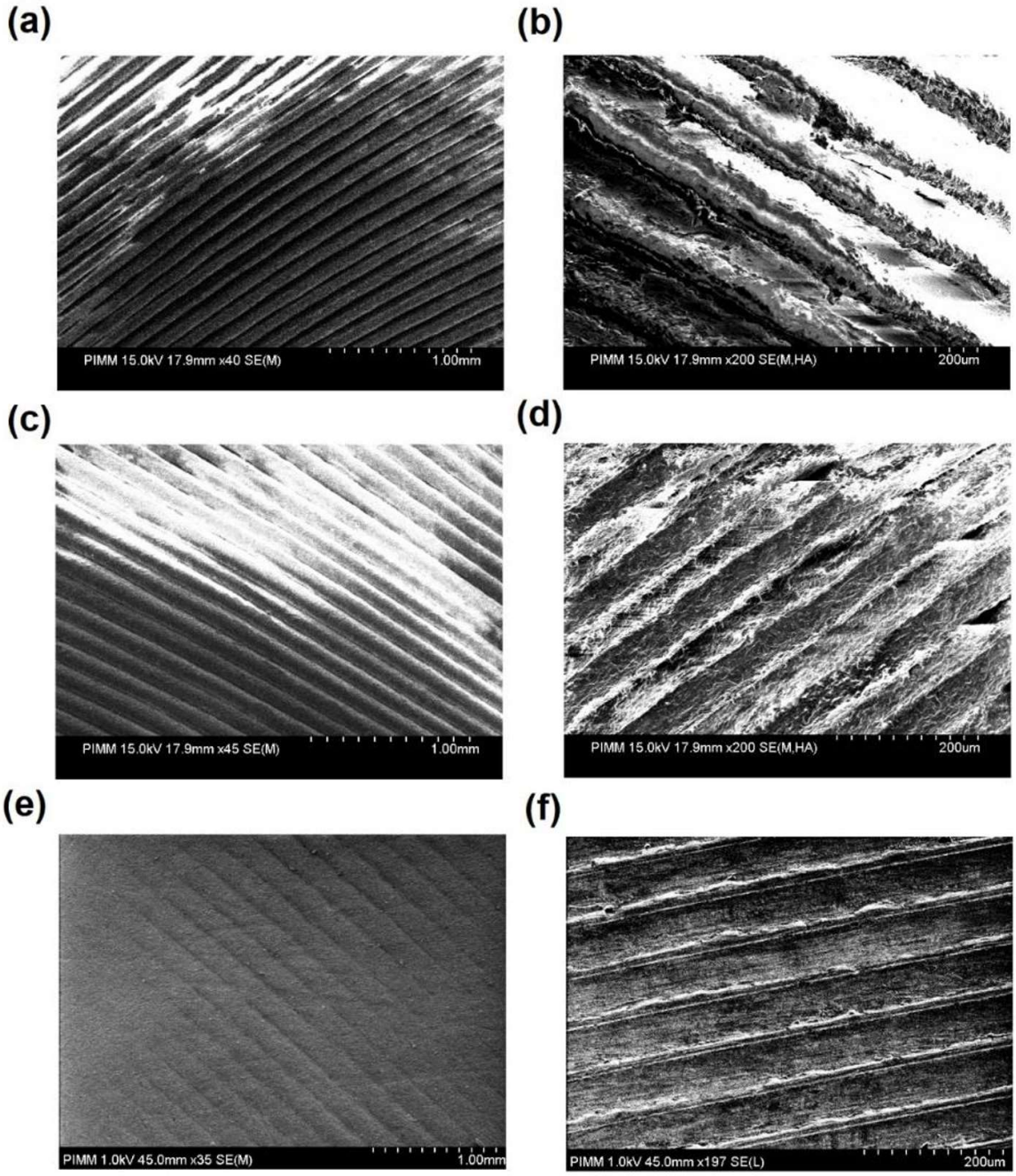

FIGURE B.40 – MEB des roues (zone de visualisation : sur la pale de la roue) : (a et b) PPS-320, (c et d) PPS-340 et (e et f) Rigide 10k

B.5.3 Effet des paramètres optimisés du processus sur la précision géométrique des pièces fabriquées

Il y a un effet important de la rugosité des surfaces sur les performances des compresseurs centrifuges. Si l'on considère la fabrication couche par couche de pièces par fabrication additive, il est possible d'obtenir différentes précisions géométriques en fonction de la précision de la technique. La hauteur des couches pendant la fabrication a été considérée comme un paramètre important qui peut avoir un impact sur la rugosité finale de la surface. Par exemple, l'impression d'une forme cylindrique par rapport à son axe central parallèle à la direction x s'accompagne d'une rugosité de surface moindre par rapport à la direction inclinée entre x et y. Pour étudier l'effet de la technique d'impression sur la rugosité de surface, l'écart entre les pièces et le fichier conçu a été analysé. Les pièces imprimées en PPS 2 et Rigid 10 K ont été scannées, puis le fichier stl. obtenu par scannage a été adapté au fichier CAO. Le logiciel Geomagic a été utilisé à cette fin, ce qui permet de minimiser l'erreur résiduelle et d'assurer une comparaison directe. La Figure B.41 (a) montre les écarts des normales de surface et a été utilisée pour la comparaison en raison de la complexité de la surface. L'erreur moyenne sur l'ensemble des mesures de distance pour le PPS 1 et le Rigid 10k était de -46 et 92 m (sous-dimensionné) avec un écart-type de ±0,09 et ±0,16 m, respectivement. Comme on peut le voir sur cette figure, Rigid 10k présente une erreur de distribution plus homogène par rapport au PPS 1. Il convient de mentionner que compte tenu de l'utilisation du support lors de la fabrication de la roue, la séparation du support s'est accompagnée de la création de trous dans l'échantillon. En outre, pour augmenter les propriétés mécaniques, le Rigid 10k a été post-cuit, et ce post-traitement peut induire un rétrécissement de l'échantillon en raison de la modification de la liaison entre le monomère résiduel et les autres chaînes

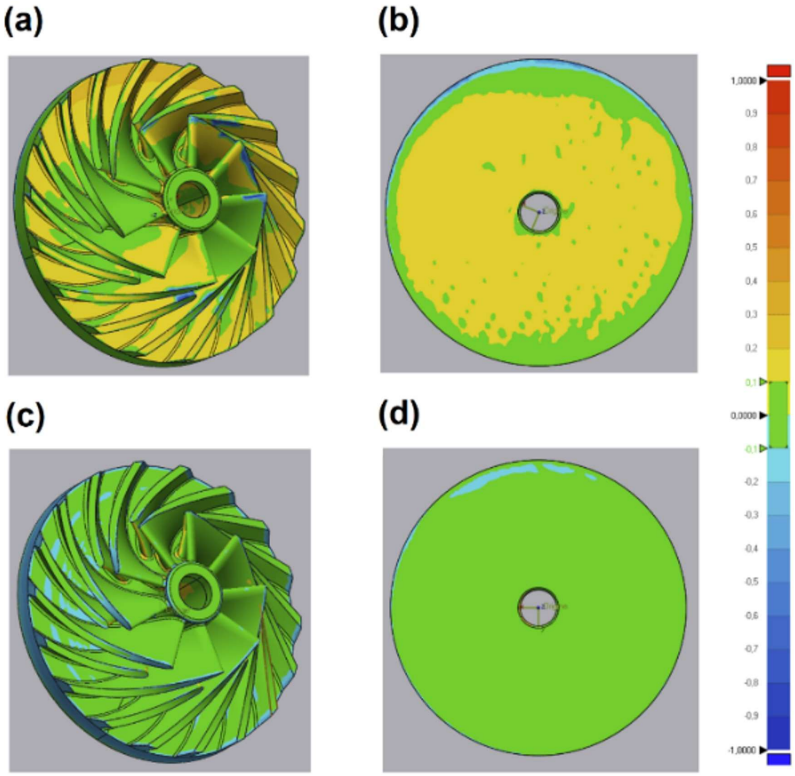

FIGURE B.41 – Comparaison locale du meilleur ajustement des données d'inducteur de forme libre par rapport à la géométrie CAO nominale

de polymères, qui passe d'une liaison de Van der Waals à une liaison de covalence. Selon les résultats des performances du compresseur jusqu'à la vitesse de rotation de 52 000 tr/min, le PPS 1 est plus efficace que le Rigid 10, ce qui signifie que l'augmentation de l'erreur de déviation du rotor diminue l'efficacité.

B.5.4 Analyse de l'écoulement

Les trois rotors de compresseur centrifuge imprimés FFF et SLA, décrits précédemment, ont été évalués expérimentalement. Pour tester les performances des rotors fabriqués, un banc d'essai de turbocompresseur a été développé. Les résultats sont présentés dans la Figure B.42. Le rotor PPS-320

donne un taux de compression plus faible, tandis que les deux autres rotors donnent des résultats équivalents plus proches de la simulation CFD. De plus, pour le PPS-340, la plage de fonctionnement présente des débits massiques de rotor nettement inférieurs à ceux des autres rotors et aux résultats de simulation CFD. Cela signifie que ce rotor génère beaucoup de pertes. L'une des raisons de ces pertes peut être la fuite du flux d'air à l'intérieur du rotor. Si tel est le cas, cela s'explique par la spécificité du procédé FFF pour lequel le matériau est déposé couche par couche. Lorsque la différence de pression entre les surfaces du rotor augmente, le flux de fuite à l'intérieur du rotor apparaît et augmente progressivement. Cette fuite entrave la circulation de l'air à l'intérieur des passages d'aubes, réduisant ainsi les performances du rotor. La taille des vides dépend des différents paramètres du processus tels que la température de la buse, la vitesse de dépôt du filament fondu, l'épaisseur de la couche et le motif de remplissage [108]. Cependant, un pourcentage croissant de remplissage s'accompagne d'une diminution de la porosité des pièces. En effet, le rotor PPS-340 présente des performances nettement améliorées, voire légèrement meilleures, que celles du rotor Rigid10k. Ceci peut s'expliquer ainsi : lorsque le rotor tourne à grande vitesse, du fait des propriétés du PPS utilisé dans la méthode FFF, il peut s'allonger (environ 4%) sous l'action de la force centrifuge dans le sens radial ce qui entraîne une augmentation le travail d'Euler du rotor. De plus, il existe encore des nervures d'impression sur les surfaces du boîtier de pale qui empêchent partiellement les fuites. Cependant, le rotor Rigid10K a un allongement plus faible (environ 1 %), de sorte que l'effet de la force centrifuge n'affecte pas les performances du compresseur.

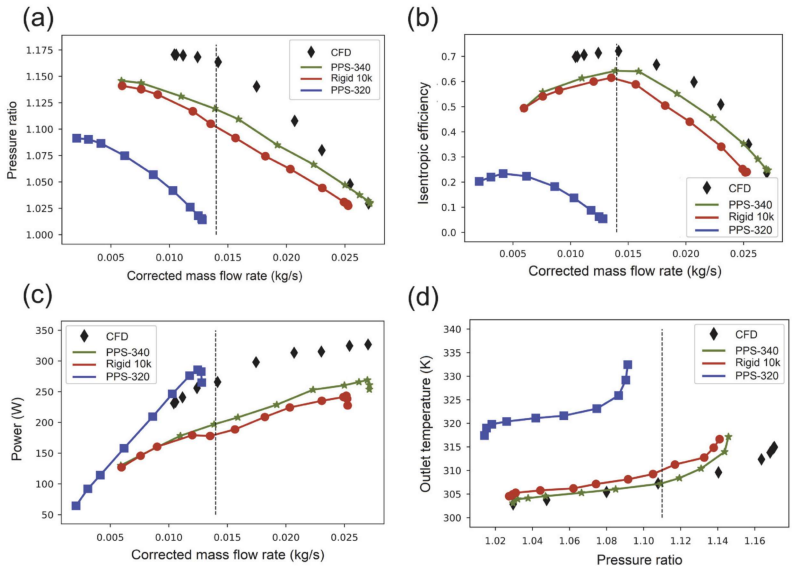

FIGURE B.42 – (a) Ratio de pression, (b) efficacité isentropique, (c) puissance du compresseur sur l'arbre par rapport au débit massique corrigé, et (d) température de sortie par rapport au ratio de pression des différentes roues.

B.5.5 Conclusions

Cette thèse a été réalisée entre deux laboratoires, LIFSE et PIMM, de l'Institut Polytechnique des Arts et Métiers pour utiliser des polymères à la place des métaux pour fabriquer la pièce du compresseur. Ce L'objectif a été réalisé sous deux aspects, l'analyse numérique et expérimentale. Deux principaux scientifiques et il faut distinguer les serrures techniques : La nécessité de comprendre la relation entre la microstructure du matériau et les performances finales du compresseur à travers une étude multi-physique et multi-échelle et en considérant les propriétés physiques, chimiques et mécaniques des échantillons concernant les paramètres du procédé. Le manque de modélisation permet une simulation structurelle et fluidique fiable des compresseurs en ce qui concerne la fabrication additive de pièces pour compresseurs. En effet, de nombreux modèles et simulations sont disponibles

dans la littérature, mais les validations basées sur des tests expérimentaux manquent. Un compresseur centrifuge est conçu sur la base de calculs itératifs d'un modèle 0D en combinaison avec des modèles de perte. Le modèle peut fournir une géométrie préliminaire du compresseur selon le cahier des charges. Ensuite, la géométrie 3D du compresseur a été optimisée grâce au calcul de dynamique des fluides computationnelle (CFD) pour trouver la meilleure géométrie et prédire ses performances. De plus, l'aspect structurel du rotor du compresseur a été analysé grâce à un modèle numérique. La microstructure des matériaux à l'aide de différentes méthodes d'analyse et de caractérisation a été étudiée. De plus, l'influence des paramètres du procédé sur cette microstructure d'une part, et les performances (mécaniques et fonctionnelles) de la pièce a été étudiée. Un thermoplastique haute performance (sulfure de polyphénylène) et une résine (Rigid 10k) ont été sélectionnés pour fabriquer les rotors. La fabrication additive a été choisie comme méthode de fabrication. La FFF et la SLA ont obtenu les pièces. Les résultats montrent le rôle clé de la coalescence entre couches adjacentes lors de la fabrication. Réduire l'adhésion intercouche peut réduire considérablement les performances. L'analyse de ce paramètre a été faite par observation microscopique et l'amélioration de l'espaceur entre les couches a permis d'augmenter le rendement de 22% à 64% pour les rotors fabriqués par FFF. Le modèle de cicatrisation développé a fourni des prévisions raisonnables sur la force de liaison en incluant les termes de diffusion ainsi que la température à l'intérieur de la pièce imprimée. Le modèle de cicatrisation d'interface développé sur la base de la théorie de la reptation a été appliqué avec succès aux expériences de soudage de polymères. Les résultats d'une force de liaison précise basée sur leurs propriétés rhéologiques et les conditions de traitement prospectives de l'acide polylactique

peuvent fournir un aperçu des informations a priori sur les propriétés du matériau et les conditions de traitement. L'effet de deux paramètres de processus, à savoir la vitesse et la température de la buse, ainsi que le temps de recuit en tant que méthode de post-traitement sur le comportement mécanique de la couche intermédiaire et le pourcentage de cristallisation des pièces imprimées, ont été étudiés. Le sulfure de polyphénylène a été sélectionné comme polymère haute performance au cours de cette étude. Les paramètres ont été optimisés grâce à une optimisation multi-réponses utilisant la méthode GRA. Les paramètres de processus et le temps de recuit ont été trois variations comme paramètres d'entrée pour obtenir les meilleures propriétés mécaniques intercouches et un pourcentage de cristallisation élevé. Analyser le Les données GRG par ANOVA et S/N ont montré les paramètres de processus optimaux de température et de vitesse de buse de 340 et 20 mm/min, respectivement, recuits à 200 °C pendant 6 h. Les résultats microscopiques montrent l'importance des paramètres de bonne coalescence entre les couches imprimées qui impactent les propriétés mécaniques et physico-chimiques. Étudier les études physiques, chimiques et mécaniques de l'uréthane résine diméthacrylate en approche stéréolithographie. Les propriétés mécaniques des échantillons verts et post-durcis ont été analysées pour les différentes orientations des sous-constructions. Le résultat obtenu explique le mécanisme de durcissement des échantillons lors du post-durcissement et la valeur de la résine résiduelle a été calculée. Le rôle clé de la résine résiduelle dans les pièces lors des analyses thermiques et mécaniques a été expliqué. Cet effet était étudié les transitions vitreuses des échantillons afin que le post-durcissement provoque l'augmentation de la transition vitreuse. Selon les résultats, une augmentation de la température de post-durcissement a augmenté la résistance à la traction, de sorte que le post-durcissement à 80 °C

a provoqué une augmentation de la polymérisation jusqu'à 98 %. Enfin, les résultats ont montré la résistance à la traction maximale dans le rang $90° < 0° < 45°$. Une simulation numérique a été réalisée pour l'analyse structurelle de la roue fabriquée de manière additive. L'analyse numérique fournit la catégorie de sélection des matériaux à différentes forces centrifuges correspondant aux différentes vitesses de rotation. Enfin, l'importance de la microstructure et des paramètres du procédé sur les performances finales du compresseur a été démontrée.